Optics of van der Waals layered systems

Jadriško, Valentino

UNIVERSITY OF ZAGREB
FACULTY OF SCIENCE
DEPARTMENT OF PHYSICS

Valentino Jadriško

Optics of van der Waals layered systems

DOCTORAL THESIS

Zagreb, 2022.

University of Zagreb

UNIVERSITY OF ZAGREB
FACULTY OF SCIENCE
DEPARTMENT OF PHYSICS

Valentino Jadriško

Optics of van der Waals layered systems

DOCTORAL THESIS

Supervisor: dr. sc. Nataša Vujičić

Zagreb, 2022.

Sveučilište u Zagrebu

SVEUČILIŠTE U ZAGREBU
PRIRODOSLOVNO-MATEMATIČKI FAKULTET
FIZIČKI ODSJEK

Valentino Jadriško

Optika van der Waals slojevitih sustava

DOKTORSKI RAD

Mentor: dr. sc. Nataša Vujičić

Zagreb, 2022.

INFORMATION ABOUT MENTOR AND PROJECTS

Name and Surname: dr.sc. Nataša Vujičić
Title: Research Associate
Institution: Institute of Physics, Zagreb, Croatia
E-addressa: natasav@ifs.hr
web: http://www.ifs.hr/people/natasa-vujicic/

Achievements in the last 5 years:
Projects:
2023. - Research Infrastructures services enabling the development of materials for a circular economy – ReMADE@ARIE, coordinator for the Institute of Physics
2019.-2023 The Integrated Initiative of European Laser Research Infrastructures — LASERLAB-EUROPE, team member
2017. - Center for Advanced Laser Techniques (CALT), infrastructural project, project team member, Ultrafast unit
2017. - Center of Excellence for Advanced Materials and Sensing Devices, infrastructural project, team member in the Science of Graphene and Related 2D Structures Research Unit
2018. - 2023 Photoexcitations in 2D Semiconductors, Installation grant, Croatian science findation, principal investigator
2017.-2021. Optical Properties of Transition Metal Dichalcogenide Heterostructures, Research Project, Croatian science findation, team member

Publications:
1. V. Jadriško, B. Radatović, B. Pielić, C. Gadermaier, M. Kralj and N. Vujičić, *Structural and optical characterization of nanometer sized* MoS_2*/graphene heterostructures for potential use in optoelectronic devices*, FlatChem 2022, 34, 100397 doi: https://doi.org/10.1016/j.flatc.2022.100397

2. B. Radatović,V. Jadriško, S. Kamal, M. Kralj, D. Novko, N. Vujičić, M. Petrović, *Macroscopic single-phase monolayer borophene on arbitrary substrates*, ACS Appl. Mater. Interfaces 2022, 14, 18, 21727–21737

3. B. Pielić, D. Novko, I. Šrut Rakić,J. Cai, M. Petrović, R. Ohmann, N. Vujičić; M. Basletić, C. Busse, M. Kralj, *Electronic Structure of Quasi-Freestanding* WS_2*/*MoS_2 *Heterostructures*, ACS Appl. Mater. Interfaces 2021, 13, 42, 50552–50563

4. I. Delač Marion, D. Čapeta, B. Pielić, F. Faraguna, S. Gallardo, P. Pou, B. Biel, N. Vujičić, M. Kralj, *Atomic-scale defects and electronic properties of a transferred synthesized* MoS_2 *monolayer*, Nanotechnology 2018, 29 305703

5. N. Saigal, I. Wielert, D. Čapeta, N. Vujičić, B.V. Senkovskiy, M. Hell, M. Kralj, and A. Grüneis, *Effect of lithium doping on the optical properties of monolayer* MoS_2, Appl. Phys. Lett. 2018, 112, 121902
Resume: 26 CC papers, 252 citations, h-index: 10 (WoS)

Editorial: Materials, Optical Properties of Two Dimensional Materials (guest editor)
Mentorship: Supervising 3 Master Students, 2 PhD Students and 2 Undergraduate students on Practical work

This thesis was made under the mentorship of dr. sc. Nataša Vujičić as part of the doctoral study at the Department of Physics, Faculty of Science, University of Zagreb. Here presented experimental work was carried out at the Institute of Physics in Zagreb, as well as at the Politecnico di Milano and Instituto de Ciencia de Materiales de Madrid. The work presented within this thesis was funded through HRZZ (projects UIP-2017-05-3869 “Photoexcitations in 2D Semiconductors” and IP2016-06-3211 “Optical Properties of Transition Metal Dichalcogenide Heterostructures”) and Center of Excellence for Advanced Materials and Sensing Devices (ERDF grant no. KK. 01.1.1.01.0001).

Acknowledgements

During my 5 year of doing PhD studies I was lucky to have dr. sc. Nataša Vujičić as a mentor who was my friend and a constant support in things connected to work and private life. I would like to thank Nataša for giving me the freedom to explore my own scientific curiosity with the necessary guidance to succeed in my goals. I am deeply grateful and will always remember Nataša for her understanding and support during my father's sickness. Nataša always had absolute trust in me to do work properly and to unreservedly stand for me in front of others when necessary. All of this allowed me to develop my scientific self esteem and prowess for which I express my gratitude to her.

International scientific experience and collaborations are one of the most important parts of a young PhD student's career. Both dr. sc. Nataša Vujičić and dr. sc. Marko Kralj enabled me to have extensive international experience abroad through their contacts and funding, which allowed me to rapidly grow my knowledge and I am deeply thankful to them. Through these collaborations I have been allowed to work with prof. dr. Christoph Gadermaier and prof. dr. Giulio Cerullo from Politecnico di Milano in Italy, prof. dr. Rudolf Bratschitsch from University of Munster in Germany, prof. dr. Carsten Busse from the University of Siegen in Germany to whom all I am grateful for their hospitality and their knowledge.

I am thankful to have a great friend and colleague working alongside me, Borna Radatović, with whom I always found some new scientific direction to explore and support when needed, my PhD journey wouldn't be as fun without you. I am thankful to both him and his mentor dr. sc. Marin Petrović to be able to explore optical properties of their Borophene samples. I thank Borna Pielić for fruitful scientific discussions and providing me with his TMDs/graphene heterostructure samples. I am thankful to have theoretical support for some of my work which was provided by dr. sc. Dino Novko, dr. sc. Vito Despoja.

I would also like to acknowledge other colleagues with whom I have worked together, namely Antonio Supina, Željko Rapljenović, dr. sc. Silvije Vdović, dr. sc. Hrvoje Skenderović, dr. sc. Damir Dominko, dr. sc. Cristian Manzoni, prof. dr. Gianluca Valentini, prof. dr. Marko Spasenović.

In the end, personally I give the biggest credit and gratitude to my parents, without them I wouldn't have developed into a person capable of doing a PhD and someone with whom people are willing to collaborate. My mother Ivanka gave me all the love and support I needed to have the courage to tackle any obstacle and achieve any goal I set my mind to. My late father Tomislav instilled the love for lab work and showed me how to be a good person and that every technical problem can be solved.

Short summary

The bandgaps of many atomically thin 2D layered materials such as graphene, blackphosphorus, semiconducting transition metal dichalcogenides (TMDs) and hBN range from 0 to 6eV. These isolated atomic planes can be reassembled in van der Waals (vdW) two-dimensional (2D) layered structures with precisely chosen vdW stacking sequences and interlayer coupling, which opens the avenues for creating new materials systems with rich functionalities and novel electronic and optical properties. Combination of TMD semiconductors such as MoS_2 and WS_2 which act as a good absorber of incident light and a conductive layer of graphene with its good mobility, efficient charge transfer and separation offers unique opportunity to capture all the advantageous properties of both types of materials to achieve efficient photodetectors. We investigated nanometer-sized islands of MoS_2 on a graphene layer on Ir(111) crystal in ultra-high vacuum (UHV) and transferred to arbitrary substrates such as Si wafer. *In-situ* and *ex-situ* surface characterization with scanning probe techniques reveals preservation of morphologic features upon exposure to atmospheric conditions and transfer to wafer. Measurements by micro-Raman and photoluminescence spectroscopy confirmed textbook optical features indicating successful transfer; the first step to utilize UHV grown 2D materials in optoelectronic applications. Additionally, we have applied the same methods to the nanometer-sized vertical and horizontal WS_2/MoS_2/graphene heterostructures and measured their optical response at 4.2 K to investigate semiconductor bandgap expansion confirming it is governed by the electron-phonon coupling. Next, we focused on the influence of the strain on optical properties of 2D TMDs which are known to withstand high levels of strain. We analyze optical bandgap shrinkage with strain increase in monolayers and twisted bilayers of WS_2. Due to changing of interlayer distances for different stackings of WS_2 bilayers, the strain gauge factors change in agreement with density functional theory (DFT) calculations. Ultrafast temporal dynamics in the strained systems showed we are able to control exciton lifetimes. Finally, we have measured Raman spectra of UHV synthesized borophene on Ir(111) before and after its transfer to Si wafer. Agreement between two experimental Raman spectra and DFT calculations validated postulation from surface characterization that borophene is successfully transferred to an arbitrary substrate and is stable.

Sažetak

Poglavlje 1 – Uvod

1959. godine Richard P. Feynman je održao svoje poznato predavanje *„Puno je mjesta na dnu: pozivnica u novo polje fizike“ (engl. ‘’There's Plenty of Room at the Bottom: An Invitation to Enter a New Field of Physics’’)* [1] s ciljem otvaranja novog polja istraživanja koje danas nazivamo nanotehnologija. Tijekom predavanja je također rekao: *„Neće nam reći puno o fundamentalnoj fizici…“,* ali i *„imati će enorman broj primjena u tehnologiji.“* (kraj citata) Također je i postavio zanimljiva pitanja poput: *„Što možemo napraviti sa slojevitim strukturama ako imamo pogodne slojeve?”* i *„Kakva bi bila svojstva tih materijala kada bi zaista mogli rasporediti atome kako želimo?”* Otkrićem grafena 2004. godine, A. Geim i K. Novoselov otvorili su novo polje fizike dvodimenzionalnih materijala, za što su dobili Nobelovu nagradu 2010. godine. „Istraživanje s dna“, kroz 2D materijale, donijelo nam je tehnološke primjene i napretke ali i novu fundamentalnu fiziku i primjenu u svakodnevnom životu. Danas, nakon više od 60 godina, i dalje je puno posla pred nama u potrazi za odgovorom kako možemo dizajnirati materijale poželjnih svojstava i uspješno ih sintetizirati na atomskoj razini. Najbliže što smo došli u ostvarenju tog cilja je tehnika epitaksijalnog rasta molekularnom zrakom višeslojnih (III-IV) heterostruktura koje je dovela do razvoja poluvodičkih lasera, vrlo brzih fotodetektora i solarnih ćelija. [2–4]

Poglavlje 2 – 2D materijali

2D materijali imaju jake kovalentne veze unutar sloja i slabe van der Waals (vdW) interakcije između slojeva što omogućuje njihovu eksfolijaciju. [5] Neočekivano, postoji veliki broj vdW slojevitih materijala u 2D obliku s izolatorskim, metalnim, polumetalnim i poluvodičkim svojstvima. [6–9] Njihova svojstva, poput veličine i prirode energetskog procjepa, mogu se se mogu kontrolirati mijenjanjem broja slojeva materijala zbog utjecaja vdW vezanja slojeva, kvantnog zatočenja i dielektričnog okruženja. Jedna od prednosti 2D materijala je mogućnost slaganja slojeva jednog na drugi, bez ograničenja, uslijed podudaranja njihovih kristalnih rešetki, što predstavlja bogatu paletu mogućnosti za stvaranje novih umjetnih 2D materijala . [5,10,11]

Dihalkogenidi prijelaznih metala (TMD) su najpoznatiji 2D materijali nakon grafena te glavni predstavnici poluvodičkih atomski tankih materijala. Njihova opća formula je X-M-X, gdje je M prijelazni metal koji se nalazi u sendviču dva halkogenida X, što je prikazano na Slikama 2.1. i 2.2., s debljinom oko 0.6 nm. Slika 2.2. također pokazuje i različite faze koje se mogu naći u 3D i 2D granici. Grafen je tanka plahta debljine jednog atomskog sloja kovalentno povezanih ugljikovih atoma složenih u heksagonalnu rešetku, s debljinom od 0.34 nm. [12,13] Svaki atom u sloju grafena je kovalentno povezan s tri susjedna ugljikova atoma u sp^2 konfiguraciju, dok preostali, slobodni elektron tvori p_z orbitale okomite na ravninu. [12] Takva struktura rezultira polumetalnom prirodom grafena s energetskim procjepom od 0 eV, prikazanim na Slici 2.4 a). [14] Unatoč debljini od samo jednog atoma, grafen apsorbira 2.3% upadne bijele svjetlosti zbog svoje jedinstvene elektronske strukture, Slika 2.3 c). [15] Sinteza 2D boron polimorfa odnosno borofena predstavlja znamenit primjer uspjeha eksperimentalne sinteze sintetičkog 2D materijala vođene teorijskim predviđanjima rasta. [16] Borofen je atomski tanak sloj atoma bora koji je zadnjih godina privukao puno pažnje zbog svojih iznimnih svojstva prikazanih na Slici 2.5. Njegova metalična i mehanička svojstva bi posebno mogla biti korisna za integraciju u heterostrukture s poluvodičkim 2D materijalima, za izradu uređaja poput Schottky dioda i tunelirajućih tranzistora te fleksibilne elektronike. [16–19]Kombiniranjem različitih 2D slojeva možemo stvarati heterostrukture poželjnih svojstava, poput kombinacije poluvodiča i vodiča, npr. MoS_2 i grafen, koji predstavljaju kombinaciju materijala odličnih optičkih svojstava (MoS_2) i visoke mobilnost i transparentnosti (grafen) u različitim konfiguracijama prikazanima na Slici 2.6. [20–25] Izrada direktno naraštanih 2D heterostruktura s najmanje tri različita materijala puno je teži zadatak nego kada su u pitanju samo dva različita materijala, te je svega nekoliko takvih primjera u literaturi, koji su prikazani na Slici 2.7. [26–29] U ovom doktorskom radu pokazali smo primjer uspješne sinteze i karakterizacije još uvijek egzotičnog materijala- borofena kao i heterostruktura načinjenih od dva i tri različita 2D materijala te istražili njihova optička svojstva.

Poglavlje 3 – Optička svojstva 2D materijala

U poluvodičima, apsorpcijom svjetlosti energije fotona veće ili jednake od njihovog energetskog procjepa elektroni se fotopobude iz valentne u vodljivu vrpcu, ostavljajući šupljine u valentnoj vrpci. Negativno nabijeni elektroni i pozitivno nabijene šupljine u različitim vrpcama se međusobno privlače Coulombovom interakcijom, pri čemu se vežu u neutralne kvazičestice koje nazivamo ekscitoni. [30]

Ekscitoni u 2D materijalima imaju iznimno visoke energije vezanje i do 1 eV, što omogućuje njihovo opažanje na sobnim temperaturama. To je omogućilo istraživanje ekscitonskih fenomena pri sobnim temperaturama te uzlet ekscitonske fizike. [31–41] Razlozi tako velikih energija vezanja leže u efektima kvantnog zatočenja i dielektričnog zasjenjenja prikazanog na Slici 3.1 a) i b). [36] Slika 3.1 c) prikazuje tipične energetske nivoe koje pronalazimo u poluvodičkim TMD materijalima, koji pokazuju bogatu ekscitonsku fiziku. Promjena dielektričnog okruženja pomoću različitih podloga i blizina drugih materijala utječe na dielektrično zasjenjenje omogućujući kontrolu svojstva ekscitona i njihovih energetskih nivoa, Slika 3.1 d). [39,42,43] U 2D materijalima opažamo svijetle i tamne ekscitone te lokalizirane ekscitone u lokalnim potencijalima uzrokovanim defektima i/ili naprezanjima, Slika 3.2. [44] Tamni ekscitoni su ekscitoni u kojim emisija svjetlosti nije moguća jer je optički prijelaz zabranjeni spinom i/ili momentom. Uz neutralna dvočestična stanja, nailazimo i na nabijena tročestična vezana stanja, koje zovemo trioni, a koji mogu biti pozitivni (posjeduju dodatna šupljinu) i negativni (posjeduju dodatni elektron). Biekscitone su neutralne kvazičestice i sastoje se od dva slobodna ili vezana ekscitona. Međuslojni ekscitoni su vezana stanja koja se javljaju u višeslojnim materijalima, s elektronom u jednom sloju i šupljinom u drugom sloju materijala, što je prikazano na Slici 3.3. [34,45–54]

Ramanova spektroskopija otkriva Ramanove aktivne fonone u 2D materijalima koji su okarakterizirani oblikom krivulje, položajem fononskog maksimuma, širinom i intenzitetom te sadrže korisne informacije o materijalu poput dopiranja, naprezanja, faznih prijelaza, broju slojeva materijala, sastavu materijla, prisutnosti slitina i dr. [55–62]

Slika 3.4 prikazuje najvažnije Ramanove modove za grafen na Slici 3.4 a) i b) te TMD-ove na Slici 3.4 c). Ramanov G mod grafena povezujemo s vibracijama atoma ugljika u ravnini grafenskog sloja, dok je D mod indikator defekata u grafenu. Iz omjera intenziteta 2D i G modova možemo odrediti da li je grafen u granici jednosloja. [63]
E simetrijski fononi u TMD-ovima odgovaraju pomaku atoma unutar ravnine sloja dok A i B simetrijski fononi odgovaraju pomaku atoma okomitom na ravninu sloja, prikazano na Slici 3.4 c). [64–67] Kao mogući put za modificiranje elektroničkih i optičkih svojstava dvodimenzionalnih (2D) materijala istražuje se utjecaj unosa naprezanja u materijal. [68] Interes za ovu temu proizlazi iz njihove otpornosti na mehaničke deformacije. Ovi sustavi podnose deformacije reda veličine 10%, [69,70] dok se konvencionalni 3D poluvodički materijali lome još pri sasvim umjerenim deformacijama od 0,5 – 1,5 %. [71] Slika 3.5 prikazuje eksperimentalne postave za ispitivanje unosa uniaksijalnog vlačnog naprezanja savijanjem. Savijanje u dvije točke koje je prikazano na Slici 3.5 a) ima nedostatak da se prilikom promjene naprezanja mijenja i položaj uzoraka u z-smjeru, što otežava optičku karakterizaciju materijala i ispitivanje promjene svojstava uslijed naprezanja. Korištenjem postava za savijanje u tri točke, koji je prikazan na Slici 3.5 b) spomenuti nedostatak je uklonjen, međutim, postav je moguće koristiti samo u refleksnoj geometriji. Postav za savijanje u 4 točke, prikazan na Slici 3.5 c), omogućava rad i u transmisiji. Za unos biaksijalnog naprezanja u 2D materijalima koriste se različite eksperimentalne tehnike, poput termalne ekspanzije Slika 3.6 a), točkasno naprezanje AFM vrškom Slika 3.6 b), mehaničkim rastezanjem podloge Slika 3.6 c) te nalijeganje 2D materijala na nano-stupove koji unose nanometarski lokalizirano naprezanje koje može uzrokovati i jedno-fotonsku emisiju. [68,72–74] Nova generacija 2D materijala ima potencijal u rješavanju trenutnih tehnoloških ograničenja u optoelektronici poput niske potrošnje energije, visoke efikasnosti, niskog ugljičnog otisaka i velika brzina. [75] Zbog svojih svojstva, 2D materijali se mogu primijeniti u razvoju novih optoelektroničkih uređaja poput onih prikazanih na Slici 3.7. Na Slici 3.7 a) je prikazan ultra osjetljivi fotodetektor na bazi MoS_2 bolji oko 10^6 puta od prvog grafenskog fotodetektora. Hetero pn spoj MoS_2 i Si možeslužiti kao uređaj koji emitira svijetlost, prikazan na Slici 3.7 b). Nova generacija ultra osjetljivih solarnih ćelija može biti napravljena od uređaja baziranih na WSe_2 u konfiguraciji prikazanoj na Slici 3.7 c). [76–78] U ovoj doktorskoj diesertaciji istraživali smo mogućnost primjene heterostruktura MoS_2 i grafena kao novog materijala za promjenu u optoelektronici.

Poglavlje 4 – Eksperimentalne tehnike i priprema uzoraka

Postoje razne metode pripremanja 2D uzoraka, jedna od prvih bila je tzv. „top-down“ tehnika mikromehaničke eksfolijacije. Prvi 2D materijal- grafen pripremljen je upravo tehnikom mikromehaničke eksfolijacije, za što je dodjeljena ranije spomenuta Nobelova nagrada Geimu i Novoselovu. U ovoj tezi koristimo dvije metode pripreme uzoraka pomoću tzv. „bottom-up“ pristupa: kemijsko taloženje para (CVD) i epitaksijalni rast iz molekularne zrake (MBE). Obje tehnike pružaju mogućnost primjene rasta 2D materijala na velikim skalama koje su potrebne za široko upotrebu u svakodnevnom životu. Uspoređujući navedene dvije metode, CVD pruža mogućnost rasta na širem izboru podloga (metalnim i nemetalnim) te jednostavniji postav u ambijentalnim uvjetima, dok je MBE metoda ograničena na metalne podloge u ultra-visokom vakuumu (UHV), uz prednost bolje kontrole parametara sinteze u odnosu na CVD tehniku. Slika 4.1 prikazuje shemu CVD peći koja se koristi za naraštanje kontinuiranog sloja MoS_2 i WS_2 jednosloja i dvosloja. U slučaju korištenja krutih prekursora, njihovo dopremanje do podloge poput Si osigurava se tokom plemenitog plina argona, a moguće je i korištenje tekućih prekursora koji se direktno nanose na podlogu na kojoj se odvija rast. MBE rast odvija se u UHV gdje se elektronskom zrakom evaporiraju prijelazni metali, a korištenjem Knudsenove ćelije halkogenidi na prije naraštani potpuni sloj grafena koji se sintetizira iz etilena na Ir(111) podlozi, kao što je prikazano na Slici 4.2. U literaturi su poznate različite metode prijenosa materijala s podloge na podlogu, svaka s određenim prednostima i nedostacim. U ovoj tezi koristili dvije različite metode prijenosa materijala: mokri prijenos, pomoću PDMS-a, za prijenos uzoraka sa Si podloge te elektrokemijsku delaminaciju pomoću PMMA za uzorke s Ir(111) podloge. Mokri transfer s PDMS-om je relativno jednostavan i brz postupak gdje se koristi 160 μm debeo PDMS i deionizirana (DI) voda s nekoliko kapi amonijaka, Slika 4.3. Elektrokemijska delaminacija je složeniji postupak te ima dva elektrokemijska koraka i još nekoliko prethodnih i naknadnih koraka, uz upotrebu stotinjak nm debelog sloja nakapanog PMMA, a sam postupak traje najmanje 24h, Slike 4.4. i 4.5. Optička mjerenja apsorpcije, fotoluminiscencije i Raman spektroskopije izvodili smo na mikro-Raman optičkom postavu kućne radinosti („home-built“) koji se sastoji lasera valne duljine 532 nm, spetrometra duljine 50 cm i hlađenog EMCCD-a i niza optičkih i optomehaničkih komponenti. Postav je prikazan na Slikama 4.6 i 4.7. Hiperspektralne mape su snimane s dvolomnim TWINS interferometrom na Politecnico

di Milano koji koristi dva pomična klina za stvaranje interferograma, CMOS kameru i laser valne duljine 532 nm, prikazan na Slikama 4.8 i 4.9. Niskotemperaturna mjerenja rađena su u protočnom optičkom kriostatu kojeg smo hladili tekućim helijem. Na Slici 4.11 prikazan je cijeli sustav za kriogeno hlađenje kriostata. Površinske analize su rađene pomoću skenirajućeg tunelirajućeg mikroskopa u ultravisokom vakuumu i mikroskopa atomskih sila u ambijentalnim uvjetima. Inicijalna karakterizacija i potvrda rasta u UHV uvjetima omogućena je niskoenergetskom elektronskom difrakcijom (LEED). Ultrabrzu dinamika uzorka pod naprezanjem istraživali smo tzv. pump-probe optičkim postavom koji se bazira na femtosekundnom laserskom pojačalu vremenske rezolucije od 100 fs.

Poglavlje 5 – Nanometarske MoS_2/grafen heterostrukture

U ovom poglavlju predstavljeni su rezultati uspješne MBE sinteze MoS_2/grafen heterostrukture i naknadni prijenos uzorka na Si podlogu, što postavlja temelj za moguću buduću primjenu visokokvalitetnih sintetiziranih TMD i srodnih heterostruktura u optoelektroničkim uređajima. Uzorak promjera 6 mm, ograničen veličinom Ir(111) podloge, u cijelosti je uspješno prebačen na proizvoljnu podlogu korištenjemi elektrokemijske delaminacije. Uzorak se sastoji od nanometarskih otoka MoS_2 na kontinuiranom sloju grafena promjera 6 mm. Uspješnost transfera je potvrđena zadržanim intrinzičnim strukturalnim i elektronskim svojstvima MBE naraštanih slojeva. Inicijalni rast grafena te zatim MoS_2 otoka potvrđen je LEED tehnikom dok je precizna morfološka ispitivanja uzorka u UHV uvjetima napravljena pomoću STM-a koja je kasnije uspoređena s topografijom dobivenom AFM-om u ambijentalnim uvjetima. AFM mjerenja prije transfera potvrđuju 22% zastupljenost MoS_2 otoka, prosječnu visinu od 1 nm te u prosjeku 6 osnovnih segmenata po otoku, potvrđujući stabilnost uzorka u ambijentalnim uvjetima. Nakon transfera elektrokemijskom delaminacijom, AFM analiza otkriva 95% uspješnost transfera s Ir(111) na proizvoljnu podlogu u ovom slučaju Si te zadržanu međuslojnu udaljenost koja je indikator održane morfološke strukture. Izmjereni spektar fotoluminiscencije pokazuje karakteristične emisijske linije A ekscitona MoS_2, s energijama usporedivim onima iz literature te se vidi utjecaj grafena na smanjenje intenziteta uzrokovan prijenosom naboja u grafenski sloj. Širina

ekscitonske linije upućuje na visoko kvalitetne uzorke usporedive s onima dobivenim mehaničkom eksfolijacijom. Izrazita kvaliteta uzorka potvrđena je i Raman spektroskopijom koja potvrđuje prisutnost heterostrukture te nisku koncentraciju defekata. Pokazali smo da MBE sintetizirane MoS_2/grafen heterostrukture u kombinaciji s pogodnom procedurom za prijenos uzorka s podloge na podlogu mogu služiti kao put k izradi visoko efikasnih optoelektroničkih uređaja na način da se fotopobuđeni elektron-šupljina parovi iz poluvodiča efikasno prenose u kontaktirani grafenski sloj, koji je u neposrednom dodiru s poluvodičem. Također, morfologija uzorka i prisutnost nanometarskih rubova može se iskoristiti za jednofotonsku emisiju.

Poglavlje 6 – Nanometarske WS_2/MoS_2/grafen heterostrukture

Nastavno na prethodno poglavlje, istraživali smo kompleksnije heterostrukture koje se sastoje od tri različita materijala. Koristeći MBE rast u UHV naraštane su vertikalne i lateralne nanometarske heterostrukture WS_2/MoS_2 na grafenu interkaliranom Mo atomima na Ir(111) podlozi. Inicijalna karakterizacija rasta nakon svakog koraka napravljena je LEED tehnikom, a analiza morfologije uzorka i njegove topografije STM tehnikom, koji je ukazao na pokrivenost uzorka od 33% za MoS_2 te 77% za WS_2 gdje je 74.6% u prvom sloju (direktno na grafenu) te 25.4% u drugom sloju (na MoS_2 otocima). Ambijentalna AFM karakterizacija na Ir(111) podlozi pokazuje očuvanu strukturu i morfologiju uzorka ukazujući na dugotrajnu stabilnost u ambijentalnim uvjetima. Prijenos s metalne na Si podlogu ponovo je izveden pomoću elektrokemijske delaminacije. Optičkom mikrografijom je potvrđeno da se uzorak nije prenio u potpunosti. AFM analiza transferiranog uzorka pokazala je da određeni dijelovi uzorka imaju kontaminacije i korugacije koje sprječavaju optički odziv WS_2/MoS_2/grafen heterostrukture. Unatoč tome, postoje veliki dijelovi uzorka bez kontaminacija i s visoko kvalitetnim optičkim odzivom koji upućuju na to da se radi o heterostrukturi. Raman spektroskopija potvrđuje prisutnost WS_2, MoS_2 i grafena nakon prijenosa uzorka na Si podlogu. Oslikavanje hiperspektralnim interferometrom pokazuje homogeni intenzitet i spektralni odaziv visoko kvalitetnih dijelova uzorka. U fotoluminiscencijskom odzivu primjetan je oslabljeni intenzitet ekscitona na energijama 617.5 nm (WS_2) i 671.6 nm (MoS_2) zbog transfera naboja u grafenski sloj. Sve tri optičke tehnike su potvrdile

prisutnost prijenosa naboja zbog prisutnosti tip-II slaganja elektronskih vrpci u heterostrukturi. Efikasan prijenos naboja je direktna potvrda netaknutog sučelja između različitih slojeva, koja potvrđuje da je tehnika prijenosa uzorka između podloga neinvazivna te ne utječe na intrinzična svojstva heterostrukture. Uspoređujući STS mjerenja kvazičestičnog energetskog procjepa na 125 K i niskotemperaturna optička mjerenja fotoluminiscencije pri istoj temperaturi, možemo izračunati energiju vezanja A ekscitona MoS_2 koja iznosi 600 meV dok je za WS_2 180 meV, što je nešto niža vrijednost od očekivane zbog utjecaja prijenosa naboja posredovanog brzim fononima. Iz ovisnosti ekscitonskih energija o temperaturi možemo izračunati energiju elektron-fonon vezanja od 47.4 meV (383.3 cm^{-1}) i 42.7 meV (344.4 cm^{-1}) koja su u skladu s energijama glavnih fononskih modova WS_2 i MoS_2. Eksperimentalno utvrđeno smanjenje energetskog procjepa u ovisnosti o temperaturi ukazuje na utjecaj fonona na širinu energetskog procjepa, koje potvrđuje jako elektron-fonon vezanje.

Poglavlje 7 – Utjecaj naprezanja na optička svojstva TMD-a

Motivacija za istraživanje utjecaja naprezanja na optička svojstva nastaje suradnjom s grupom R. Bratschitscha i objavom rada na temu efikasnog prijenosa naprezanja kroz granice zrna u kontinuiranim CVD sintetiziranim MoS_2 jednoslojevima. Nastavak istraživanja usmjeren je na CVD sintetizirane dvosloje WS_2 s različitim orijentacijama od 0° i 60°, odnosno, AA i AB slaganje. Korištenjem tehnike savijanja u 3 točke proučavali smo ovisnost mjernih faktora (eng. *gauge factors*) naprezanja za različita slaganja dvosloja. Statistička analiza za utvrđivanje položaja i FWHM ekscitona A pokazuje vrijednosti mjernih faktora naprezanja od -34.77 meV/% za AA i -37.76 meV/% za AB slaganje. Usporedba s dobivenim teorijskim vrijednostima od -56.45 meV/% za AA i -60.25 meV/% za AB slaganje, ukazuje da imamo dobar trend u odnosu na različite orijentacije slojeva, uz određeno očekivano odstupanje zbog eksperimentalnih uvjeta i odziva uzorka uslijed naprezanja. Navedene teorijske vrijednosti predstavljaju gornju granicu na dobivene eksperimentalne vrijednosti. Opažen je i utjecaj na FWHM u dvoslojnom WS_2 koji nije opažen u jednoslojnom materija, obzirom da je dvoslojni materijal indirektni poluvodič, gdje fononi igraju ulogu u ekscitonskim raspršenjima, zbog čega naprezanjem možemo kontrolirati FWHM u dvoslojevima.

Istraživali smo i ultrabrzu vremensku dinamiku pod naprezanjem u jednoslojnom WS_2, primjenom eksperimentalne tehnike savijanja u 2 točke u kombinaciji s pump-probe tehnikom. Rezonantna ekscitonska energija pri 0% naprezanju je za jedan uzorak bila 636 nm, dok je za drugi bila 611 nm. Razlika u mjerenim energijama je uzrokovana različitim uvjetima rasta i defektima samih uzoraka što se odrazilo i u vremenkoj dinamici mjerenih uzoraka. Mjerni faktori naprezanja su manji nego oni očekivani iz literature i utvrđeni prijašnjim mjerenjima, što ukazuje na neefikasan prijenos naprezanja. Vremenska dinamika prvog uzorka sastoji se od jednoeksponencijalnog raspada vremenske konstante od 1 ps, dok je u drugom uzorku prisutan dvoeksponencijalni raspad s dvjema vremenskim konstantama: brzom vremenskom konstantom od 0.3 ps te sporijom od 6 ps. Brza konstanta raspada u oba uzorka ima jednaku, konstantnu ovisnost o naprezanju, od otprilike 55 fs/% (femtosekundi po postotku naprezanja) ukazujući na isto porijeklo brzih relaksacijskih procesa u oba uzorka. U slučaju sporog vremena raspada u drugom uzorku, ovisnost o naprezanju je 26 ps/%, odnosno, tri reda veličine veća. Spora vremenska konstanta raspada raste sve do 20 ps za 0.6% naprezanja. Pokazali smo da pomoću naprezanja možemo kontrolirati vremena života ekscitona što otvara nove mogućnosti u primjeni ovih materijala. Tako, na primjer, za primjenu u fotovoltaicima pogodniji su kratkoživući ekscitoni, zbog brze disocijacije eksctona na slobodne nositelje naboja, dok, prilikom naprezanja, nastaju dugoživući ekscitoni koji su korisni za primjenu u ultrabrzim pulsnim laserima. Prema našim saznjima i uvidom u literaturu, ovo su prva provedena eksperimentalna mjerenja vremenske dinamike poluvodičkih TMD pod naprezanjem te predstavljaju originalan doprinos u istraživanju optičkih svojstava vdW slojevitih materijala.

Poglavlje 8 – Optička karakterizacija borofena

U suradnji s kolegama iz grupe, istraživali smo borofen naraštan u UHV uvjetima na Ir(111) podlozi, nakon čega je transferiran elektrokemijskom delaminacijom na proizvoljnu podlogu, u ovom slučaju opet Si podlogu. Prva potvrda uspješnog transfera dana je AFM-om, elektronskim mikroskopom (SEM) i optičkim mikroskopom koji su pokazali uspješno prenesen skoro milimetarski velik uzorak borofena. Fokus ovog poglavlja je bio na optičkoj karakterizaciji borofena prije i poslije transfera te usporedba ekperimentalnih rezultata s rezultatima DFT računa. Obzirom da je borofen bio fizički,

a ne kemijski adsorbiran na metalnoj površini iridija Ir(111) bili smo u mogućnosti izmjeriti Ramanove fononske modove borofena na metalnoj podlozi. Nakon prijenosa borofena na Si podlogu ponovili smo Ramanova mjerenja na istom uzorku borofena, a dobiveni Ramanovi spektri su, uz potpis borofena, pokazivala i Ramanov mod Si podloge, no ne i prisutnost zaostalog PMMA kojeg smo koristili prilikom prijenosa materijala između dvije podloge. Usporedba eksperimentalnih rezultata s izračunatim DFT gustoćom stanja za slobodnostojeći borofen daje dobra slaganja teorije i eksperimenta, čime je dodatno potvrđen uspješan transfer borofena i njegova ambijentalna stabilnost. Mala neslaganja intenziteta i položaja Ramanovih modova među spektrima dolaze od utjecaja podloge na dielektrično okruženje, kemijske modifikacije uzorka tijekom transfera i otpuštanje naprezanja nakon transfera. Naši rezultati predstavljaju veliki korak prema upotrebi borofena u obećavajućim primjenama poput pohrane energije, optoelektronike i fleksibilne elektronike gdje je uspješna manipulacija borofena od kritične važnosti.

Poglavlje 9 – Zaključak

2D materijali obično pokazuju jaku interakciju svijetlosti i materije te rezultati u ovoj tezi koriste tu interakciju za istraživanje četiri različita slojevita materijala kako bi dobili fundamentalno znanje o fizikalnim procesima i mehanizmima u tim sustavima te naglasili njihovu moguću tehnološku primjenu. Uložili smo veliki trud ne samo u razumijevanje optičkih svojstva, nego i njihovo povezivanje s procedurom i tehnikom rasta uzoraka, metodama prijenosa uzoraka, kristalnom morfologijom i orijentacijom slojeva. Eksperimentalni rezultati na četiri različita sustava su prikazani slijedećim redom: MoS_2/grafen heterostrukture (poglavlje 5) i WS_2/MoS_2/grafen heterostrukture (poglavlje 6), jednoslojni i dvoslojni WS_2 (poglavlje 7) te borofen (poglavlje 8). U poglavlju 5 smo pokazali uspješan rast MoS_2/grafen heterostrukture na Ir(111) podlozi i prijenos na Si podlogu, pri čemu je heterostruktura zadržala morfološka i intrinzične strukturalna svojstva uzorka koja su potvrđena površinkom AFM tehnikom, optičkim mikroskopom te mjerenjem fotoluminiscencije i Ramanovih signala. Optička mjerenja su potvrdila visoko kvalitetne transferirane uzorke s malo defekata te prijenos naboja iz MoS_2 u grafen. Nastavili smo isti smjer istraživanja u poglavlju 6, gdje smo istraživali vertikalne i lateralne nanometarske WS_2/MoS_2 heterostrukture na grafenu s interkaliranim Mo atomima između grafena i Ir(111) podloge. Usporedba ambijentalnih

AFM mjerenja i STM mjerenja u UHV pokazuju zadržanu i stabilnu morfologiju uzorka nakon izlaganja ambijentalnim uvjetima. Korištenjem elektrokemijse delaminacije, prebacili smo uzorak s metalne na Si podlogu. Uz značajne visoko kvalitetne dijelove uzorka čije prisustvo je potvrđeno trima optičkima tehnikama, sve tri tehnike ukazuju na efikasan prijenos naboja kao potvrda očuvane međuslojne strukture. AFM analiza prenešenog uzorka pokazala je da određeni dijelovi uzorka imaju kontaminacije i korugacije koje sprječavaju optički odziv WS_2/MoS_2/grafen heterostrukture. Usporedbom STS mjerenja kvazičestičnog energetskog procjepa i optičkog energetskog procjepa iz spektra fotoluminiscencije mogli smo izračunati energije vezanja ekscitona sukladne onima otprije zabilježenima u literaturi. Temperaturno ovisna mjerenja i izračun elektron-fonon vezanja pokazuju fonon posredovano smanjenje energetskog procjepa. Nakon uspješne međunarodne suradnje koja je urodila člankom koji opisuje efikasan prijenos naprezanja kroz granice zrna na uzorku, u poglavlju 7 nastavljamo s istraživanjem naprezanja u dvoslojima WS_2 različitih AA i AB slaganja. Statistička analiza mjernih faktora naprezanja pokazuje razliku između AA i AB slaganja koje je u skladu s dobivenim DFT računom. Vremenska dinamika jednosloja WS_2 pokazuje ovisnost o parametrima sinteze i količini defekata kroz pojavu novog relaksacijskog kanala i vremena raspada. Pokazali smo da se naprezanjem može mijenjati vrijeme života ekscitona što je korisno za primjernu, gdje kratkoživući ekscitoni su pogodniji za materijale za izradu fotoćelija, dok su dugoživući ekscitoni poželjniji za primjenu u ultrabrzim pulsnim laserima. Borofen, nasljednik grafena, je materijal čija smo optička svojstva proučavali kako na metalnoj Ir(111) podlozi, tako i nakon prijenosa na Si podlogu. Rezultate mjerenja prije i poslije prijenosa te usporedba s dobivenim DFT računom prikazani su u poglavlju 8. Eksperimentalna Ramanova spektroskopija je potvrdila AFM i SEM mjerenja, odnosno, uspješnu sintezu, prijenos materijala između podloga i ambijentalnu stabilnost uzorka, uz dobro slaganje s izračunatim Ramanovim spektrima.

Keywords

2D materials, transition metal dichalcogenides, van der Waals layered materials, monolayers, bilayers, graphene, MoS_2 on graphene, WS_2, MoS_2/WS_2 on graphene, borophene, lateral and vertical heterostructure, optical properties, strain, photoluminescence, Raman spectroscopy,, electron-phonon coupling, temporal dynamics

Contents

1 Introduction

In 1959., Richard P. Feynman gave his famous lecture *There's plenty of room at the bottom* [1] with the intent of opening a new research field which we call today nanotechnology. At the time he said going this route "it will not tell us much of fundamental physics" but "it would have an enormous number of technical applications." He also asked some very interesting questions "What could we do with layered structures with just the right layers?" and "What would the properties of materials be if we could really arrange the atoms the way we want them?". Today, more than 60 years later, we have still more work to do to be able to design and fabricate materials at the atomic level, the closest we got is with molecular beam epitaxy of multilayer (III-IV) heterostructures which lead to development of semiconducting lasers, high speed photodetectors and solar cells.[2,3] However, with the discovery of graphene in 2004. by A. Geim and K. Novoselov, a new field of physics opened with 2D materials, for which a Nobel prize award was granted in 2010. In the end, researching at the bottom, did not only give us technological applications but with discovery of 2D materials also new fundamental physics arose and possible new applications of 2D materials in everyday life.

A van der Waals (vdW) 2D material is defined as a layered material that possesses anisotropic bonds, strong covalent bonds in the eV/atom range within the plane, and weak vdW bonds in meV/atom range perpendicular to the planar direction. [4] One good example of a single-component vdW material is a graphite with strong covalent bonds of 7.3 eV/atom within the plane and vdW interaction of 30−60 meV/atom along the c-axis with an interlayer distance of 3.4 Å. In contrast to graphene with a flat atomic layer, black phosphorus (BP) is a puckered layered material of slightly stronger vdW interaction than graphite with a shorter interlayer distance (3.2 Å). Transition metal dichalcogenides (TMDs) belong to the group of vdW 2D materials which are the subject of particular interest due to unique band structure that provide potential to encode eight bits of information, (instead of two) by a single charge carrier thanks to extra degree of freedom given by the spin and valley index that can be relatively easy controlled in these materials under circularly polarized light excitation. Therefore, the investigation of optical properties of van der Waals layered systems is of paramount importance for their future applications in optoelectronics and spintronics.

In addition to the semiconducting 2D materials, a wide range of other physical properties can be designed in vdW materials: insulators, metals, ferroelectrics, magnetics, and superconductors. [6–9] In addition, the transition between various phases (e.g., semiconductor-to-metal, metal-to- superconductor) can be robustly engineered in two dimensions by external variables, such as strain, charge injection, and defects. [79–82] A combination of these materials in the lateral and vertical heterostructures can establish a vast class of novel materials with exceptional physical and chemical features that have never before been realized. Layered 2D materials can be considered as a surface with high surface area-to-volume ratios, which is completely exposed to the environment and, therefore, can be easily functionalized by chemical substances, leading to new exotic properties or can be exploited as sensors due to various reaction sites. [83] These materials are sensitive to strain by external forces, which can robustly modify their structure and transform their intrinsic properties.

Combination of TMD semiconductor such as MoS_2 and WS_2 and conductive layer of graphene offers unique opportunity to capture all the advantageous properties of both types of materials: while semiconducting layer of TMD acts as a good absorber of incident light, graphene due to its excellent mobility offers opportunity to achieve efficient charge transfer and separation which, in combination, can be employed in high-performance photodetectors. TMDs/graphene heterostructure with interfacial bonding yields excellent electrical characteristics that facilitate charge injection by reducing contact resistance.

Their possible applications and many exquisite physical phenomena present in 2D materials are described in Chapters 2 and 3. These Chapters will also give the reader necessary theoretical background to go through and understand other chapters. Chapter 4 first tells the reader how we grow and prepare our samples to be able to measure desired properties described in later chapters. In the second part of Chapter 4 we describe the experimental techniques used. A lot of research and growth in 2D materials done in ultra high vacuum stays there and isn't investigated with ambient optical, transport and surface characterizations techniques. We wanted to bridge these two communities and fields in 2D materials by transferring samples grown on Ir(111) to arbitrary substrates suitable for optical characterization and application in devices. In Chapter 5 we have shown the results of a successful transfer of the sample with nanometer-sized MoS_2 islands on a millimeter-sized graphene sheet from Ir(111) to Si wafer and investigated their surface and optical properties. As-grown three-layer heterostructures of van der Waals layered materials are not easy to grow and there have been only a few reports on that subject. In Chapter 6 we have continued the work outlined in the previous chapter by

transferring a three-layer heterostructure sample of nanometer sized vertical and lateral WS_2/MoS_2 islands on a millimeter graphene sheet to a wafer and additionally investigating spatial and low-temperature optical properties. Both samples in Chapter 5 and 6 are very interesting for their applications in optoelectronic devices such as photodetectors, solar cells and single photon emitter based photonics. Because of their mechanical flexibility and strength, strain in 2D semiconductors is a very interesting tool to investigate changes of optical properties with it. In Chapter 7 we have researched both static and ultrafast optical response of WS_2 monolayers and bilayers under strain. Borophene is one of the first synthetic 2D materials, meaning it doesn't have its counterpart in bulk form. Because its synthesis was first computationally predicted, it serves as a proof-of-concept for experimental discovery of other synthetic 2D materials. To be able to utilize borophene and its interesting properties in future devices there are still obstacles such as single-phase growth, air-stability and transfer to arbitrary surfaces. In Chapter 8, we have explored our solutions to mentioned problems by using Raman spectroscopy.

2 2D Materials

2D materials represent a unique class of nanomaterials, which have generated significant interest over the past two decades. The isolation of mechanically exfoliated graphene in 2004 [84] sparked research on 2D materials that is growing at a tremendous rate [85] resulting in the discovery of several other 2D classes of materials, displaying a broad palette of properties. 2D materials have strong in-plane covalent bonds and between the layers a weak van der Waals interaction, which enables their exfoliation. [5] Unexpectedly, there is a large number of van der Waals layered materials which can be found in the 2D limit. They are not only limited to monoelemental materials such as graphene, borophene, silicene, phosphorene, germanene, antimonene or black arsenic [5,86,87] some of which are shown in Figure 2.1, but also to binary ones such as boron nitride, metal oxide and transition metal monochalcogenides [5,88], dichalcogenides and trichalcogenides. [5,89,90] We can also find group IV-V compounds [5,91] and some hybrid perovskites [5,92] in the 2D limit. Layered materials which we can find in their 2D limit include insulators, metals, semimetals and semiconductors. [6–9] Their properties can be tuned by varying number of layers because of interlayer coupling, quantum confinement and dielectric environment influence on the bandgap size and nature. [4,5] In some materials, such as TMDs, a change in both the bandgap size (from near infrared to visible) and its nature (from indirect to direct bangap). In some layered materials, just the change of bandgap size occurs, for example, in black phosphorus thinning the material from bulk to a few layers results in widening of gap from mid infrared to visible. [5,89,93–102] One of the advantages of layered 2D materials is ability to stack them onto each other without limitations of lattice mismatch which provides rich playground to manufacture new tailored properties in such 2D material stacks. [5,10,11]

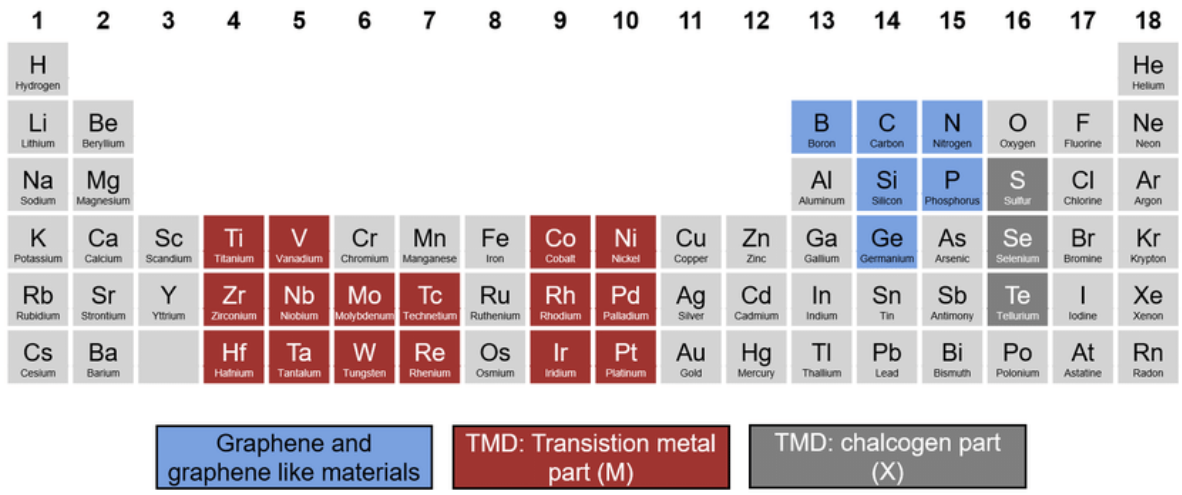

Figure 2.1 Periodic table highlighting elements of single atomic 2D materials (dark blue) and TMDs (red and gray). Adopted from [12].

2.1 Transition metal dichalcogenides

Transition metal dichalcogenides (TMDs) are the most known 2D materials after graphene and the main representative of semiconductive atomically thin materials. Their general formula is MX_2 where M is transition metal and X is chalcogenide, which can be seen in Figure 2.1.

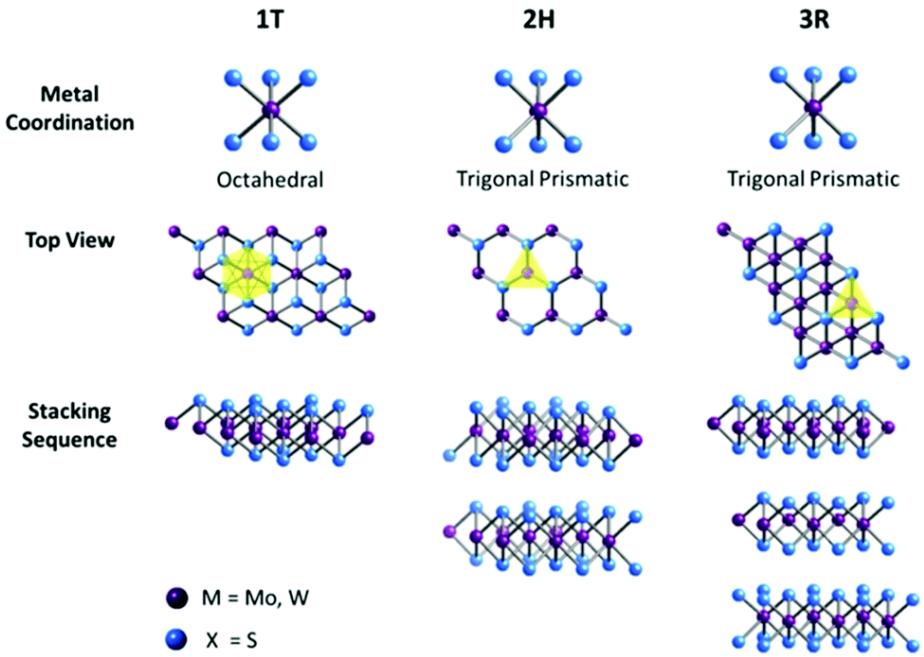

Figure 2.2. Metal coordinations and stacking sequences of TMDs structural unit cells. For tetragonal symmetry (1T), hexagonal symmetry (2H) and rhombohedral symmetry (3R). Adopted from [103]

Monolayer transition metal atoms are positioned in a sandwich-like structure between two chalcogenides, X-M-X where the metal atom is bound to 6 chalcogenide atoms with covalent bonds. Thickness of this "trilayer" TMD monolayers is around 0.6 nm. Individual layers, when stacked on each other, are connected with the weak van der Waals interaction. In the bulk TMDs, three different unit cell structures with tetragonal (1T), hexagonal (2H) and rhombohedral symmetry (3R) can be found, see Figure 2.2. Approaching the monolayer limit, only 1T and 2H are present. Monolayers have broken inversion symmetry which can be even preserved in bulk. [5,104] In general 2H phase is thermodynamically stable while 1T is metastable and easily converted back to stable 2H. [105] Electronic structure of phases differ and in 2H phase we observe semiconducting behavior while in 1T metallic, which can be interesting for fabrication of devices. When the phase of MoS_2 is not specifically noted as in this thesis, it is meant that it is 2H phase.

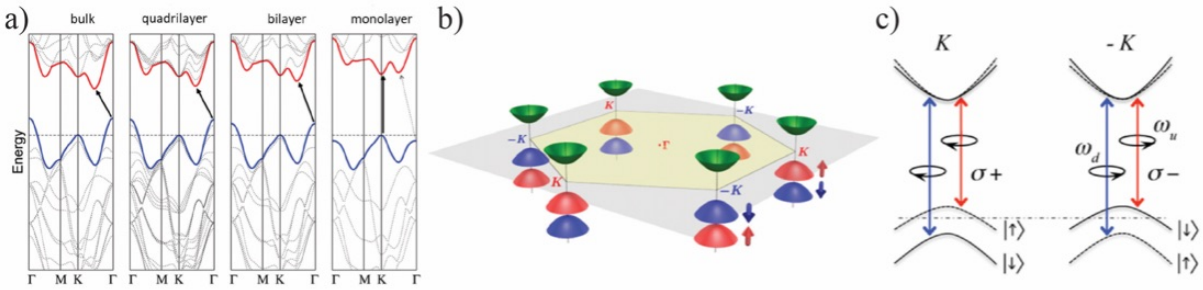

Figure 2.3 a) Calculated band structures for MoS_2 from bulk to quadrilayer, bilayer and monolayer. Taken from [99]. b) Schematic representation of the band structure at the band edges located at K points. c) Valley and spin optical transition selection rules. Solid (dashed) curves denote bands with spin-down (-up) quantized along the out-of-plane direction. The splitting in the conduction band is exaggerated. ω_u and ω_d are, the transition frequencies from the two split valence-band tops to the conduction band bottom, respectively. b) and c) taken from [106].

Calculated band structure from the first principles for bulk and few layer MoS_2 reveals maximum of valence band (VBM) at Γ point while minimum of conduction band (CBM) is between K and Γ point. [5,107] This is evident in Figure 2.3 a) where bulk, quadrilayer and bilayer have indirect bandgap while in the monolayer limit bandgap is direct and located at K points which are corners in hexagonal Brillouin zone. [5,99] DFT gives insights how the bandgap barely changes with number of layers in K point of Brillouin zone while the indirect bandgap from Γ point of VBM to midpoint between K and Γ of CBM increases monotonically with decreasing number of layers, seen in Figure 2.3 a). When Splendiani *et al.* [99] and Mak *et al.* [108] measured emerging strong photoluminescence from monolayer MoS_2 they first attributed it to the direct bandgap nature of monolayers. This abrupt change of the bandgap nature and its decrease with increasing number of layers has been experimentally confirmed for MoS_2 and for other $MoSe_2$, WS_2, WSe_2, soon after[99,108–110] 2D TMDs are also interesting for their spin-orbit coupling (SOC) properties present in the valence band, with energies ranging from 146 meV to 461 meV. [31,111] However, SOC in conduction bands is less pronounced. [112] As mentioned before in monolayer TMDs we observe broken inversion symmetry which makes two valleys K and -K in points of a 2D hexagonal Brillouin zone not equal, as seen in Figure 2.3 b). [5] Combined with SOC and time-reversal, it correlates the valley index with the spin index; a spin-valley locking, which gives rise to valley dependent optical selection rules shown in Figure 2.3 c). [106] In K and -K points interband transitions are coupled with optical helicity $\sigma+$ ($\sigma-$) which gives the ability to manipulate carrier spin in a certain valley using circularly polarized light, making them a good platform for valleytronics and spintronics research and applications. [5,106]

2.2 Graphene

Graphene is a one-atom thick sheet of covalently bonded carbon atoms arranged in an in-plane hexagonal lattice structure with two atoms per unit cell and a thickness of 0.34 nm. [12,13] Each atom in the graphene layer is connected to three neighboring covalently bonded carbon atoms in sp^2 configuration while the fourth free electron forms π orbitals perpendicular to the plane. [12] Electron and atom configuration of graphene result in semimetalic material [14] with zero bandgap shown in Figure 2.4 a). Due to its very steep slope at the Dirac point, a free-standing exfoliated graphene has very high electron mobility of 200 000 $cm^2\ V^{-1}\ s^{-1}$. [14,113,114] However, when CVD graphene is placed to silicon dioxide (SiO_2) surface mobility drops to 1500 $cm^2\ V^{-1}\ s^{-1}$ because of the interaction with the substrate and due to the graphene grain boundaries which limits the electron free path and increases extrinsic scattering. [12,115,116] Synthesis parameters and defect density can significantly vary the electron mobility and other electronic and optical properties. [117] Another important observation is that graphene's zero-field conductivity σ does not disappear in the limit of vanishing *n,* concentration of charge carriers, but instead exhibits values close to the conductivity quantum e^2/h per carrier type. Figure 2.4 b) shows the lowest conductivity σ_{min} measured near the neutrality point for nearly 50 single-layer devices. [118] Interestingly, the opacity of suspended graphene is defined solely by the fine structure constant, $\alpha = e^2/\hbar c \approx 1/137$ (where c is the speed of light), the parameter that describes coupling between light and relativistic electrons and that is traditionally associated with quantum electrodynamics rather than materials science. Despite being only one atom thick, graphene is found to absorb a significant ($\pi\alpha$= 2.3%) fraction of incident white light, a consequence of graphene's unique electronic structure, as seen in Figure 2.3 c) [15] Graphene has exceptional mechanical properties as well due to very strong intralayer σ-bonds, as seen in Figure 2.4 d). Tensile strength of Young's modulus is measured at 1.1 TPa [119] and intrinsic strength at 90-120 GPa in pristine graphene [119,120] with flexibility and stretchability up to 20% of strain. [121]

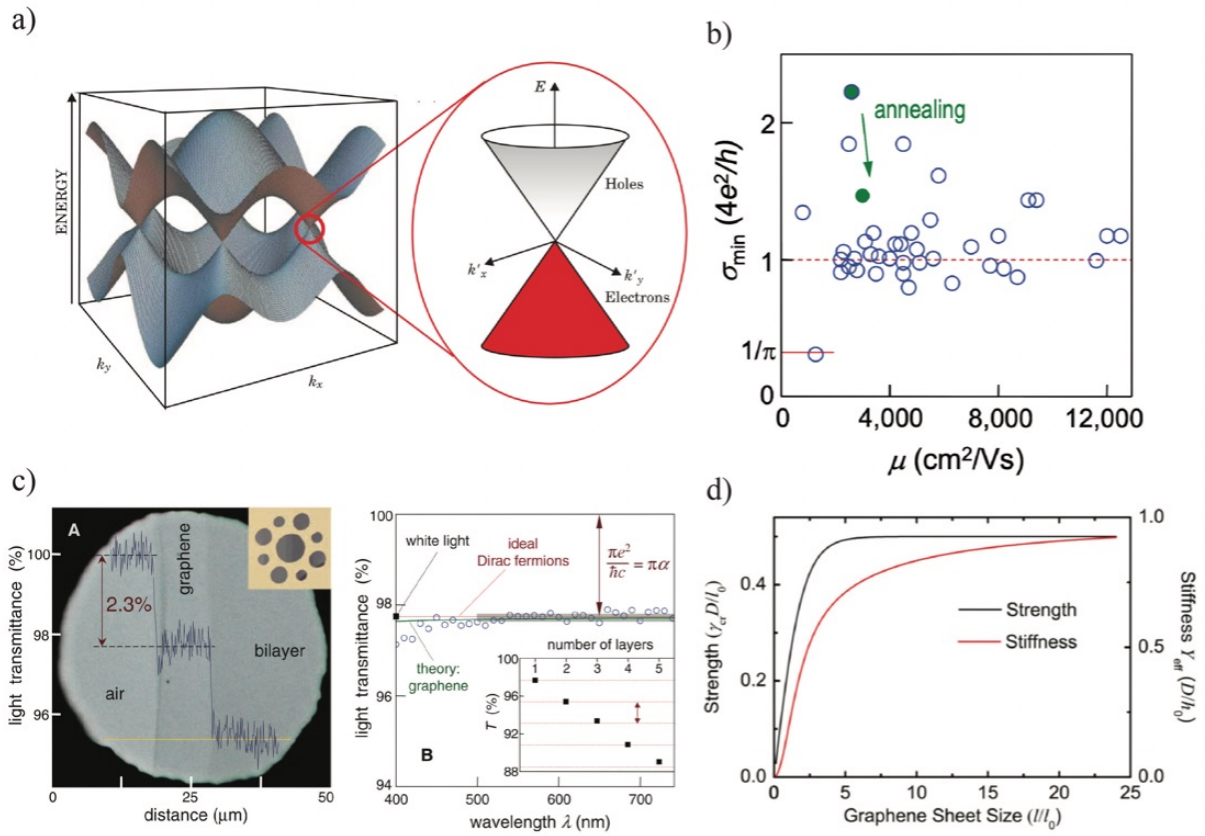

Figure 2.4 a) Graphene band structure with enlargement (red circle) of the band structure close to K and K' points showing the Dirac cones. Adopted from [122]. b) Minimum conductivity of graphene. Independent of their carrier mobility μ_η, different graphene devices exhibited approximately the same conductivity clustering at around ~ $4e^2/h$. Adopted from [118]. c) (A) Photograph of a 50-um aperture partially covered by graphene and its bilayer. The linescan profile shows the intensity of transmitted white light along the yellow line. (B) Transmittance spectrum of single-layer graphene. (Inset) Transmittance of white light as a function of the number of graphene layers (black squares). The dashed lines correspond to an intensity reduction by $\Pi\alpha$ with each added layer. Adopted from [15] d) The strength and stiffness of graphene-based nanocomposites. Adopted from [123].

2.3 Borophene

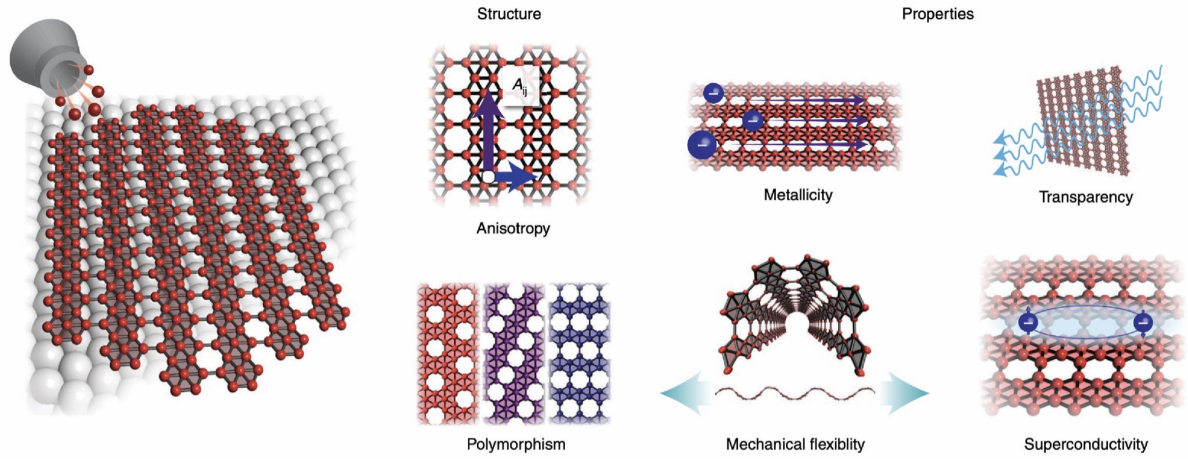

Figure 2.5 Summary of borophene structure and properties. Borophene synthesized on a Ag(111) surface through evaporation exhibits structural anisotropy (where *A*ij denotes a generic anisotropic property tensor component) and polymorphism, which results in a range of properties unique to 2D materials including a combination of metallicity, mechanical flexibility, transparency and superconductivity. Taken from [16].

With the discovery of graphene many new 2D materials followed with interesting properties but all stemmed from their layered bulk counterparts. In parallel, the theoretical search for completely synthetic 2D materials with no analogous bulk layered allotropes promises a substantial variety of materials with the diverse structural options afforded by substrate-dependent epitaxy. Successful growth of such 2D materials promises to unleash a number of fundamental and technological advances where theory can guide experiment towards materials with optimal properties or unique attributes. [124] Synthesis of 2D boron polymorphs (that is, borophene) provides a notable example of such success where synthesis of 2D material has been theoretically guided and, later, experimentally realized. [16] Borophene (Bo) is an atomically thin sheet of boron atoms which gathered a lot of interest in the past few years due its new and unique properties, as seen in Figure 2.5. As Bo has a polymorphic nature, a lot of its properties can be tuned with synthesis parameters and depend on phases present in the borophene sample. Many polymorphs have similar formation energy, making them appear simultaneously during the growth procedure and it is hard to achieve single-phase growth. [125] Interest in borophene stems from its mostly metallic nature making it the lightest 2D metal, as opposed to semimetals, [124] while also showing avid mechanical properties and optical transparency. [17,126,127] Also, borophene is anticipated to be among the best

candidates for optically transparent electrode applications. The intrinsic metallicity of borophene has been predicted to give rise to conventional phonon-mediated superconductivity, especially given the strong electron–phonon coupling resulting from the low mass of boron. [16] Big aspect of application and further research of borophene is its susceptibility to oxidation when exposed to air [128,129] and transfer from metallic substrate electrically insulating one. [16] These aspects, in addition with single-phase growth are discussed in the paper we published [125] and Chapter 8. Borophene metallic properties could be particularly useful for integration in the heterostructure with other 2D materials, such as semiconducting 2D materials, to design the devices [18,19] like Schottky diodes and tunneling transistors. [16] By further coupling the bending flexibility and mechanical stretchability of borophene with its superlative in-plane elasticity and intrinsic metallicity, borophene may prove to be an ideal choice for flexible and transparent electronic interconnects, electrodes and displays. [17,130]

2.4 Van der Waals heterostructures (vdW HSs)

Two-dimensional (2D) materials offer a platform that allows creation of heterostructures with a variety of properties. These van der Waals heterostructures are an assembly of multilayers of TMDs, graphene, boron nitride and other 2D systems, bound together by the weak van der Waals forces. Such thin crystals now comprise a large family of materials, collectively covering a very broad range of properties. [11] A plethora of opportunities arise when 2D crystals start to combine in one vertical stack and synergetic effects become very important. Neighboring crystals properties and relative orientations influence the electronic properties of a composite, inducing processes of charge transfer between (even distant) layers. The extended range of functionalities of such heterolayers yields a range of novel possible applications in future photovoltaic and light-emitting devices. One of the fundamental parameters in vertical heterostructures is the interlayer twist, which is closely related to the interlayer coupling.

2.4.1 MoS_2/graphene

Combining different 2D layers with complementary characteristics can lead to new vdW heterostructures with tunable properties leading to an outstanding range of possible applications. [20,21] Among these systems, the combination of a transition metal dichalcogenide (TMDCs) such as MoS_2 and graphene, forming a heterostructure is very interesting, since it combines the excellent optical properties of MoS_2 and the high mobility and transparency of

graphene. [22–24,131] A metal-semiconductor interface, as epitaxial graphene - molybdenum disulfide is of great interest from the standpoint of fundamental science, as it constitutes an outstanding platform to investigate the interlayer interaction in van der Waals heterostructures. [132] MoS_2/graphene heterostructures can be made in several ways; micromechanically exfoliating and stacking each material, separately grow MoS_2 and graphene and then stack them together or as-grown MoS_2/graphene heterostructure directly on the substrate. As usual as-grown samples offer better interlayer couplings and interfaces without any additional manipulation of the sample. However, even the stacked heterostructures can be made of good-quality by post-processing like annealing the sample. Main motivation for MoS_2/graphene heterostructures are photodetectors where graphene, as a semimetal, can expand the working wavelengths of MoS_2-based photodetectors to IR range because of the broadband characteristics, which comes from its zero bandgap. [133] Figure 2.6 a) shows graphene/MoS_2/graphene vertical heterostructure photodetector design where by introducing graphene to a MoS_2 based photodetector, an enhanced responsivity ($414AW^{-1}$ at 532nm and $376AW^{-1}$ at 2 000nm) and a broad working wavelength range (ranging from 405 nm to 2000 nm) has been obtained. Besides, a relatively fast response speed of the device has been achieved because of the shortened transmit distance for the photogenerated carriers between the source and drain electrodes in the vertical heterostructure. [133] In design shown in Figure 2.6 b) another strategy for improving photodetector performance using a graphene/MoS_2 heterojunction phototransistor with a short channel length and a tunable Schottky barrier is demonstrated. The channel length of sub-30 nm, shorter than the diffusion length, decreases carrier recombination and carrier transit time in the channel and improves phototransistor performance. Furthermore, the presented graphene/MoS_2 heterojunction phototransistor employs a tunable Schottky barrier that is only controlled by light and gate bias. It maintains a low dark current and an increased photocurrent. As a result, demonstrated graphene/MoS_2 heterojunction phototransistor showed ultrahigh responsivity and detectivity of 2.2×10^5 A/W and 3.5×10^{13} Jones, respectively. [134] Figure 2.6 c) is a design of Van der Waals pn junction by stacking a p-type graphene layer with an n-type MoS_2 flake. They propose to use the electrolyte gating to reduce the operating bias of a graphene-MoS_2 heterojunction and observe that its behavior can be tuned from a diode to a resistive operating mode, thanks to gate bias. In work done related to Figure 2.6 d) they have investigated optical properties of heterostructure with several monolayer MoS_2 flakes on graphene. They revealed that the PL signal of MoS_2 in the case of graphene underlayer is strongly quenched (about 60–70% with respect to the MoS_2 on SiO2 substrate). This phenomenon is the signature of electron transfer from MoS_2 to the

graphene which hinders the recombination of electron−hole pairs created by the photoexcitation, for which they find evidence in Raman signature as well. This electron transfer is not attributed to a strong coupling between MoS_2 and graphene (since we consider a weak van der Waals interaction for this structure), but rather to a standard hopping from an electron in MoS_2 conduction band to an unoccupied state at the same energy in graphene. [132]

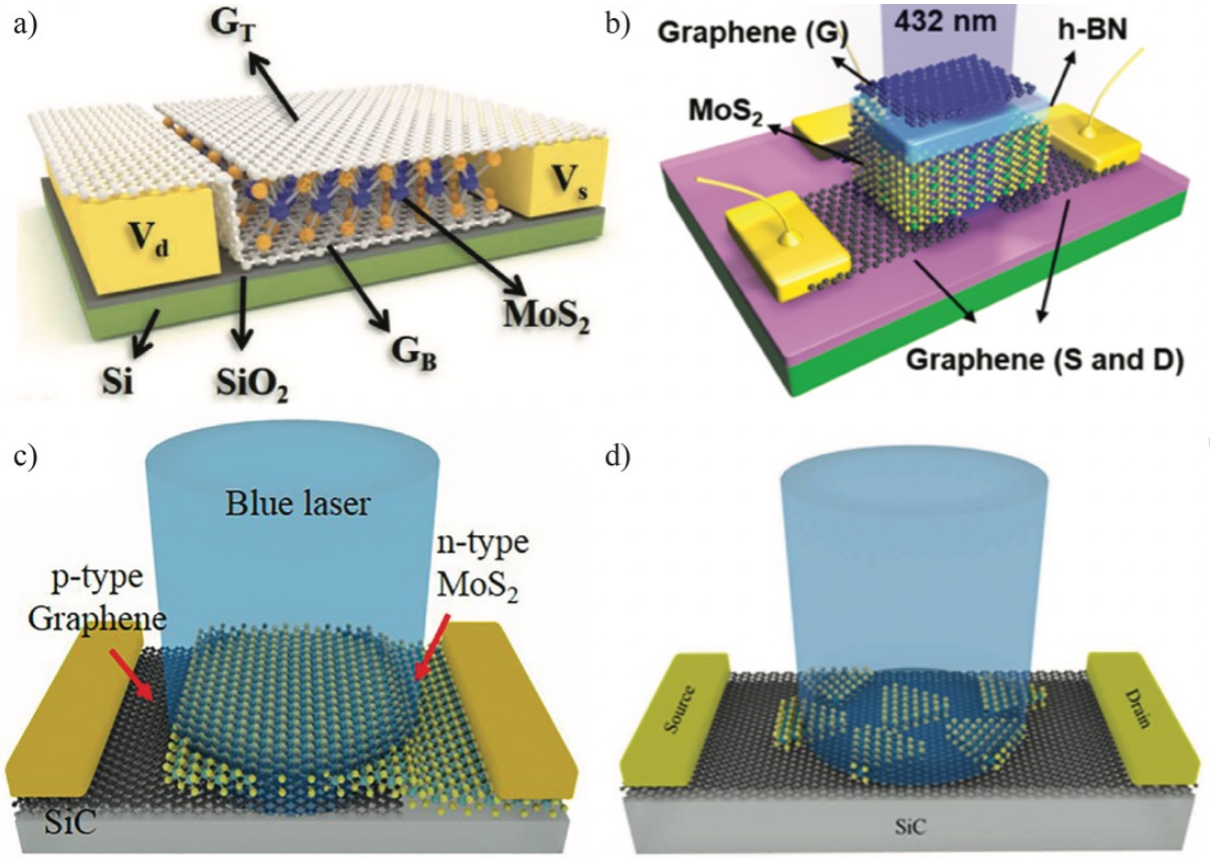

Figure 2.6 Schematic representation of different implementations of MoS_2/graphene heterostructures. a) Graphene/MoS_2/graphene vertical heterostructure. From the bottom to the top are graphene, MoS_2, and graphene. Adopted from [135]. b) MoS_2/graphene heterostructure where graphene is used as source, drain and gate electrodes. Adapted from [136]. c) MoS_2/graphene heterostructure with p-type graphene and n-type MoS_2 p-n junction. Adapted from [137]. d) Device based on epitaxial graphene with MoS_2 flakes on top. Adapted from [138].

2.4.2 WS_2/MoS_2/graphene

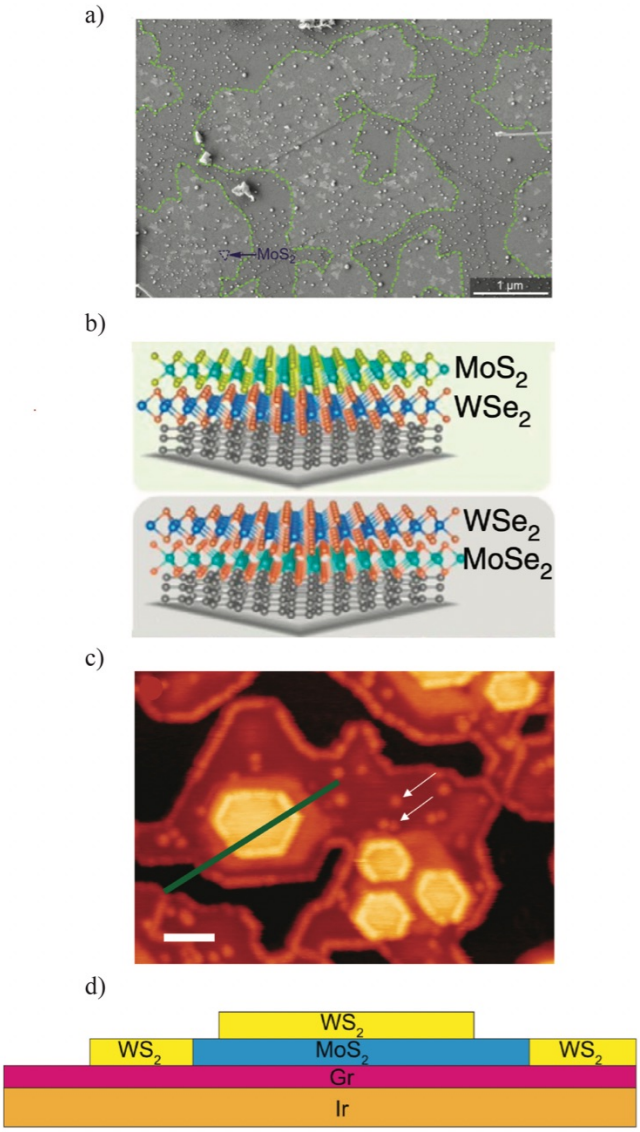

Figure 2.7 a) SEM image (secondary electrons contrast) showing the topography of the MoS_2/WS_2/graphene heterostructure, with preferential growth of 2D MoS_2 over WS_2 flake. WS_2 flakes are marked with a green outline, and an exemplary MoS_2 crystal is marked with a violet outline. Adapted from [29]. b) Schematic diagram of MoS_2/WSe2 and WSe2/MoSe2 heterostructures on three-layer graphene, rare literature example of as-grown heterostructure with three different 2D materials. Adapted from [139]. c) STM image of the WS_2 grown on MoS_2/Gr/Ir(111), which results in the formation of lateral WS_2-MoS_2 and vertical WS_2/MoS_2 on Gr/Ir(111). White arrows denote point defects in WS_2. White line is the scale bar of 10 nm. Adopted from [140]d) Schematic sectional view along the green line in c). Adopted from [140]

Fabrication of as-grown low-dimensional heterostructures with at least three different materials is a much more difficult task than growth of the heterostructures made of two different materials. There is only a handful of reports of the growth of lateral 2D heterostructures [141–143], and only recently 1D vdW HSs have been demonstrated. [144,145] Unfortunately, these geometries do not fully harness the application potential of vdW HSs. Hence, vertically stacked vdW HSs are favorable as they enable large-area electrical contact between layers, allowing the production of high-performance electronic devices. Lin *et al* were the first to show transfer-free MoS_2 /WSe2 /graphene and WSe2 /MoSe2 /graphene vertical stacks with three-layer graphene, see Figure 2.7 b), which they used to fabricate a tunnel diode. [146] The only works presenting the all as-grown ternary or higher-order vertical vdW HS without the transfer step is in Figure 2.7 a), c) and d). [29,140] They observe typical PL quenching due to charge transfer of photoexcited electrons to graphene and show that, opposed to MoS_2 /WS_2 heterostructures, there is no interlayer (IL) exciton on graphene, which they attribute to efficient charge transfer caused by the conductive graphene channel. [29] STM image of the sample in Figure 2.7 c) and its schematics in d) are made by B. Pielić et al. and it was the groundwork for Chapter 6 with very similar sample morphology. Pioneered investigation of MoS_2/WS_2 system due to its promising applications as photodetector devices [147], in combination with graphene as the channel material [29] was done as a part of experimental work presented in this Thesis.

3 Optical properties of 2D materials

3.1 Excitons in 2D materials

In semiconductors by absorption of light with photon energy equal or higher than their bandgap size, electrons get photoexcited from the valence band to the conduction band, leaving a hole in the valence band. Two particles, negatively charged electrons and positively charged holes in different bands, attract each other through Coulomb potential, binding them together. [30] Hydrogen model is a good approximation for electron-hole interaction in 3D bulk semiconductors, however in 2D materials it has discrepancies. Bound electrons and holes form neutral quasiparticles called excitons, if they are tightly bound to a unit cell they are Frankel excitons, and if they have wave function delocalized, as in most semiconductors, they are Wannier-Mott type excitons. [5,30] Excitons in 3D semiconductors have very small binding energy (E_b) of around 5 meV and wave function radius of around 15 nm. [148] Such a low exciton binding energy makes observing excitons in 3D bulk semiconductors at room temperature impossible, so excitonic physics was generally reserved to low-temperature regime until the advent of 2D semiconductors because thermal energy was too high. It was predicted that in monolayer TMDs exciton binding energy can go as high as ~ 1 eV which allows them to be present and investigated at room temperatures. [31–35] With their large binding energy and wave functions localized in k-space and extended in real-space they are also of the Wannier-Mott type. [42,149] Using optical spectroscopy and scanning tunneling spectroscopy it is possible to experimentally measure exciton binding energies with reported energies range between 0.2 eV and 0.7 eV. [36–41] Experimental determination of the exciton binding energies is something we did also in Chapter 6 of this Thesis. Origin of the large exciton binding energy in TMDs is illustrated schematically in Figure 3.1 a). In contrast to the bulk, the electron and hole forming an exciton in monolayer TMDs are strongly confined to the plane of the monolayer and additionally experience reduced screening due to the change in the dielectric environment. [36] These effects have two major implications on the electronic and excitonic properties of the material, shown by a schematic representation of optical absorption spectra in 3D and 2D limits, see Figure 3.1 b). First, the quasiparticle band gap is expected to increase in the monolayer limit. Second, the enhanced electron-hole interaction is expected to increase the exciton binding energy. [36] Quenched dielectric screening effect, yields in the exciton binding energy that is a factor of 4 larger in 2D than in 3D. Figure 3.1 c) shows energy level diagram

of monolayer TMDs where there is a direct bandgap, exciton energy level, known as optical bandgap is defined as energy bandgap reduced for the exciton binding energy, ($\Delta_{Exciton}$), charged exciton (trion) energy level below neutral exciton energy level. Trion energy level is defined as an optical bandgap reduced for trion binding energy (Δ_{Trion}). The scheme also presents the splitting of the valence band due to SOC and respective radiative recombinations: A exciton resonance represents optical relaxation from the optical bandgap minimum to higher splitted valence band maximum, B exciton is optical relaxation from the optical bandgap minimum to lower splitted valence band maximum and A^- represent optical relaxation of trions. Changing the dielectric environment of 2D material can be used to change the dielectric screening and thus control the properties of excitons and their energy levels, as seen in Figure 3.1 d). [39,42,43]

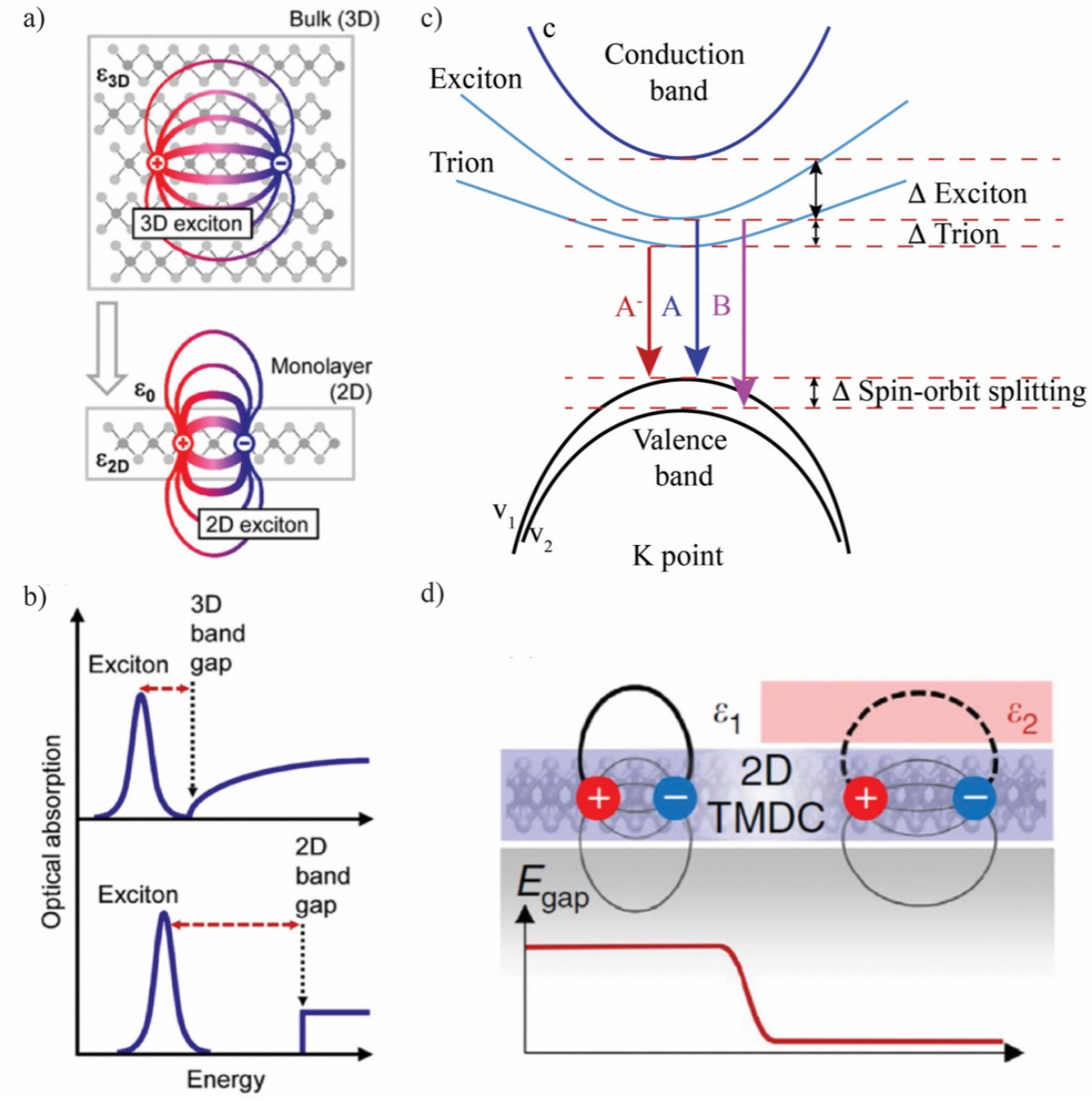

Figure 3.1 a) Real-space representation of electrons and holes bound into excitons for the 3D bulk and a quasi-2D monolayer. The changes in the dielectric environment are indicated schematically by different dielectric constants ε_{3D} and ε_{2D} and by the vacuum permittivity ε_0. Taken from [36] b) Impact of the dimensionality on the electronic and excitonic properties, schematically represented by optical absorption. The transition from 3D to 2D is expected to lead to an increase of both the band gap and the exciton binding energy (indicated by the dashed red line). The excited excitonic states and Coulomb correction for the continuum absorption have been omitted for clarity. Taken from [36] c) Energy level diagram for semiconducting TMDs. d) Schematic illustration of a semiconducting 2D TMD material, partially covered with an ultra-thin dielectric layer. The strong Coulomb interaction between charged particles in low-dimensional systems affects both the exciton binding energy and the quasiparticle bandgap. The interaction can be strongly modified by modulating the environmental dielectric screening on atomic length scales. Taken from [43].

TMDs and related VdW heterostructures present a new paradigm for fundamental exciton physics, as excitonic features are stable at room temperature, they dominate the optical response and non-equilibrium dynamics of these materials. Weak dielectric screening and strong geometrical confinement give rise to an extraordinarily strong Coulomb interaction resulting in fascinating many-particle phenomena, such as the formation of different types of excitons including optically allowed and forbidden dark excitons and locally trapped in an impurity-induced potential, see Figure 3.2. [44]

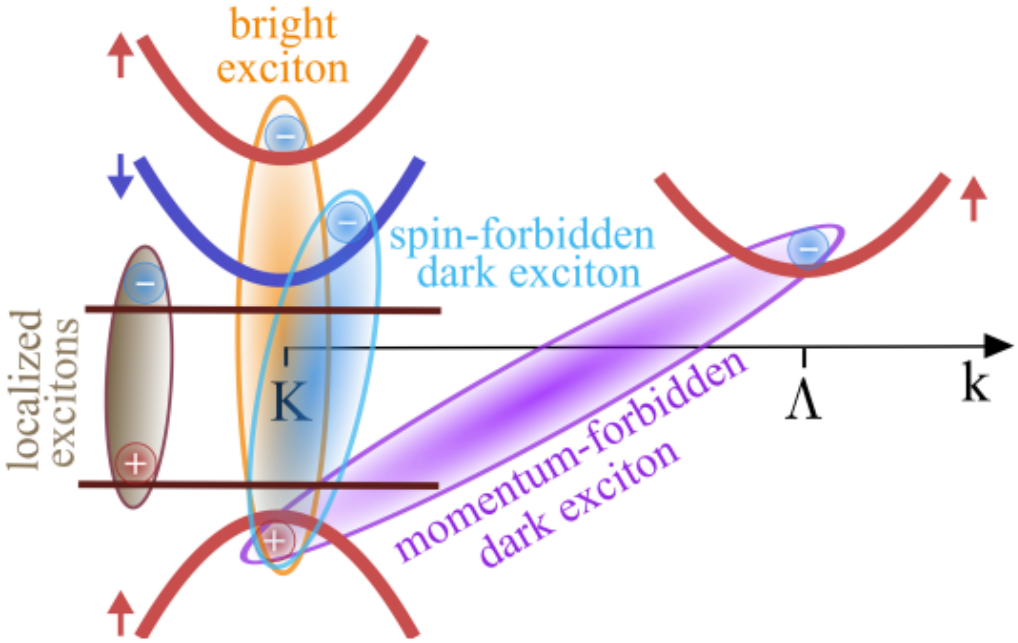

Figure 3.2. Schematic representation of different types of excitons. Taken from [44]

Excitons are Coulomb-bound electron- hole pairs (ovals in the picture). Momentum-forbidden dark excitons consist of electrons and holes located at different valleys in the momentum space. Spin-forbidden dark excitons consist of electrons and holes with opposite spin. These states cannot be accessed by light due to the lack of required momentum transfer and spin-flip, respectively. Electrons and holes in localized excitons are trapped into impurity-induced potential traps.

3.2 Other photoexcitations

In addition to already mentioned bright and dark excitons, shown in Figure 3.2, exciton physics of 2D materials is rich with trions, biexcitons, and interlayer excitons with their energy levels below intralayer exciton, as seen in Figure 3.3 a), all of them can be observed even at room temperatures. [47]

Because of the significant Coulomb interactions in 2D materials, when excitons are in the presence of excess charge they can capture an additional charge to form a trion, a charged exciton with three particles, as seen in Figure 3.3 c). Trion can be negative or positive depending on its composition: a negative trion (A^-: e–e-h) is a system of two electrons and one hole and a positive trion (A^+: h–e-h) is a system of two holes and one electron. [47] As seen in Figures 3.1 c) and 3.3 a) energy level of trion is below the energy of neutral exciton; with their surprisingly large binding energies ranging from 15-45 meV in monolayer TMDs and longer population relaxation time up to tens of picoseconds their impact on both transport and optical properties can be easily detected and manipulated towards trion-based optoelectronics. [34,47,49–53] In 2D materials there are also present 4-particle systems or rather an exciton molecule called biexciton and consisting of two free excitons, they were also first observed in monolayer TMDs. [48,150] The biexciton is identified as a sharply defined state in photoluminescence at high exciton density due to the high photoexcitation density of excitons. Figure 3.3 d) shows a scheme of bound and unbound configurations of biexcitons, where the first is defined as a single quasiparticle while the second as two excitons isolated from each other due to repulsive Coulomb interaction. [45–47] Biexcitons in monolayer TMDs have unusually large binding energies E_B^b of about 50 meV and have been of interest for both fundamental studies and device applications. [151]

All of the above exciton systems were intralayer, but in bilayered systems of same or different material, an interlayer exciton can also be formed and observed at room temperatures, again because of the strong Coulomb interaction, as seen in Figure 3.3 e). Interlayer excitons have electrons in one layer and holes in other, usually with energies lower than the intralayer exciton. [152,153] Interlayer excitons form with electrons and holes traveling from one layer to another more energetically favorable excitonic state with the help of phonons and, as in the case of intralayer excitons, interlayer excitons can also be bright or dark depending on the spin and momentum. [47,154,155]

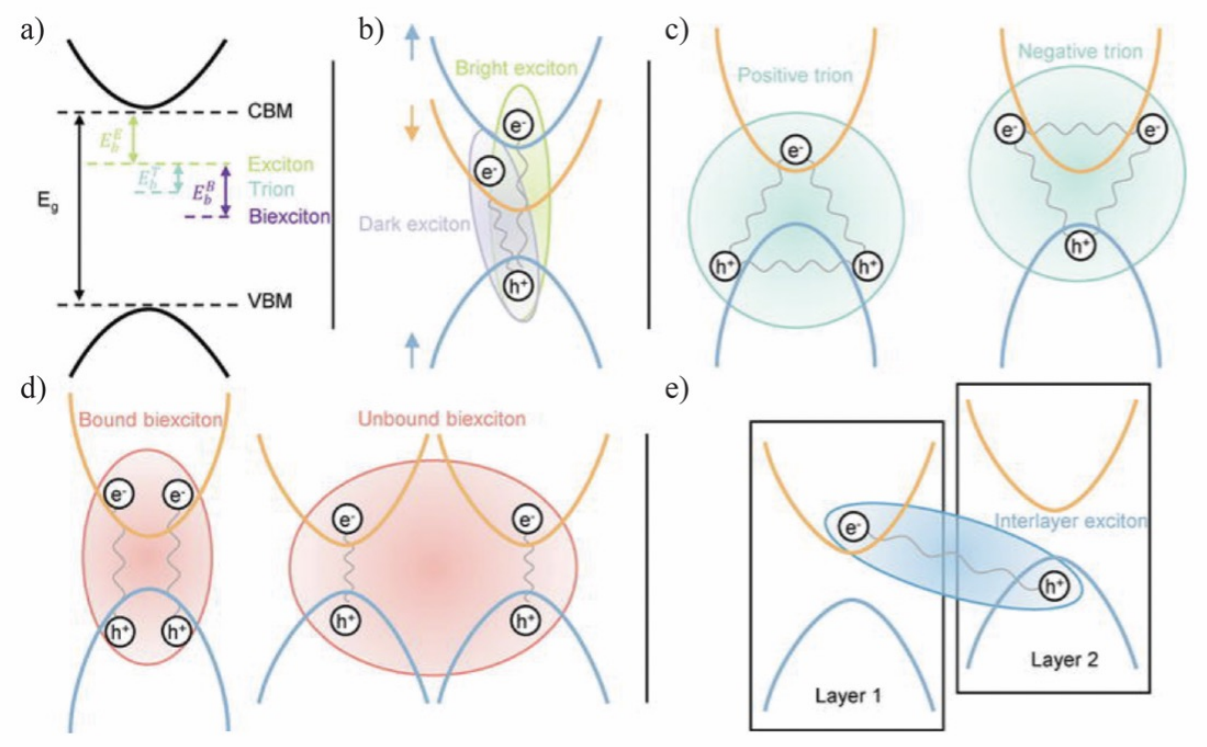

Figure 3.3 Different exciton types in atomically thin nanomaterials and related heterostructures. a) The schematic for the energy level. b) Excitons are coulomb-bound electron hole pairs (ovals in the picture): Bright excitons consist of electrons and holes with antiparallel spins, while dark excitons consist of electrons and holes with parallel spins. c) Trions emerge when an additional electron (hole) joins the exciton. d) Biexcitons are created from two free excitons with different total momenta. e) Interlayer excitons appear when electrons and holes are located in different layers. Taken from [54].

3.3 Phonon excitations

Among the variety of characterization methods, Raman spectroscopy, one of a fast and nondestructive characterization method with high spatial and spectral resolution, stands out and is applicable at both laboratory and mass-production scales. [156] With Raman spectroscopy we can detect Raman active phonons (i.e. lattice vibrations) in 2D materials that exhibit several prominent features, including line shape, peak position, full width at half maximum (FWHM), and intensity, which contain useful information to characterize physical and chemical properties of 2D materials or to probe their fundamental properties. [55,57,58,157] Raman characterization provides us with information on electrostatic doping, straining in material, phase transition triggered by defect, thickness-dependent intralayer and interlayer modes, and

two-dimensional alloys with tunable compositions etc [57,59–62,157,158] As Raman signal is a very weak physical phenomenon, most of the light is elastically scattered via Rayleigh scattering. Only one in $1x10^7$ photon is inelastically scattered with change of the energy by either laser light receiving energy from phonons (Anti-stokes scattering) or giving to them (Stokes scattering). [12] Stokes scattering is a more probable event, so it has stronger intensity, and it is easier to detect. [55,57,157,159] Figure 3.4 shows the most important Raman phonon modes for graphene in Figure 3.4 a) and b) and TMDs in Figure 3.4 c). For instance, in graphene there are two prominent Raman modes: primarily G mode, shown in Figure 3.4 a), is associated with in-plane vibrations and D mode, shown in Figure 3.4 b), indicates defects such as atomic defects, edges, or grain boundaries. The G peak corresponds to the high-frequency E^2_g optical phonon at the Γ point of the Brillouin zone. The D peak is due to the breathing modes of six-atom rings and requires a defect for its activation. [63] It comes from TO phonons around the Brillouin zone K point. [160,161] Besides, 2D second-order D-peak overtone originates from a momentum-conserving two-phonon process of opposite wave vectors, hence no defects are required for its activation and it is always present in the graphene Raman spectrum. [63,157] E symmetry phonon modes in TMDs indicate in-plane movement of atoms in crystal structure, whereas A and B symmetry shows out-of-plane displacements of atoms. [12,64–67]

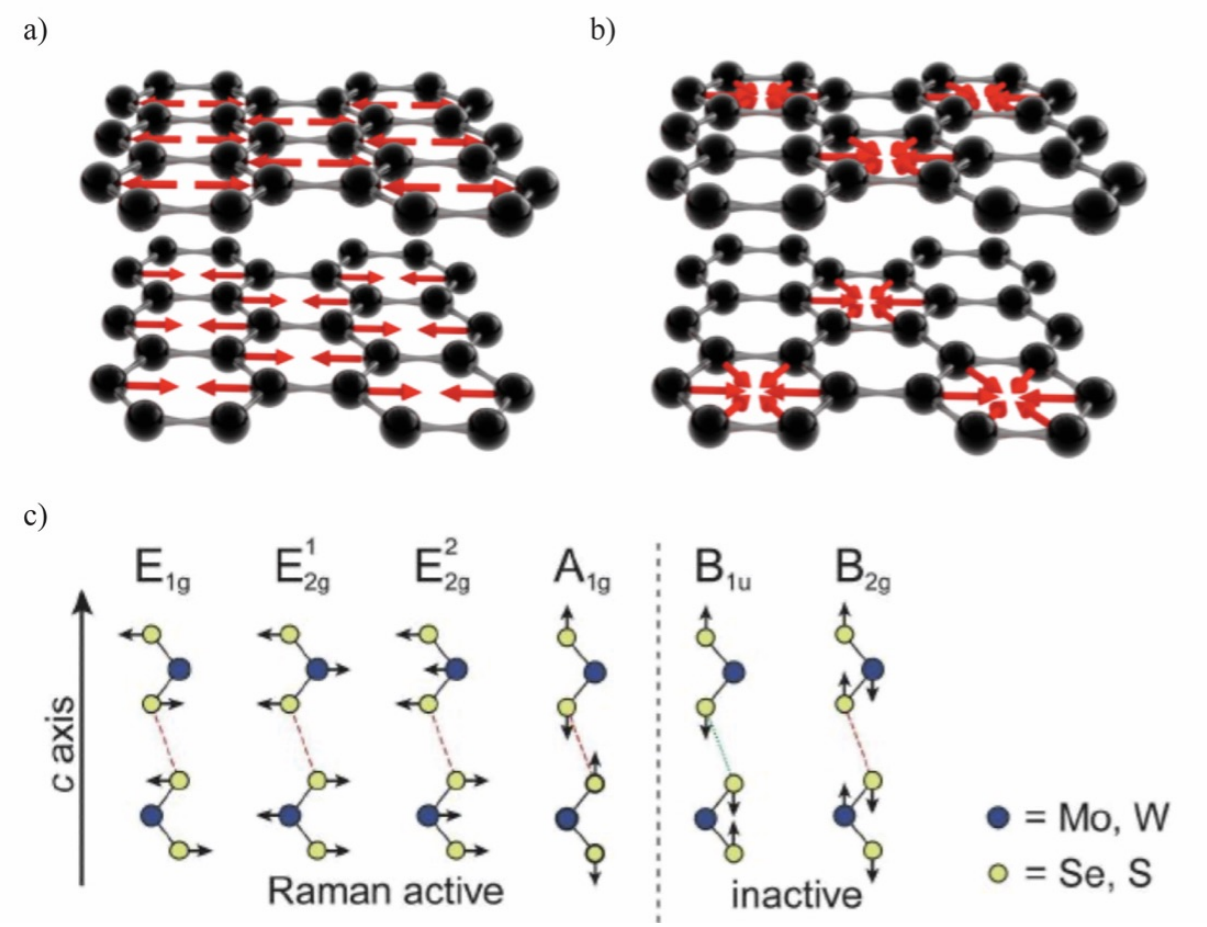

Figure 3.4 Raman vibrational modes of graphene responsible for phonons the a) G and b) D and 2D. Taken from [12] c) Schematic drawing of the four Raman active and two inactive modes of the transition metal dichalcogenides MX_2 (M = Mo, W and X = Se, S). Taken from [110]

3.4 Strain in 2D materials

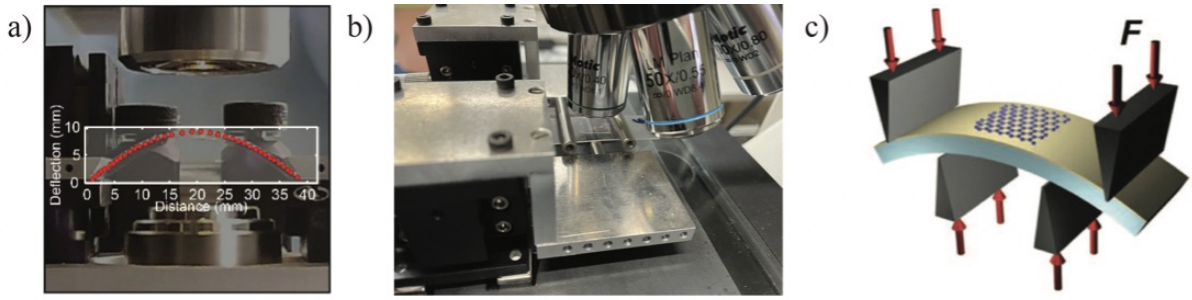

Figure 3.5 Bending setups for applying uniaxial tensile strain. a) Photo of the setup with the bent substrate. The red dots indicate a sine fit to the shape of the bent substrate. Adapted from [162]. b) 3-point bending setup suitable for application in reflection measurements configuration d) 4-point strain setup which is suitable for application in transmission optical setups. Taken from [68,163]

Strain engineering has been proposed as a prospective route to modify the electronic and optical properties of two-dimensional (2D) materials. [68] The interest in this topic is motivated by their resilience to mechanical deformations. These systems stand strain deformations of the order of 10%, [69,70] while conventional 3D semiconductors break at quite moderate deformations of 0.5–1.5%. [68,71] Apart from the mechanical toughness, another key question of strain engineering of 2D materials is how they can be conveniently and reproducibly strained. While 3D systems are typically stressed by epitaxially growing them onto substrates with a certain lattice parameter mismatch, strain in 2D systems can be applied more directly by folding, stretching and bending. [68] Experiments on MoS_2 single-layer and few-layer flakes have already demonstrated that the optical band gap is tunable by 50 meV/% for uniaxial strain [164,165] and 100 meV/% for biaxial strain. [68,166] These results open the door to fabricate devices whose optical and electronic properties can be externally controlled by the application of strain. [68,167] Combination of nondestructive optical measurement methods, typically including absorption, reflectance, photoluminescence, and Raman spectroscopies, can be readily exploited to quantitatively determine strain-engineered optical properties that come as result of bandgap shrinkage, and when the strain is sufficiently large, even to a direct-to-indirect bandgap transition or an indirect-to-direct bandgap transition. Apart from homogenous in-plane strains, local inhomogeneous strains can also be induced by local strain engineering, providing

other exciting avenues for tailoring distinctive optical properties of 2D materials on the nanoscale, such as funneling effect. Strain in 2D materials can also influence its nonlinear optical properties or even phase transitions. [168] Most of the strain measurements currently present in the literature are focused on uniaxial strain mainly because of the ease of applying said strain in 2D materials. In Figure 3.5 several bending setups for uniaxial tensile strain are shown. One of the first approaches was two-point bending, Figure 3.5 a), where from the geometry and radius you can calculate strain, as explained in Chapter 7. b). Advancement of this approach is a three-point setup, Figure 3.5 b), which offers constant z-position of the sample as strain is increased, this makes optical measurements, where objective focus is important, much faster and easier. However, it allows only measurements in reflection geometry, to overcome this a four-point bending setup as seen in Figure 3.5 c) is utilized which offers constant z-position and ability to do transmission measurements.

A more complete approach to strain investigation would be to apply biaxial strain both compressive and tensile. In Figure 3.6 some of the methods for applying these are shown, all having some advantages and disadvantages. Thermally controlled stage and substrate with adequate thermal expansion coefficient can serve as a platform for applying biaxial tensile and compressive strain, as seen in Figure 3.6 a). Drawback of this method is that properties we want to investigate in dependence on strain could be also dependent on temperature, so it makes it harder to distinguish the source of the observed change. Suspending the 2D material over a hole or a trench to be in a freestanding form allows us to use the AFM tip to indent and pressure the material downwards and apply direct strain, as seen in Figure 3.6 b). Strain in this method is applied on a very constricted area and there is a possibility to puncture the material with an AFM tip. Figure 3.6 c) shows biaxial stretching of 2D material on PDMS where macroscope tensile strain is induced, in this particular case the system is used as a strain grating sensor. This kind of setups cannot be used to apply compressive strain. Figures 3.6 d) and e) show fabrication of localized strain fields in 2D materials with patterned substrate, this very localized strain can create quantum wells and single photon emitters in 2D materials.

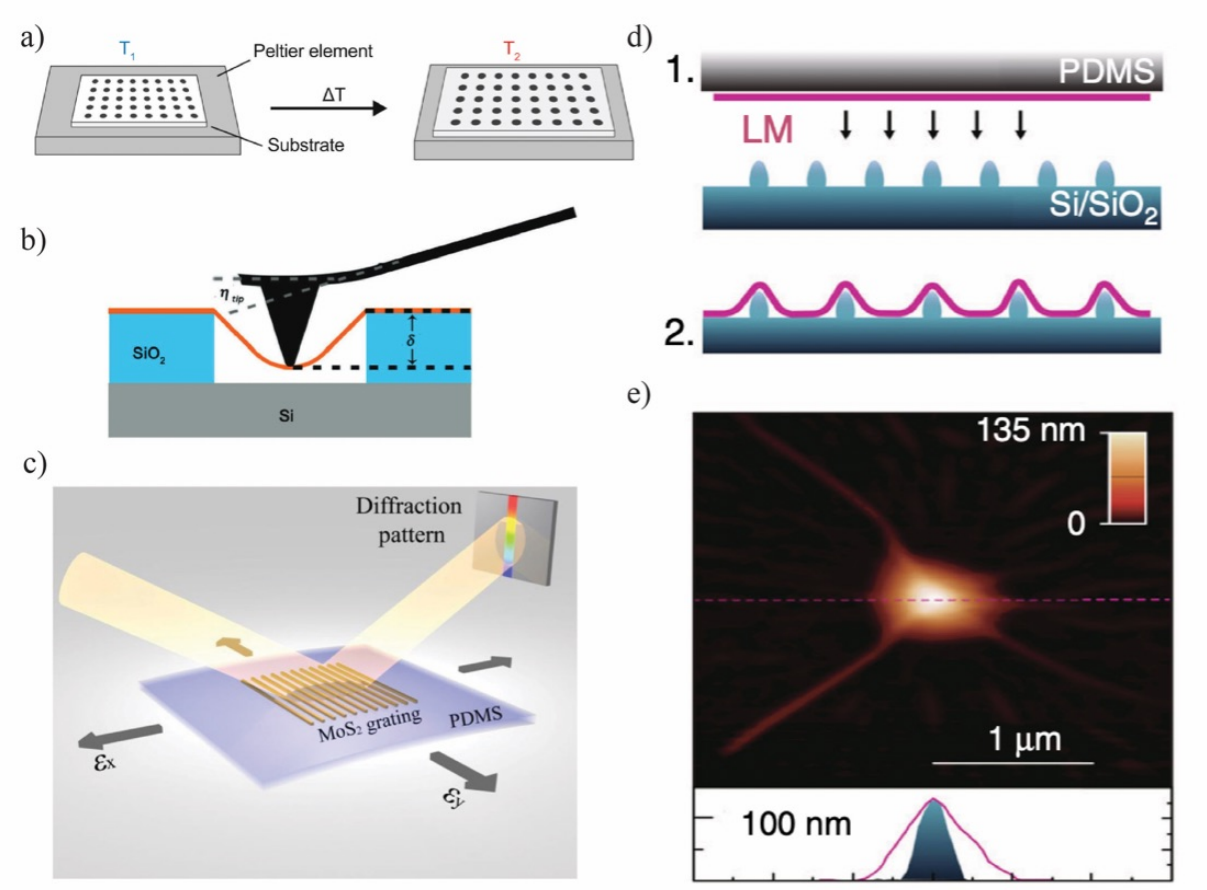

Figure 3.6 Methods to apply biaxial strain in 2D materials. a) Schematic of the temperature-dependent experiment. Substrate heating (cooling) causes the thermal expansion (contraction) of the substrate that induces biaxial strain on the flake pre- deposited on top. Control over the temperature is achieved with a Peltier heating/cooling element. Taken from [68]. b) Schematic illustration of the mechanical properties measurement setup with AFM. Used for strain application through AFM indentation in 2D materials. Taken from [72]. c) Schematic illustration of MoS_2-based grating sensor on a flexible substrate of PDMS for biaxial strain gauges. Taken from [73]. d) Fabrication procedures for a layered material (LM) on the nanopillars. e) AFM image of monolayer WSe2 on a silica nanopillar (upper panel), and height profiles of the nanopillar before (blue area) and after (pink line) LM deposition (lower panel). d) and e) taken from [74]

3.5. Optoelectronics in 2D materials

Optoelectronics is the study of optical power from light-detecting devices, which functions as an electrical-to-optical or optical-to-electrical transducer. However, the challenges in light-matter interactions and optical integration for large-scale production have been the subject of concern for a long time and the future integrated circuits must aim to attain lower power consumption, high efficiency, lower carbon footprint, and higher speed [75] The next-generation 2D materials can address these challenges due to their excellent tunable band structure, ultra-fast carrier mobility, and ultra-high nonlinear co-efficiency can be utilized in various applications in optoelectronic devices. Also, through vdW forces, 2D materials can directly combine with other structures.

As monolayer MoS_2 is a direct-bandgap semiconductor due to quantum-mechanical confinement it could be suitable for applications in optoelectronic devices where the direct bandgap would allow a high absorption coefficient and efficient electron–hole pair generation under photo-excitation. [76] In paper from O. Lopez-Sanchez et al. an ultrasensitive monolayer MoS_2 photo-detector with a photoresponsivity reaching 880 A W^{-1}, which is a 100,000-fold improvement over previous reports for monolayer MoS_2 phototransistors is demonstrated, see Figure 3.7 a). [76] This is a consequence of its improved mobility, as well as the contact quality and positioning technique. Because of the direct bandgap, ultrasensitive MoS_2 photodetectors have a photoresponsivity that is ~10^6 better than the first graphene photodetectors (~0.5 mA W^{-1}). [76,169]

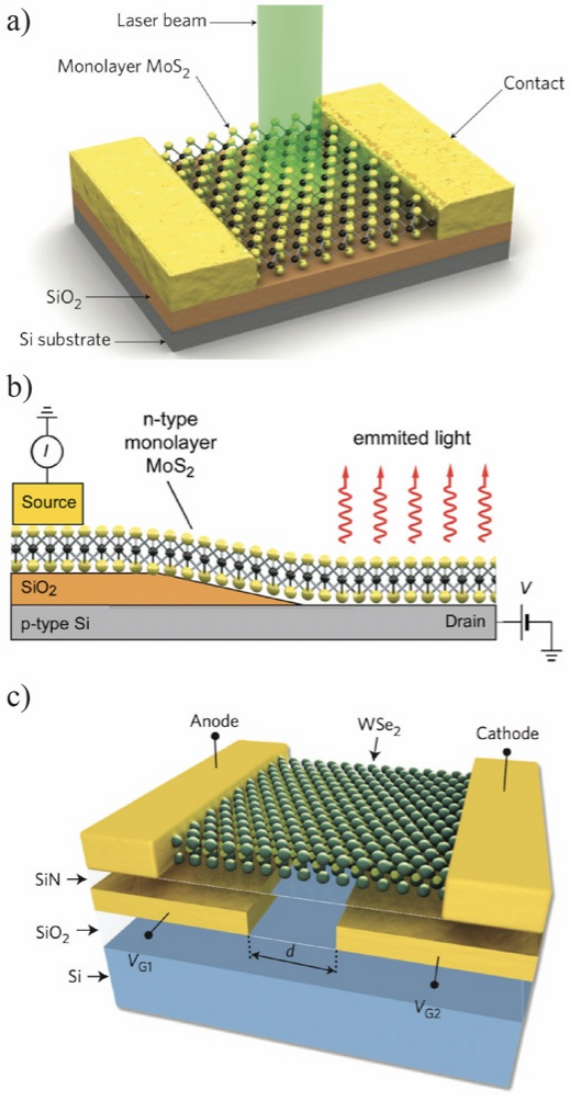

Figure 3.7 a) Monolayer MoS_2 phototransistor. Three-dimensional schematic view of the single-layer MoS_2 photodetector and the focused laser beam used to probe the device. Single-layer MoS_2 flake serves as the conductive channel in our photodetector. The device consists of a field-effect transistor with two gold contacts and a gate using a degenerately doped silicon substrate. Taken from [76]. b) Geometry of the MoS_2/Si heterojunction light-emitting diode. Cross-sectional view of the structure of the device together with electrical connections used to induce light emission from the heterojunction. Electrons are injected from n-type MoS_2, while holes are injected from the p-Si substrate. Taken from [77]. c) Schematic of WSe_2 monolayer device with split gate electrodes. Taken from [78].

Figure 3.7 b) shows an electroluminescent device and solar cell based on heterojunctions composed of monolayer MoS_2 and p-type silicon serving as the hole injection layer. [170] The entire junction area in the device participates in light emission with a low emission threshold

power, allowing future large-area light emitters and lasers based on MoS_2. [77] This choice of materials combines the advantages of the direct bandgap and thickness of 2D MoS_2 with the established silicon-based fabrication processes and could show the way to implementing 2D semiconductors as enabling materials in standard semiconductor fabrication lines. The heterojunction diode can also operate as a photovoltaic device, converting incoming light into electrical power with an external quantum efficiency (EQE) of 4.4% . [77] The EQE could be further enhanced by careful control over doping levels of MoS_2 and Si, which would reduce the series resistance of the device, by use of large-area grown or deposited materials[70,171] and by incorporating additional 2D semiconducting layers such as WSe_2 with complementary absorption spectra. [77] In Figure 3.6 c) electrostatic doping is used to form a monolayer WSe_2 lateral p–n junction diode. Split gate electrodes couple to two different regions of a WSe_2 flake, biasing one gate with a negative voltage and the other with a positive voltage draws holes and electrons, respectively, into the channel, and a p–n junction is realized. [78] In the future, low-cost, flexible and semi-transparent solar cells could be deployed on glass facades or other surfaces for energy harvesting. Two-dimensional light-emitting diodes could lead to new generations of large-area lighting units and transparent, flexible displays. [78]

4 Experimental techniques and sample preparation

4.1 Sample preparation

There have been many ways to prepare 2D material samples, the first one from Geim & Novoselov was micromechanical exfoliation of graphene from graphite, which is still used today for exfoliating new van der Waals layered 2D materials. Advantage of the micromechanical exfoliation method is that it offers a quick and cheap way to prepare a high-quality sample ready for optical, transport and surface characterization. We have also used this method for some materials and sample preparation but results presented in this Thesis do not include this method for sample preparation. The biggest disadvantage of this method is inability to be scaled to mass production and substantial surface coverage. Methods for synthesizing samples like chemical vapor deposition (CVD) and molecular beam epitaxy (MBE) offer scalability, complete coverage, large size of the sample and high-quality if carefully prepared. Nevertheless, they also come with certain shortcomings, for instance the MBE method uses UHV and metallic samples which are not suitable for optical and electronic characterization and application. CVD method can be volatile and very sensitive to uncontrollable conditions of precursors and ambient environment. One way to overcome shortcomings of the MBE method is to have a suitable transfer process for transferring as-grown samples to arbitrary substrates, which is shown in this thesis with good success. Disadvantages of CVD can be dealt with using Metal-organic chemical vapour deposition MOCVD setup which is more expensive but offers excellent controllability of growth parameters to give good uniformity of the growth rate and doping levels, and sharp layer interfaces. [172] Here we present two methods used in our labs MBE and CVD to achieve growth of high-quality 2D materials.

4.1.1 Chemical Vapor Deposition

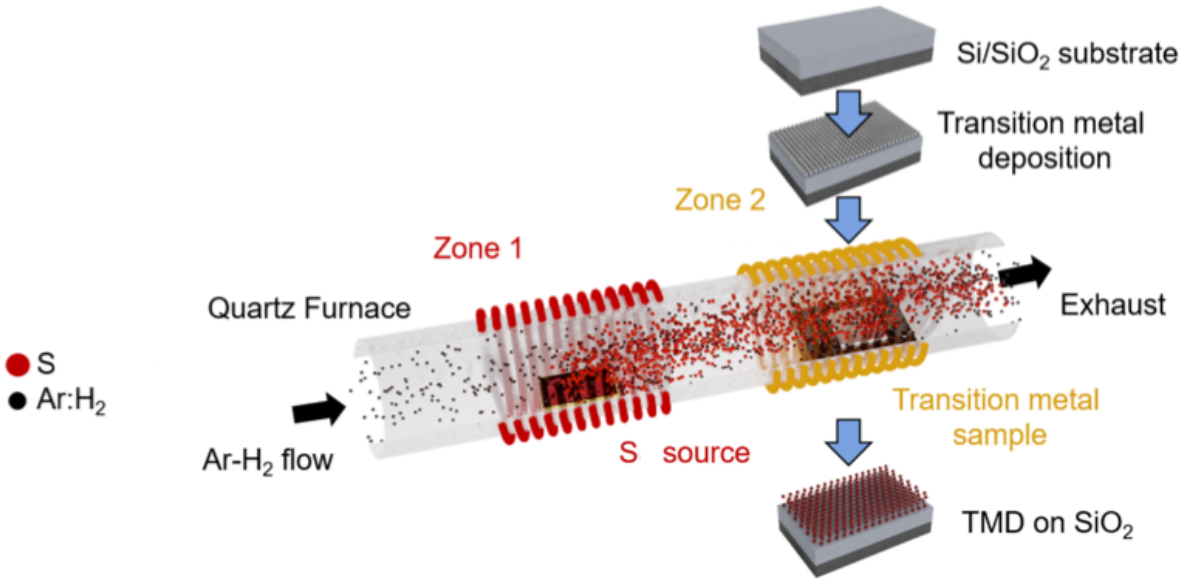

Figure 4.1 Schematics of quartz tube for CVD synthesis of TMDs on Si substrates. Adopted from [12].

Chemical vapor deposition is a process of depositing gaseous reactants on substrate for growing materials. It offers the creation of stable and high-quality layers and thin films. Gas molecules of precursors are often transported via inert gasses in quartz tube toward reaction zone (Zone 2 in Figure 4.1) and deposited on substrate where they chemically react to form a new layer of material. Excess of gasses and byproducts is vented out with inert gas stream flowing outside the quartz tube in order to reduce unwanted products and contaminations. Growth quality depends on growth temperature, substrate, precursors and overall ability to control all growth conditions in a designated system. [173] Though, CVD method and its variations offer one of the most promising sample quality and scalability in the future, there are disadvantages such as toxicity of byproducts, due to using precursor gasses which easily evaporate, in order to be able to react with the substrate.

Here we use a CVD oven to grow TMD monolayers and bilayers for which we need two precursors, one for chalcogenides and one for transition metals, shown in Figure 4.1. Some of the main parameters influencing the end result of growth are: choice of precursors, geometry

of the quartz tube, sample and precursor position, physical parameters such as temperature of growth and precursors and pressure as well as choice and flow of inert gas.

Here we used two different types of precursors for transition metals; either powder and liquid one. While for sulfur we used powder which was heated and transferred via inert Argon gas to sample substrate in quartz tube. Initially for growth of continuous monolayers of MoS_2, the powder MoO_3 precursor has been used and transferred to a polycarbonate substrate in collaboration with I. Niehues et al. MoS_2 was grown with a homemade chemical vapor deposition (CVD) system from MoO_3 (99.99%) and S (99.9999%) precursors using 100 sccm argon (6N) as a carrier gas. Sulfur vapor was produced by heating a ceramic boat containing sulfur to 140 °C by an additional heater in front of the main furnace. The growth substrate was a highly doped Si wafer with 285 nm SiO_2 on top (University Wafer). It was placed in the center of the furnace and heated to 750 °C during growth, which typically lasts 10 minutes. After growth, the substrate was cooled in the furnace to 200 °C in an Argon stream, before it was removed into ambient conditions. [174]

Later we have focused on liquid precursors for transition metals both molybdenum and tungsten. [173] Using ammonium heptamolybdate and sodium molybdate in equal ratios as a liquid precursor with growth temperature between 800°C and 900°C while sulfur temperature was around 140°C and 150°C depending on the ambient conditions resulted in optimal growth parameters for good sample quality. Similar method was also used for growing monolayer and bilayer WS_2 samples with liquid precursor.

4.1.2 Molecular Beam Epitaxy

Using vdW MBE in UHV as the growth method allows for high-quality TMDs samples with unprecedented on-demand control of lateral dimension, orientation, shapes and types of heterostructures on a large scale, which is important for potential mass-scale adoption in industry. [175–177]

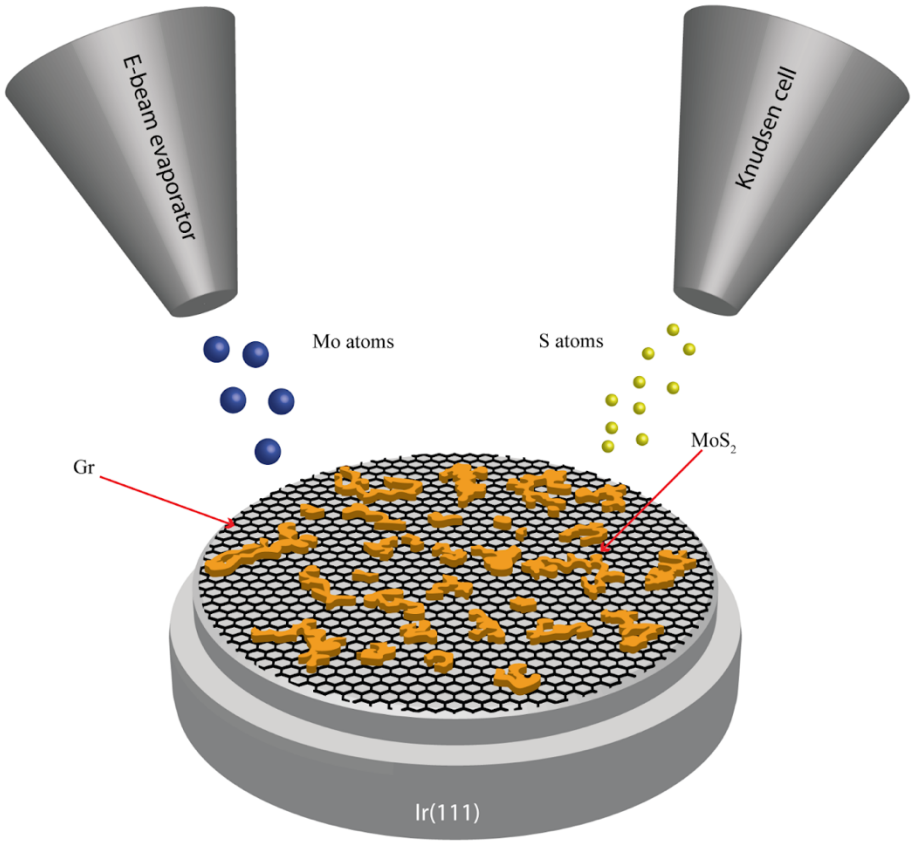

Figure 4.2 Schematic representation of a MoS_2 synthesis. Simultaneous exposure of graphene/Ir(111) to S vapor and Mo flux at room temperature (1st step), and annealing to high temperature in S vapor (2nd step), result in the formation of MoS_2 islands. Adopted from [178].

As a default step in vdW MBE sample preparation, the growth of the vdW layer, namely, epitaxial graphene on Ir(111) is performed. Graphene is grown by exposing the Ir(111) crystal to ethylene at room temperature until saturation and heated to 1300 K. The process is called temperature-programmed growth, resulting in well-oriented graphene islands. Afterwards, in order to achieve full layer growth of graphene, CVD is done by exposing the sample to 200 L

ethylene at 1200 K. [179,180] As a result, the obtained graphene layer is continuous over the large scale, containing relatively low amount of defects [181], and is expected to interact only weakly with the MoS_2 through van der Waals interaction.[182]

Preparation of MoS_2 islands requires a two-step procedure [182]: (i) growth step and (ii) annealing step. Although carrying out only the growth step would require sufficiently higher temperatures that would allow for creating the islands of optimized epitaxy, shape and flatness, the growth temperature remains 300 K. This is because the growth at higher temperatures results in the sulfur residence time drop (i.e. the time of unreacted sulfur on graphene), inhibiting the reaction between molybdenum and sulfur to MoS_2, resulting in a phase impure system with substantial Mo atom intercalation under graphene (Mo atoms residence time is infinite) and Mo cluster aggregation with MoS_2 islands. However, growth at 300K has its own setbacks in the form of nonuniform shape, randomly oriented, uneven sample flatness and with the presence of the bilayers. To overcome this issue and to promote additional growth, the second, annealing step is introduced, where the sample is quickly heated up to the higher temperature, remaining in the constant sulfur vapor pressure for a short time interval until the heating is switched off. During this second step, the islands become epitaxial and compact due to island diffusion and coalescence as well as step edge diffusion, while the small bilayer islands mostly dissociate, leaving the monolayer MoS_2 island on the sample. Schematics of the growth are depicted in Figure 4.2.

Growth recipe for MoS_2 consists of exposing graphene/Ir(111) to 300K with a Mo flux of 6×10^{14} m^{-2} s^{-1} in background sulfur pressure of 1×10^{-8} mbar and a growth time of 15 min. Afterwards, the sample is heated for annealing at 1160K and left in sulfur vapor pressure for 1 min until the heating is switched off. Successful growth is achieved in surplus of sulfur atoms while the growth rate is determined with the flux of metal and not sulfur pressure which just needs to be enough to have all the Mo atoms react to MoS_2, but also not too high because it leads to growth of bilayers and intercalation. Higher annealing temperature results in MoS_2 islands with larger lateral dimensions.

4.1.3 Transfer methods

In the literature there are many available transfer methods regarding 2D materials with some good but also some bad features and different end results[183–191] Many of them are tailored to a specific purpose and sample type. Here we present two different sample transfer techniques employed in two different types of samples. They both have some similar counterparts known from the literature [183,192], but here we modified them to be more user-friendly, faster, have better success rate and, most importantly, to be universal for different types of samples. Successful and easy-to-use transfer methods are paramount for both research and application of 2D materials. Often samples are grown on substrates not suitable for some kind of research like optical or transport measurements so we need to transfer them to a desirable substrate. Also, of great importance is investigation of influence of substrate on samples itself whether it be thermally induced strain during growth and cooling or doping. In our case, the transfer of samples was done either because we wanted to strain them so we needed to place them on a flexible substrate or because the growth substrate was not suitable for investigation of optical properties.

4.1.3.1 Wet stamping transfer (PDMS)

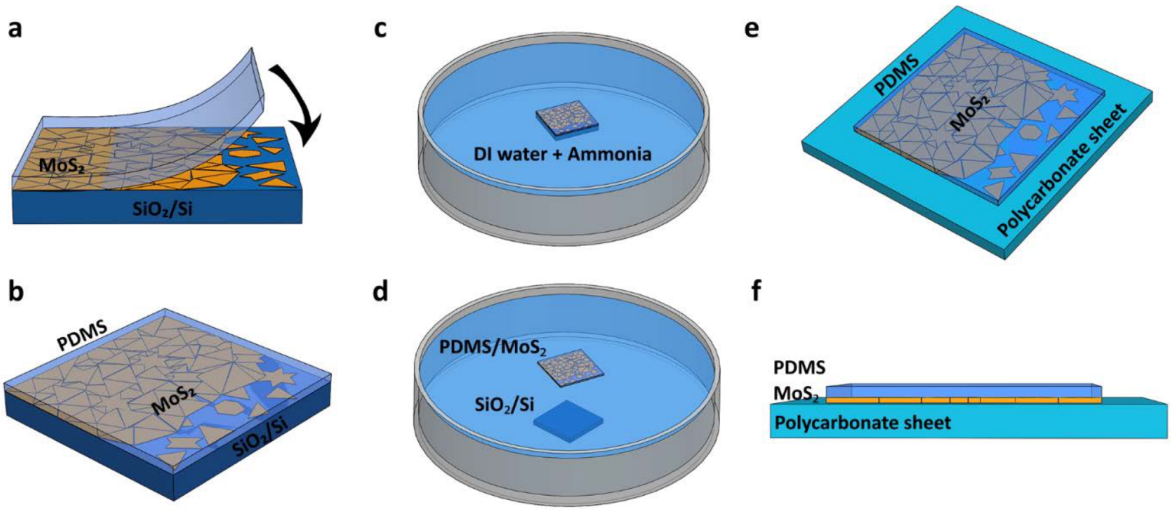

Figure 4.3 Transfer procedure consisting of 6 consecutive steps. Process starts with a) adding polydimethylsiloxane (PDMS) on sample substrate, without any pressure. b) PDMS covers all the sample material on the wafer and it sticks to both wafer and sample. c) Wafer sample with PDMS on top is added to deionized (DI) water with a few drops of ammonia. Sample is left to float in DI water. d) After a few minutes the wafer is detached and sinks to the bottom of the DI water dish. Floating on top is left PDMS with all of the samples. e) PDMS with samples is gently put onto a polycarbonate flexible substrate and dried. After which is ready for use in straining measurements. f) Side view of the prepared sample sandwich with PDMS on top and sample crystals in between top layer and bottom polycarbonate. Taken from [174].

A lot of 2D materials are grown on Si wafers or sapphire substrates which are suitable for further characterization. Sapphire substrates are excellent for optical measurements, especially when a transparent substrate is needed. Si wafer is an industry standard platform for electrical measurements, transport characterization or optical measurements in reflection. In the case if 2D material is grown on sapphire and there is a need to integrate the sample in a device than it has to be transferred to Si wafer. Another way around is when we need to conduct optical measurements in transmission and the sample is grown on Si wafer - in that case sample has to be transferred to the sapphire substrate. Currently there are no growth procedures on flexible substrates which can be used for straining measurements. The reason for this is that flexible substrates are mostly polymers which do not sustain high growth temperatures of synthesizing 2D materials. In all afore-mentioned cases, sample transfer procedure has to be implemented.

Procedure for transferring as-grown complete continuous monolayer or monolayer flakes of 2D materials such as MoS_2 or WS_2 from wafer to flexible substrate starts with adding Gel-Pack polydimethylsiloxane (PDMS) of 160 um as a support layer on top of the wafer where the sample is. We gently put this PDMS support layer without using additional pressure as it is important that in later step water is able to protrude between layers. To accelerate this process we can even use carbon fiber on the end of the wafer to not let PDMS completely stick to the wafer and offer entrance to water protruding. The size of PDMS layer is roughly the size of a wafer but not smaller. We prepare in a clean petri dish a DI water with a few drops of Ammonia solution. Wafer with PDMS on top is put on top of the DI water with PDMS on top and the wafer floating in water. In a matter of tens of minutes or shorter Si wafer should detach from the PDMS and drop to the bottom of the petri dish, while PDMS with 2D materials is left floating on the surface of DI water. With twissors we gently pick up PDMS/2D materials and remove the water from it with nitrogen gas or just leave it for water to evaporate. We used 500 um thick polycarbonate as a flexible substrate but also it can be used with others like PMMA of similar thickness. On this flexible substrate, polycarbonate we gently put our PDMS with 2D material beneath trying to avoid any wrinkles and bubbles of PDMS layer, in the end we can gently apply pressure to achieve better cohesion in the sandwich of PDMS/2D material/polycarbonate to have more efficient strain transfer in the forthcoming experiments. We leave the PDMS layer on top in this case as it serves as a capping layer which additionally helps for efficient strain transfer by limiting slippage of 2D material on polycarbonate while it is strained to higher strains.

This procedure depicted in Figure 4.3 is used for transfer of continuous MoS_2 monolayers in work we did in paper I. Niehues et al. [174] and later on twisted bilayers of WS_2 research, both presented in Chapter 7.

4.1.3.2 Electrochemical delamination (PMMA)

Atomically thin heterostructure system such as MoS_2/graphene holds potential for photodetection applications. [135,193,194] However, the MBE growth method relies on metallic substrates that are unsuitable for integration in electrical circuits for further (opto)electronic application. In addition, metallic substrates notoriously quench the optical signals depending on the interaction between film and substrate. [195] Having all in mind, it is of paramount importance to develop the transfer technique that will maintain intrinsic structural and electronic properties of the MBE grown layer.

The transfer method presented here is one of the variants of electrochemical transfer methods often named the "bubbling method". [189,191] This name comes from the utilization of the small hydrogen bubbles which originate at metal substrate and infuse between grown material and metal substrate which enables delamination of target material for further transfer. From previous literature, a complete film transfer of single layer 2D materials such as graphene or h-BN from metallic substrates is known and well documented. [196,197]

We have already used the same method for transferring monolayer film of borophene from metal to arbitrary surface which is in detail described in B. Radatovic et al. [125] Here we use the same method to achieve an almost cm size transfer of TMDs/graphene heterostructure, proving the versatility and universality of the method. Whole transfer procedure is illustrated in Figure 4.4.

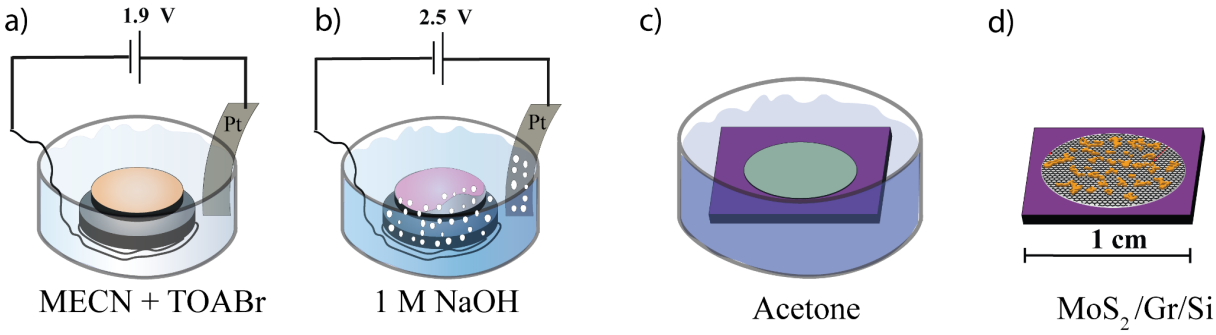

Figure 4.4 Scheme of the transfer process. a) Ir crystal with HS is immersed into solution of MECN and tetra-n-octylammonium bromide during which crystal is connected with Ni wire to negative potential and platinum foil is immersed into the same solution and connected to positive potential after which potential difference up to 1.9 V is applied. b) Ir crystal with HS and layer of poly(methyl methacrylate) (PMMA) is immersed into 1M NaOH solution and connected to negative potential via Ni wire and Pt foil is immersed and connected to positive potential after which potential difference up to 2.5 V is applied, during which layer of HS with PMMA on top is separated from Ir crystal leaving it floating, c) After picking up HS with PMMA with Si wafer, PMMA is removed by immersing the wafer into acetone d) As a result of the whole process, clean HS is left on top of Si wafer. Taken from [178].

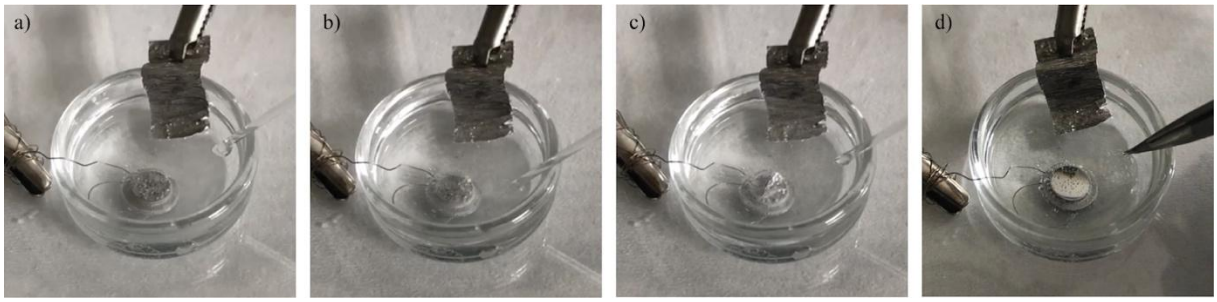

Figure 4.5 Photographs of the delamination step of the transfer process, showing gradual formation of bubbles and subsequent delamination of PMMA/MoS_2/graphene from Ir (111). Photographs are taken every 60s a) – d) subsequently. Taken from [178].

In its core it is an electrochemical delamination method based on a two step electrochemical process during which Ir crystal is connected to negative potential and Pt foil is used for positive potential. First part is based on an electrochemical process during which large (TOA+) ions, under applied bias voltage in solution of MECN and tetra-n-octylammonium bromide, intercalate between graphene and metal substrate for weakening their interaction. [196] In the second part, the sample is coated with poly(methyl methacrylate) (PMMA), which will later be used as a supporting layer. After solidification of PMMA, the second electrochemical step starts where the coated sample is immersed in a 1M NaOH solution where under potential difference bubbles are formed on the interface of graphene and metal. [189]As can be seen in Figure 4.5. gradual formation of bubbles protrudes through and PMMA/MoS_2/graphene is detached and left floating. In the next step, we use an arbitrary surface, in our case 280 nm silicon oxide coated Si wafer, to pick up a PMMA coated sample. In the final part, the PMMA coating is removed with acetone. After each individual step, the sample is rinsed with DI water to ensure removal of any previous liquid used. The result is the successful transfer of an almost complete 6 mm diameter sample from Ir(111) to the desirable substrate.

4.2 Micro-Raman and PL spectroscopy

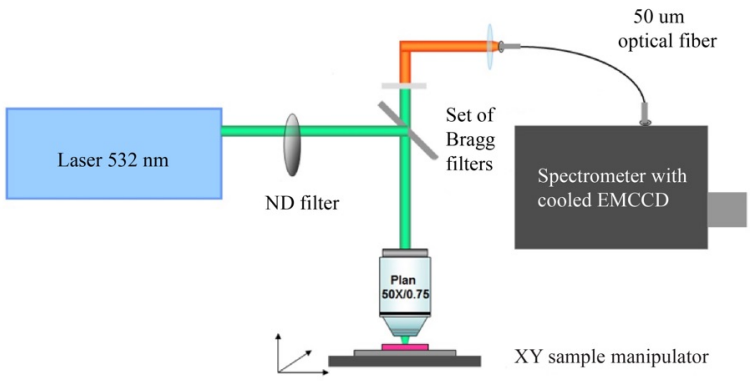

Figure 4.6 Optical setup scheme based on confocal micro-Raman spectrometer with EMCCD for measuring Raman, photoluminescence and absorption spectra.

We use an optical setup based on a confocal microscope in backscattered configuration for absorption (contrast reflectivity), photoluminescence and Raman spectra measurements shown in Figures 4.6 and 4.7. The 488 nm, 532 nm and 630 nm excitation laser lines can be used and maintained sufficiently low to avoid damage to the sample. The setup is home-made micro-Raman with two different spectrometers and detectors and two objectives 10x and 50x (N.A. 0.75). System is confocal microscope based on cage system design equipped with an appropriate set of filters, dichroic mirrors or set of Bragg mirrors, polarization plates and objective lens together with xy-translation stages which use sequential sample movement and spectrum acquisition to collect data from the defined sample area with sub-micron resolution. Collected backscattered light is guided through an optical fiber with a 50 μm core diameter, which acts as a confocal detection pinhole. Coupled light from fiber is guided to either a 30 cm (Andor Shamrock 303i) or 50 cm (Andor Shamrock 500i-B1) long spectrometer systems with three different gratings (150, 300, 1800 l/mm) to either a cooled CCD (Andor iDus DV420A) or an EMCCD (Andor Newton 971), respectively. EM-CCD technology offers significant increases in sensitivity for challenging samples with low signal levels.

Optical images with magnification of 5x, 10x and 50x were taken in a home-built microscope in backscattered reflection configuration with a Quartz-Tungsten-Halogen lamp as a white light source in Koehler illumination configuration.

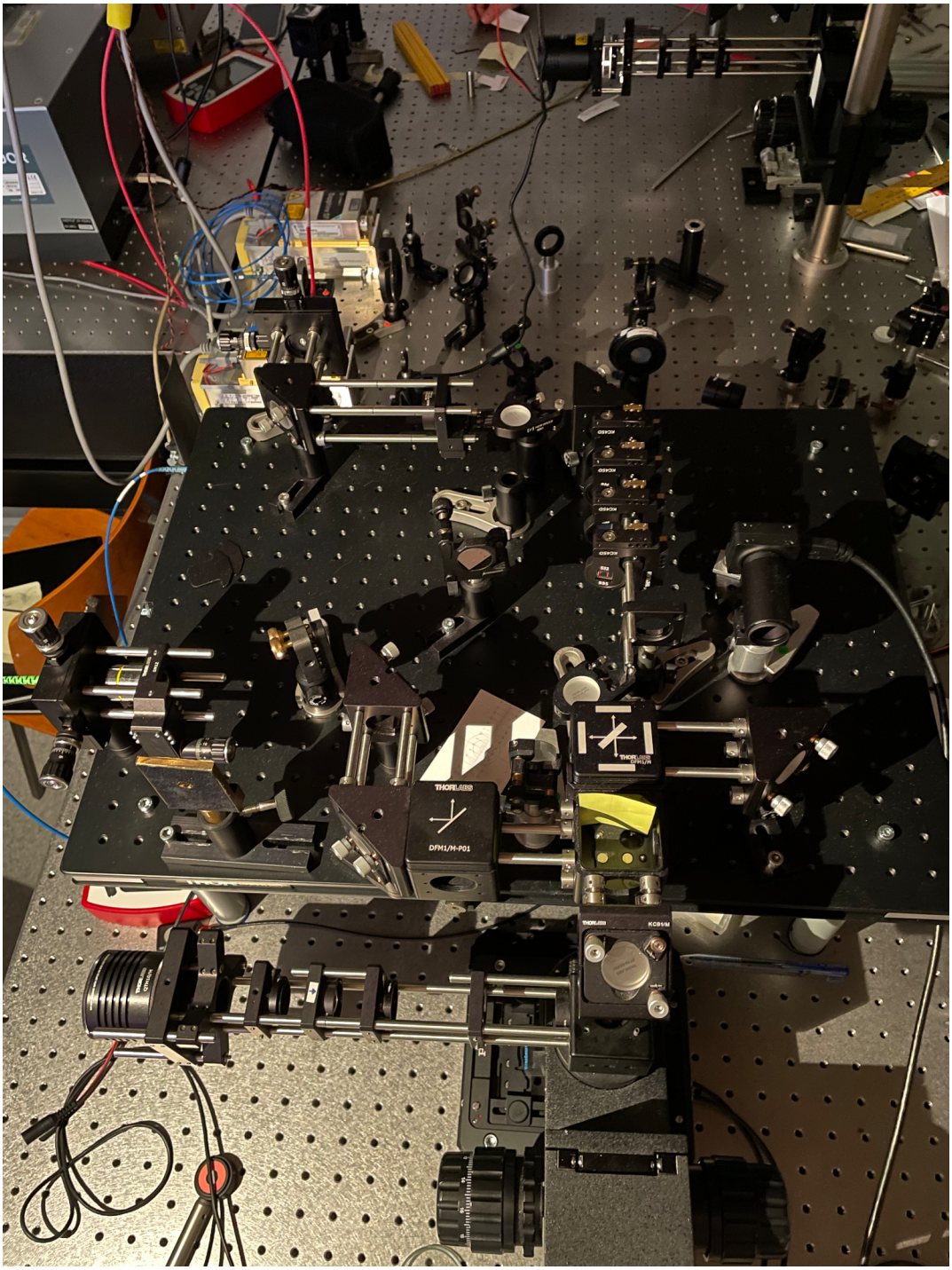

Figure 4.7 Image of the home-made micro-Raman spectrometer used for optical measurements at the Institute of Physics, Zagreb.

4.3 Birefringent TWINS interferometer (hyperspectral imaging)

We used a high-performance hyperspectral camera based on the Fourier-transform approach. Where the two delayed images are generated by the Translating-Wedge-Based Identical Pulses eNcoding System (TWINS) [198] a common-path birefringent interferometer that combines compactness, intrinsic interferometric delay precision, long-term stability and insensitivity to vibrations. In this imaging system, TWINS is employed as a time-scanning interferometer and generates high-contrast interferograms at the single-pixel level. The camera exhibits high throughput and provides hyperspectral images with a spectral background level of −30 dB. It is able to take high-quality spectral measurements of absolute reflectance, fluorescence and transmission. [199]

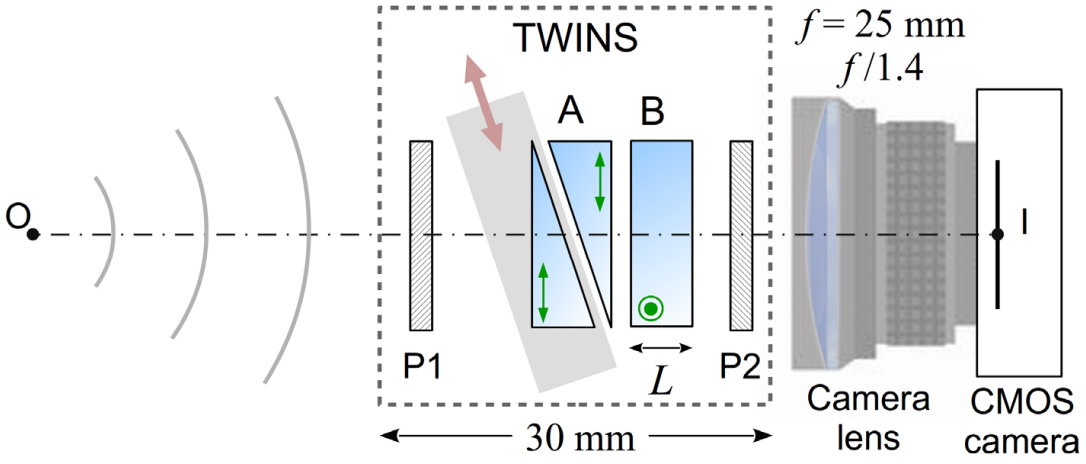

Figure 4.8 Schematic setup of the hyperspectral camera. P1 and P2: wire-grid polarizers; A block: α-BBO wedges, with optical axis parallel to the plane (green double arrow); B block: α-BBO plate, with optical axis normal to the plane (green circle). The brown double arrow indicates the wedge translation direction. O: object; I: image. Taken from [199].

A scheme of the hyperspectral camera is shown in Figure 4.8 It consists of a TWINS interferometer (P1, A, B and P2) followed by a monochrome imaging system. A and B are birefringent blocks made of α-barium borate (α-BBO), P1 and P2 are wire-grid polarizers with extinction ratio >5000 at wavelengths from 400 nm to 2 μm. P1 polarizes the input light at 45° with respect to the optical axes of A and B. Block B is a plate with thickness L = 2.4 mm and aperture diameter D = 5 mm; it introduces a fixed phase delay between the two orthogonal

polarizations that propagate along the fast and slow axes of the material. Block A has an optical axis orthogonal to the one of block B (see green arrows and circle in Figure 4.8, respectively), thus applying a delay with the opposite sign. The overall phase delay introduced by the TWINS ranges from positive to negative values according to the relative thickness of the two blocks. To enable fine tuning of the phase delay, block A is shaped in the form of two wedges with the same apex angle (7°), one of which is mounted on a motorized translation stage (L-402.10SD, Physik Instrumente) with a maximum travel range of 13 mm. Interference between the two replicas is guaranteed by P2, which is also set at 45° with respect to the optical axes of A and B, and projects the two fields to the same polarization. The spectral resolution of the interferometer is inversely proportional to the total phase delay. For example, scanning the position of the wedges ± 1mm around the zero path delay (ZPD) introduces a delay of ± 50 fs to the replicas of a wave at $\lambda = 600$ nm; this corresponds to spectral resolution of 15 THz (~18 nm). The camera lens has focal length $f = 25$ mm and maximum aperture $f/1.4$. The detector is a monochrome CMOS silicon camera with size 6.78 mm × 5.43 mm (1/1.8" format), 1280 × 1024 pixels, with 10-bits depth and spectral sensitivity from 400 nm to 1100 nm. The total angular field of view of the combined camera lens and detector is 15.4° (19° along the sensor diagonal). [199]

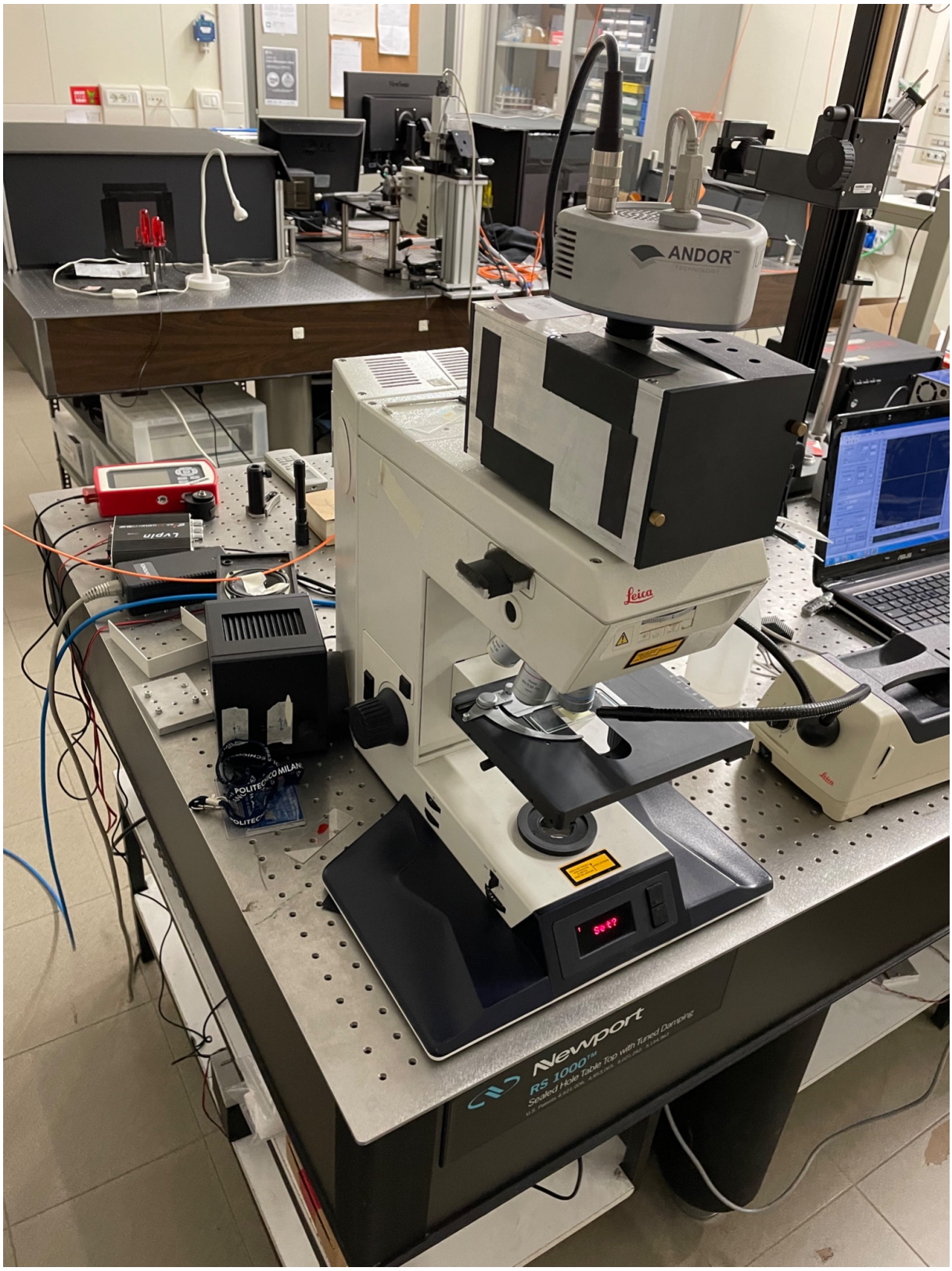

Figure 4.9 Image of the used home-made hyperspectral TWINS interferometer built in Leica microscope at Politecnico di Milano.

Figure 4.10 Image of the TWINS interferometer with wedges, translator stages and CCD camera for use in macroscopic objects such as art paintings.

4.4 Cryogenic measurements

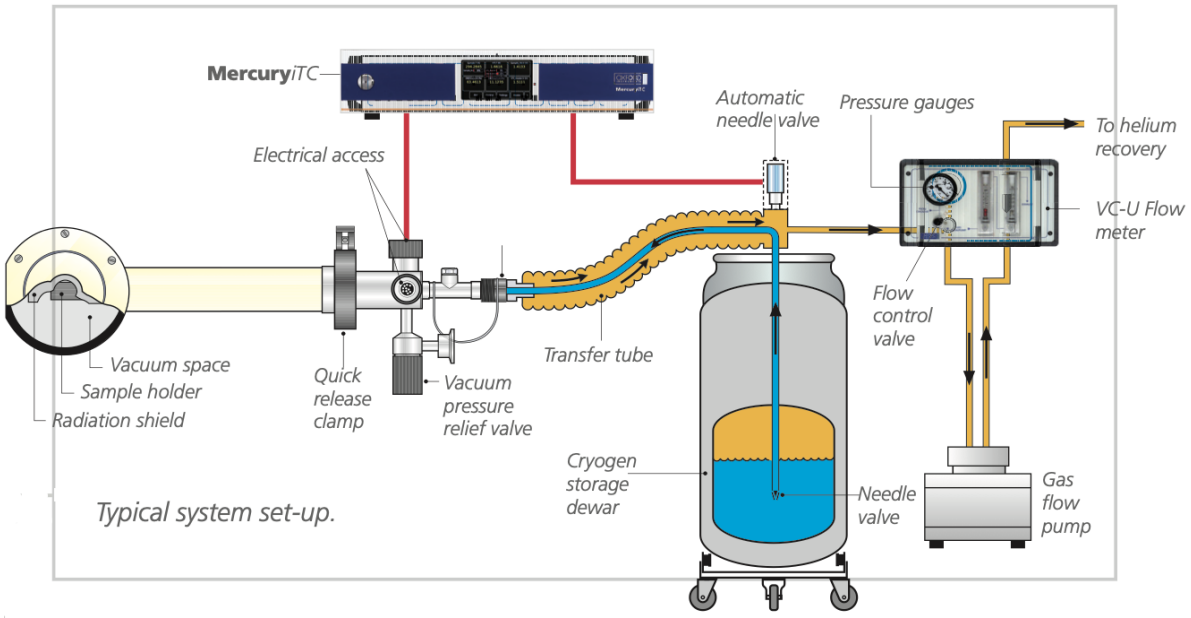

Figure 4.11. Oxford Instruments cryogenic system based on continuous flow cryostat Microstat HiRes which consists of a temperature controller, gas flow controller and pump, dewar and transfer line. Taken from [200].

We have used Oxford Instruments continuous flow cryostat system to measure optical response of the samples at low temperature, in the temperature regime from 4.2 K up to 500 K using helium as a coolant. Continuous flow cryostats are based on the flow of coolant liquid which after cooling the sample heats and becomes gaseous. In our case we have used liquid helium from our cryogenic dewar connected with a flexible transfer tube to cryostat. Transfer tube has a dewar leg which goes inside the dewar with liquid helium and a cryostat arm which brings liquid helium to flow through the cold finger which cools down the sample. After it is heated it becomes gas and is transferred again through a transfer tube (but different path) to the helium recovery line at the Institute of Physics which can store and reliquefy helium gas. The flow of helium gas is controlled by VC-U flow meter and by gas flow pump GF-4. Inside of the cryostat there is a temperature sensor and a heater which are connected to the temperature controller Mercury ITC which control and stabilize temperature in the cryostat. This system is very convenient because of its user-friendliness, low helium consumption of less than 1 l/h, low

vibrations below 20 nm, low sample drift 150 nm/h, ability to heat the sample to 500 K, lightweightness of 1.5 kg and ability to do electrical measurements with electrical contacts feedthrough. This cryostat can be used both in reflection and transmission, but we have used it in reflection.

a) b)

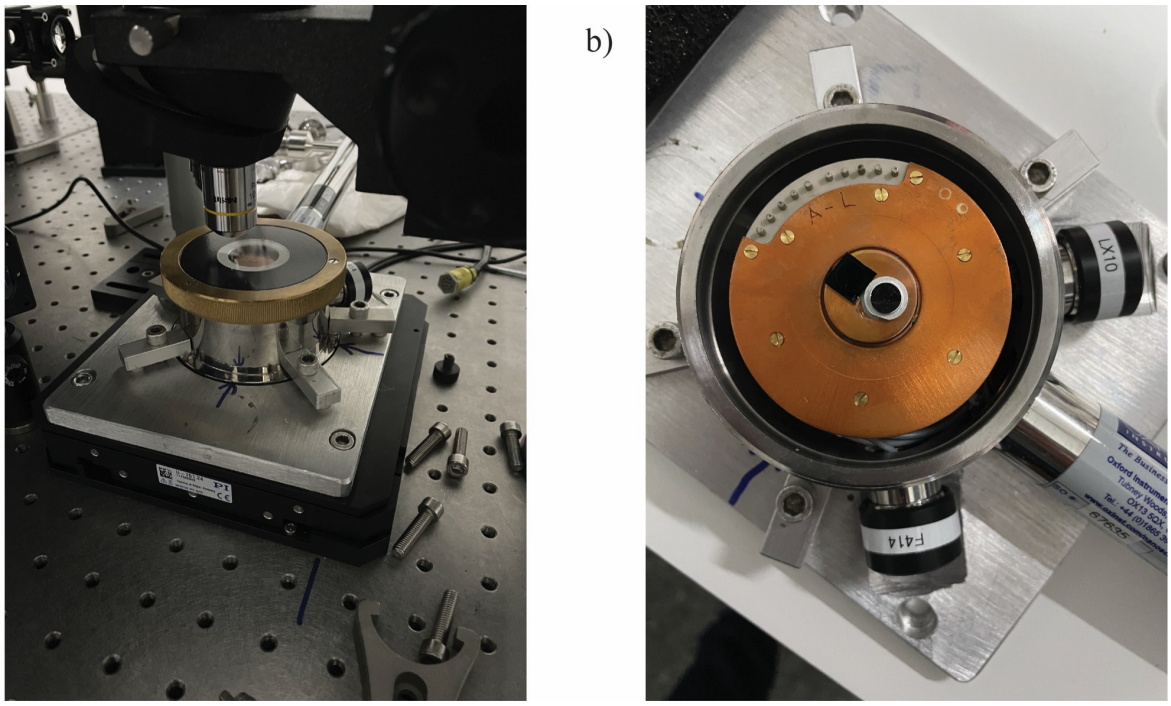

Figure 4.12 a) Image showing an optical cryostat mounted on the xy stage under the microscope objective. b) Inside of a cryostat which shows a cold finger for mounting and cooling the sample and contacts for an outside wiring connection.

4.5 Structural characterization techniques

Scanning probe microscopy (SPM) techniques offer a unique approach to characterize the surface of 2D materials and are of particular use for 2D materials, where the entire sample is a surface. SPM was a key invention in nanoscience and had spread to a wide spectrum of fields, allowing for a paradigm shift in the understanding and perception of matter at its nanoscopic and even atomic levels. Using a sharp tip to physically raster-scan the samples and locally collect information from the surface, various signals can be detected with atomic resolution which gives insights to structural, vibrational, electronic, optical, magnetic, (bio)chemical and mechanical properties. [201]

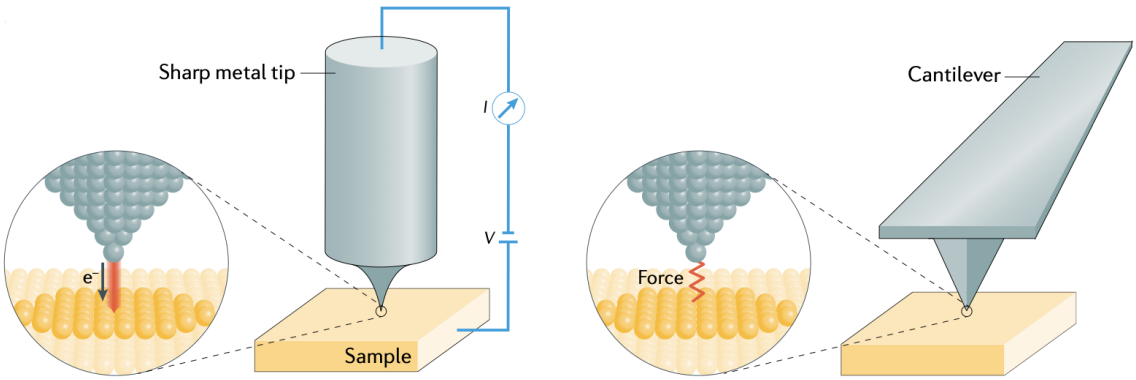

Figure 4.13 Basic set-up for scanning probe microscopy. Scanning tunneling microscopy (STM) and atomic force microscopy (AFM) both use a tip to scan the sample. Both techniques use different feedback signals to maintain constant tip–sample interaction, but their basic principle of operation and image acquisition mechanisms are similar. a) STM collects the tunneling current between the tip apex and the sample when a bias voltage is applied. b) AFM detects local forces and corresponding mechanical parameters through a spring-like cantilever. Taken from [201].

4.5.1 Scanning tunneling microscopy

Visualizing atoms on a solid surface has been a long-standing dream for researchers, and was finally fulfilled by the invention of scanning tunneling microscopy (STM) in 1981 by Rohrer, Binnig and Gerber at IBM Zürich. [202] STM uses an atomically sharp biased metal tip to collect small currents from the metal surface, based on the quantum mechanical tunneling effect (Figure 4.13 a)). Owing to the highly localized nature of the tunneling current, atomically resolved images could be obtained by raster-scanning the tip over the surface while using a feedback loop to keep the tunneling current constant. [201]

Scanning tunneling measurements (STM) were done with Aarhus type STM from Specs where the sample is thermally and electrically isolated from the metal block and STM is hanging on the springs from it. As a STM tip 99.9% pure tungsten wire is used which is required to etch the tip in base NaOH enhanced with voltage pulses. WsXM is used for analyzing STM images. [203]

4.5.2 Atomic force microscopy

Soon after the invention of STM, Binnig et al. were able to map the tip–sample interaction by atomic forces instead of the tunnelling current, which led to the birth of atomic force microscopy (AFM)[204] (Figure. 4.13 b)). AFM uses a sharp tip on a cantilever to determine information about the morphology of a surface. The cantilever can oscillate and, depending on the method used, measure different properties from the surface. A laser is focused on the end of the reflective cantilever, and its displacement is measured by a position sensitive photodetector. The tip raster scans across the surface and the frequency of oscillations (the force measured) changes in reaction to variations in the height of the surface. Similar to STM, a feedback loop keeps the frequency constant, and the amount it must be adjusted to remain at the correct level is used to determine the size of features it scanned over. [201] AFM is able to image almost any type of surface, unlike STM that requires conducting or semiconducting samples. AFM can work in two modes, contact and tapping, and both modes use similar operating principles but, as the names suggest, they are either in contact or repeatedly tapping the surface as they move along it. As AFM measurements are particularly sensitive to ambient noise, AFM is contained in isolated acoustic enclosures on vibration isolating tables. Atomic force microscopy (AFM) characterization was performed with a JPK Nanowizard Ultra Speed AFM (Bruker GmbH). Non-contact AC (tapping) mode was used for image acquisition with a setpoint around 50%. Bruker FESP-V2 silicon tips with a nominal spring constant of 2.8 N/m, a tip radius of 8 nm and a resonance frequency of 75 kHZ were used. Images were processed with JPK Data Processing software and WSxM software. [203]

4.5.3 Low Energy Electron Diffraction

Low energy electron diffraction (LEED) is a technique used in UHV. It consists of monochromatic beam of low energy electrons. Electrons bombard the surface of the sample and are back-scattered to form a diffraction pattern on a fluorescent screen revealing crystal surface structure. Electron energies ranging from 10 to 100 eV have an inelastic mean free path of only 1 – 2 atomic layers ensuring high surface sensitivity. With CCD camera reciprocal lattice patterns on LEED screen are recorded, for representation its contrast is always inverted and enhanced. [178]

4.6 Ultrafast femtosecond pump-probe

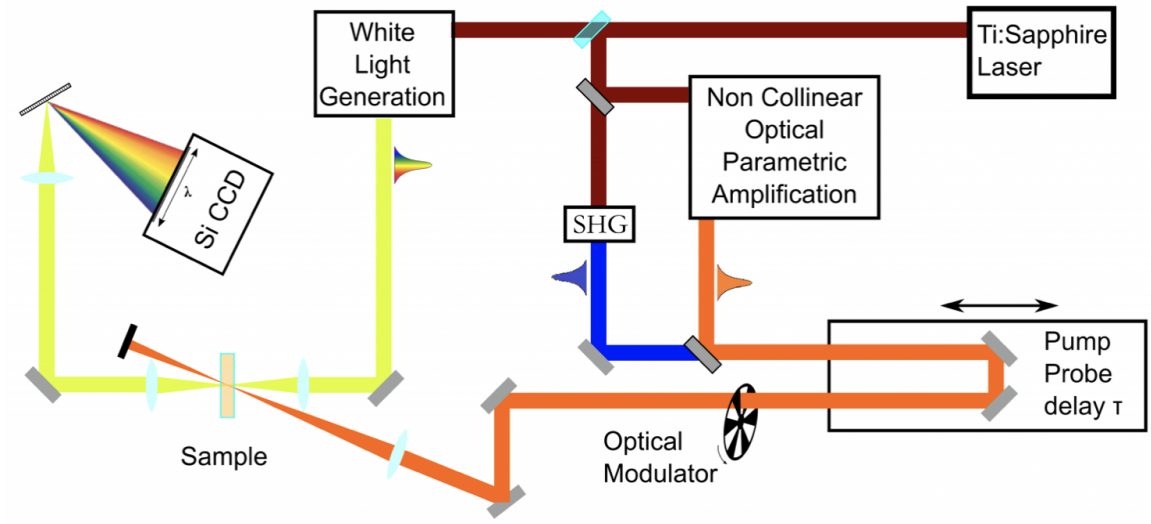

Figure 4.14 Schematic representation of ultrafast femtosecond pump-probe with Ti:Sapphire laser, spectrometer and Si CCD. Taken from [205]

For ultrafast dynamics measurements of sample upon applied strain, a pump-probe setup was employed, see Figure 4.14. An ultrafast laser system provides both the pump and the probe pulses for the measurements. A Ti:Sapphire amplifier is used to pump a non colinear optical parametric amplifier (OPA), which generates down-converted photons. In the measurements, the pump pulse excites photocarriers in the sample. The presence of these photocarriers alters the complex index of refraction of the sample or it absorption properties via various mechanisms. [85] Second pulse is used for measuring the change of the complex index of refraction and will be sensed by measuring transient absorption, defined as the normalized change of the probe transmission induced by the pump, $\Delta T/T = (T - T_0)/T_0$. The probe is tuned near the excitonic resonances. The transient absorption is measured as a function of the probe delay, defined as the arrival time of the probe pulse with respect to the pump pulse. In pump-probe experiment, the probe delay is controlled by sending the pump or probe beam to a retroreflector that is installed on a translational stage. Moving the retroreflector changes the optical path length of the corresponding pulse, and hence its arrival time at the sample.

The setup we used is located in Politecnico di Milano in Giulio Cerullo's group and called "Clark Long". It is seeded by an amplified Ti:Sapphire laser emitting 100-fs pulses at 800nm,

with a repetition rate of 2 kHz. The “Clark Long” setup offers an average temporal resolution of ~ 100 fs. It can be turned into several layouts to study different sample configurations, from solid state targets to solutions, across ultrabroad bandwidths and ultralong temporal windows, from a few hundreds of femtoseconds to 1.5 nanoseconds.
As for the pump we have 3 options; we can use the fundamental laser beam at 800 nm, we can frequency double the fundamental, i.e. Second Harmonic Generation (SHG) at 400 nm, or we can exploit a frequency tunable NOPA; in this last case, the excitation beam can continuously cover all the wavelengths from 480 nm to 1.6 μm, with a bandwidth of 10-20 nm.

The same versatility applies for the broadband probe, obtained by White Light Generation (WLG) by thin highly nonlinear plates. The 800 nm pumped Sapphire plate generates light in the range of 430-780 nm (Visible) and 840-1200 nm (Near IR). With 800 nm pumped CaF2 crystals the WL probe beam can be extended to the UV region, down to 340 nm. [178,205]

5 Nanometer sized MoS_2/graphene heterostructures

5.1 Motivation

Two-dimensional semiconductors such as transition metal dichalcogenides combine strong light-matter interaction and rich exciton and valley physics with good chemical stability and scalable fabrication techniques, and are thus excellent prospects for (nano)electronic, optoelectronic, photonic and light-harvesting applications.[19,22,117,206–208] Scalable fabrication of high-quality TMD monolayers and related heterostructures (HSs) with high-quality interfaces and controlled stack orientation is still challenging and hinders their adoption for technological application. [209] Three approaches are primarily used to fabricate TMD monolayers and HSs: (1) mechanical exfoliation, where the monolayers are cleaved from a bulk crystal using adhesive tape[195,210] and transferred onto desired substrates or other monolayers; (2) chemical vapor deposition (CVD), where the layers are formed out of a gaseous phase *via* a chemical reaction [211,212] and (3) molecular beam epitaxy (MBE), where the constituents are provided in the form of a molecular beam under ultra-high vacuum (UHV) conditions. [140,182,213,214] The top-down exfoliation from bulk crystals offers high sample quality but cannot be scaled up towards mass production. The bottom-up CVD and MBE methods, on the other hand, are scalable to industrial quantities. Among the two, MBE offers superior control of growth parameters that allows for epitaxial layer-by-layer growth and tailoring of the sample morphology and the functional properties derived from it. [38,215,216]

Applications of MBE grown TMD MLs and their HSs require substrates whose properties are specific to the application. For instance, for a transistor the substrate will typically be a gate dielectric. Likewise, for fluorescence applications, the substrates that favor photoexcited charge or energy transfer are inadequate. [195] MBE growth of TMDs has enabled high purity films and novel HSs [140,217,218] MoS_2/graphene HSs hold potential for photodetection applications. A MoS_2/graphene photodetector would benefit from MoS_2 enhanced responsivity, broad spectral absorption bandwidth and a relatively fast response speed of the device that has been obtained because of the shortened channel between the source and drain electrodes for photogenerated carriers in the vertical heterostructure. [135,193,194] However, the MBE growth of such HS requires a metallic substrate, which is not suitable for integration in electrical circuits for further (opto)electronic applications. Having that in mind, large scale transfer of atomically thin semiconductor layers onto a targeting substrate has received strong interest from both academia and industry [190] and references therein. Layer transfer via chemical epitaxial

lift-off (ELO) [186,219,220] laser assisted lift-off (LLO) [221–223] and by mechanical release [224–226] are the most common large scale transfer methods. Since each transfer method has its own advantages and limitations, care must be taken to choose the right transfer method for a specific application that will maintain the quality of the transferred epitaxial layer.

Here we show the growth of a high-quality HS of nm size monolayer MoS_2 islands on a macroscopic graphene sheet on Ir(111) and the transfer of the heterostructure to 280 nm thick silicon dioxide layer grown on silicon wafer (hereafter referred to as Si wafer), and show its excellent structural and spectroscopic properties. We use an UHV two-step MBE synthesis with elemental sulfur to grow MoS_2 islands on an 6 mm diameter wide graphene sheet on Ir(111). [227,228] In-situ LEED and STM and ex-situ AFM measurements confirm the good quality of grown samples and quantify the MoS_2coverage and grain size distribution of MoS_2 islands. To become independent of the metallic substrate, the HS is transferred via an electrochemical delamination process from Ir(111) to a more suitable substrate, in our case a Si wafer. The transfer method consists of two successive electrochemical treatments. The first step weakens the interaction between graphene and Ir(111), after which PMMA is coated to support MoS_2/graphene HS during the transfer. In the second electrochemical step the PMMA/MoS_2/graphene layer is completely detached from Ir(111) due to bubble formation on the Ir(111) surface [125,197] and placed onto the Si wafer. Post-transfer characterization of samples unveils successful transfer of the samples, stability to ambient conditions, and high quality of the samples confirmed by their optical response. We expect this procedure to enable transfer of a broad range of 2D materials onto almost any substrate, thus overcoming one of the major limitations for device applications.[178]

5.2 UHV *in-situ* characterization

We characterize the sample *in-situ* inside the MBE UHV chamber using LEED and STM. Prior to TMD growth, the first order diffraction spots of graphene and Ir align (Figure 5.1 .a)) and a well-known moiré satellite spot indicates a uniform layer of R0 phase graphene. [229] After the two-step growth of MoS_2 islands, the MoS_2 diffraction spots (LEED pattern in Figure 5.1 b) align with graphene and Ir, up to a small azimuthal broadening (± 4°). The graphene surface is partly covered by monolayer MoS_2 islands (STM image in Figure 5.1 c)) that are composed of MoS_2 segments connected by grain boundaries (blue arrows). We find that the average segment diameter is 36 ± 4 nm. Grain boundaries and edges display brighter STM contrast as a consequence of their metallic character. [182,230] Red arrows indicated in Figure 5.1 c) point to small bilayer islands remaining after the annealing step. On top of monolayer MoS_2, we also note small bright spots that are marked by white arrows in Figure 5.1 d), which we attribute to point defects in MoS_2 due to S deficiency in the annealing step. To avoid them it is necessary to have an excess of sulfur which, on the other hand, could lead to additional MoS_2 bilayer growth. Therefore, the applied growth conditions are a compromise that ensures that both bilayer and point defect occurrences are low. The STM line profile along the green line in Figure 5.1 .d), shown in Figure 5.1 e) displays the apparent height of the monolayer segment, as well as the small MoS_2 island on the second layer (schematic in Figure 5.1 f)). Furthermore, it reveals that the metallic edges of the monolayer are apparently higher by 0.2 nm than the inner part of the island.

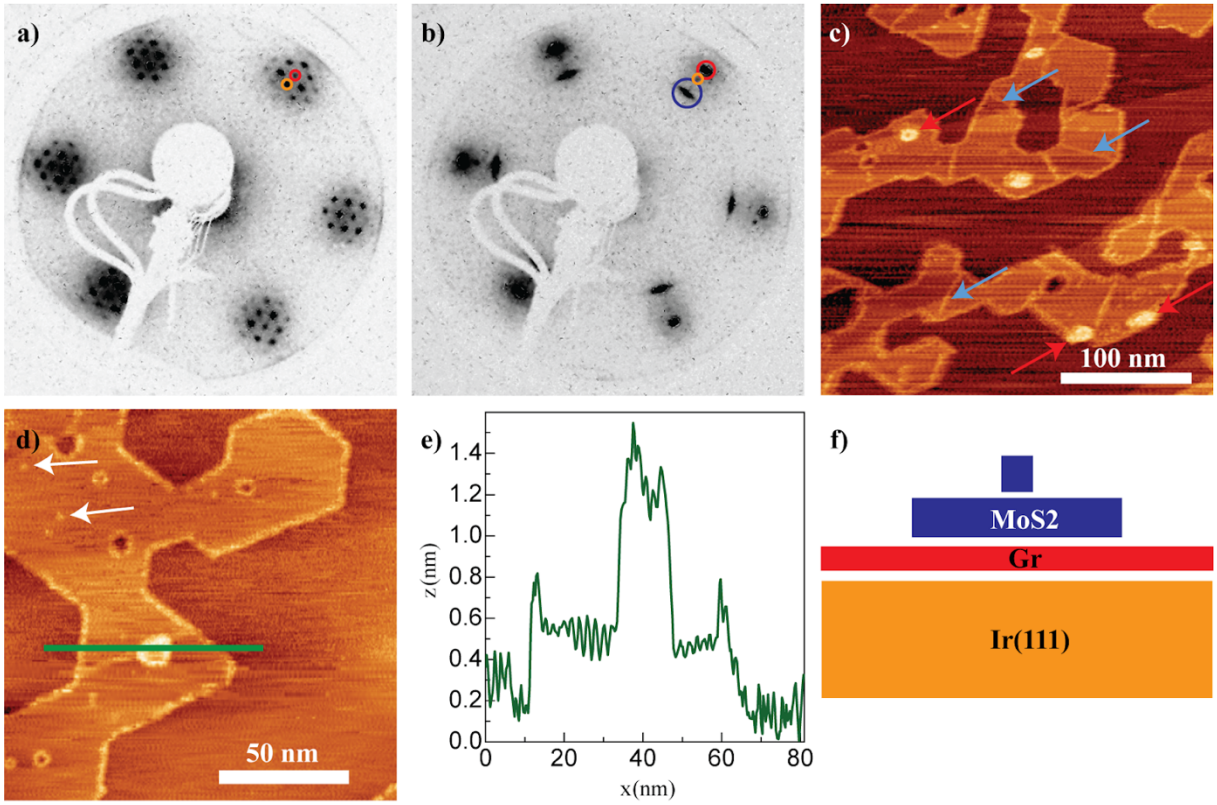

Figure 5.1. a)-b) LEED patterns of graphene/Ir(111) and MoS_2/graphene/Ir(111), respectively. Diffraction spots of graphene (red), Ir (orange) and MoS_2 (blue) are marked by circles. Electron energy was 73 eV in each case. c)-d) STM images of monolayer MoS_2 islands. Grain boundaries (blue) and point defects (white) in monolayer MoS_2, as well as bilayer islands (red), are indicated by arrows. Tunneling current, bias voltage: -0.67 nA, -1.36 V. (e) STM line profile along the green line in d). f) Schematic sectional view along the line profile in e). Taken from [178]

5.3 Ambient *ex-situ* pre-transfer characterization

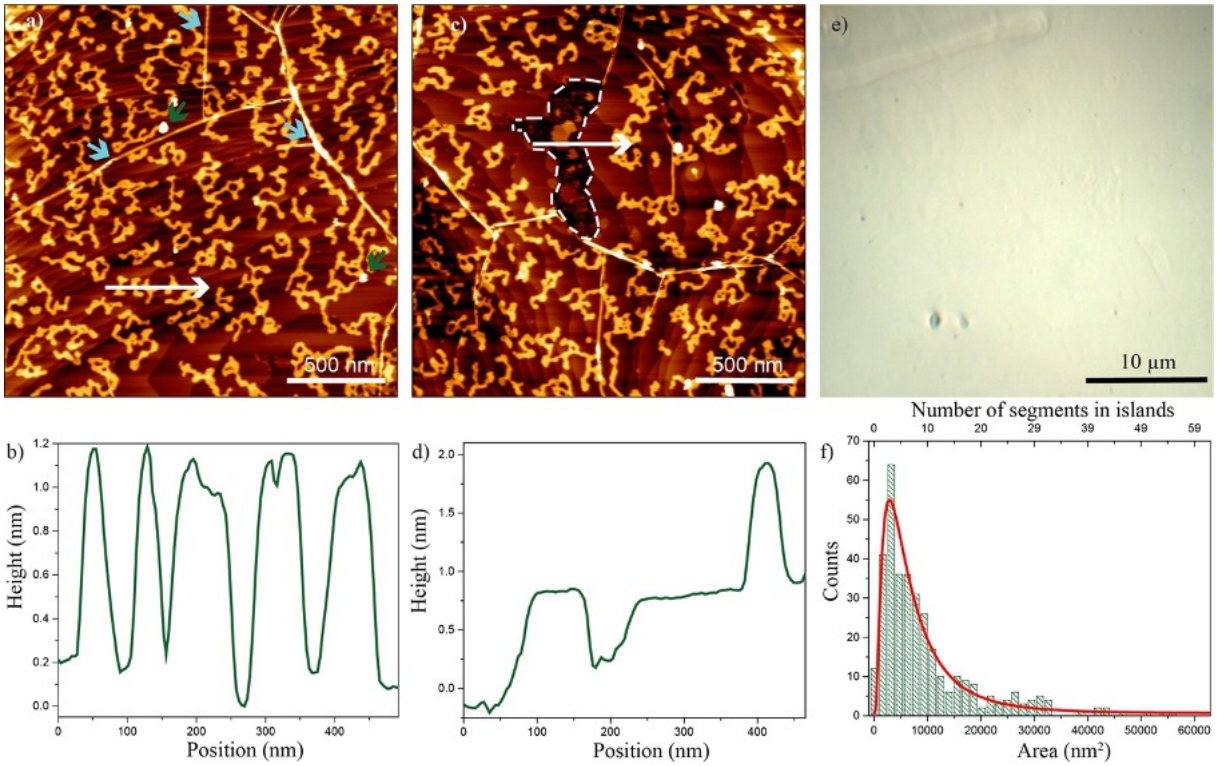

Figure 5.2a) AFM image of MoS_2 grown on graphene on top of Ir (111) taken after extraction from UHV. b) Height profile along the white arrow in a) which shows the thickness of several MoS_2 monolayer islands. c) AFM image of a sample area with an etched graphene area outlined by a white dashed line. d) Height profile along the white arrow in c) which shows the thickness of the graphene sheet and one MoS_2 island. e) Optical image of sample. f) Distribution of MoS_2 islands sizes (histogram) and fit to a log-normal distribution (red line). Taken from [178]

After the growth and *in-situ* characterization in UHV, the sample was characterized under ambient conditions with AFM. The characteristic surface topography is presented in Figure 5.2 a). MoS_2 islands cover around 22% of the complete surface while the rest of it is clean graphene extended over Ir(111) steps. Graphene wrinkles which emerge upon sample cooling after graphene growth at elevated temperature due to difference in thermal expansion coefficients of graphene and Ir(111) are marked with cyan arrows and molybdenum clusters [140] are marked with green arrows. The thickness of MoS_2 islands is around 1 nm, which can be determined from the height profile shown in Figure 5.2 b). The variation of height between STM and AFM measurements is mostly due to different physical origins of the signal. [231] Moreover, under

ambient conditions the height of MoS_2 islands is increased compared to UHV due to water adsorption which forms a thicker film on MoS_2 than on graphene due to the larger water affinity. [48,49] Besides these small differences inherent to the STM and AFM methods, the comparison between Figures 5.1 and 5.2 confirms that the MoS_2/graphene HSs remain intact after their removal from UHV. Compared to a previous publication on the two-step growth procedure[182], we use an annealing sulfur pressure increased by a factor of five and a higher annealing temperature. As a result, while Hall et al. report predominantly compact monolayer MoS_2 islands, we observe dendritic islands composed of regularly shaped segments. Such morphology comes as a result of the previously mentioned coalescence of the islands during the annealing step as an indicator of their increased mobility. We correlate this effect with a significant decrease of intensity of graphene moiré spots in LEED (see Figure 5.1 b)), which indicates that the graphene layer became flatter. We propose two mechanisms that could possibly contribute to the graphene flattening: 1) etched graphene areas that enable release of the stress in graphene lattice and 2) interaction of graphene with MoS_2 that introduces a van der Waals (vdW) force on C atoms of opposite direction in comparison to the one produced by Ir-C interaction. The above mentioned graphene etching happens most probably during the MoS_2 growth due to the chemical reaction with the sulfur. When graphene is exposed to high sulfur pressure at high temperature, C atoms can react with S and detach from graphene, possibly forming some stable gas molecules, like CS_2. [232] Since MoS_2 islands are not stable on Ir(111), they decompose and leave Mo islands, while S atoms might contribute to further etching. [232] One such region is shown in Figure 5.2 c). The etching of graphene is relatively rare; the affected areas are limited and they generally occur on larger Ir(111) terraces. Graphene strongly sticks to Ir steps [233] where it has reduced mobility and reactivity in comparison with areas on terraces [180] which explains why it is more likely to be etched by sulfur on larger Ir(111) terraces. The thickness of graphene is around 0.6 nm which can be determined from Figure 5.2 d) which shows an etched graphene area next to the graphene sheet with a MoS_2 island. From the optical microscopy image of MoS_2/graphene on Ir(111) shown in Figure 5.2 e) it is evident that the Ir crystal itself has some imperfections which could lead to growth defects, but apart from that the HS sample is optically uniform. From the AFM measurements on multiple locations along the sample the surface size distribution of MoS_2 islands can be retrieved, see Figure 5.2 f). Size distributions of 2D and 3D grains as well as exfoliated 2D materials flakes are often modeled with a log-normal distribution. [234,235] Such distribution fits well to our histogram and yields an average size of MoS_2 islands of ~ 6000 nm^2, which corresponds to an average of 6 seed segments per island. [178]

5.4 Surface post-transfer characterization

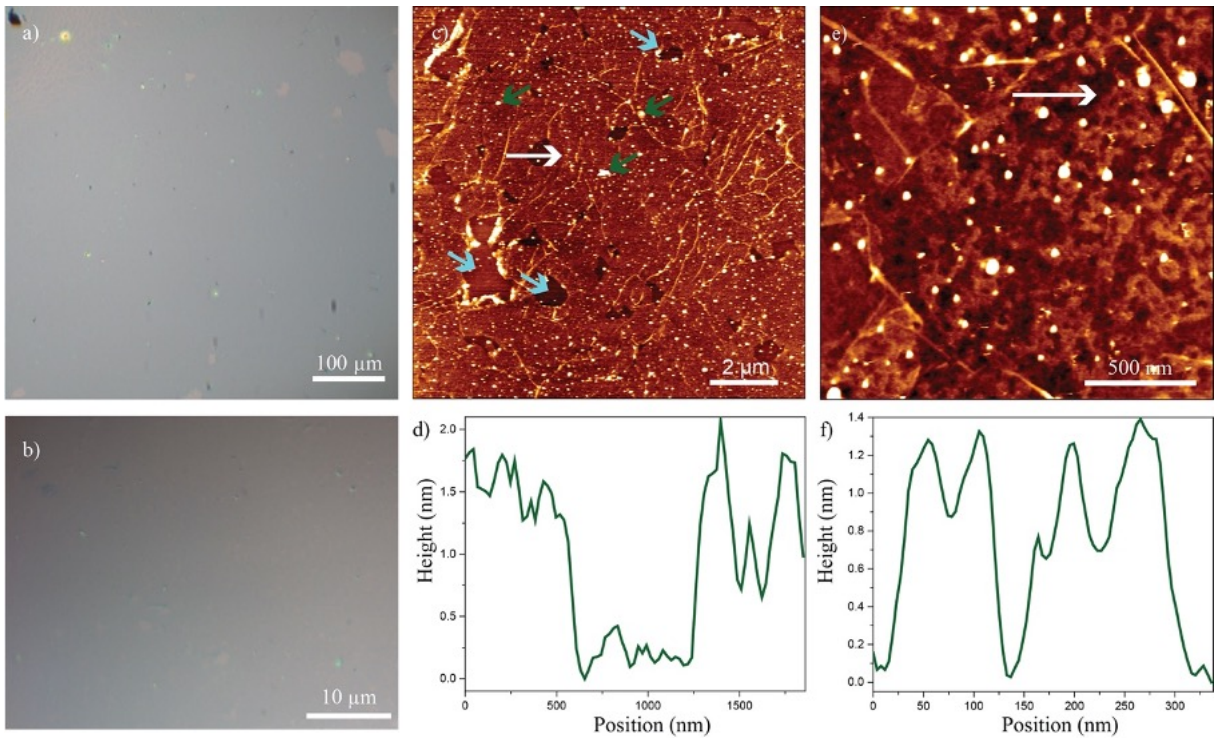

Figure 5.3 Optical micrographs a) and b) showing complete transfer of the MoS_2/graphene sample from Ir(111) to the wafer substrate. c) AFM image of transferred MoS_2/graphene sample with graphene wrinkles still present, tears in the graphene sheet are highlighted with cyan arrows and residual PMMA with green arrows. d) Height profile along the white arrow on c) showing the thickness of transferred graphene. e) Larger magnification AFM image of transferred MoS_2/graphene structure with distinguishable MoS_2 islands. f) Height profile along the white arrow in e) showing the thickness of MoS_2 islands. Taken from [178]

A first confirmation of the successful transfer is given by the optical micrographs of the transferred MoS_2/graphene HS in Figures 5.3 a) and 5.3 b), indicating that the graphene sheet was efficiently transferred on the Si wafer with only few macroscopic defects and contaminations as a result of the transfer procedure. On the microscopic level, Figure 5.3 c) shows the 10 × 10 μm^2 large AFM image of the transferred sheet confirming successful transfer of more than 95% of the sample area, where holes in the graphene sheet come as a result of the NaOH etching during electrochemical delamination. Tears and contaminations from residual PMMA are marked by cyan and green arrows, respectively. The thickness of the transferred

graphene sheet is 1.5 nm, as determined from the height profile shown in Figure 5.3 d), taken over a clean Si wafer surface between one of the larger tears of graphene. The measured increase of the graphene thickness after transfer is expected; the presented transfer procedure involves various solutions which are known to be reactive to 2D materials resulting in the aforementioned etching and also lead to intercalation between substrate and graphene sheet and increased water affinity, evident by an increase of the measured graphene layer thickness from 0.6 nm on Ir (111) to 1.5 nm on Si wafer. [233,236]

The MoS_2 islands were also successfully transferred, as revealed by the AFM image of smaller scan size, shown in Figure 5.3 e). The thickness of the islands, determined from the line profile in Figure 5.3 f) is about 1.1 nm, compared to 1 nm before transfer, confirming that the MoS_2/graphene structure was intact with respect to its interlayer distance and that the described transfer method can be used for large scale exploitation of MoS_2/graphene HSs or other combinations of 2D materials. [178,233]

5.5 Optical post-transfer characterization

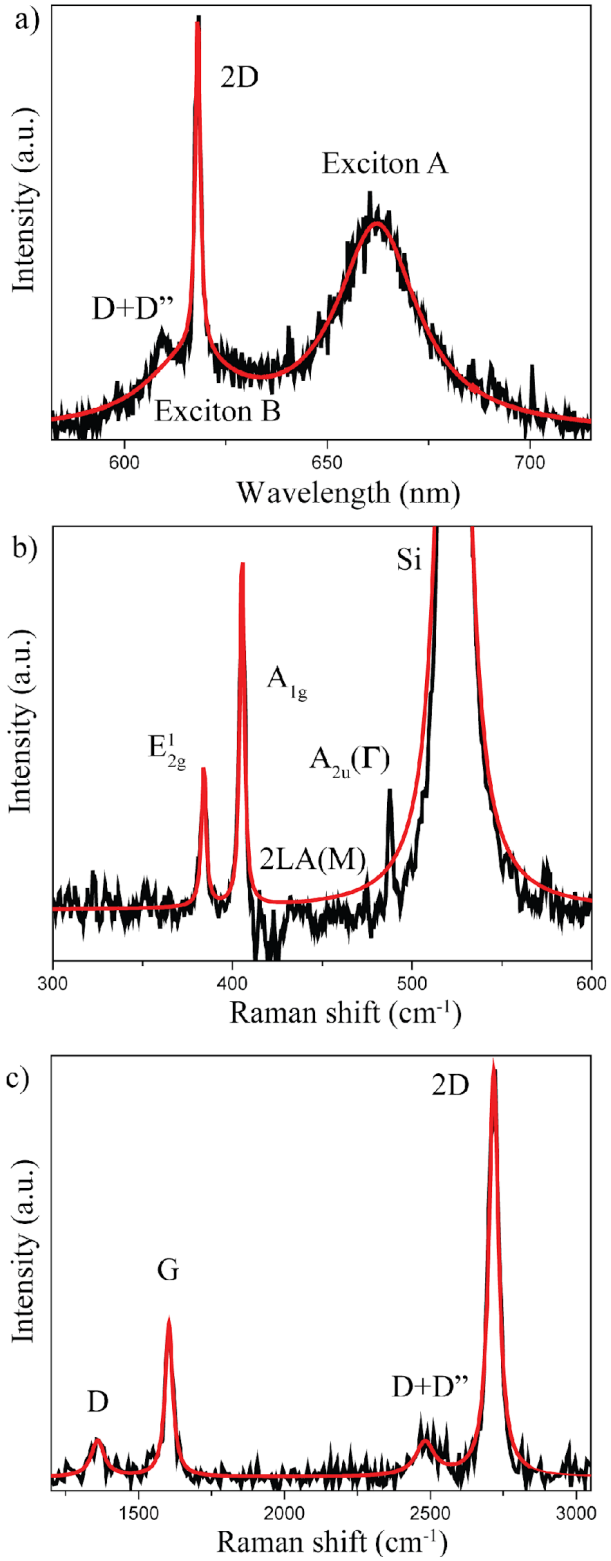

Figure 5.4 Room temperature PL and Raman characterization. The black line presents the measured spectrum while the red line is the Lorentzian cumulative fit. a) PL spectrum of MoS_2 with 2D graphene Raman peak. Raman spectrum of b) MoS_2 and c) graphene. Taken from [178]

Having obtained the HS sample on a suitable, insulating substrate, we now characterize its optical quality using PL and Raman spectroscopy. This was not possible for our sample on Ir(111) since this metallic substrate completely suppresses any optical signal. Ehlen et al reported low temperature Raman and PL measurements on MoS_2/graphene/Ir(111) in UHV[228] obtained using a similar sample synthesis technique and attributed this observation to the weak MoS_2-graphene interaction in their sample, induced by Li intercalation as an additional step. The presence of the Raman signal as a measure for the sample-substrate interaction strength has been discussed by Starodub et al. [236] who investigated two rotational variants of graphene (R0 and R30) grown on Ir(111). For the R30 variant, the charge transfer between graphene and the substrate is weak, the substrate does not significantly perturb electronic bands of graphene, and Raman-active phonons were observed. For the R0 variant, the perturbation of the electronic bands due to the iridium substrate highly favors electronic excitations of iridium states by graphene phonons, which reduces the graphene phonon lifetime and quenches Raman scattering. In our case, the graphene monolayer is grown on Ir(111) in the R0 variant, which strongly interacts with the substrate. The strong interaction between graphene and Ir(111) also affects the MoS_2 islands and precludes the observation of PL or Raman spectra on Ir(111).

After HS transfer from the metallic substrate to the Si wafer we observe the expected Raman signatures of graphene and MoS_2 as well as PL from the MoS_2 monolayer. The PL spectrum shown in Figure 5.4 a) exhibits the characteristic exciton resonances A and B at 1.87 eV (662 nm) and 2.01 eV (616 nm), respectively. They originate from optical transitions between the conduction band and highest spin-orbit split valence band at the K-points in Brillouin zone. [98,237,238]The measured A and B emission energies agree well with literature values. [99,138] The energy difference of 140 meV between A and B results from the valence band maximum (VBM) energy splitting due to strong spin-orbit coupling (SOC). [239,240] From the electronic quasiparticle bandgap measurements for monolayer MoS_2 on graphene [140] of 2.47 eV we can extract an A exciton binding energy of 600 meV, in good agreement with DFT predicted values. [32,33,241,242] In the MoS_2/graphene HS, exciton dissociation via electron transfer from the conduction band in MoS_2 to the conduction band of graphene is energetically favorable. [215,243,244] This electron transfer has twofold influence on the exciton A emission line: it results in exciton linewidth broadening as a result of stronger exciton-carrier scattering [245] and hinders the electron-hole pair recombination, thus quenching the PL signal of MoS_2. [138,243,246] Indeed, in the paper of Ehlen *et al.* on the HS on Ir(111) an increase in linewidth

broadening and line intensity drop for temperatures above 100 K is observed and does not allow comparison with our room temperature PL. On the other hand, obtained exciton A linewidth of around 68 meV at room temperature is in a good agreement with high quality mechanically exfoliated samples[174,247] and even comparable to h-BN capped MoS_2 when taking in account laser power broadening. [248,249] Regarding the influence of PMMA and acetone on PMMA-processed MoS_2 and graphene layers during transfer, it is known from previous works [250–252] that they retain their optical or transport properties and we consider exhibited quenching behavior of photoluminescence as a result of the charge transfer effect between MoS_2 and graphene.

The Raman spectrum of MoS_2/graphene HS on Si wafer in the range from 300 up to 600 cm^{-1}, displayed in Figure 5.4 b) shows prominent peaks at 384 cm^{-1} and 405 cm^{-1}, which correspond to the E^1_{2g} and A_{1g} MoS_2 characteristic Raman modes [253] respectively, and the Si 523 cm^{-1} peak which comes from the Si wafer. [254] The MoS_2 peaks have the same positions and splitting of 21 cm^{-1} as reported for a comparable HS in ref. [228] and close to other monolayer MoS_2 samples. [134,255] The Raman linewidth can be an indication of defects and it depends on temperature. [256–259] We measure linewidths of 3 cm^{-1} and 2.9 cm^{-1} for E^1_{2g} and A_{1g}, respectively, which are in agreement with high quality mechanically exfoliated samples [260] or even narrower [255–258,261] indicating low defect density and high sample quality.

Finally, the Raman spectrum in the range from 1300 cm^{-1} to 3000 cm^{-1} shown in Figure 5.4 c) exhibits the most prominent graphene phonons: the primary in-plane vibrational mode G and the 2D second-order overtone of a different, weaker in-plane vibration D, at the frequencies 1584 cm^{-1}, 2679 cm^{-1} and 1336 cm^{-1}, respectively. The G peak corresponds to the high-frequency E_{2g} optical phonon at the Γ point of the Brillouin zone. The D peak is due to the breathing modes of six-atom rings and requires a defect for its activation. [63] It comes from TO phonons around the Brillouin zone K point [63,160], is activated by double resonance [161,262], and its energy depends on the laser excitation energy. [263] The 2D peak is the D-peak overtone and originates from a momentum-conserving two-phonon process of opposite wave vectors, hence no defects are required for its activation and it is always present. Compared to published values for neutral graphene, the G peak is shifted to higher and the 2D peak to lower wavenumber. [64] As the laser power used was low enough not to induce heating, we can rule out strain as the origin for G and 2D peak shifts. Rather, the shifts correspond to light induced electron doping from MoS_2, which is another evidence of charge transfer from MoS_2 to graphene. [138] Besides the D, G and 2D peaks, an additional D+D" peak is also present in

the graphene Raman spectrum, at ~2,450 cm^{-1}. The D" phonon belongs to the LA branch at ~1,100 cm^{-1} in defected samples when measured with visible light; we do not observe it in our data. Therefore, the D+D" peak is caused by a scattering process involving one TO and one LA phonon with opposite momenta and not from defects. [64]

The Raman linewidths, in particular of the D peak, [61,65,264] as well as the intensity ratio I(2D)/I(G) [265,266] are often used as indicators of the sample quality. We can expect rather narrow Raman linewidths due to the similar lattice structure between graphene and MoS_2, reduced substrate surface roughness and the absence of impurities in the MoS_2/graphene interface. [138,267,268] We observe narrow linewidths of 10 cm^{-1}, 15 cm^{-1}, and 34 cm^{-1}, for the D, G, and 2D modes, respectively, and a I(2D)/I(G) ratio above 2. Comparing our results with Raman spectra on Ir(111) in similar systems [228,236] we observe Raman spectra characteristics in terms of linewidths and intensity ratio that are comparable or even better. In transferred graphene from similar Ir crystals to Si, Raman phonons have comparable characteristics. [189,233] In Ehlen *et al.*, MoS_2 Raman linewidths in the MoS_2/graphene system seem broader, which could however arise from the resolution of the Raman spectrometer. [267] Our Raman linewidths and intensity ratio indicate a high quality graphene monolayer. [56,236,269–272]

5.6 Application in optoelectronics and photonics

From the reported results of MoS_2/graphene heterostructure optical response, we demonstrate how the charge transfer of excited electrons from MoS_2 to the energetically favorable graphene tailors the optical response of MoS_2 exciton emission line in the form of PL signal quenching and graphene Raman peak shifting. [25] Having that in mind, by exploiting the vertical geometry of TMD/graphene heterostructural stacking, high-performance photodetectors can be fabricated [273], where the MoS_2 monolayer is used to absorb light and produce electron-hole pairs and graphene layer as the carrier transport path. The photoexcited electron-hole pairs are separated at the MoS_2 and graphene interfaces, where the electrons move to graphene due to the presence of a perpendicular effective electric field created by the combination of the built-in electric field, the applied electrostatic field and, typically present, charged impurities or adsorbates. [25,273,274] When utilizing the polymer support layer to transfer and stack the 2D

materials it leads to contaminations of residual polymers at hetero-structure interfaces [273] which hinders the perfomance.

In addition to being an as-grown pristine quality heterostructure, our sample could also have other performance improvements compared to other MoS_2/graphene photodetectors. It is known from the literature that some of the most important limiting factors of high-performing photodetectors are Schottky barrier height dependent on Fermi level pinning and channel vs. diffusion length. [134,275,276] Also, monolayer MoS_2 edges have a metallic character in the form of 1T phase[230] Being nanometer-sized in lateral dimension, the metallic edge states in our samples have a substantial impact on MoS_2 monolayer behavior than in their micrometer sized counterparts which improves the charge transfer efficiency between MoS_2 2H-1T junction [275–277] and graphene. When using 2D metal in the 2D semiconductor/2D metal heterostructure junction Fermi level pinning is weak because it is influenced by van der Waals interaction that minimizes the Schottky barrier. [275,277] Furthermore, the MBE method offers the possibility of tuning the MoS_2 island shape from circular to the more dendritic ones [[182] and, therefore, by scaling the channel length (L_{ch}), one can improve the phototransistor performance since the gain is inversely related to transit time of the channel. [134,278,279] Reducing the channel length is an effective way to increase phototransistor performance by decreasing transit time and decreasing recombination during carrier movement. Also, if the L_{ch} is shorter than the diffusion length (L_{diff}), the phototransistor performances could benefit from the reduced channel length i.e. reduced sample lateral dimensions. The diffusion length is defined as the average distance that an excited carrier will move between generation and recombination. Further, the diffusion length of MoS_2 is known to be approximately 220 nm. [134,280] If the channel length is longer than the diffusion length, a significant number of carriers cannot travel from the source to the drain because of recombination in the MoS_2 channel.

There is another interesting aspect of MBE epitaxial grown 2D semiconducting materials and it is related to quantum confinement effects (QCE). The exciton Bohr radius of MoS_2 is about 2 nm [281,282] so it is unlikely to observe QCE in our nanostructures of several tens of nm in lateral size. [283–286] However, it has already been pointed out how the MBE method allows for tuning not only the island shape but also its physical size, enabling it to achieve lateral dimensions of only several nm where QCE could be observed. The QCE is also possible in the grain boundaries and edges of MBE epitaxially grown 2D semiconducting structures [140] which could give rise to single photon emission. Form of grain boundaries called 4|4E mirror twin boundary and edges in similar MoS_2/graphene systems exhibit 1D defects with quantized

energy levels in the valence band wherever upward band bending takes place. In analogy to TMD semiconductor point defects having bound excitons and serving as single photon emitters, the quantized VB states next to 1D defects in MoS could also be utilized as quantum emitters. [287–289] The well-defined band bending and localization of charges at 4|4E MTBs and edges could find application in a wide range of electronic and photonic platforms. These aspects of integration and scaling of quantum emitters into electro-optic devices and systems can be examined by already available spectroscopy methods at the atomic scale.

5.7 Conclusion

In conclusion, this chapter presents the results of the successful MoS_2/graphene heterostructure MBE synthesis and subsequent transfer procedure on Si wafer laying the ground for the future high-quality TMDs and related heterostructures sample synthesis and their utilization in optoelectronic devices. With the two-step growth procedure, the unprecedented on-demand control of lateral dimension, crystal quality and types of heterostructures on a large scale has been proved. The success of the transfer procedure lies in the transfer of the macroscopic, 6 mm in diameter, graphene layer covered with nanometer sized MoS_2 islands that has maintained the intrinsic structural and electronic properties of the MBE grown layers.

Both the growth and the transfer procedure successful outcomes have been confirmed and supported by detailed sample characterisation prior to and after the transfer procedure. We have characterized the epitaxial grown MoS_2/graphene/Ir(111) system combining the in-situ LEED and STM and ex-situ AFM measurements confirming the good quality of our grown samples, proving that the for the given growth conditions mostly monolayer MoS_2 islands with few point defect occurrence cover the continuous micrometer-sized graphene layer. With AFM measurements we confirmed that MoS_2 islands cover around 22% of the complete graphene surface and that the MoS_2/graphene heterostructures were intact after removal from UHV since the MoS_2 island thickness of approximately 1 nm was measured. The grain size distribution of MoS_2 islands, which corresponds to an average of 6 seed segments per island was also confirmed.

After a two-step electrochemical delamination transfer method, MoS_2/graphene heterostructure was removed from Ir crystal after which the heterostructure has been placed on an oxidized Si wafer and characterized by post-transfer AFM measurements, PL and Raman measurements. The high-resolution AFM inspection of sample morphology confirms successful transfer of

more than 95% of sample, confirming that MoS_2/graphene structure was intact in respect to their interlayer distance and that the transfer method can be utilized for large scale exploitation of MoS_2/graphene heterostructures or any other 2D material or heterostructures.

Photoluminescence spectra showed characteristic exciton emission lines with the emission energies comparable with the literature values where the exciton A line intensity was slightly influenced by the graphene presence and related interlayer charge transfer. The exciton A linewidth is in good agreement with the high quality mechanically exfoliated samples, confirming the long exciton lifetimes. The Raman spectrum of MoS_2/graphene heterostructure on Si substrate confirms not only the presence of the heterostructure but also its post-transfer high quality. The Raman mode peak positions, their linewidths and relative peak intensities are in excellent agreement with the exfoliated samples indicating low defect density and high sample quality.

Therefore, we have demonstrated that the MBE synthesized MoS_2/graphene heterostructure in combination with the suitable transfer procedure may serve as a route to the high efficiency optoelectronic devices that could benefit from the combination of the electron-hole photoexcitations in MoS_2 (or any other suitable 2D semiconducting material) in combination with the electrically contacted graphene layer and favorable sample morphology that could also be exploit as quantum emitters in 2D systems. In addition, the effectiveness of presented synthesis and subsequent transfer procedures have been also proved in other systems, such as WS_2/MoS_2/graphene heterostructure and borophene, as will be demonstrated in following Chapters.

6 Nanometer sized WS_2/MoS_2/graphene heterostructures

6.1 Motivation

In the previous chapter we have investigated MoS_2/graphene heterostructure grown in UHV condition with MBE technique. In this Chapter, research on three layer van der Waals heterostructure WS_2/MoS_2/graphene is presented. Van der Waals heterostructures (vdWHSs) provide a unique playground to study fundamental physics and practical applications of 2D materials. However, most 2D heterostructures are prepared by transfer, hindering their technological implementation and performance. MBE has proven to yield high-quality and uniform 2D materials allowing for the fabrication of 2D materials in a repeatable and scalable manner. Fabrication of low-dimensional heterostructures with three different constituent materials is challenging. There are a handful of reports of the growth of lateral 2D heterostructures [26–28], and only recently 1D vdWHSs have been demonstrated. [29,290,291] Concurrently, not only fundamental studies are performed on vdWHSs, but several applications utilizing 2D stacks have been found, including transistors [292] memory devices [293], photodetectors [294], or light-emitting diodes [295]. [29] Lin *et al* were the first to show transfer-free MoS_2/WSe_2/graphene and WSe_2 /$MoSe_2$/graphene vertical stacks with three-layer graphene, which they used to fabricate a tunnel diode. [29,296] Here we report a sample preparation where graphene was grown in zero step, the same as in Chapter 4 and 5. After that MoS_2 is grown by one-step preparation (simultaneous growth and annealing) under following conditions: $p = 2 \times 10^{-5}$ mbar, T = 1025 K, I = 4.83 A, t = 8.5 min, P = 26 W. Second TMD layer - WS_2 was grown by two-step preparation, with separated growth and annealing steps. Growth step required following conditions: $p = 1 \times 10^{-6}$ mbar, T = RT, I = 4.65 A, t= 15.5 min, P = 48 W and annealing step was done under $p = 1 \times 10^{-6}$ mbar, T= 1025 K. Its characterization and properties are discussed below.

6.2 UHV characterization

In Figure 6.1. a) STM image of heterostructure MoS_2/Mo/graphene is presented. It shows different contrasts and intensities corresponding to rich morphology of the sample from Mo intercalation, graphene layer and MoS_2 islands in monolayer and bilayer form. Green line corresponds to line scan presented in Figure 6.1 c) where height steps can be seen in the sample morphology along the green line. Schematic presentation of the sample morphology is given in Figure 6.1 e) from which we can deduce that the whole sample is covered with a graphene layer. There are two intensities of the graphene layer; darker is graphene on Ir(111) and brighter is graphene intercalated with Mo atoms. Graphene without intercalation is less present in the sample compared to graphene with intercalation. Differences in graphene with and without intercalation should not be confused with the changes in contrast of graphene due to higher and lower iridium terraces. From line scan in Figure 6.1 c) we can extract the height of MoS_2 monolayer ~ 0.7 nm which is expected. After growth of MoS_2 we continue to grow the WS_2 layer creating WS_2/MoS_2/graphene heterostructures, see Figure 6.1 b). LEED inset in Figure 6.1 b) shows no new spots but evidence of WS_2 growth is seen as increased intensity of MoS_2 spot and rings, which confirms WS_2 and MoS_2 being of the same orientation and rotationally aligned to graphene. The Ir(111) diffraction spots were absent as LEED became less sensitive to deeper layers due to a significant increase of grown material on top layers. [140] STM image in Figure 6.1 b) shows rich sample morphology with both lateral and vertical WS_2/MoS_2 heterostructures. Black arrows indicate defects in WS_2 monolayer islands; these defects are present only in WS_2 islands and can be used to distinguish WS_2 from MoS_2 regions. Hexagons denoted with black dashed lines outline the regions with the MoS_2 layer present on the graphene layer. As MoS_2 is only present in these areas this means that these outlined hexagons also represent areas with lateral and vertical WS_2/MoS_2 heterostructures. Understanding of the sample morphology is made easier with the schematics in Figure 6.1 f). Green line in the STM image is the position of the line scan in Figure 6.1 d) from which we can extract WS_2 monolayer height of ~ 0.7 nm in agreement with literature.

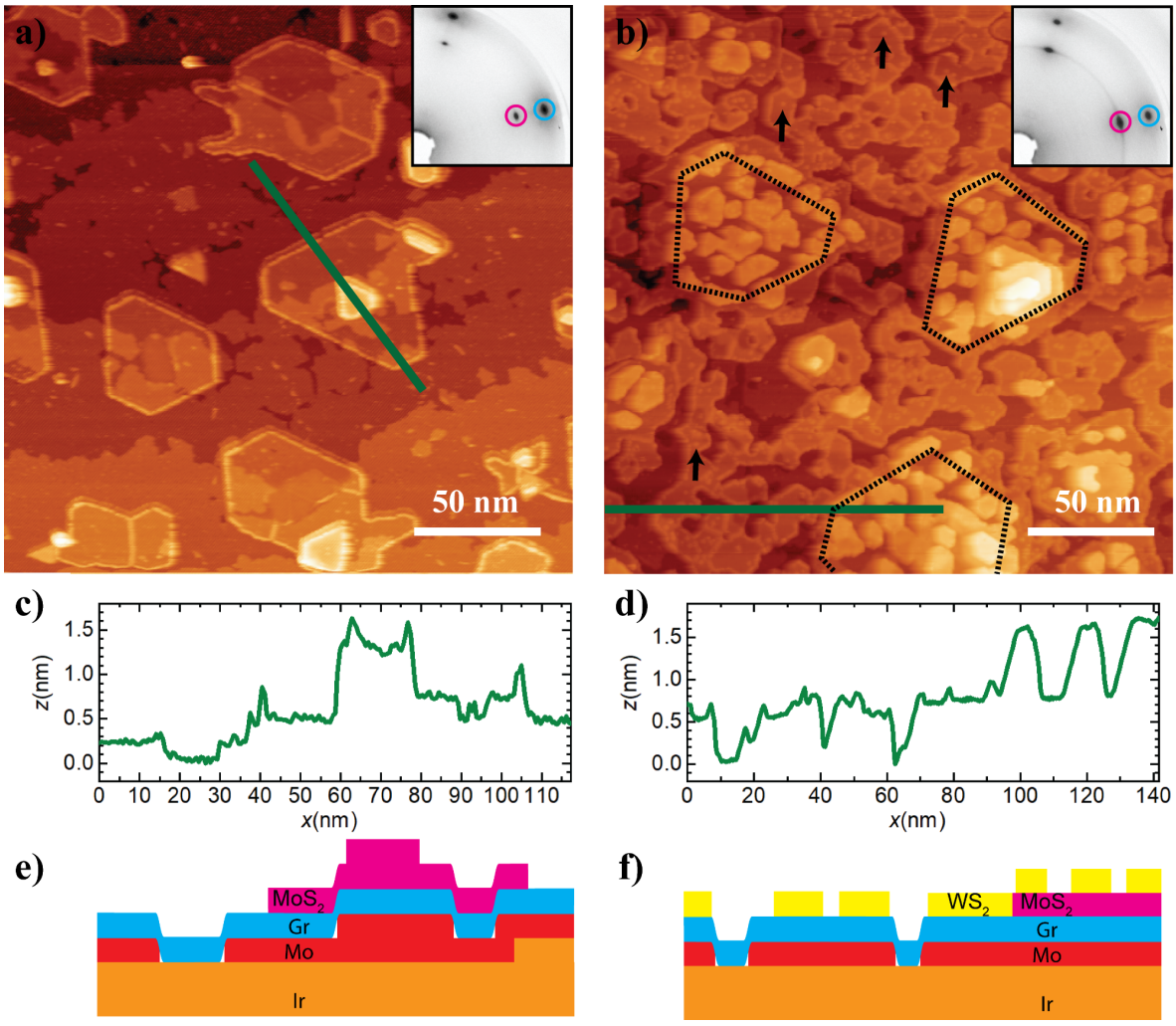

Figure 6.1 a) STM image after first step growth with mostly monolayer MoS_2 islands on graphene with Mo intercalation. Green line depicts linescan over monolayer and bilayer MoS_2. Inset in the right upper corner shows the LEED pattern of MoS_2/Mo/graphene/Ir(111). Diffraction spots of graphene (blue) and MoS_2 (pink) are marked by circles. b) STM image of final sample morphology with vertical and lateral WS_2/MoS_2 heterostructures on graphene with Mo intercalation. Green line depicts linescan over the first layer of TMD monolayer islands of WS_2, graphene and second layer of TMD monolayer islands of MoS_2. Dashed black lines show regions of vertical and lateral WS_2/MoS_2/graphene heterostructures. Black arrows show WS_2 monolayer islands on graphene. Inset in the right upper corner shows the LEED pattern of WS_2/MoS_2/Mo/graphene/Ir(111). Diffraction spots of graphene (blue) and WS_2/MoS_2 (pink) are marked by circles. c) and d) Linescans from a) and b) depicted in green lines, respectively. e) and f) schematic representation of the sample morphology along the line scans in a) and b).

6.3 Ambient pre-transfer characterization

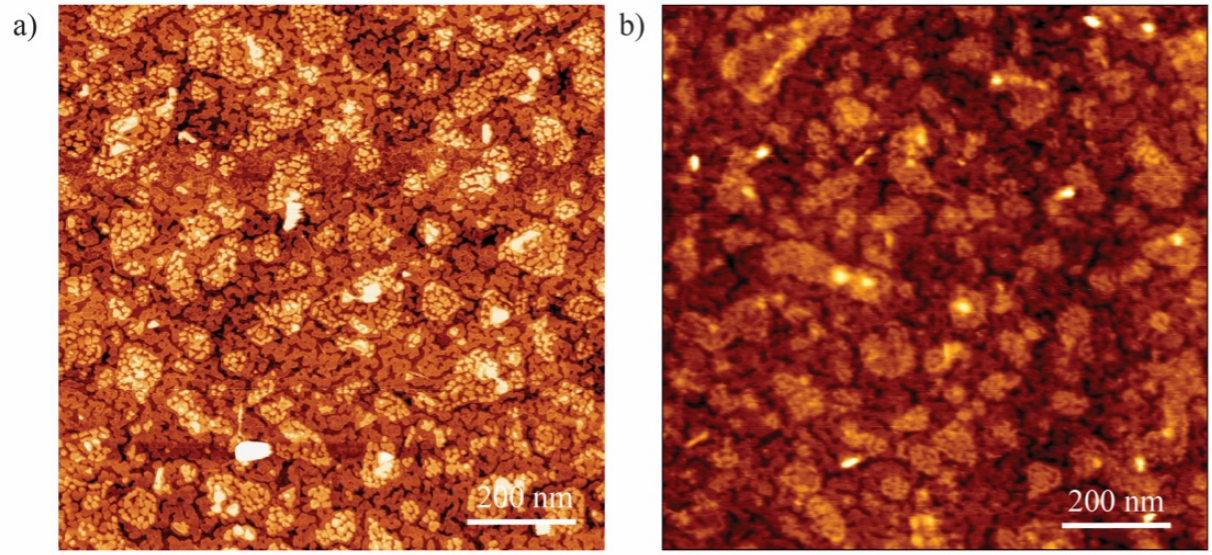

Figure 6.2 a) *in-situ* STM image showing sample morphology of WS_2/MoS_2/graphene heterostructure on larger view of 1 um by 1 um. b) *ex-situ* AFM image of heterostructure from a) in ambient room conditions showing the same morphology features as a).

First requirement for successful transfer from UHV and Ir(111) substrate to arbitrary substrate and its subsequent processing is ambient stability of the sample. Otherwise, we would have to use an inert atmosphere glove box for sample transfer and hexagonal boron nitride (h-BN) as a passivation capping layer. Figure 6.2 a) shows *in-situ* STM image 1 um x 1um measured in Siegen, Germany where characteristic sample morphology is seen on a larger scale. From it we can calculate MoS_2 coverage of 33% and total WS_2 coverage of 77 %. WS_2 is present in two forms; as a first TMD layer on top of graphene with coverage of 51.6 % and as a second TMD layer on top of MoS_2 with a coverage of 25.4 %. In Figure 6.2 b) AFM image of the same sample was taken on the same scale of 1 um x 1 um after it was sent by mailpost from Germany to Croatia, showing the preserved sample structure and morphology in ambient conditions, even for days after it was exposed to ambient conditions. Characteristic brighter areas where WS_2/MoS_2 heterostructures are present on the sample are visible in Figure 6.2 b) in the same manner as in Figure 6.2 a). AFM tip resolution is lower than STM tip which impacts the quality of the image and nanostructures resolvement in Figure 6.2 b) is not a signature of sample degradation.

6.4 Surface post-transfer characterization

WS_2/MoS_2/graphene heterostructure sample was transferred from Ir(111) to Si wafer with the electrochemical delamination method described in Chapter 4. Transfer of the sample was successful but not the whole 6 mm diameter was 100% transferred from Ir(111), as seen in Figure 6.3 a). Also, as we will see later, not all transferred regions have the same properties and appearances. Darker contrast regions in Figure 6.3 a) will show expected good quality optical response from WS_2/MoS_2/graphene heterostructure while more transparent and brighter contrast regions will have very broad and luminescent optical response which originates from amorphous and contaminated sample structure during transfer. For the future references we will call them (optically) good and bad regions, respectively. Figure 6.3 b) shows an AFM image from black rectangle in Figure 6.3 a) with white arrow having direction from the brighter (bad) region across the wafer surface to the darker (good) region of the sample where linescan is taken. In the AFM image, Figure 6.3 b), we can see four different regions of sample morphology across white arrow. First region is dense with contamination in the form of corrugations which are later inspected. Second region is bilayer overlap of the heterostructure sample which is seen from the height profile in linescan shown in Figure 6.3 c). Third region is just the substrate surface from the Si wafer. The last region is the one with good optical signal and with the least roughness and contaminations. All of the regions have the same height, approximately 6 nm; bilayer overlap is 12 nm, which is consistent with the conclusion that the bilayer is an overlap. Heights of 6 nm are not theoretically expected as the graphene layer should have a height of around 0.3 nm and one TMD layer of 0.6 nm. We exclude Mo atom intercalation as individual atom transfer is highly unlikely as Mo atoms are chemisorbed to Ir(111). Reasons for obtained differences in measured height profile compared to expected ones can be found in literature. [125,187] Usually, it is due to water molecules, adsorbents and varying tip-sample interactions between the sample and substrate. [297,298] Corresponding height steps of different regions are present in Figure 6.3 c) linescan. First region has the highest roughness of R_a = 2.9 nm and R_q = 3.8 nm while the last region has significantly lower roughness of R_a = 0.85 nm and R_q = 1.4 nm indicating low presence of contaminations and corrugations which is consistent with optical signal measurements. Bilayer region has wrinkles due to the folding of the second layer over the first one. Close look at contaminations and corrugations in the first region is given in Figure 6.4, where Figure 6.4 a) shows the biggest area of 2 um x 2 um dimension with the least corrugations in this region. Roughness analysis of this region gives R_a = 0.92 nm and R_q = 2.26 nm but still higher roughness than in the last region. Figures 6.4 b) and c) show a highly corrugated area of the first region with R_a = 4 nm and R_q = 4.8 nm.

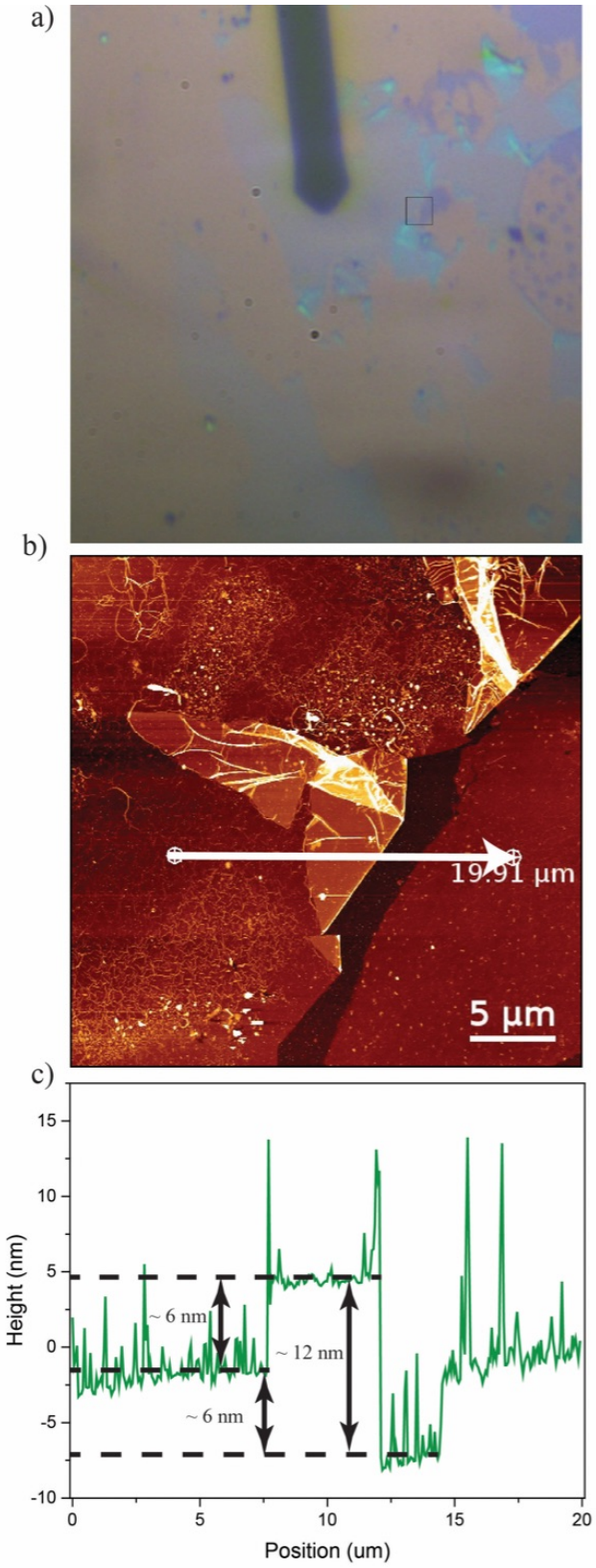

Figure 6.3 Heterostructure after transfer to wafer. a) Optical image from AFM setup of broader region of interest for scanning. Black rectangle represents the scanned area. Horizontal size of the image is 1000 um. b) AFM topography of the region denoted in a). White line shows the linescan position. c) Linescan from b) marked with white line.

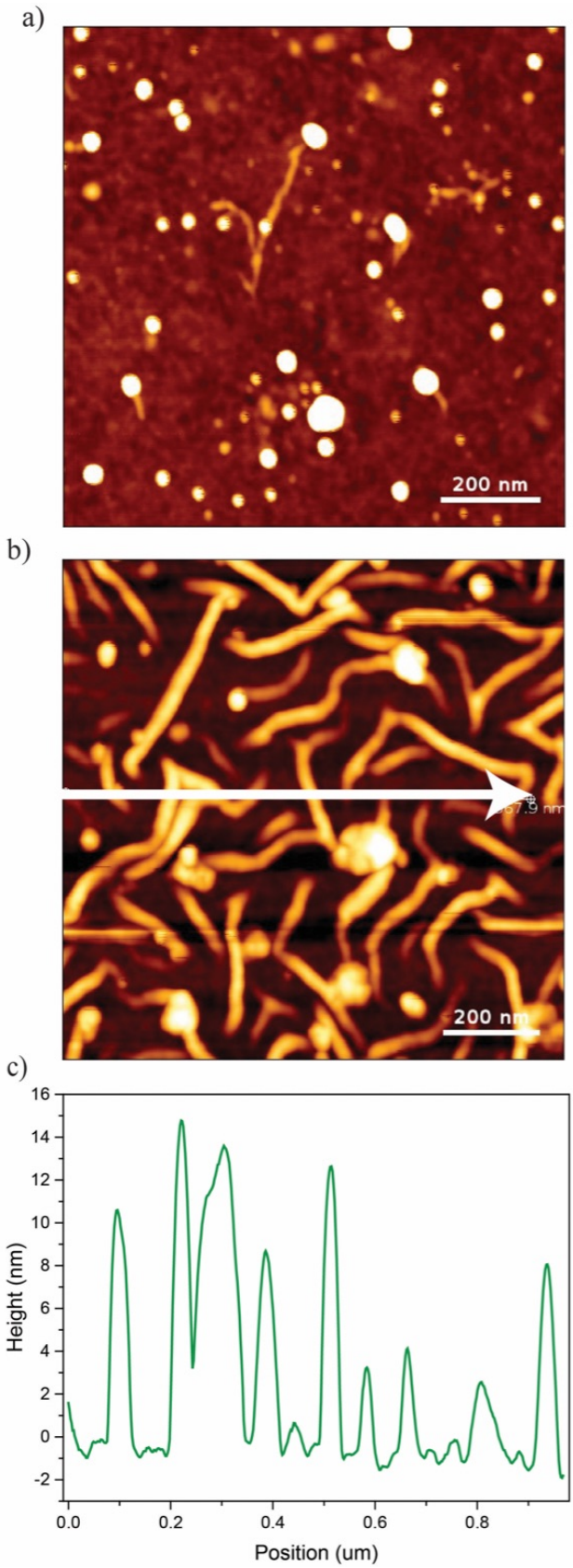

Figure 6.4 Optically bad regions analyzed with AFM. a) Area with least roughness and corrugations. b) Area with dense corrugations present. White line depicts linescan shown in c).

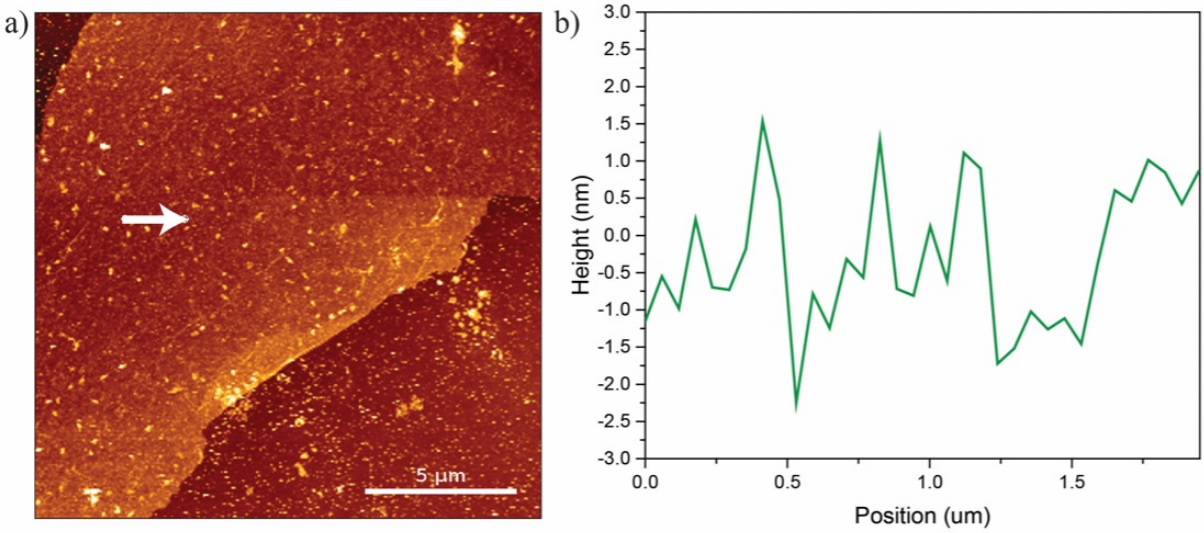

Figure 6.5 AFM image of optically good region shown in a) with white line denoting linescan position in b).

Corrugations height in linescan shown in Figure 6.4 c) ranges from 5 nm to 20 nm which we assign to leftover polymer chain strands. Figure 6.5 a) shows an AFM image of the last region from the Figure 6.3 b) which has good optical signal, low roughness of R_a = 0.85 nm and Rq = 1.4 nm and no contaminations. White arrow indicates where the linescan shown in Figure 6.5 b) was taken. Linescan height variations are on the order of a few nm which are in agreement with the total height of WS_2/MoS_2 heterostructure hexagonal islands. Surface analysis shows that much of the graphene layer has been transferred, however some parts of graphene had been overlapped forming bilayer regions and some have been contaminated with polymer corrugation. We believe that in regions with bad optical signal, WS_2/MoS_2/graphene spectral signature has been masked by broad luminescent optical signal from these amorphous polymer corrugations. To conclude, there is a clear distinction in surface properties between regions of good optical signal showing Raman and PL signatures of WS_2/MoS_2/graphene heterostructure and other contaminated ones without Raman and PL signatures.

6.5 Ambient optical post-transfer characterization

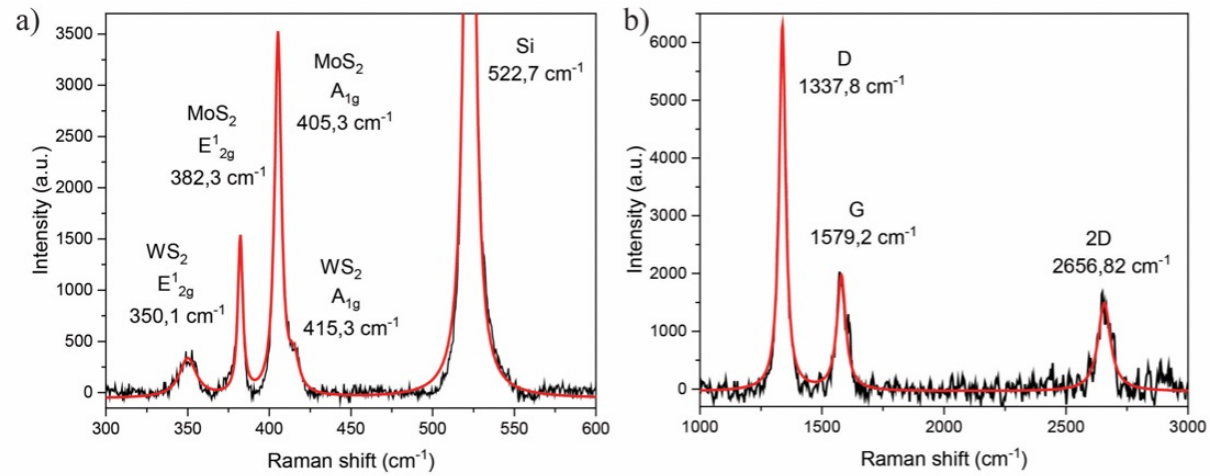

Figure 6.6 Raman spectrum showing peaks from WS_2/MoS_2 a) and graphene b) on Si wafer.

-1

Raman spectroscopy is an excellent tool to identify material presence in order to confirm successful transfer of WS_2/MoS_2/graphene heterostructure. In Figure 6.6 a) Raman spectrum in 300 cm^{-1} up to 600 cm^{-1} range is presented, indicating WS_2, MoS_2 and Si Raman peaks proving the WS_2/MoS_2 vertical heterostructure presence on Si substrate. Main MoS_2 Raman peaks belonging to E^1_{2g} and A_{1g} Raman modes at 382.3 cm^{-1} and 405.3 cm^{-1}, respectively. Their energies and intensities confirm the presence of MoS_2 in heterostructure, comparable to the sample in Chapter 5. The presence of WS_2 monolayer has been confirmed by two Raman peaks at 350.1 cm^{-1} and 415.3 cm^{-1} belonging to E^1_{2g} and A_{1g}, respectively. In Figure 6.6 b) Raman spectrum in the range from 1000 cm^{-1} to 3000 cm^{-1} shows characteristic graphene phonon modes, confirming the presence of the graphene layer as well. Compared to Figure 5.4 c) in Chapter 5 Raman signatures of graphene are not textbook comparable to pristine monolayers. Reasons for that could be charge transfer doping of the graphene layer and/or changes to the graphene layer during transfer. [189,233,299]

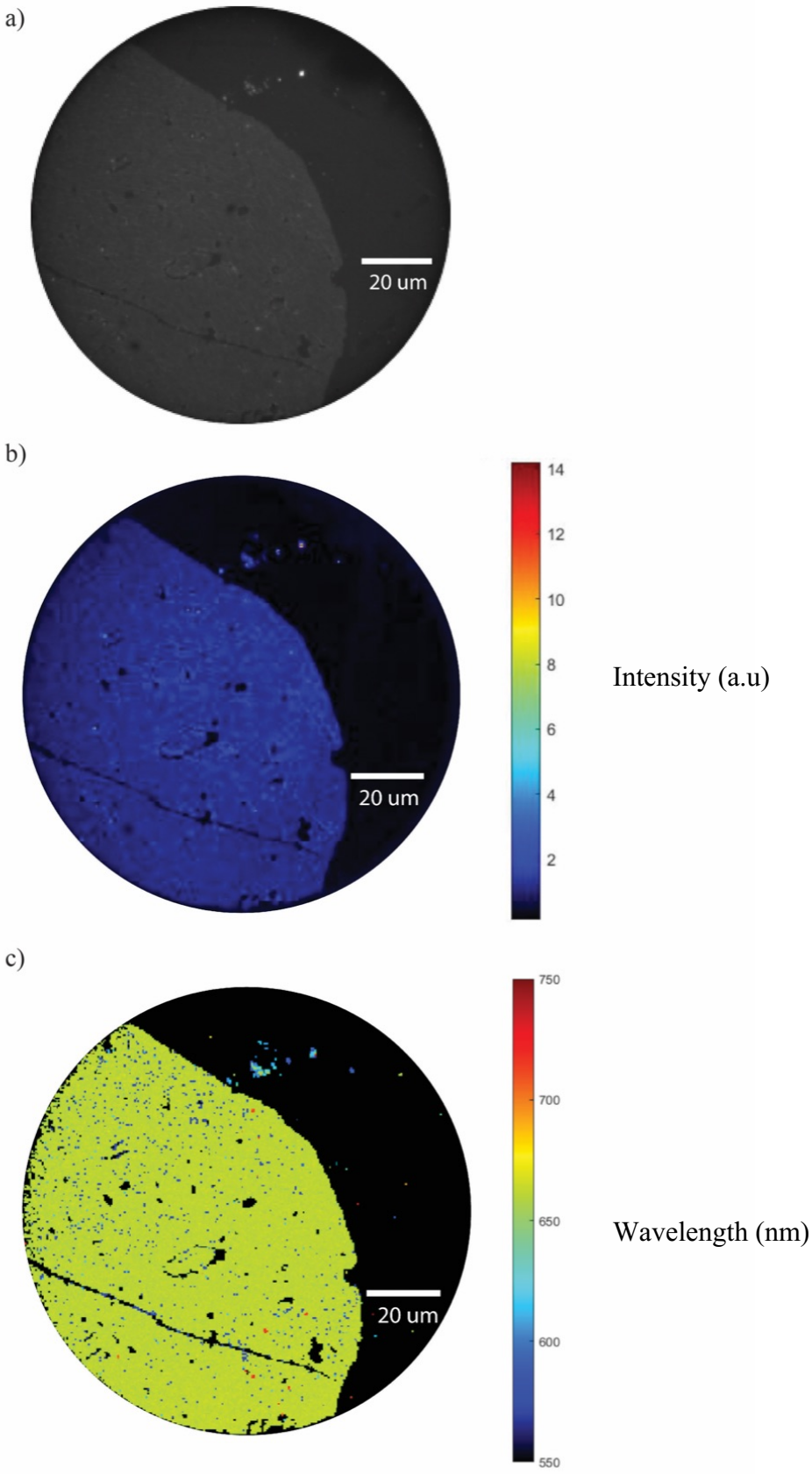

Figure 6.7 Optical reflection image of optically good area a). Hyperspectral images showing intensity map b) and spectral map c) of WS_2/MoS_2/graphene heterostructure. Taken with the Hyperspectral TWINS interferometer.

Figure 6.7 shows optical characterization with white-light microscope and hyperspectral TWINS interferometer microscope of the large scale area of WS_2/MoS_2/graphene heterostructure without visible contaminations and corrugations. Figure 6.7 a) shows white-light microscope image on which we can observe cracks and tears in our transferred material on Si wafer. There is no evidence of macroscopic contaminants. In Figure 6.7 b) intensity map is shown from the hyperspectral TWINS interferometer. We observe uniform intensity across all of the samples indicating high-quality homogenous heterostructure sample. Cracks and tears are seen also in intensity map as dark regions, expectedly without any signal as there is also no material. Spectral map from hyperspectral interferometer is shown in Figure 6.7 c) with a wavelength range from 550 nm to 750 nm in color scale. Homogenous spectral map with 99% of the sample area showing highest intensity at MoS_2 exciton A wavelength of around 670 nm, however there are small spots spread around the sample with highest intensity at WS_2 exciton A wavelength energies of around 620 nm. Homogeneity of optical signal on a large scale in both intensity and spectral position is excellent confirmation of high-quality of the sample and successful transfer of the sample area without any change and contamination to it.

However, rather unexpectedly we observe that the MoS_2 exciton A emission has the strongest PL emission across the sample. Taking into consideration much higher WS_2 coverage than MoS_2, we would expect for WS_2 emission signal to be the strongest. We attribute this to charge transfer quenching of the PL signal due to transfer of electrons from WS_2 to MoS_2 and to graphene. As discussed in Chapter 6.2., WS_2 forms vertical heterostructure with MoS_2 on graphene (WS_2/MoS_2/graphene) and with graphene only (WS_2/graphene), see Figure 6.1.f). In both cases charge transfer from WS_2 to the beneath layer occurs: in the case of vertical WS_2/MoS_2/graphene heterostructure type-II band alignment [140,300] is created where photoexcited electrons from the WS_2 conduction band get transferred to MoS_2 conduction band and, from there, since it is in contact with graphene they transfer to it; in the case WS_2/graphene heterostructure, charge transfer occurs directly, as described in Chapter 5. In both cases, charge transfer affects the WS_2 layer and it is visible also on the PL intensity profiles, which has been confirmed also in low-temperature regime, see Chapter 6.6. This charge transfer quenches the PL WS_2 signal but is also an evidence of high-quality interface between the layers in the heterostructure, ensuring effective charge transfer otherwise not possible. Similar behavior was observed also in Chapter 5 MoS_2/graphene heterostructures. [178]

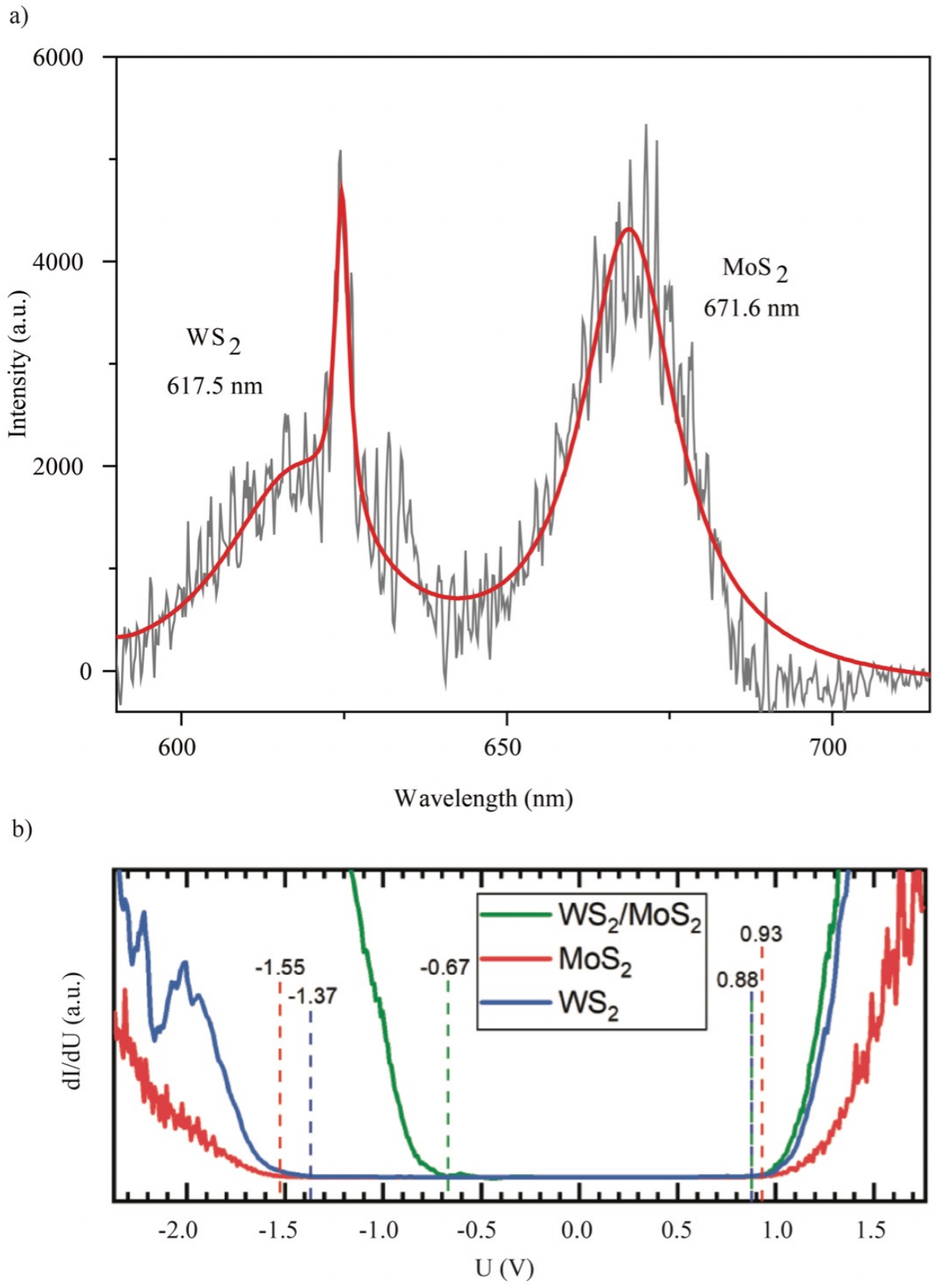

Figure 6.8 a) Room temperature photoluminescence spectra taken with confocal micro-Raman spectrometer showing A excitons from WS_2 and MoS_2 in heterostructure and graphene 2D Raman peak. b) STS data taken at 120 K which show the quasiparticle bandgap of WS_2, MoS_2 and heterostructure WS_2/MoS_2.

Figure 6.8 a) shows PL spectra of the heterostructure taken in ambient conditions at room temperature with the confocal micro-Raman spectrometer. Prominent features of the spectra include signal from WS_2 and MoS_2 exciton A and 2D Raman peak from graphene. Exciton A from WS_2 is present at 617.5 nm while exciton A from MoS_2 is at 671.6 nm consistent with the literature and Chapter 5 and 7. We also observe strong quenching of the PL signal from the heterostructure owing to efficient charge transfer in WS_2/MoS_2/graphene heterostructure, mentioned before. PL signal from MoS_2 has higher intensity than WS_2, even though usually WS_2 has better quantum yield and it is more luminescent. This has been also observed in J. Sitek et al [29] where it is explained with charge transfer quenching of the PL. As discussed in Chapter 5 in MoS_2/graphene heterostructure when photoexcited electrons are able to transfer to a lower energy state before their radiative recombination, the PL signal of MoS_2 is quenched because of this charge transfer. Another consequence of charge transfer due to the graphene presence is the interlayer exciton absence in PL spectra. [29] In Figure 6.8 b) scanning tunneling spectroscopy taken at 120 K measured quasiparticle bandgap of MoS_2, WS_2 and interlayer bandgap between MoS_2 conduction band and WS_2 valence band their respective values are 2.48 eV, 2.25 eV and 1.55 eV. We will use these values to compare them to optical bandgap at comparable temperatures to calculate exciton binding energies, see Chapter 6.6.

6.6 Low-temperature optical post-transfer characterization

Figure 6.9 a) shows a temperature dependent spectral map with colors for intensity. Temperature dependent measurements were done with liquid helium as a coolant liquid from 4.2 K to room temperature of 290 K. At 125 K optical bandgaps are of MoS_2 is at 1.88 eV and of WS_2 is at 2.07 eV. Deducting optical bandgap values from quasiparticle values we can calculate exciton binding energies. For MoS_2 we calculate 600 meV and for WS_2 180 meV. Binding energy for MoS_2 perfectly agrees with the one in Chapter 5 and literature values [32,33,241,242] while WS_2 has somewhat lower binding energy than expected. P. D. Cunnigham et al reported and explained photoinduced bandgap renormalization and exciton binding energy reduction in WS_2 and measured comparable exciton binding energy of 220+/-20 meV for higher excitation densities which corresponds with our measurement-based calculations of binding energy. [301] Such a low WS_2 binding energy value can be also explain through the momentum space picture[302]: when the initially electron density increases due to the resonant excitation, as a result of Pauli-blocking, the phase space available to the electron

which is interacting with the hole via the Coulomb potential is reduced for small momenta. Energy can be minimized better if the exciton wavefunction spreads to larger momenta that are unoccupied. Consequently, the exciton radius decreases in real space but, as a trade-off, its kinetic energy associated with the relative electron-hole motion increases and, therefore, the exciton binding energy decreases.

PL intensity map of the neutral emission changing with temperature between 4.2 and 300 K show the same trend as on room temperature: (1) presence of both MoS_2 and WS_2 PL signals and (2) intensity of WS_2 signal is lower than intensity of MoS_2 signal due to previously mentioned charge transfer for the whole temperature range. Figure 6.9 b) shows exciton peaks position dependence on temperature for MoS_2 and WS_2. Temperature dependent peak energy positions are fitted with function [303]

$$E(T) = E(0) - S[\coth\left(\frac{E_{ph}}{2k_BT}\right) - 1]$$

from which we can extract the energy of electron-phonon coupling. $E_g(0)$ is the transition energy at T = 0 K, S is a dimensionless constant describing the strength of the electron-phonon coupling, and E_{ph} represents the average phonon energy involved in electron-phonon coupling. Good fit agreement and electron-phonon coupling energies of 47.4 meV (382.3 cm^{-1}) for WS_2 and 42.7 meV (344.4 cm^{-1}) for MoS_2, corresponding to energies of main phonon modes we observe in Raman spectrum, confirming phonon mediated temperature dependent semiconductor bandgap reduction. The influence of optical phonon modes on interlayer charge transfer for a type-II heterobilayer has been discussed in [304]. They propose the following scenario for electron (hole) interlayer charge transfer mechanism mediated by the Q_c (v) valley and phonons. For a type-II heterobilayer with the conduction (valence) band edge located at K_c(v) point, a high energy photoexcited electron in K_c valley can relax to one of the Q_c valleys through scattering with phonons, other carriers, or impurities/defects. As Q_c valleys are strongly layer-mixed, this electron can further relax to the K_c valley of another layer. DFT calculations suggest that electrons in the conductive K_c valley couple strongly with LA and A1 phonons with wave vectors in the vicinity of M point [305], which leads to scatterings between Kc and Q valleys. On the other hand, holes in Kv valley couple strongly with TA phonons with wave vectors in the vicinity of K, which leads to scatterings between K_v and Γ valleys. The domination of phonons in the intervalley scattering of electrons in WS_2 is additionally amplified due to the resonant excitation with 532 nm laser.

By fitting the emission spectra presented in Figure 6.9 a) with Lorentz function, we extracted the PL intensities of WS_2 and MoS_2 emission lines and plotted them as a function of 1/T as shown in Fig. 6.9 c). As temperature increases,the intensities of MoS_2 and WS_2 peaks first gradually increase then dramatically decrease. The temperature dependence of the PL peak intensities is given by[306]

$$I_{PL} = I_0/\left[1 + \gamma/\left(\exp\left(E_{ph}/k_B\,T\right) - 1\right)\right]$$

where I_0 is the PL intensity at T= 0 K, k_B is the Boltzmann constant, and γ and E_{ph} are fitting parameters. E_{ph} represents the activation energy for the normal thermal quenching process at certain temperatures due to electron-phonon coupling. Reasonable fitting parameters were obtained only for MoS_2, with E_{ph} value of 21 meV, which corresponds to 243 K, i.e., the temperature where MoS_2 emission line intensity becomes significantly lower, as can be seen from Figure 6.9 a). Presented model does not give meaningful fitting parameters in the case of WS_2. Again, we attribute this to the presence of charge transfer originating from type-II band alignments of WS_2/MoS_2 mediated by phonons and the presence of a graphene layer which quenches PL intensity independently of the temperature.

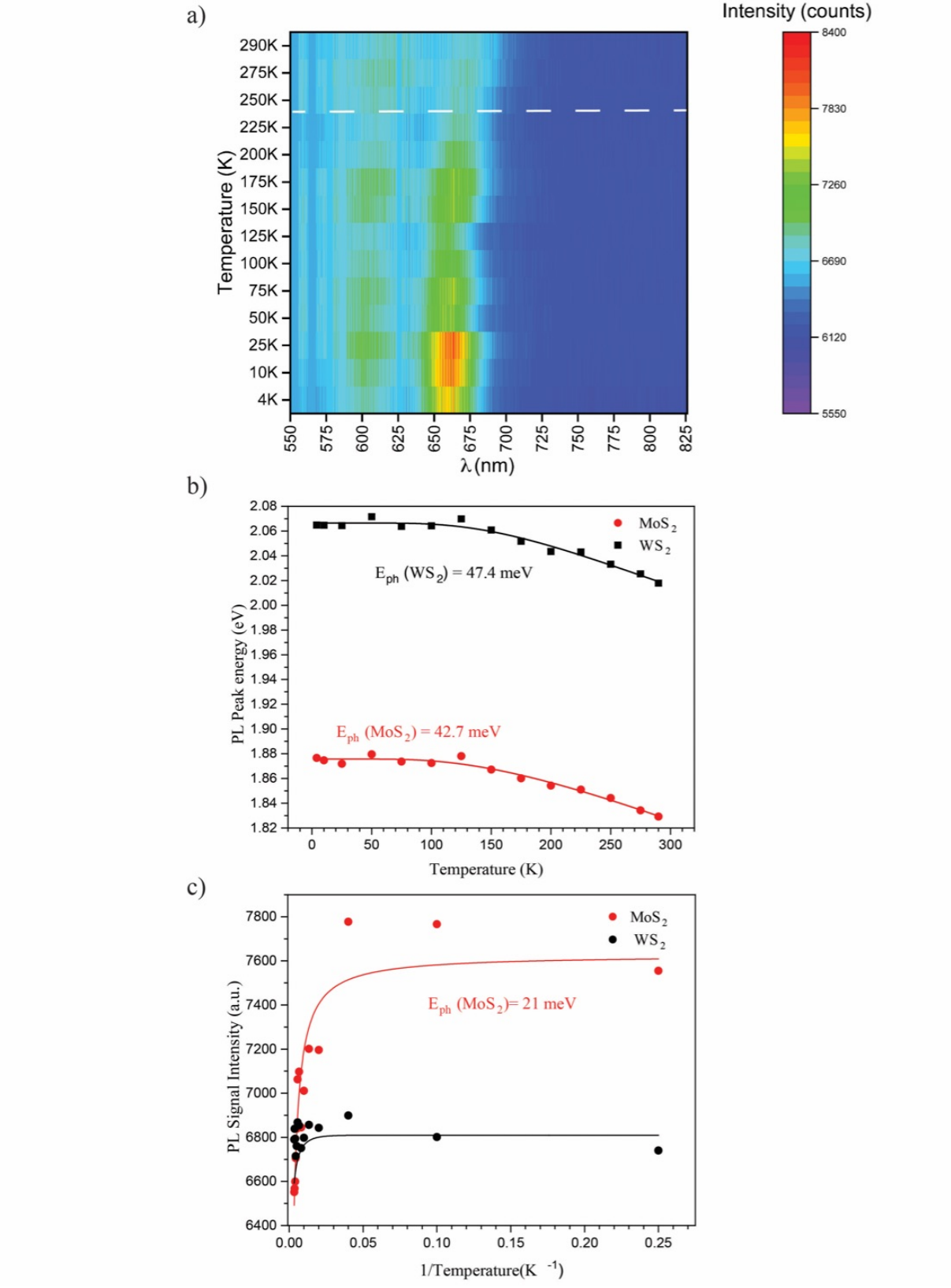

Figure 6.9 a) Temperature dependent PL spectral map from heterostructure. Exciton energy shift b) and Intensity dependence c) of WS_2 and MoS_2 on temperature. Black line in c) is just an eye-guide.

6.7 Conclusion

We have investigated UHV grown WS_2/MoS_2/graphene heterostructure on Ir(111) with initial Mo atom intercalation that has not been preserved after the transfer. *In-situ* characterization with LEED and STM revealed vertical and lateral heterostructures of WS_2/MoS_2 on a complete graphene layer over the Ir(111) sample. Monolayer MoS_2 islands cover 33% while WS_2 77% where 74.6% is in the first TMD layer (directly on graphene) and 25.4% in the second TMD layer (on MoS_2 islands). Ambient characterization with AFM on Ir(111) reveals preserved sample structure and morphology indicating room condition stability even after a longer time period. Transfer to an arbitrary substrate, in this case Si wafer, was done with electrochemical delamination. Not all the parts of the sample were completely transferred, which was confirmed by optical micrographs of the sample. Some parts of the sample had contaminations and corrugations which hindered optical response from WS_2/MoS_2/graphene heterostructure. Nevertheless, there are substantial parts of the sample that were completely transferred, without any contaminations and with high-quality optical signals from the heterostructure. Raman spectroscopy confirmed the presence of WS_2, MoS_2 and graphene after the transfer. Using hyperspectral interferometer imaging we reveal homogenous intensity and spectral response from the high-quality sample parts. Obtained photoluminescence spectra show quenching of the exciton signal at 617.5 nm and 671.6 nm that corresponds to WS_2/MoS_2 emission lines. All three applied optical techniques confirmed the evidence of charge transfer from WS_2 to MoS_2 due to Type-II band alignment and from WS_2 to graphene. Interlayer charge transfer mechanism is mediated by the Q valley presence and domination of phonons, where the intervalley/interlayer scattering of electrons from WS_2 to MoS_2 is additionally amplified due to the resonant excitation with 532 nm laser. Efficient charge transfer, as we observe it, is a direct confirmation of a pristine interface between layers of the heterostructure indicating a non-perturbing nature of the transfer process where the sample maintained intrinsic structural and electronic properties of the MBE grown layers. Comparing STS measurements at 125 K with temperature dependent PL measurements at comparable temperature we can calculate exciton binding energy of MoS_2 600 meV is in agreement with previous results in Chapter 5 and literature. However, binding energy for WS_2 is lower than expected from the literature, due to the fast phonon mediated charge transfer. From exciton peak position temperature dependence we can extract energy from the electron-phonon coupling of 47.4 meV (382.3 cm^{-1}) and 42.7 meV (344.4 cm^{-1}) which are in good agreement with the major phonon modes of WS_2 and MoS_2, respectively. Electron-phonon coupling reveals phonon mediated temperature dependent semiconductor bandgap reduction.

7 Influence of strain on optical properties of TMDs

7.1 Motivation

2D materials, because of their interesting optical and electrical properties, are often thought of being applied to device fabrication. Mechanical flexibility and ability to sustain high strain is an additional important property which makes them potentially suitable to impact the flexible electronics industry. Many groups have been doing research on strain in 2D materials, and some of the leading ones are the groups of A. Castellanos-Gomez and R. Bratschitsch that we have both collaborated with. In this chapter we focus on TMDs and their optical properties upon applied strain. TMDC monolayers are extremely flexible, sustaining mechanical strain of about 10% without breaking, with excitonic properties strongly dependent on strain. With applied strain their quasiparticle energy bandgap is changing, with tensile strain it is shrinking while with compressive strain it is widening. For example, exciton energies of TMDC monolayers significantly redshift under uniaxial tensile strain. [307] This change of quasiparticle bandgap is also evident in optical bandgap, as a shift of exciton resonances, which we can measure with absorption/reflection or emission measurements. This shift of exciton resonance with strain is defined as strain gauge factor and it is expressed as energy shift (in meV) per one percent of strain, i.e. meV/% units. Strain gauge factor is the main physical quantity that describes change in optical properties of TMDs under applied strain. For instance, if we are building a flexible photodetector its maximum efficiency energy will change with strain, and knowing the strain gauge factor we can predict and construct desired behavior. Most of the research on optical properties of TMD and strain were done on mechanically exfoliated samples that offer great quality and uniformity and are easy to prepare but they are not suitable for production scaling and application in fabrication of flexible devices. For that reason, it is necessary to investigate strain properties of the CVD grown monolayers of TMD which offer continuous centimeter-scale coverage of material. Continuous monolayer films of TMD are not single crystals but polycrystals divided by grain boundaries. [174] In collaboration with the group of R. Bratschitsch, we have set to investigate if the strain uniformly transfers across grain boundaries of CVD grown samples, the same as in exfoliated single crystals.

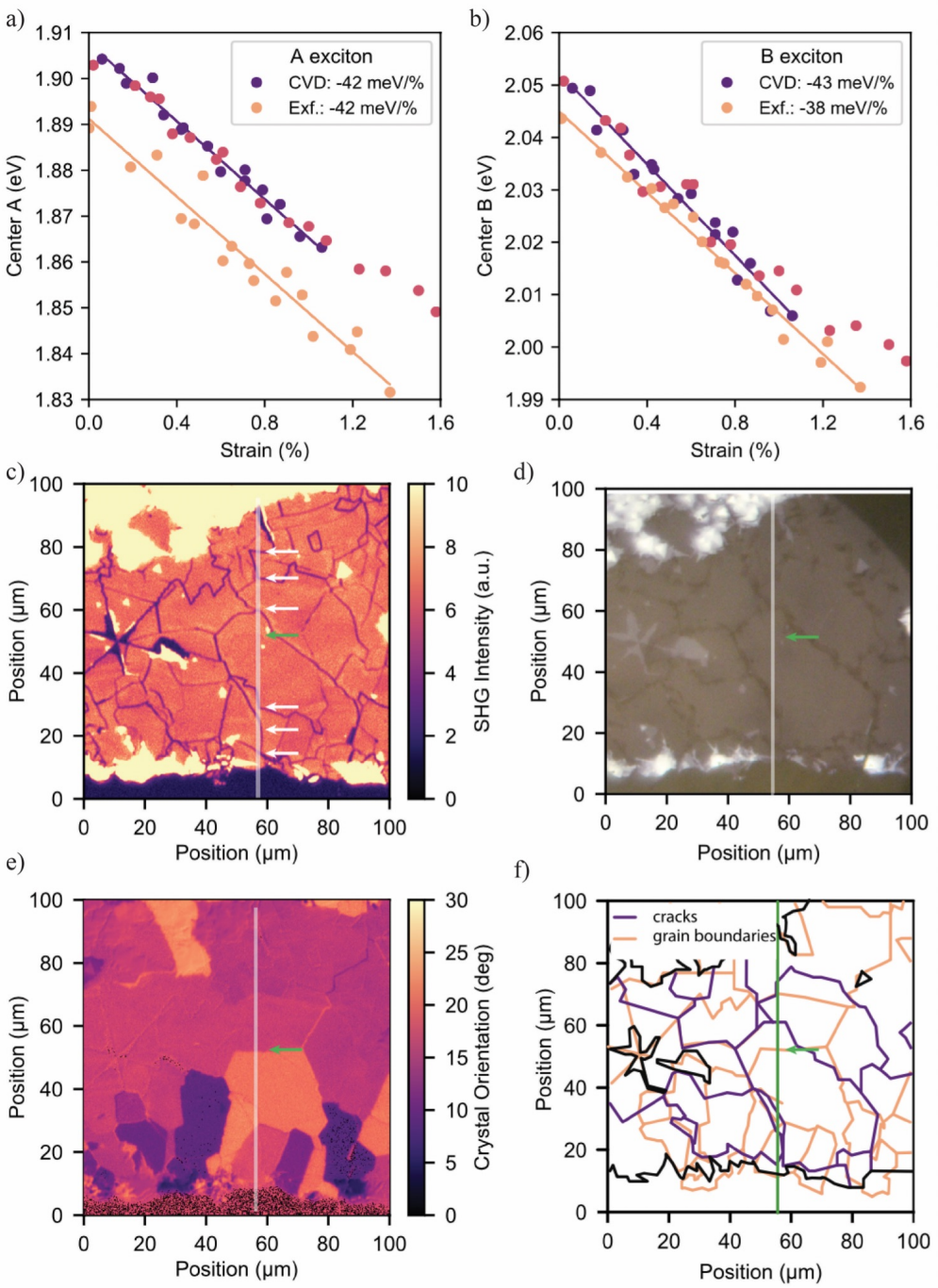

Figure 7.1. a) and b) show comparison of strain gauge factors for A and B exciton, respectively, between CVD grown and exfoliated samples of MoS_2. c) Intensity map of second harmonic generation which shows cracks and grain boundaries. Cracks are noted with white arrows along the white line where absorption spectra were taken. d) White-light reflection image of sample after strain measurements. Cracks are visible as darker contrast lines. e) Angle-resolved second harmonic generation map which distinguishes different domain orientation and grain boundaries. Green arrow indicates one prominent grain boundary. f) Extracted positions and lines of cracks (purple) from d) and grain boundaries (orange) from e), black lines are few layers. Adopted from [174].

Using absorption spectroscopy (Figure 7.1 a) and b)), angle-resolved second harmonic generation (Figure 7.1. c) and e)) and white-light microscopy (Figure 7.1 d)) we have measured comparable strain gauge factors in CVD samples to exfoliated ones and concluded that strain transfer across grain boundaries is efficient but expectedly it cannot transfer through physical cracks in material, Figure 7.1 f). This initial work was the motivation to continue the research on strain in 2D materials, especially in bilayer (2L) TMD crystals, which are particularly attractive for applications in thin film transistors, [308] logic devices,[309] and sensors [310] owing to their high density of states, carrier mobility and stability at room temperature. [311] Moreover, bilayer materials are important basic structures for studying atomic interaction between single layers. [109,165,308,312–316] In this Chapter we present results of investigation of strain on optical properties of WS_2 homobilayers - from sample preparation and characterization up to systematic measurements of absorption spectra for different percentages of the applied strain. The last part of the strain research is related to investigation of the ultrafast relaxation process in strained 2L WS_2 systems. The aim of our research of strain in 2L TMD was to find out if different orientations of layers influence the gauge factors. We investigated two types of CVD grown WS_2 homobilayers with creating two different stacking orientations between two individual layers, known as AA and AB. [317] Also, to the best of our knowledge, no study has been conducted to investigate the time dynamics in strained systems so far and results reported here present pioneer work on this topic.

7.2 Straining twisted bilayers of WS_2

7.2.1 Strain setup

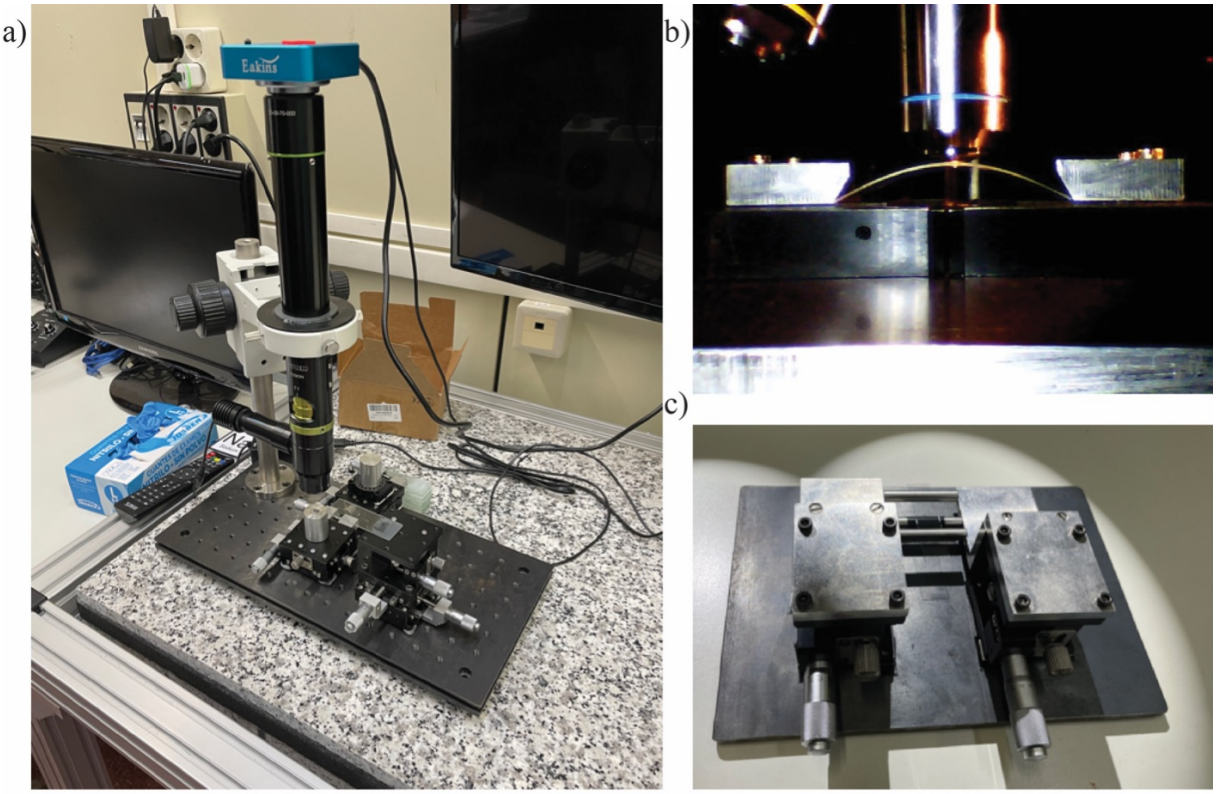

Figure 7.2 a) Stamping setup for transfering 2D materials with PDMS stamps to desired substrate. b) 2-point uniaxial bending setup used for the first batch of measurement strain in twisted bilayers of 2D materials. c) 3-point uniaxial bending setup with fixed z-axis focus during strain measurements.

In the 2D research community, strain engineering is typically achieved by stamping the material on a flexible arbitrary substrate that can be mechanically bended or stretched. [318] In Figure 7.2 a) a stamping setup used for deterministic transfer of desired flakes to an arbitrary substrate is shown. It is composed of white-ligh camera microscope and one xyz-rotation stage and xyz stage with a monitor. Prior to transfer the sample on the flexible substrate, the sample is attached to a support layer (stamp) made of a viscoelastic material, such as poly-dimethylsiloxane (PDMS), as described in Chapter 4.1.3.1. This procedure allows for controllable transfer of the sample on the desired substrate by slowly detaching the stamp leaving the 2D flakes behind on the flexible substrate, such as polycarbonate.

There are several ways to apply strain on flexible substrates with samples as seen in Chapter 3.4 and one of them used here is by bending the samples. We have used two types of the strain

stages for bending of samples: 2-point bending stage, presented in Figure 7.2 b) and 3-point bending stage presented in Figure 7.2 c). Using a 2-point bending requires less space in the z-direction but it has one disadvantage that during the strain application due to the sample bending, sample focus is changing which requires additional focus adjusting and introduces possible inaccuracy in measurements. Also, focus adjusting is time consuming. Using a 3-point bending setup requires more space in z-direction but sample focus is fixed, which is very convenient since measurements are more accurate and less time-consuming.

Figure 7.3 gives a schematic representation of a 2-point and 3-point bending setup with details on applied strain calculation for given setup geometry.

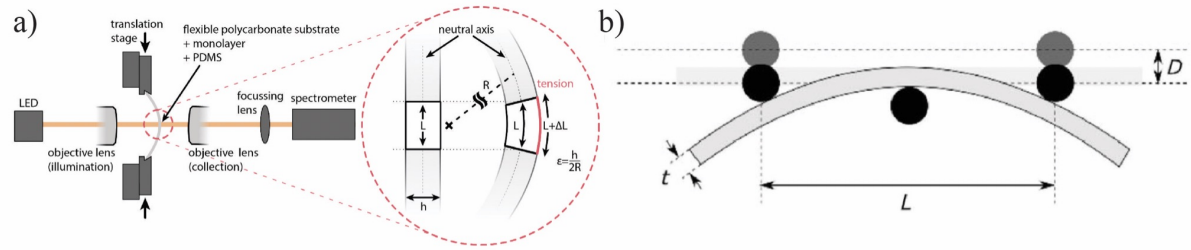

Figure 7.3 Schematic representation of 2-point a) and 3-point b) bending setup with described parameters for calculation of applied strain. Adopted from a)[174] and b) [319].

It can be seen that the 3-point bending setup offers the additional advantage of simple calculation of applied strain with just using experimental formula:

$$\varepsilon = \frac{6Dt}{L^2}$$

where D is the deflection of the substrate, t is thickness of the substrate and L is the distance between the pivotal points. Strain calculation for 2-point bending setup is more extensive, as can be seen from in Figure 7.3 a) where the important parameters for applied strain calculation are shown. Strain in the 2-point bending setup is calculated by dividing the thickness of the substrate h with the radius in the point of measurement of strain R. Thickness of the substrate we know from manufacturer specifications of used flexible substrate, in our case polycarbonate with 500 um thickness, as our 2D material is atomically thin its thickness is irrelevant. To calculate radius R we first need to take a photo of the bended substrate for a certain bending position and point the dots on the curvature of the bended substrate. The dots position simulates the shape of a bended substrate and we fit it with the sine function:

$$y(x) = d \cdot \sin\left(\frac{\pi}{L} \cdot x\right)$$

where L stands for distance between two clamping points and d is the maximum deflection of the substrate at the bending center, i.e. amplitude of the bended substrate for a given amount of applied strain. In order to get real values of vertical (y) and horizontal (x) distances, we have to calibrate dimensions on the taken photo with the real experimental dimension that we are interested in. Calculation of radius R is done from the formula for the curvature of the arbitrary function [162]

$$R = \left|\frac{(1+y'(x)^2)^{\frac{3}{2}}}{y''(x)}\right|$$

From relation:

$$\varepsilon = \frac{h}{2R}$$

the applied strain ε is calculated for a given bend substrate position.

7.2.2 Optical characterization after transfer

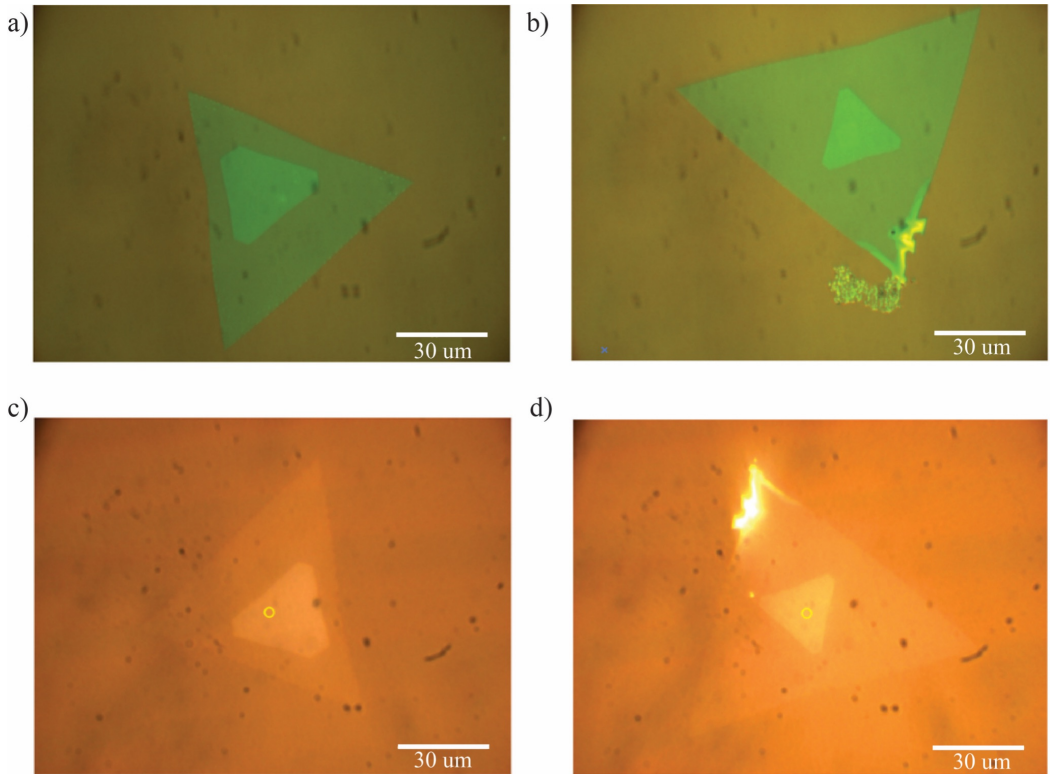

Figure 7.4 a) and b) show typical bilayers of AA and AB stacking WS_2 bilayers on Si wafer before transfer, respectively. c) and d) show the same bilayers after transfer to a polycarbonate flexible substrate and capped with PDMS.

After using the wet transfer technique described in Chapter 4.1.3.1 we are able to achieve complete, crack-free transfer of bilayers from their as-grown Si wafer in Figure 7.4 a) and b) to flexible polycarbonate substrate in Figures 7.4 c) and d). Optical micrographs presented in Figures 7.4 c) and d) are a bit blurry because samples are sandwiched between two layers: transparent 500 um thick polycarbonate from below and capped with 160 um PDMS from above. As the PDMS stamp is very clean it electrostatically attaches dust particles on the top layer but it does not influence the quality of the optical data measurements. Dust particles visible on all four optical micrographs come from the dust in the optical system. In Figure 7.4 a) AA stacking bilayer of WS_2 is shown which means the orientation of the second layer is 0 degrees to the first layer. In Figure 7.4 b) AB stacking bilayer is seen with 60 degree rotation between layers.

7.2.3 Results

Initial strain measurements on WS_2 homobilayes were done on the part of the samples where only the monolayer is present. We found these measurements suitable for testing our sample and how it behaves under strain, since there are already literature data results on monolayer flakes straining measured absorption spectra. [307] Our strain setups allow us to apply only uniaxial tensile strain. Expected influence of strain on TMDs is shrinkage of the bandgap which we can observe as a redshift of exciton peak positions to lower energies. In order to avoid sample distraction and slippage of material we only apply up to 0.65% strain, which is a safe limit to have reproducible results. Applied strain increment was 0.05% to give enough points to be able to conclude on sample behavior under straining. Figure 7.5 shows differential reflectance spectra acquired on a monolayer WS_2 flake with a home-built micro-reflectance microscope. [320] To obtain the differential reflectance spectra we first collect the light reflected from the substrate (R_s). Then we collect the light reflected by the desired WS_2 flake (R_f) and we calculate the differential reflectance as: $\Delta R/R = 1 - R_f/R_s$. [320] The spectra displayed in Figure 7.4 show two strong transitions in assigned to the A and B excitons (~2.02 eV and ~2.39 eV respectively) originated from direct band gap transitions at the K point of the Brillouin zone.

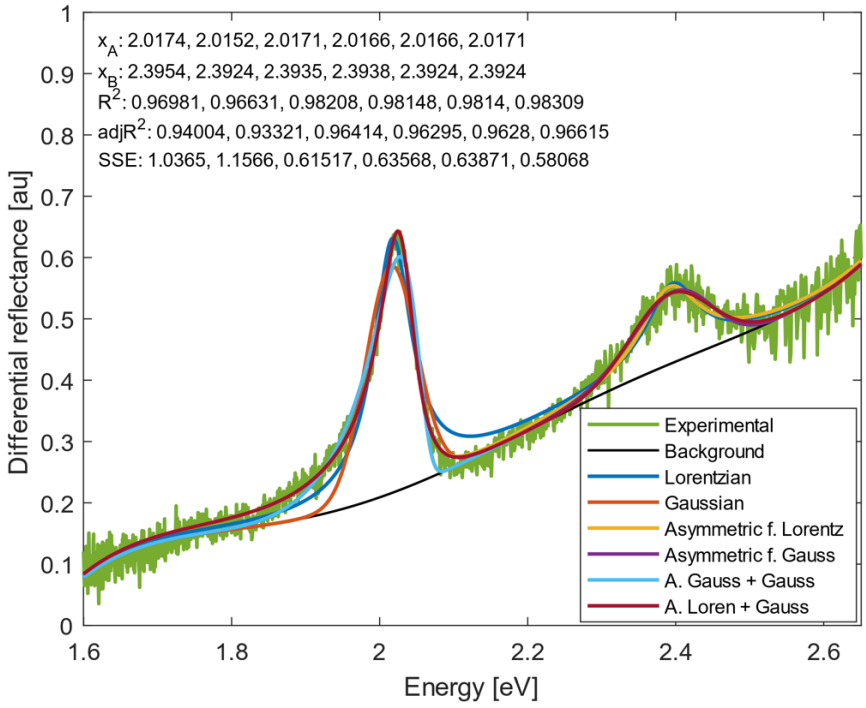

Figure 7.5 Differential reflectance spectra of monolayer PDMS/WS_2/PC sample fitted with different function and background polynomial.

Experimental data (thick green line) representing differential reflectance spectra of monolayer WS_2 are fitted on various peak functions, where thin lines are total fit to the data; each fitting function is assigned by a different line color and each of them is composed by the sum of a background and two peak functions. Searching the literature, different fitting functions for fitting the exciton absorption spectra and background are used. The aim of this investigation is to do a systematic approach toward experimental data fitting procedure and draw the conclusions from it. We have first set out to investigate which fitting function gives the best fit for our measurement data. In order to quantify the measure of goodness of the fit we use the sum of squares due to error (SSE) function:

$$SSE = \sum_i (y_i - f_i)^2$$

Lower the SSE value is, the function gives better fitting for the given set of data. We have employed normal and asymmetric Lorentzians and Gaussians, as well as different combinations of functions, as can be seen from Figure 7.5 that lead to the best agreement between the predictions of the model and the experimental data. Fitting function should fit both exciton absorption lines and reproduce their absorption line profiles both on peak maximum and its

wings. For fitting the data background, we used polynomials up to the sixth degree and found out that our data is best fitted with the fifth degree polynomial. This result was unexpected, since second degree polynomials and at most third degree [307] were sufficient for fitting the background. This result can lead to the conclusion that there may be some underlying physical phenomena in spectra which we require fitting with higher degree polynomial function instead of modeling it separately, such as anomalous reflections inside PDMS and polycarbonate layers, defects in WS_2 bilayers or experimental artifacts. For that reason, we have done thorough investigation of the sample and measured absorption spectra on different flakes, as will be discussed later.

Figure 7.6 a) summarize experimental results for exciton A peak position as a function of applied strain for six different fitting functions used for absorption lines fitting and for the fifth-degree polynomial function for the background. All six fitting functions reproduce the expected linear decrease of A exciton energy (peak position) with strain. Linear fit of the exciton A peak position as a function of applied strain gives a strain gauge factor of around -50 meV/% depending on the choice of the fitting function. The best fitting function with minimum SSE was asymmetric Gauss function which gives (50.398 $\pm$0.005) meV/% for gauge value factor. Obtained result is in agreement with the literature experimental result [307] shown in Figure 7.6 b) with strain gauge factor of -55 meV/%. Discrepancies between different experimental results are to be expected due to a variety of reasons such as non-efficient strain transfer, slippage of layers, bubbles, intrinsic material defects and errors in calculation of strain. [319] Experimental results were compared to calculated DFT absorption spectra shown in Figure 7.6 c). Calculations were done using DFT functionals Perdew–Burke-Ernzerhof (PBE) exchange energy, quasiparticle interaction through GW and incorporating electron-hole interaction in an excitonic shift for uniaxial and biaxial straining of monolayer and bilayer WS_2. Final result for exciton energy shift is calculated by subtracting PBE energy shift from GW energy shift due to 1% strain and adding uniaxial excitonic shifts. Excellent agreement between the calculated strain gauge factor for uniaxial straining (-48 meV/%) of material and experimental results is obtained.

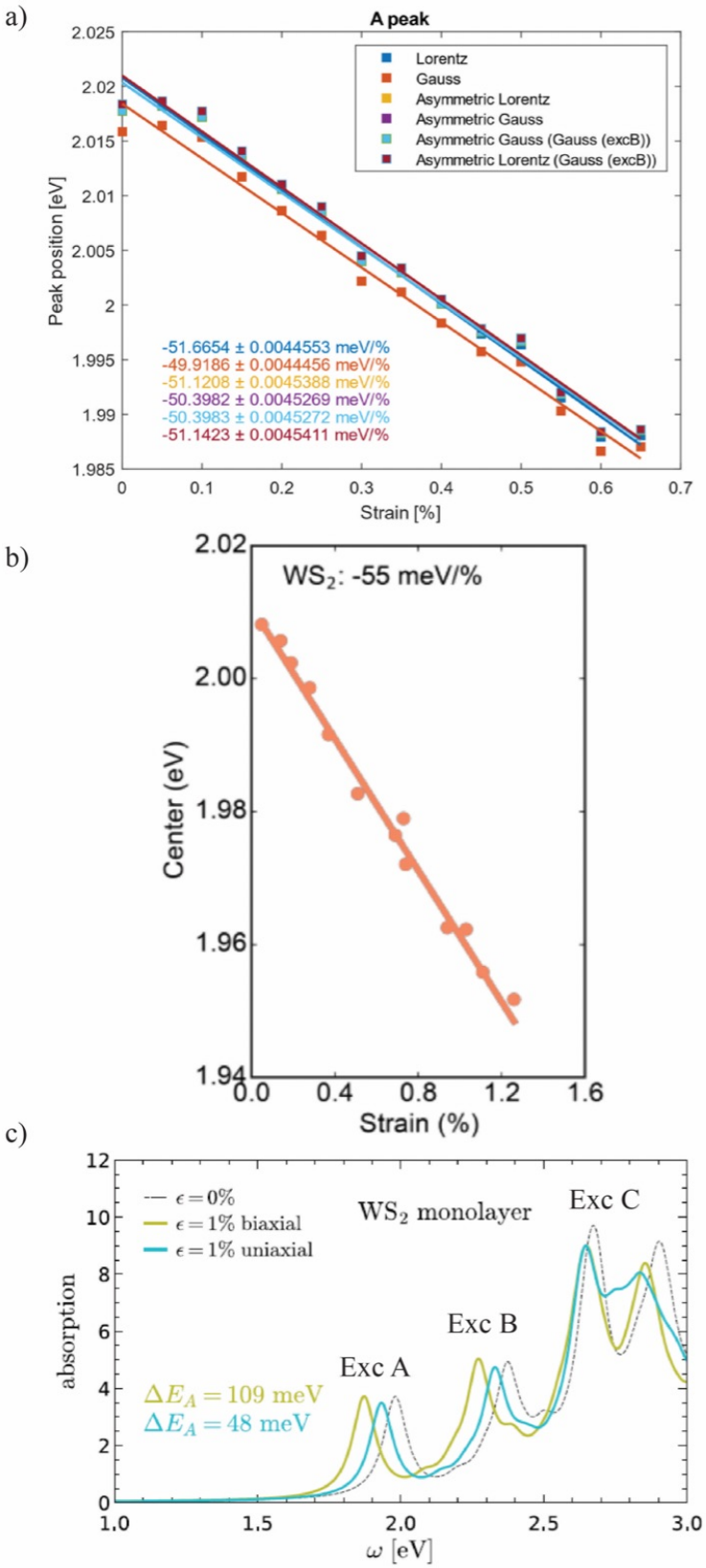

Figure 7.6 a) Experimental strain gauge factors from different fitting functions for straining monolayer WS_2. b) Experimental literature value for comparison. [307] c) Calculated spectra from DFT for strain gauge factors for uniaxial and biaxial strain in monolayer WS_2.

Results obtained for the monolayer WS_2 showed the quality of the prepared sample and verification of the experimental techniques. Since excitonic features dependance on uniaxial straining for different stacking orientation have not been studied so far we found it interesting to explore if van der Waals interaction due to the different stacking orientations influence gauge factors. In Figure 7.7 a) optical image of one of the measured flakes with AA orientation on the same sample is shown. During this project we measured different homobilayers (both AA and AB stackings) present on the same transferred sample in order to do statistical analysis of our measurements. Whitelight spot size was around 2 - 3 μm in diameter and the measurement position in the bilayer was located away from the nucleation center point (bright spot in the center of the homobilayer presented in Figure 7.7 a)). In the case of spot sizes with diameters above 20 μm, the area over which we average our signal could include the parts of the sample with inhomogeneous strain transfer. For that reason, it is better to reduce spot size and measure restricted sample area and make more measurements on different areas within the flake but also for different flakes. Another important parameter is the position of the spot in the measured flake. It is important to choose the position of the flake where we observe consistent and efficient strain transfer without any intrinsic defects and inhomogeneities which can influence optical response under strain. Figure of merit for quality of strain transfer on a measured sample is the exciton peak shift in absorption spectra that can be obtained just by eye as smooth, continuous redshift of absorption spectra with the applied strain, see Figure 7.7 b).

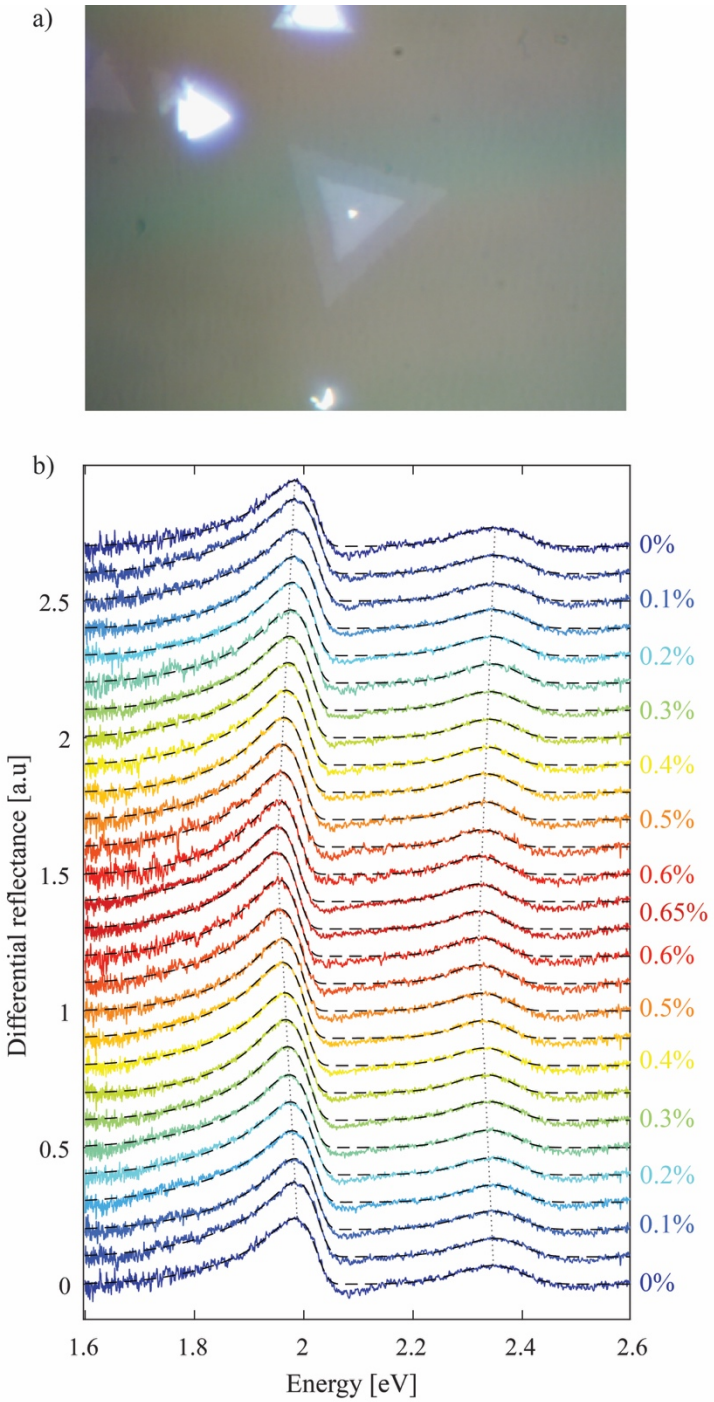

Figure 7.7 a) AA stacking bilayer WS_2 sample and its corresponding b) Differential reflectance spectrum shifting with different strain from 0% to 0.65% of the flake a).

As we have determined that the best functions to fit exciton features are asymmetric Gauss and for background the fifth degree polynomial we show in Figure 7.8 a) to f) how it behaves for different strain levels. We wanted to check if this fitting procedure is also adequate for all strain levels, not just by using SSE but also by close inspection with eye. Obtained fitting results confirm that the fitting procedure is suitable for all strain levels. One of the concerns was that

with higher applied strain the appearance of new excitonic features such as interlayer excitons, dark to bright exciton funneling [321], strain mediated trion creation [322] or indirect to direct transition [323] for which the fitting procedure should be tested. However, obtained excitonic features are created under much higher locally applied strain.

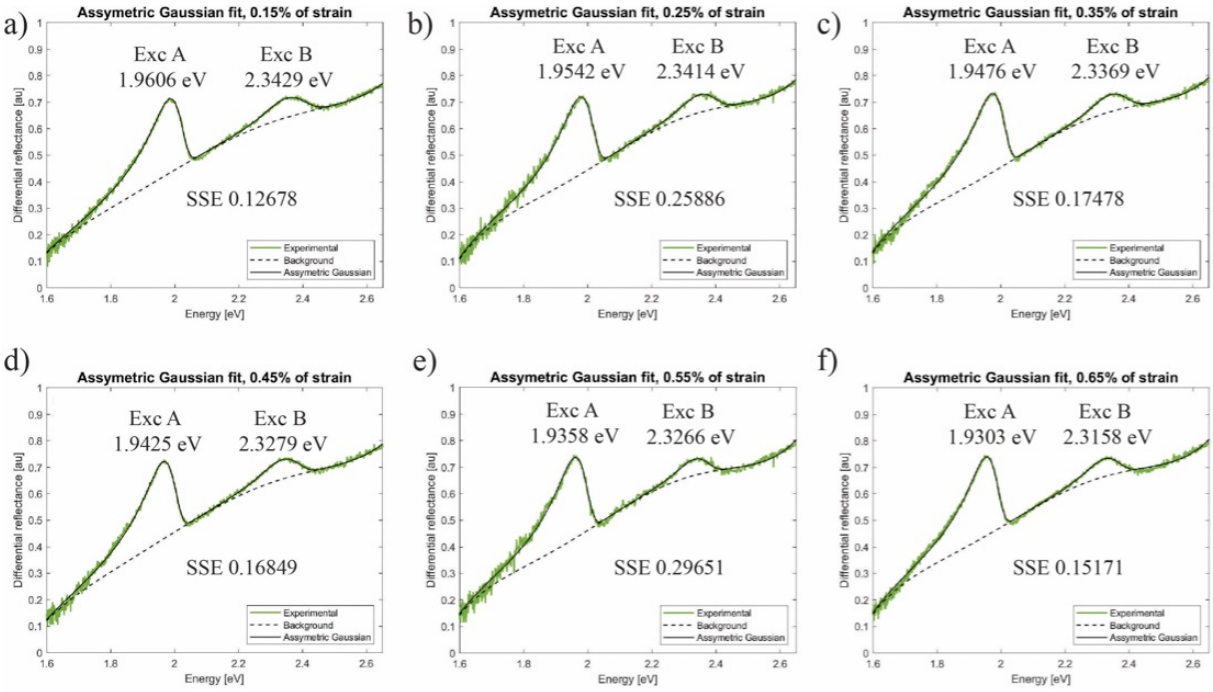

Figure 7.8 Asymmetric Gaussian fits of bilayer spectra with background fitted with 5th degree polynomial for different strains from. a) 0.15% strain to f) 0.65 %.

Calculated strain gauge factors of about -55 meV/% and - 49 meV/% for excitons A and B for AA stacking, are given in Figure 7.9 a) and b), respectively. Similarly, to fitting results for WS_2 monolayer, small differences between obtained fitting results for different fitting functions can be seen in the peak position values for a certain fitting function and for a certain value of applied strain. However, from the line slopes obtained for different fitting functions, we conclude these discrepancies between fitting functions results in the constant offset and does not influence the value of the strain gauge factors which include only relative shifts of peak energies with strain. Exciton B strain gauge factor differs from A which is not unexpected. [324]

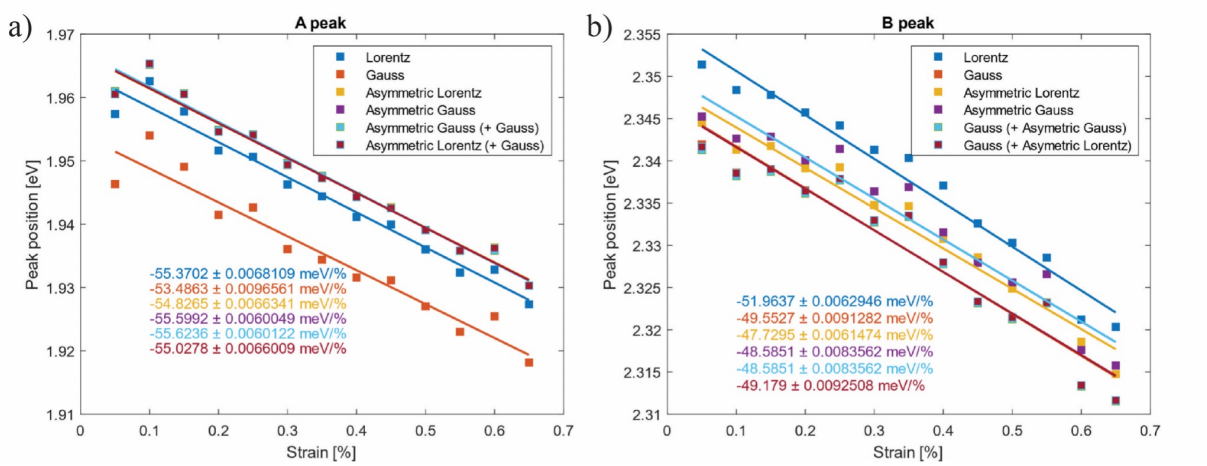

Figure 7.9 Strain gauge factors for exciton A peak a) and B peak b) of bilayer AA stacking WS_2 calculated with different fitting functions.

In order to get more reliable results of the difference in strain gauge factors of different bilayer stacking, we measured more flakes and analyzed the results. Measurements were conducted on seven different bilayer flakes with AA stacking and four flakes with AB stacking for the same applied strain and under the same experimental condition (beam diameter, position on the flake etc.) Results for the strain gauge factors for different stackings and for both A and B excitons are presented in Figure 7.10 and summarized in Tables 7.1 and 7.2, where the gauge factors for different stackings are given. We observe that the absolute median value for AB stacking is higher than for AA stacking with comparable mean values and differences in both maximum and minimum values. For the exciton B, the difference in the strain gauge values is much more pronounced between AB and AA for median, mean, maximum and minimum and absolute strain gauge factor is higher for AA stacking.

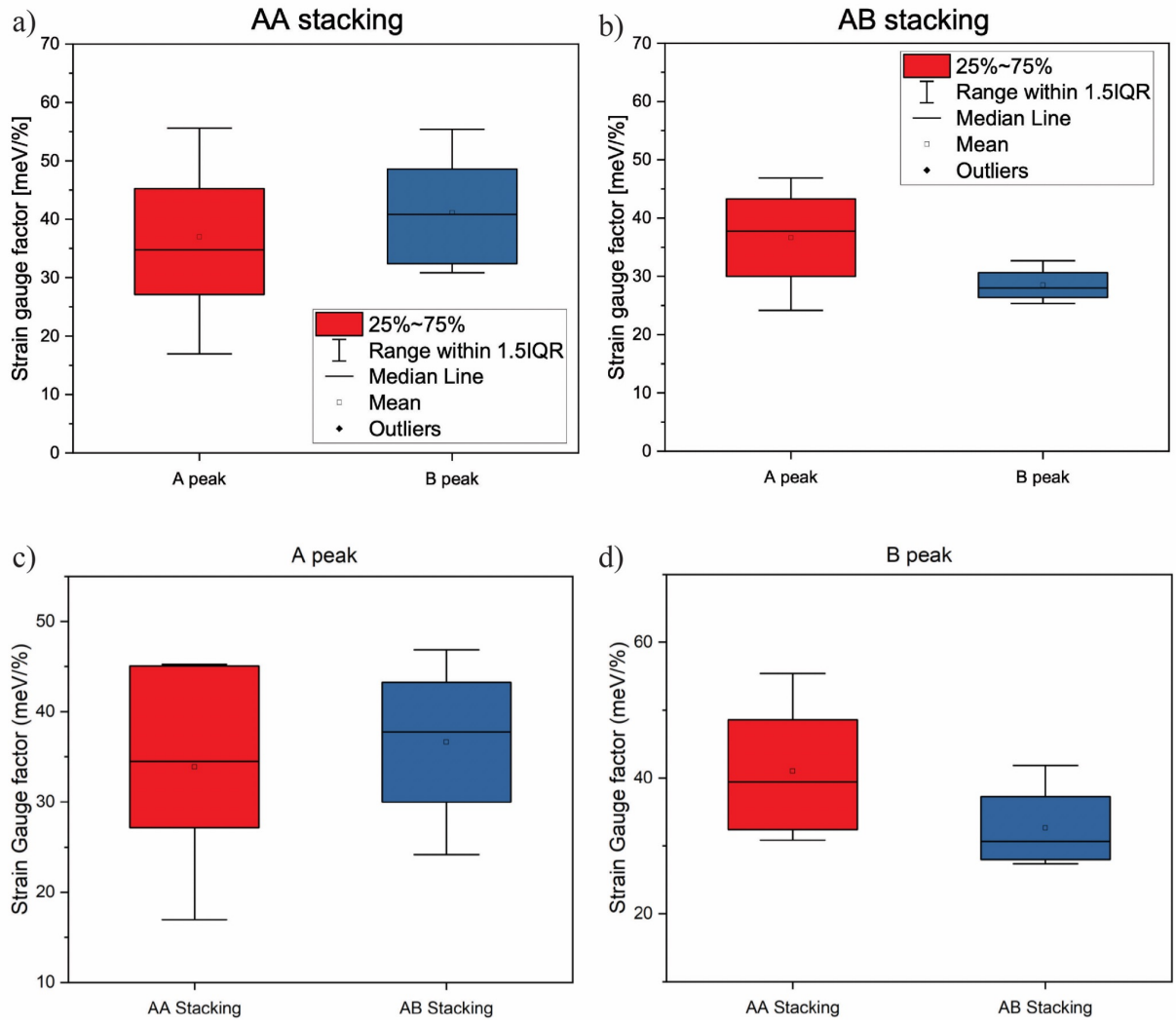

Figure 7.10 Statistics on strain gauge factors of AA a) and AB b) stacking bilayers of WS_2 for excitons A and B on different flakes. Comparison of strain gauge factors in different stackings for A exciton c) and B exciton d).

Table 7.1 Statistical values for AA stacking strain gauge analysis of exciton A and B

	Exciton A (meV/%)	Exciton B (meV/%)
Median	-34,77	-40,85
Mean	-36,99	-41,14
Maximum	-55,60	-55,40
Minimum	-16,95	-30,86

Table 7.2 Statistical values for AB stacking strain gauge analysis of exciton A and B

	Exciton A (meV/%)	Exciton B (meV/%)
Median	-37,76	-27,98
Mean	-36,65	-28,50
Maximum	-46,86	-32,69
Minimum	-24,16	-25,35

Obtained experimental results were compared with the results of DFT calculation for exciton energy shifts under 1% strain for AA and AB stacking. Calculations shown in Figure 7.11 a) to c) were done with the same parameters as described for Figure 7.6 c), they give results energy band shifts for Γ, Q and K points in the Brillouin zone with 1% strain. Calculated strain gauge values for AA stacking of -56,45 meV/% and -60,25 meV/% for AB stacking are obtained. Difference in calculated strain gauge values is very subtle but that is somewhat to be expected as we think this comes from different interlayer distances in AA and AB stacking. [325] Different interlayer distances affect interlayer coupling which influences band structure, mechanical properties and required energy to change atomic structure.[325]

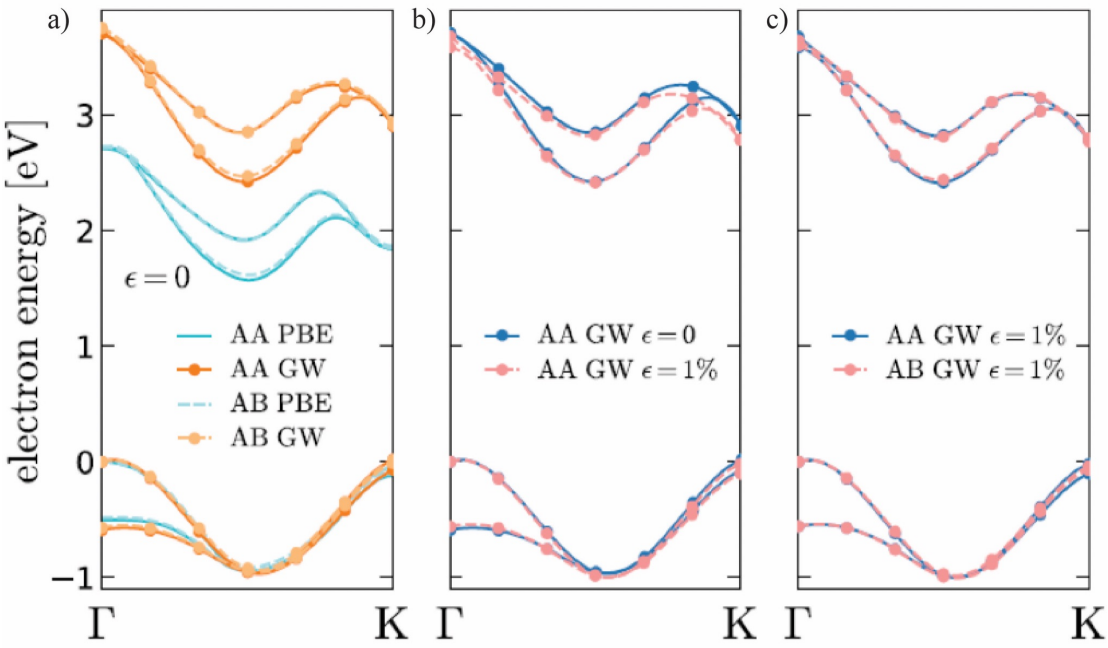

Figure 7.11 Calculated DFT energy bands for bilayer WS_2 with AA and AB stacking. a) Comparison of PBE and GW approach for 0% strain. Change in energy bands for AA b) and AB c) stacking between 0% and 1% strain.

Comparing the calculated strain gauge factors with the statistically analyzed experimentally measured ones we see very good agreement in relative differences between AA and AB stackings. However, regarding absolute values experimental values have lower values which is somewhat to be expected. Differences between experimental and theoretical values come as a result of intrinsic sample imperfections due to the inhomogeneity of the CVD samples, structural defects, modifications induced during the transfer procedures, influence of the surrounding, etc., which calculation does not take into account because it models a perfect bilayer structure. Also, discrepancies can come as a result of experimental procedure and it is related to interaction and adhesion forces of bilayer flakes between bottom flexible polycarbonate substrate and top PDMS capping layer, bubbles in-between this sandwich, slippage of material due to strain which can lose its bending properties and become irreversible after couple of straining cycles. All this can influence the strain transfer effectiveness that reflects on the observed change in optical properties for different applied strain levels. If we think of distribution of experimentally measured data between minimum and maximum values which encompasses all the possible cases of quality of the sample and the strain transfer, only the upper part of the distribution is in very good agreement in terms of absolute values of calculated gauge factors. In other words, calculated theoretical values sets the upper value for realistic systems experimental data.

At room temperature, the width of the exciton transitions is governed by the exciton−phonon interaction leading to strongly asymmetric line shapes. Here, we demonstrate that the width and the asymmetric line shape of excitonic resonances in TMDC monolayers can be controlled with applied strain. [307] In the paper Niehues et al. it was found that the A exciton in the selenium-based monolayer materials substantially narrows and becomes more symmetric, while no change is observed for atomically thin WS_2. For MoS_2 monolayers, the line width increases. These effects are due to a modified exciton−phonon coupling at increasing strain levels because of changes in the electronic band structure of the respective monolayer materials. Results presented there demonstrate that moderate strain values on the order of only 1% are already sufficient to globally tune the exciton−phonon interaction in TMDC monolayers and hold the promise for controlling the coupling on the nanoscale. [307] There is limited understanding of the microscopic mechanisms governing exciton−phonon scattering rates during the transition from the direct bandgap monolayer to the indirect bandgap bilayer semiconductor. The impact

of interlayer coupling and hybridization, and that of exciton−phonon scattering through intra- and intervalley channels are of particular interest in this context. [326]

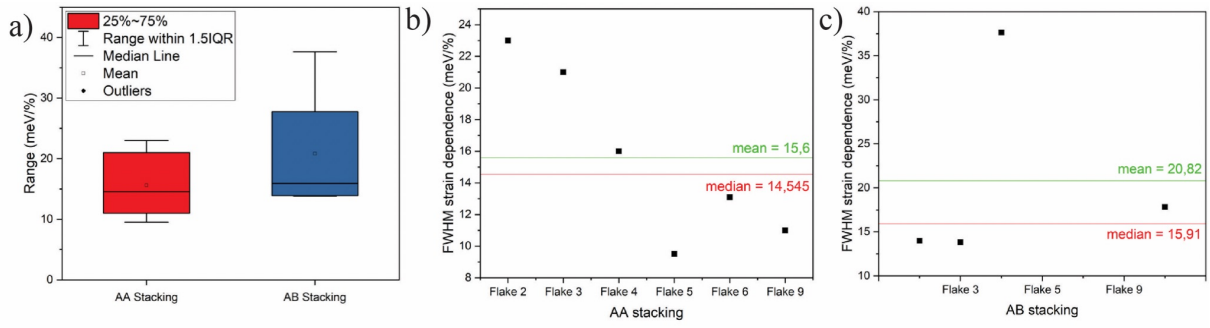

Figure 7.12 a) Comparison of statistical analysis of exiton resonance full width half maximum (FWHM) change with strain for AA and AB stacking. Plotted FWHM strain dependence for AA b) and AB c) stacking for different flakes.

In Figure 7.12 a) we show statistical analysis of strain gauge factors for FWHM of exciton A in AA and AB stacking bilayers of WS_2, median and mean values for AA b) and for AB stackings c) stacking are 14,55 meV/% and 15,91 meV/%, respectively. In contrast with the no strain dependence in monolayer WS_2 samples where the optical bandgap transitions are direct without the assistance of phonons. We know that strain can influence exciton-phonon scattering mechanism in monolayer TMDs so it is expected that in bilayer samples with indirect phonon assisted exciton recombination the scattering mechanism will be even more influenced with strain which results in lifetime and FWHM strain dependence in bilayers.

7.2.4 Conclusion

In this subchapter 7.2 we have presented results of investigation of WS_2 twisted bilayers under applied uniaxial tensile strain via 2-point and 3-point bending setups. Bilayer WS_2 were transferred from as-grown surface Si wafers to polycarbonate substrate and capped with PDMS. Due to sample CVD growth limitation we had only angles of 0 and 60 degrees which correspond to AA and AB stacking, respectively. We strained both AA and AB bilayers only up to 0.65% to be sure to avoid slippage of flakes and inefficient strain transfer. Analyzing statistics on flakes of AA and AB stacking we get the median value of strain gauge factor of - 34.77 meV/% and -37.76 meV/%, respectively. These values are in good agreement with calculated ones for AA stacking of -56.45 meV/% and -60.25 meV/% for AB stacking. Comparing calculated values with statistically analyzed experimental data we conclude that theoretical values set the upper value for realistic systems experimental data.

In addition to energy shifts of excitons, strain can also have an influence on absorption line FWHM. Despite monolayer WS_2 not showing any FWHM strain dependence, we have shown that in the bilayer due to its indirect bandgap nature phonons play role in exciton-scattering processes which are influenced by strain and, thus, we can control FWHM of bilayers with strain.

7.3 Ultrafast dynamics under uniaxial strain

Previous section has finished with the investigation of strain influence on FWHM in bilayer WS_2 CVD samples which is governed by exciton-phonon coupling. In this chapter we continue exploring exciton-phonon coupling in monolayer WS_2 and their temporal dynamics under applied strain. As from the Heisenberg uncertainty principle, the width of exciton linewidth spectra features corresponds to their lifetime; the wider the linewidths, the shorter the lifetime is and vice versa. Here we use an ultrafast femtosecond laser system, described in Chapter 4, to measure pump-probe signals from CVD grown monolayer WS_2 samples. In the previous work of I. Niehues et al [307] the change of FWHM with strain has not been observed, which is also confirmed by time-resolved photoluminescence measurements where the decay rate was constant with strain. They have used micro-mechanically exfoliated WS_2 monolayers which can have a lower amount of defects, brighter photoluminescence, and narrower linewidths. Our used samples were CVD grown samples, which can result in high-quality samples but also introduce defects which open new exciton-phonon scattering mechanisms and dark exciton relaxation channels. This can lead to strain dependence of linewidths and lifetimes of CVD grown monolayer samples. As mechanically exfoliated samples will not be used in mass scale industry application for electronics, optoelectronics and flexible electronics it is paramount to investigate strain-related exciton-phonon couplings and influence on linewidths and lifetimes in CVD grown samples.

7.3.1 Experimental setup for the strain dynamics measurements

Ultrafast measurements were done at Politecnico di Milano on the pump-probe setup in transmission configuration with non-collinear pump and probe beams. This optical setup required designing and building a new strain stage which allows the probe beam to get the spectrometer and CCD camera. Figure 7.13 shows 2-point uniaxial strain bending setup for transmission optical setups. Basic principles of applying and calculating strain are the same as described in subsection 7.2.4. This strain setup can work in both horizontal and vertical planes, depending on the geometry requirements of the optical experiment.

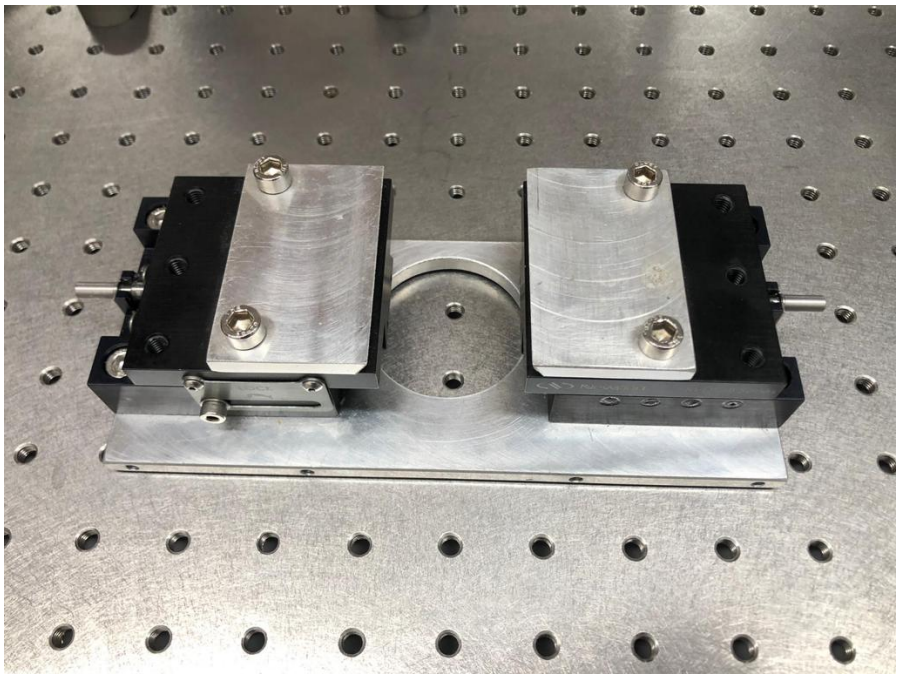

Figure 7.13 2-point uniaxial strain bending setup for use in transmission optical setups used for measuring ultrafast temporal dynamics under strain.

7.3.2 Temporal dynamics in strained systems

We have investigated two CVD grown monolayer WS_2 samples synthesized in the same batch at the Institute of Physics, Zagreb. The samples were grown on Si wafers after which they were transferred and prepared for straining in the same way as in subsection 7.2.3. In Figure 7.14 a) and b) differential transmission spectra are presented showing significantly different exciton resonance energies in two samples even for the strain difference of only 0.1%.

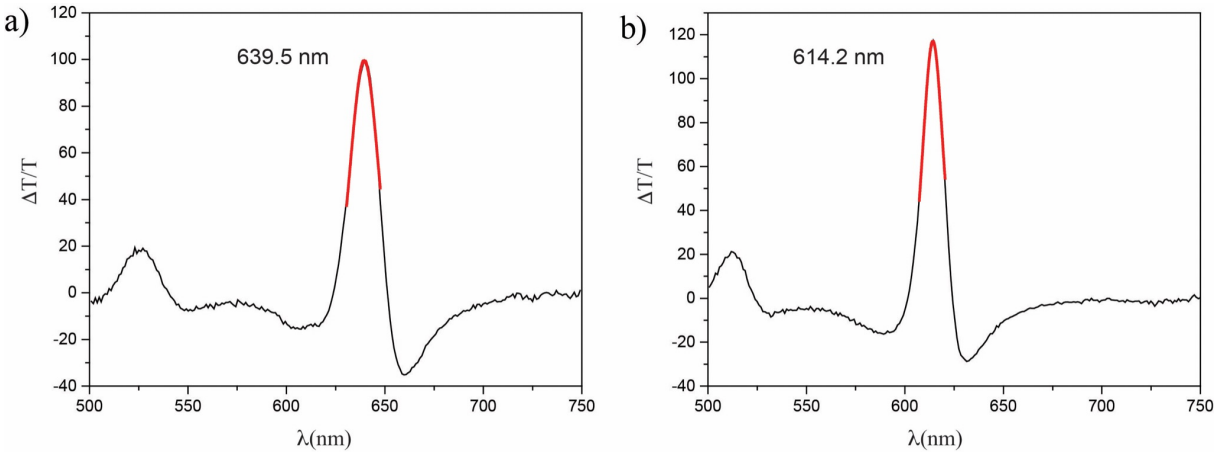

Figure 7.14 Differential transmission spectra after pump excitation taken at 300 fs delay time. Red lines denote Lorentzian fit of the exciton resonance energy. a) Strain level 0.48 % for monolayer WS_2 sample 1. b) Strain level 0.6 % for monolayer WS_2 sample 2.

Even when the two samples exhibit the same applied strain of 0.6% or zero the difference between their emission peaks is around 15 nm which is unusual for the same batch samples and hints to differences in growth conditions in two samples and possible defects. Spectra in Figure 7.14 were extracted from the data at 300 fs time delay and fitted with the Lorentzian shape function. In the left part of the spectrum at higher energies, at 525 nm B exciton is also evident.

Temporal dynamics of the sample 1 and 2 are shown in Figure 7.15 a) and b), respectively. Ultrafast dynamics was extracted at exciton A resonance energies of 639.5 nm for sample 1 and 614.2 nm for sample. Figure 7.15 a) shows single exponential decay dynamics fitted accordingly and with decay lifetime of 1152.5 fs for a strain level of 0.6% in sample 1. In sample 2 presented in Figure 7.15 b) temporal dynamics undergo double exponential decay with a fast decay time of 331.45 fs and a slow decay time of 15059.88 fs at strain level of 0.48%. Exciton radiative lifetimes are on the order of a few picoseconds at low temperatures, because of the large oscillator strength. However, the nonradiative decay rate is very high.

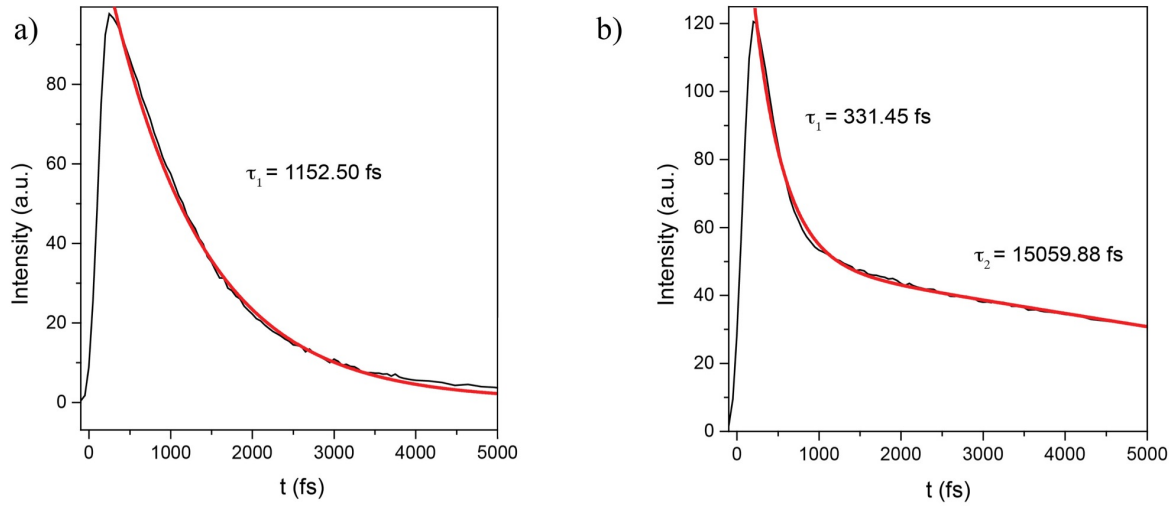

Figure 7.15 a) Temporal dynamics taken at 639.5 nm for monolayer WS_2 sample 1. b) Temporal dynamics taken at 614.2 nm for monolayer WS_2 sample 2. Sample 1 a) is fitted with one exponential decay (red line) and Sample 2 b) is fitted with two exponential decay (red line). Pump delay time is denoted with t on the x axis.

After photoexcitation, only a small fraction of the excitonic population resides within the light cone, while the remaining fraction is scattered outside by electron-phonon scattering, on a timescale of a few hundreds of femtoseconds, forming momentum-forbidden dark exciton states. [327] Observed very fast decay time could be explained by introduction of new exciton-phonon scattering non-radiative channels which arise from defects in CVD grown samples. [328] Temporal dynamics of atomically thin van der Waals systems can greatly vary among similar materials but also among the same material and different samples. [329] This is especially evident in CVD grown samples which can have inhomogeneity and defects. Another contributing factor in particular our case is that the transfer method we used could also affect it through additional carrier injections. Also, different dielectric environment choice of substrate also influences dynamics. [328] However, to the best of our knowledge, there is no ultrafast pump probe study of TMDs on polycarbonate substrates.

In Figure 7.16 a) and b) strain gauge factors for samples 1 and 2 are shown, respectively. Obtained values of -15.7 meV/% and -24.8 meV/% are significantly lower than expected for monolayer WS_2 and compared to the one measured in Figure 7.6 a). Strain gauge factor for monolayer WS_2 should be around -50 meV/% [307] for a strained sample. As discussed in previous subchapters, lower strain gauge factor indicates that there are problems intrinsic to the sample or measurement itself, such as inefficient strain transfer, intrinsic material defects, etc. but in our case it could be due to another reason not previously mentioned in the literature.

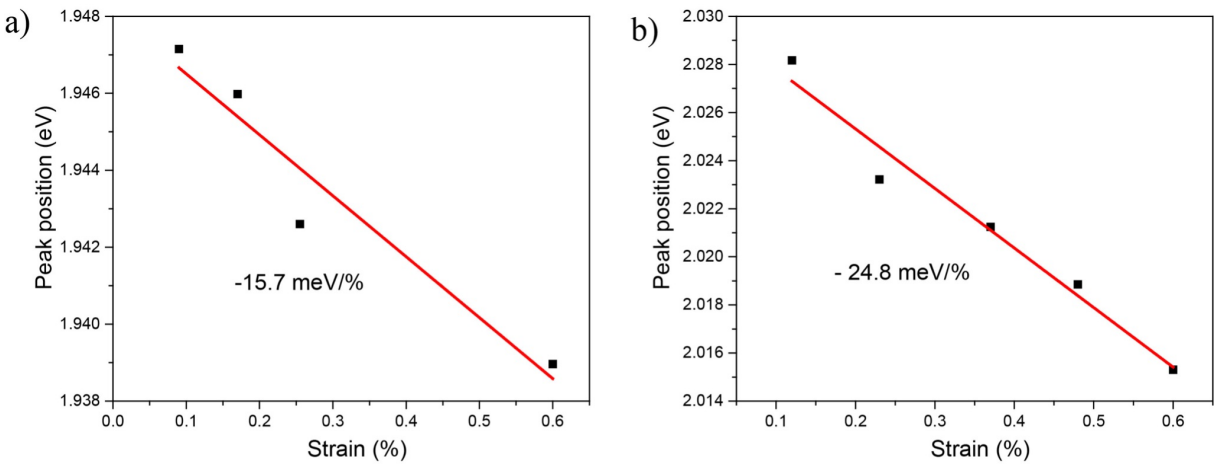

Figure 7.16 Strain gauge factors of exciton peak positions for sample 1 a) and sample 2 b).

Usually strain measurements are done with a microscope-based optical setup which has spot size in the range of 500 nm up to a few micrometers, depending on the light source used for the experiment. On these spatial scales applied strain on the substrate is uniform, which is not true for our sample since the shear size of the probe spot is around 250 um. Pump-probe setup used for this measurement is not a collinear microscope-based setup but pump and probe come from different angles and intersect on the sample, focused by the lens. On these lateral scales, applied strain non-uniformity in the substrate could arise from geometry alone. Also, from Figure 7.3 it is visible that applied strain is calculated through curvature fitting and radius of this curvature in the center of the substrate - apex; with such a big probe spot size we are collecting signal from the part of the substrate not only from the apex but also from surrounding part of the strained sample with a different applied strain. Therefore, collected signal is averaged out from the signal coming from the different parts of the sample.

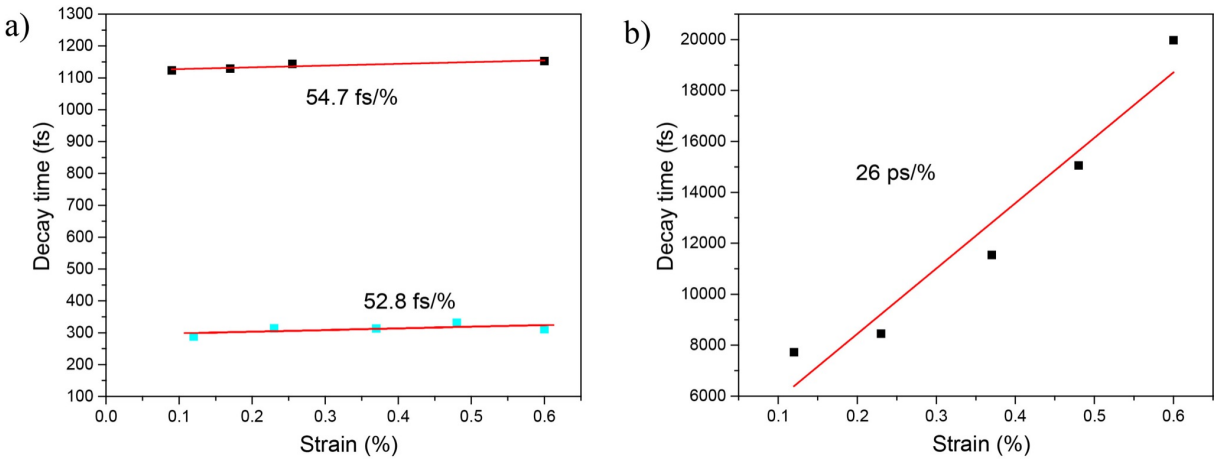

Figure 7.17 a) Change of fast decay time with strain for sample 1 (black dots) and 2 (cyan dots). b) Change of additional slow decay time with strain seen in sample 2.

Figure 7.17 a) shows comparison of fast decay time under strain influence for sample 1 and 2. We see a comparable, almost the same, decay time change per % of applied strain for two samples of 52.8 fs/% and 54.7 fs/% albeit their absolute values of decay time are different. The same strain dependence of the fast decay times indicates that the same exciton-phonon scattering channels are involved with the same exciton-phonon coupling to the strain. In Figure 7.17 b) slow decay time strain dependence from sample 2 is shown. Change of decay time with strain is 26 ps/%, three orders of magnitude higher than for the fast component presented in Figure 7.17 a). These results suggest how temporal dynamics of atomically thin TMD materials can be tuned with applied strain. Having the ability to control whether to generate short-lived or long-lived electron–hole pairs in 2D-TMD monolayers opens a new horizon for the application of these materials. For instance, long-lived electron–hole pairs are appropriate for photo-voltaic devices, but short-lived excitons are more beneficial for lasers with ultrashort pulses. [330]

7.3.3 Conclusion

Temporal dynamics in strained CVD grown monolayer WS_2 samples was measured with non-collinear pump-probe setup. Differential transmission spectra ($\Delta T/T$) taken at 300 fs show distinguishably different exciton resonance energy with peak position on 636 nm and 611 nm for initial strain and for sample 1 and sample 2, respectively. Differences in exciton peak positions of as much as 15 nm is a result of differences in growth conditions of two samples and indication of defects that reflects their temporal dynamics. Strain gauge factors reveal disparate values to the one reported in literature and in Figure 7.6. Besides inefficient strain and/or intrinsic material defects another major cause could be very large probe spot size which averages optical signal over the sample, collecting the probe signal from the sample area with uneven applied strain. Temporal dynamics reveal single exponential decay in sample 1 with the decay time on the order of 1 ps. In the second sample double exponential decay is present with fast decay time on the order of 0.3 ps and the slow decay time which starts at 6 ps and goes up all the way to 20 ps with 0.6 % strain. Fast decay times in sample 1 and 2 have almost the same strain dependence of around 55 fs/% indicating the same origin of relaxation process while the slow decay time observed in sample 2 has three orders of magnitude bigger dependence of 26 ps/%. We have shown that with strain we are able to control exciton lifetimes. This opens a new horizon for application in photo-voltaics where short-lived excitons typical for unstrained systems are more favorable while long-lived excitons that appear in the strained systems are more beneficial for ultrashort pulsed lasers.

8 Optical characterizations of Borophene

8.1 Motivation

As with other 2D materials, some of which have been mentioned in previous chapters, with Borophene also there is a challenge in development of synthesis protocols, substrate choice and tools which would bring it closer to mass-scale production and application in industry. Borophene research is still mostly limited to UHV growing procedures on metallic substrates and *in-situ* characterization standing in the way toward device fabrication, optical characterization and transport measurements. In order to overcome this problem a millimeter sized borophene growed on Ir(111) metallic substrate was successfully transferred to arbitrary substrates such as Si wafer for further analysis. In this chapter we focus on optical properties of borophene, namely its Raman spectrum analyzed in different dielectric environments; on Ir(111) and Si. Experimental results were compared to theoretically spectra obtained by DFT calculation for a free-standing borophene sheet. Raman spectroscopy is a powerful tool which enables us to confirm the presence of borophene before and after transfer and also to exclude any possible contaminations and degradation due to transfer procedure and possible air-instabilities. After initial UHV epitaxial growth on Ir(111) via borozene, first in-situ characterization was performed by LEED measurements and later, in ambient conditions, with AFM. Using transfer procedure with PMMA described in Chapter 4., borophene was successfully transfered to Si wafer. Figure 8.1 shows an almost millimeter-sized transferred borophene sheet on a wafer confirmed with different microscope techniques. Scanning electron microscope in Figure 8.1 a), optical microscope on b) and atomic force microscope on c) and d). Borophene flake is homogenous but some cracks (yellow arrows) and holes (cyan arrows) can be seen in both optical and electron microscope images. Overall, the sample is flat and free of large-scale defects and thickness inhomogeneities, as shown in Figure 8.1 e) and f), which indicates that our transfer method did not leave any notable mesoscopic PMMA contamination on the Bo layer. [125] In Figure 8.1 e) line profile height indicates formation of a bilayer due to the borophene layer folding on the crack edges and tears, also seen in SEM images. Measured heights of borophene monolayer in Figures 8.1 e) and f) are orders of magnitude bigger than before the transfer, due to the affinity for water adsorption. [125]

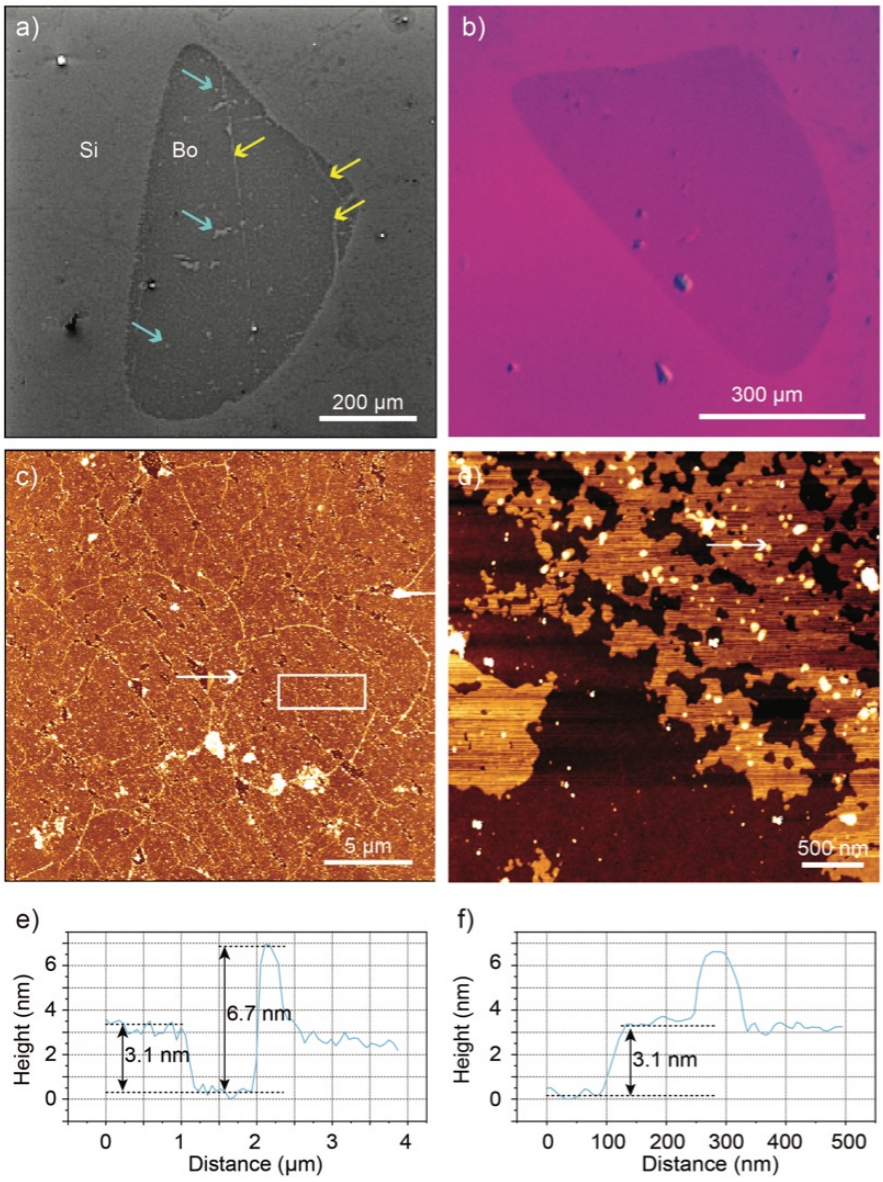

Figure 8.1. Largest transferred borophene fragment imaged with SEM a) and optical microscope b). c) AFM Topography of the central region of the largest transferred Bo flake, where white rectangle indicates the area inspected for roughness analysis. d) Topography of the edge of the largest transferred Bo flake. (e) and (f) Line profiles extracted from panels (c) and (d) (as marked by arrows), respectively, with heights of the transferred monolayer and bilayer Bo indicated. Adopted from [125]

8.2 Optical characterization and comparison with DFT

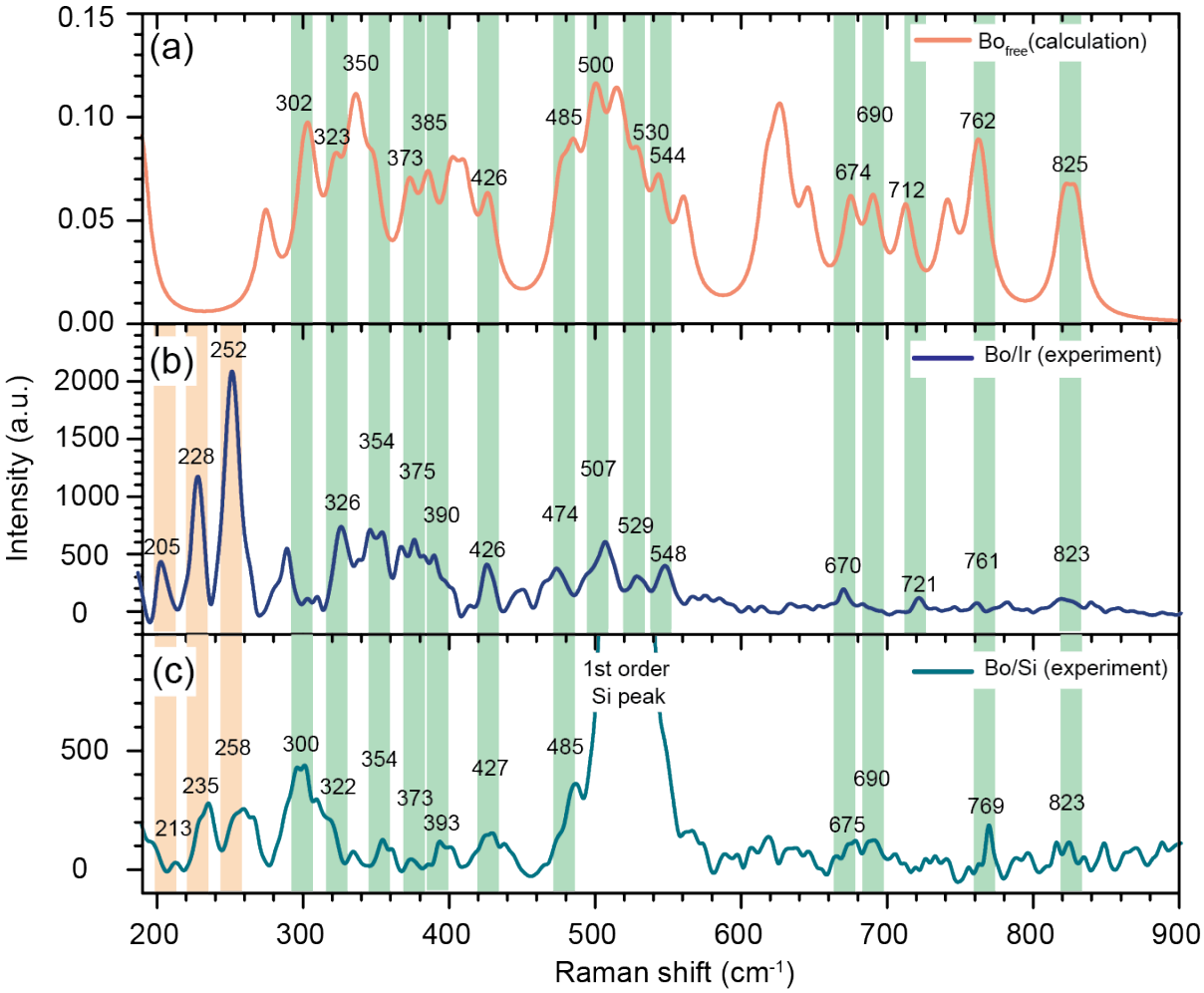

Figure 8.2 Raman characterization of Bo. (a) DFT-calculated Raman spectrum of a freestanding Bo layer (Bo$_{free}$). (b) Measured Raman spectra of Bo/Ir (after background subtraction) and (c) of Bo/Si. Vertical colored stripes are guides to the eye which indicate common Raman modes. Energies (in cm^{-1}) of indicated Raman modes are given as numerical values in each panel. Taken from [125]

We investigated vibrational modes of χ_6 polymorph of Bo both on an as-grown Ir(111) substrate, transferred on Si substrate and DFT calculated freestanding form. Results obtained from DFT calculations are presented in Figure 8.2 a) and compared with measured Raman spectra shown in Figure 8.2 b) on Ir(111) and c) on Si wafer. It is known from the literature that interaction between the Bo layer and iridium surface is such that no significant charge transfer to or from the Bo layer occurs. [331] Moreover, Bader charge analysis shows that χ_6 polymorph of Bo donates two electrons per unit cell, in total 0.08 electron per B atom. From the interaction of Bo layer with the Ir surface and electron transfer to Ir surface depopulation of electronic states near the Fermi level in the supported Bo occurs. This metallic character of Bo on Ir(111) substrate has been confirmed both experimentally [332] and theoretically [331]. In the paper of Vinogradov et al. [331] a significant redistribution of charge density with electron accumulation in the interface area between Bo layer and metallic substrate has been discussed, indicating the formation of chemical bonding between layers. However, the presence of Raman features of χ_6 polymorph Bo on Ir(111) indicates that Bo layer is physisorbed on Ir surface since the interaction with the Ir substrate results in weak depopulation of electronic states in the Fermi level compared to freestanding Bo layer and p doping due to the electron transfer to the Ir. The strength of the film-substrate interaction measured as the ability to observe the Raman-active phonons has been discussed in the paper of Starodub *et al.* [236] where two rotational variants of graphene (R0 and R30) grown on Ir(111) have been investigated. For the system with weak charge transfer and in the case where substrate does not significantly perturb electronic bands (R30 variant of graphene) Raman-active phonons are obtained. In the case of R0 variant, the perturbation of the electronic bands that Ir substrate produces in R0 graphene are such that electronic excitations of Ir states by graphene phonons are highly favored, limiting the phonon lifetime and thus destroying conditions needed to observe Raman scattering in the R0 phase. Therefore, the fact that Raman modes are observable while Bo is still bonded to the Ir(111) structure supports our findings that Bo being physisorbed on Ir(111) substrate. [189,236]
Experimentally obtained Raman modes are compared to the calculated phonon density of states (DOS) for 0-1000 cm^{-1} energy range. Calculated Bo spectrum is obtained by the ground-state density-functional-theory (DFT) calculations that were done by means of the Quantum Espresso package[333] with a plane-wave cutoff energy of 70 Ry. Optimized norm-conserving Vanderbilt pseudopotentials were used with the PBE exchange-correlation functional.[334] A freestanding (6 × 2) hexagonal structure with five vacancies and unit cell parameter of a = 5.432 Å was taken as a most stable phase of boron on Ir(111) surface.[331] Two adjacent Bo layers are separated by 30 Å vacuum space in the supercell approach. Momentum space was sampled

with a 4 × 12 × 1 Monkhorst−Pack grid (with a Gaussian smearing of 0.01 Ry). Phonon frequencies at the center of the Brillouin zone were obtained by means of density functional perturbation theory.[335] Final calculated Raman spectra has been generated by applying Lorentzians (with the broadening of 11 cm^{-1} = 1.4 meV) to this set of discrete phonon modes. [125] Background subtracted spectrum of Bo on Ir(111) substrate (Bo/Ir) is presented in Figure 8.2 b) and compared to calculated freestanding Bo Raman spectrum, see Figure 8.2 a). In Figure 8.2 c) Raman spectrum of the transferred Bo layer on oxidized Si wafer (Bo/Si) is presented. Common Raman modes are indicated with vertical green lines as guides for the eye. Obtained results suggest that the majority of experimentally obtained peaks on weakly interacted substrate are present in calculated spectra of freestanding Bo single layer. In Figure 8.3 six Raman active modes for χ_6 polymorph of freestanding Bo are presented. We explicitly show these six modes since their energies, amplitudes and correlations with experimental values are indicative for the types of interaction that are present in these systems that influence optical response.

For all Bo Raman active modes, experimentally obtained peak positions on Ir, Si and theory have slightly different energies due to the influence of different substrates and their dielectric environment, the mismatch in thermal expansion coefficients of Bo and the substrate during the growth procedure causing the strain release during the transfer process and energy shift of Raman modes. [331,336,337] Chemical environment can also have an effect on energy shift (i.e., the presence of adsorbates originating from the transfer process), for example, Raman mode shifts have been identified for organic and oxygen adsorbates on Bo. [338,339] High laser power needed to detect Raman scattering increases the temperature of the sample which changes the Raman positions of atomically thin materials depending on the type of the substrate. [340] Peak intensity decrease can also be caused by strain release during the transfer,[341] or by defects and compositional modifications of Bo during different steps of the transfer,[125,185,189,342] driven by chemical reactivity.

Raman modes obtained below 280 cm^{-1} are present only in experimental data (marked by orange vertical lines) which is in agreement with previous work [343] where for both χ_3 and β_{12} phases the theoretical model is not able to predict experimentally obtained lower energy Raman modes. In the case of supported Bo layer, coupling between Bo layer and substrate gives rise to new Raman modes which can be explained by various factors such as reduction of symmetry

due to substrate symmetry which activates some of the previously inactive modes [344–346] or interaction with substrate which give rise to interaction mode of lower energy indicating weak coupling between Bo and substrate. [347] Raman interaction mode should be substrate dependent and we observe in the Ir and SiO_2 substrate a slight shift in frequencies. [337,347–349] Raman interactive mode frequencies on Ir and Si are below 300 cm^{-1} which is consistent with substrate induced phonons in Bo on Al(111). [51] This interaction also induces significant mismatch obtained for B_g mode at 305 cm^{-1} between results obtained for Bo/Ir system and theoretical calculations, due to the large difference between the masses of boron and Ir atoms. Since our theoretical model is made for freestanding Bo sheets, this interaction has not been taken into account, and, therefore these modes are not present in the calculated spectrum or do not adequately describe the experimental results.

On the high-frequency part of the spectrum, B-B stretching vibration modes around 760 and 820 cm^{-1} strongly interact with electron bands, which leads to broadened and lower intensity of these Raman modes in Bo on Ir(111). [350,351] This interaction of boron atoms with metallic substrate has been obtained in MgB_2 system and plays a crucial role in the high T_c superconductivity of MgB_2. [350] It is predicted that in Bo, electron-phonon interaction is even larger than in MgB_2. [350,351]

Comparison between Bo/Ir(111) and Bo/Si Raman spectra shows good overlap of Raman peak positions and they are in good agreement with theoretical modes, such as B_g modes with energy of 427 and 485 cm^{-1} presented in Figure 8.2 a). However, for the vibrational energies around 520 cm^{-1} Bo/Si Raman signal is completely screened due to the prominent Si Raman peak.

Intensity of Raman modes are lower for post-transferred Bo on Si wafer, as can be obtained for A_g mode on 674 cm^{-1}. One of the possible reasons for obtained decreased intensity is electrochemical change of material during the electrochemical delamination of Bo where physisorbed material is detached from the support and exposed to reactions with chemical reagents presented in solution. [185,189,342] With transfer of Bo to wafer, residual strain in the material is released and changed which can influence Raman signal intensity. [341] Although the Raman spectrum of Bo/Si is suppressed on Si wafer, no typical PMMA Raman modes are obtained in Figure 8.4 a) and b), indicating that PMMA residuals have been successfully removed from the material. [125]

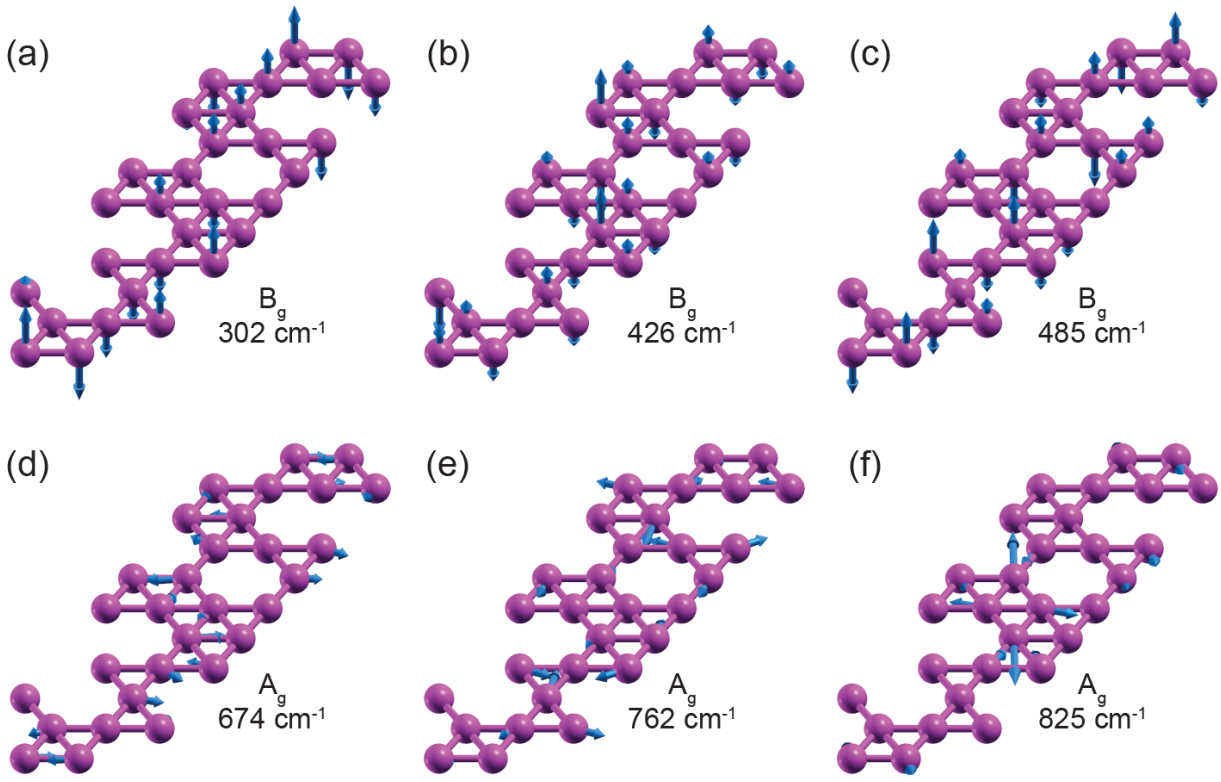

Figure 8.3. Perspective view of six calculated Raman active modes for the freestanding Bo χ_6 polymorph. (a-c) B_g symmetry.and (d-f) A_g symmetry with indicated energy for each mode. The blue arrows and their lengths denote the directions and relative amplitudes of atomic vibrations, respectively. Taken from [125]

8.3 Analysis of possible PMMA contamination

PMMA or Poly(methyl methacrylate) is a polymer which can leave contamination of parts of the PMMA chain as by-product of transfer procedure. Investigation of contamination with PMMA or possible other contaminants was done by comparing the Raman signals from PMMA on Si wafer and borophene on Si wafer. PMMA has the most prominent Raman peaks around 3000 cm^{-1} as seen in Figure 8.4 b). In the region from 190 cm^{-1} to 800 cm^{-1} shown in Figure 8.4 a) where the majority of borophene Raman peaks are observed; PMMA does not have prominent peaks [352] which is confirmed also in our experiment.

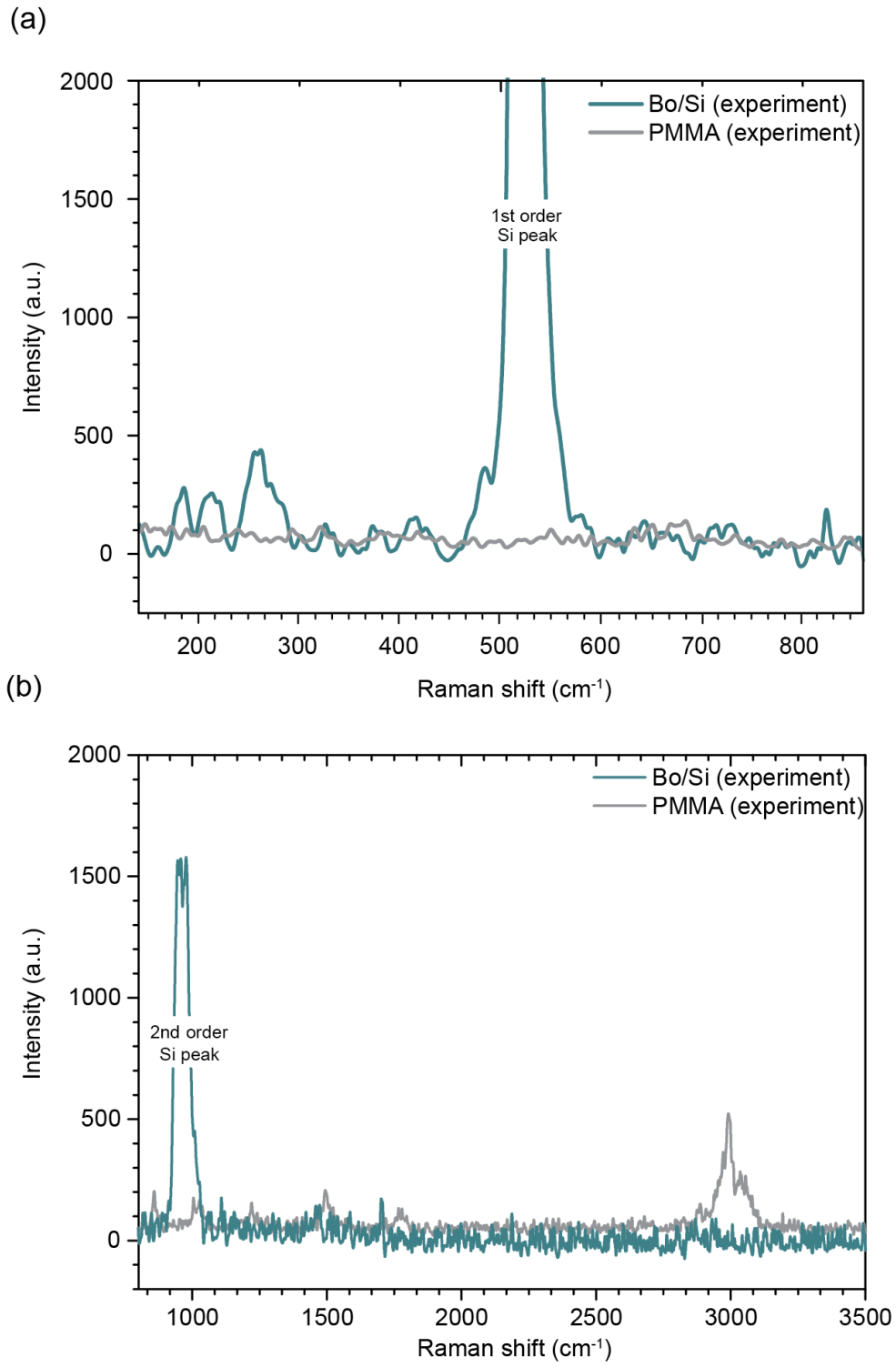

Figure 8.4 Comparison of Raman spectra of Bo/Si and a reference PMMA sample for two different spectral ranges: a) from 190 up to 800 cm^{-1} and b) from 801 up to 3500 cm^{-1}. The spectra of both samples have been measured under the same experimental conditions. Taken from [125].

Our results confirm that, if present, PMMA residues are not visible in the Raman spectrum on post-transfer Bo/Si sample. Nevertheless, if such PMMA chain residues exist on the surface of borophene they do not significantly change their properties. During preparation of this sample more care could be taken to ensure a clean surface. Such procedures would include leaving the sample in acetone over the span of 24 hours; this would help remove PMMA and after annealing the sample in vacuum or inert gas at around 135 °C for a couple of hours. If we want to further protect the sample from ambient contaminations in the air we could capped it with a few-layer thick h-BN. [125]

8.4 Conclusion

In collaboration with colleagues from our group, we investigated borophene grown in UHV conditions on Ir(111) after which it was transferred to Si wafer. First confirmation of successful transfer was done with AFM, SEM and an optical microscope which revealed that almost a millimeter-sized borophene flake had been transferred. Our focus was optical characterization of borophene before and after the transfer and consequent comparison with DFT calculations. As borophene is not a semiconductor we could only observe Raman peaks associated with borophene. We were able to measure the Raman spectrum of borophene on Ir(111) due to it being physisabsorbed on the metallic Ir(111) surface. After the transfer we repeated Raman spectroscopy on the millimeter-sized borophene flake. In addition to Raman peaks from borophene, a very strong Si peak from the Si wafer appeared. Comparing the experimental results with the calculated DFT Raman density of states for freestanding borophene we obtained good agreement with a few minor quantitative differences. The energy shift and intensity differences come from different dielectric environments, i.e., different substrates (Ir(111), Si wafer and freestanding), chemical modulation during transfer and strain release after the transfer.

Calculated phonon energies based on DFT calculations of a freestanding Bo χ_6 polymorph are in good agreement with both experimental Raman spectra which indicates moderate binding of Bo to the examined substrates.

Our results represent a major step towards further utilization of Bo in promising applications, e.g., energy storage, optoelectronic and flexible electronic devices, where physical manipulation of 2D boron sheets will be essential. [125]

9 Conclusion

Two-dimensional materials usually exhibit strong light-matter interactions and results presented here utilize this interaction for investigation of four different layered materials in order to gain fundamental knowledge on physical processes and mechanisms in such systems and also to emphasize possible technological applications. Extensive efforts have been made not only to investigate their optical properties but also to relate obtained results with sample growth procedure, post-growth transfer procedures, its crystal morphology and layer orientations. Experimental results on four different systems are presented, including MoS_2/graphene heterostructure, WS_2/MoS_2/graphene heterostructure, WS_2 monolayers and bilayers and borophene. Thesis begins with reviewing layered materials investigated here (Chapter 2) and the main spectroscopic features usually present in photoexcited samples (Chapter 3). Chapter 4 focuses on sample growth and preparation techniques which were used to fabricate samples investigated here, as well as on various experimental techniques that we employed for sample characterisation and for the measurements. Later Chapters (5-8) include experimental results on four different material systems; each Chapter gives a summary of the key findings and outlook for future exploration of the presented 2D system.

In Chapter 5 we present the results on MoS_2/graphene heterostructure. HS is synthesized on a macroscopic graphene sheet decorated with MBE grown monolayer MoS_2 islands of tens of nm lateral size, which cover a total of 22% of the graphene area. With subsequent successful transfer on Si wafer, it is laying the ground for the future high-quality TMDs and related heterostructures sample synthesis and their utilization in optoelectronic devices. The success of the transfer procedure lies in the transfer of the macroscopic, 6 mm in diameter, graphene layer covered with nanometer sized MoS_2 islands that has maintained the intrinsic structural and electronic properties of the MBE grown layers. Both the growth and the transfer procedure successful outcomes have been confirmed and supported by detailed sample characterisation prior to and after the transfer procedure. We have measured photoluminescence spectra that showed characteristic exciton emission lines with the emission energies comparable with the literature values where the exciton A line intensity was slightly influenced by the graphene presence and related interlayer charge transfer. The exciton A linewidth is in good agreement with the high quality mechanically exfoliated samples, confirming the long exciton lifetimes. The Raman spectrum of MoS_2/graphene heterostructure on Si substrate confirms not only the

presence of the heterostructure but also its post-transfer high quality. The Raman mode peak positions, their linewidths and relative peak intensities are in excellent agreement with the exfoliated samples indicating low defect density and high sample quality. We believe this lays the groundwork for future high-quality clean TMD-related HS synthesis and transfer. This procedure allows the harnessing of the high quality samples and control over their morphological and functional properties afforded by MBE growth procedure independently of the substrate requirements for the application in (quantum) photonic and (opto)electronic devices.

Chapter 6 presents extended research results compared to the previous chapter, where we investigate a more complex system: UHV grown WS_2/MoS_2/graphene heterostructure by adding an additional TMD layer on the previous structure. Synthesis and i*n-situ* characterization with LEED and STM revealed vertical and lateral heterostructures of WS_2/MoS_2 on a complete graphene layer over the Ir(111) sample. Monolayer MoS_2 islands cover 33% of the graphene ground layer and WS_2 77%. WS_2 grows mostly directly on graphene, as lateral HS (55.6%) while 25.4% as second TMD layer, on MoS_2 islands creating vertical heterostructure. Ambient characterization with AFM on Ir(111) reveals preserved sample structure and morphology indicating room condition stability even after a longer time period. Using the same electrochemical delamination transfer procedure, the sample was partially transferred to Si wafer. Some parts of the sample had contaminations and corrugations which hindered optical response from WS_2/MoS_2/graphene heterostructure. Nevertheless, there are substantial parts of the sample that were completely transferred, without any contaminations and with high-quality optical signals from the heterostructure. Raman spectroscopy confirmed the presence of WS_2, MoS_2 and graphene after the transfer. Using hyperspectral interferometer imaging we reveal homogenous intensity and spectral response from the high-quality sample parts. Obtained photoluminescence spectra show quenching of the exciton signal at 617.5 nm and 671.6 nm that corresponds to WS_2/MoS_2 emission lines. All three applied optical techniques confirmed the evidence of charge transfer from WS_2 to MoS_2 due to Type-II band alignment and from WS_2 to graphene. Efficient charge transfer, as we observe it, is a direct confirmation of a pristine interface between layers of the heterostructure indicating a non-perturbing nature of the transfer process where the sample maintains intrinsic structural and electronic properties of the MBE grown layers. Comparing STS measurements at 125 K with temperature dependent PL measurements at comparable temperature we can calculate exciton binding energy of MoS_2 600 meV is in agreement with previous results in Chapter 5 and literature. However, binding energy

for WS_2 is lower due to the fast phonon mediated charge transfer. From exciton peak position temperature dependence we can extract energy from the electron-phonon coupling of 47.4 meV (382.3 cm^{-1}) and 42.7 meV (344.4 cm^{-1}) which are in good agreement with the main phonon modes of WS_2 and MoS_2, respectively. Electron-phonon coupling reveals phonon mediated temperature dependent semiconductor bandgap reduction.

In the first part of Chapter 7 we have presented results of an investigation of WS_2 twisted bilayers of AA (0 degree) and AB (60 degree) stacking under applied uniaxial tensile strain via 2-point and 3-point bending setups. Analyzing the statistics on flakes of AA and AB stacking we get the median value of strain gauge factor of - 34,77 meV/% and -37,76 meV/%, respectively. These values are in good agreement with calculated ones for AA stacking of -56,45 meV/% and -60,25 meV/% for AB stacking. Comparing calculated values with statistically analyzed experimental data we conclude that theoretical values set the upper value for realistic systems experimental data. In addition to energy shifts of excitons, strain can also have an influence on the absorption line FWHM. Although the monolayer WS_2 was not showing any FWHM strain dependence, in the bilayer WS_2 due to its indirect bandgap nature phonons play role in exciton-scattering processes which are influenced by strain and, thus, we showed how FWHM can be controlled with the strain. In the second part of Chapter 7 non-collinear we have investigated temporal dynamics under strain in CVD grown monolayer WS_2 samples. Differential transmission spectra taken at 300 fs upon photoexcitation show 15 nm different exciton resonance energy for two samples at initial strain, which is the result of differences in growth conditions and possible defects. Experimental results reveal different decay dynamics: single exponential decay in sample 1 with the decay time on the order of 1 ps and double exponential decay dynamics with fast component of the order of 0.3 ps and a slow component in few ps time for sample 2. Slow decay rates increase with the strain. Fast decay times in sample 1 and 2 have almost the same strain dependence of around 55 fs/% while in sample slow decay time has three orders of magnitude bigger dependence of 26 ps/%. We have shown that with strain we are able to control exciton lifetimes. This opens a new horizon for application in photo-voltaics where short-lived excitons are more favorable while long-lived excitons are more beneficial for lasers with ultrashort pulses.

In final Chapter 8, we investigated borophene grown in UHV conditions on Ir(111) and its subsequent transfer to Si wafer. Post-transfer characterization with AFM, SEM and an optical microscope revealed that almost a millimeter-sized borophene flake had been transferred to Si

wafer. Our focus was the optical characterization of borophene before and after the transfer and consequent comparison with DFT calculations. We were able to measure the Raman spectrum of borophene on Ir(111) due to it being physisabsorbed on the metallic Ir(111) surface. After the transfer we repeated Raman spectroscopy on the millimeter-sized borophene flake. Comparing the experimental results with the calculated DFT Raman density of states results for freestanding borophene, we obtained good agreement with a few minor quantitative differences. The energy shift and intensity differences come from different dielectric environments, i.e., different substrates (Ir(111), Si wafer and freestanding), chemical modulation during transfer and strain release after the transfer. Calculated phonon energies based on DFT calculations of a freestanding Bo χ_6 polymorph are in good agreement with both experimental Raman spectra which indicates moderate binding of Bo to the examined substrates. Our results represent a major step towards further utilization of Bo in promising applications, e.g., energy storage, optoelectronic and flexible electronic devices, where physical manipulation of 2D boron sheets will be essential.

Bibliography

[1] R.P. Feynman, There's Plenty of Room at the Bottom, 1960.

[2] Z.I. Alferov, Nobel Lecture: The double heterostructure concept and its applications in physics, electronics, and technology, Rev Mod Phys. 73 (2001) 767. https://doi.org/10.1103/RevModPhys.73.767.

[3] Z. Alferov, Heterostructures for optoelectronics: History and modern trends, Proceedings of the IEEE. 101 (2013) 2176–2182. https://doi.org/10.1109/JPROC.2013.2274912.

[4] D.L. Duong, S.J. Yun, Y.H. Lee, Van der Waals Layered Materials: Opportunities and Challenges, ACS Nano. 11 (2017) 11803–11830. https://doi.org/10.1021/ACSNANO.7B07436/ASSET/IMAGES/LARGE/NN-2017-074362_0020.JPEG.

[5] Z. Nan, N. Zhang, Electronic properites of MoS2/MoSe2 van der Waals heterostructures, n.d. https://tel.archives-ouvertes.fr/tel-03185900.

[6] Y. Zhou, C. Duan, Z. Huang, al -, S. Wei, X. Liao, C. Wang, G. Zhao, X. Ke, X. Li, X. Wang, K. Du, Y. Yang Fredrik Liu, P. Hu, J. Zhang, Q. Zhang, M. Hon Samuel Owen, X. Lu, C. Kwan Gan, P. Sengupta, C. Kloc, Q. Xiong, Raman spectroscopy of atomically thin two-dimensional magnetic iron phosphorus trisulfide (FePS3) crystals, 2d Mater. 3 (2016) 031009. https://doi.org/10.1088/2053-1583/3/3/031009.

[7] Y. Yu, F. Yang, X.F. Lu, Y.J. Yan, Y.H. Cho, L. Ma, X. Niu, S. Kim, Y.W. Son, D. Feng, S. Li, S.W. Cheong, X.H. Chen, Y. Zhang, Gate-tunable phase transitions in thin flakes of 1T-TaS2, Nat Nanotechnol. 10 (2015) 270–276. https://doi.org/10.1038/NNANO.2014.323.

[8] W. Ding, J. Zhu, Z. Wang, Y. Gao, D. Xiao, Y. Gu, Z. Zhang, W. Zhu, Prediction of intrinsic two-dimensional ferroelectrics in In2Se3 and other III2-VI3 van der Waals materials, Nature Communications 2017 8:1. 8 (2017) 1–8. https://doi.org/10.1038/ncomms14956.

[9] A.F. Kusmartseva, B. Sipos, H. Berger, L. Forró, E. Tutiš, Pressure Induced Superconductivity in Pristine 1T-TiSe2, Phys Rev Lett. 103 (2009) 236401. https://doi.org/10.1103/PHYSREVLETT.103.236401/FIGURES/4/MEDIUM.

[10] A.K. Geim, I. v. Grigorieva, Van der Waals heterostructures, Nature 2013 499:7459. 499 (2013) 419–425. https://doi.org/10.1038/nature12385.

[11] K.S. Novoselov, A. Mishchenko, A. Carvalho, A.H. Castro Neto, 2D materials and van der Waals heterostructures, Science (1979). 353 (2016). https://doi.org/10.1126/SCIENCE.AAC9439/ASSET/4B54077E-F0A2-4BB2-BFA1-BC557DC78A9D/ASSETS/GRAPHIC/353_AAC9439_F6.JPEG.

[12] S. Wagner, 2D materials for piezoresistive strain gauges and membrane based nanoelectromechanical systems, 2018.

[13] X. Chen, F. Tian, C. Persson, W. Duan, N.X. Chen, Interlayer interactions in graphites, Scientific Reports 2013 3:1. 3 (2013) 1–5. https://doi.org/10.1038/srep03046.

[14] K.S. Novoselov, A.K. Geim, S. v. Morozov, D. Jiang, M.I. Katsnelson, I. v. Grigorieva, S. v. Dubonos, A.A. Firsov, Two-dimensional gas of massless Dirac fermions in graphene, Nature 2005 438:7065. 438 (2005) 197–200. https://doi.org/10.1038/nature04233.

[15] R.R. Nair, P. Blake, A.N. Grigorenko, K.S. Novoselov, T.J. Booth, T. Stauber, N.M.R. Peres, A.K. Geim, Fine structure constant defines visual transparency of graphene, Science. 320 (2008) 1308. https://doi.org/10.1126/SCIENCE.1156965.

[16] A.J. Mannix, Z. Zhang, N.P. Guisinger, B.I. Yakobson, M.C. Hersam, Borophene as a prototype for synthetic 2D materials development, Nature Nanotechnology 2018 13:6. 13 (2018) 444–450. https://doi.org/10.1038/s41565-018-0157-4.

[17] L. Adamska, S. Sadasivam, J.J. Foley, P. Darancet, S. Sharifzadeh, First-Principles Investigation of Borophene as a Monolayer Transparent Conductor, Journal of Physical Chemistry C. 122 (2018) 4037–4045. https://doi.org/10.1021/ACS.JPCC.7B10197/ASSET/IMAGES/LARGE/JP-2017-10197Y_0003.JPEG.

[18] A.K. Geim, I. v. Grigorieva, Van der Waals heterostructures, Nature. 499 (2013) 419–25. https://doi.org/10.1038/nature12385.

[19] D. Jariwala, V.K. Sangwan, L.J. Lauhon, T.J. Marks, M.C. Hersam, Emerging device applications for semiconducting two-dimensional transition metal dichalcogenides, ACS Nano. 8 (2014) 1102–1120. https://doi.org/10.1021/NN500064S.

[20] K.S. Novoselov, V.I. Fal'Ko, L. Colombo, P.R. Gellert, M.G. Schwab, K. Kim, A roadmap for graphene, Nature 2012 490:7419. 490 (2012) 192–200. https://doi.org/10.1038/nature11458.

[21] C. Lu, S. Yu, K.S. Novoselov, A.H. Castro Neto, Two-dimensional crystals-based heterostructures: materials with tailored properties, Phys Scr. 2012 (2012) 014006. https://doi.org/10.1088/0031-8949/2012/T146/014006.

[22] Q.H. Wang, K. Kalantar-Zadeh, A. Kis, J.N. Coleman, M.S. Strano, Electronics and optoelectronics of two-dimensional transition metal dichalcogenides, Nat Nanotechnol. 7 (2012) 699–712. https://doi.org/10.1038/NNANO.2012.193.

[23] L. Britnell, R.M. Ribeiro, A. Eckmann, R. Jalil, B.D. Belle, A. Mishchenko, Y.J. Kim, R. v. Gorbachev, T. Georgiou, S. v. Morozov, A.N. Grigorenko, A.K. Geim, C. Casiraghi, A.H. Castro Neto, K.S. Novoselov, Strong light-matter interactions in heterostructures of atomically thin films, Science (1979). 340 (2013) 1311–1314. https://doi.org/10.1126/SCIENCE.1235547/SUPPL_FILE/BRITNELL.SM.PDF.

[24] K. Roy, M. Padmanabhan, S. Goswami, T.P. Sai, G. Ramalingam, S. Raghavan, A. Ghosh, Graphene-MoS2 hybrid structures for multifunctional photoresponsive memory devices, Nat. Nanotechnol. 8 (2013) 826–30. https://doi.org/10.1038/nnano.2013.206.

[25] W. Zhang, C.P. Chuu, J.K. Huang, C.H. Chen, M.L. Tsai, Y.H. Chang, C. te Liang, Y.Z. Chen, Y.L. Chueh, J.H. He, M.Y. Chou, L.J. Li, Ultrahigh-Gain Photodetectors Based on Atomically Thin Graphene-MoS2 Heterostructures, Scientific Reports 2014 4:1. 4 (2014) 1–8. https://doi.org/10.1038/srep03826.

[26] Z. Zhang, P. Chen, X. Duan, K. Zang, J. Luo, X. Duan, Robust epitaxial growth of two-dimensional heterostructures, multiheterostructures, and superlattices, Science (1979). 357 (2017) 788–92. https://doi.org/10.1126/science.aan6814.

[27] P.K. Sahoo, S. Memaran, Y. Xin, L. Balicas, H.R. Gutiérrez, One-pot growth of two-dimensional lateral heterostructures via sequential edge-epitaxy, Nature. 553 (2018) 63–67. https://doi.org/10.1038/nature25155.

[28] C. Berger, A. Ougazzaden, J. Gigliotti, X. Li, S. Sundaram, D. Deniz, V. Prudkovskiy, J.P. Turmaud, Y. Hu, Y. Hu, F. Fossard, J.S. Mérot, A. Loiseau, G. Patriarche, Highly ordered boron nitride/epigraphene epitaxial films on silicon carbide by lateral epitaxial deposition, ACS Nano. 14 (2020) 12962–71. https://doi.org/10.1021/acsnano.0c04164.

[29] J. Sitek, I. Pasternak, K. Czerniak-ŁOsiewicz, M. Swiniarski, P.P. Michałowski, C. McAleese, X. Wang, B.R. Conran, K. Wilczynski, M. Macha, A. Radenovic, M. Zdrojek, W. Strupinski, Three-step, transfer-free growth of MoS2/WS2/graphene vertical van der Waals heterostructure, 2d Mater. 9 (2022) 025030. https://doi.org/10.1088/2053-1583/AC5F6D.

[30] I. Pelant, J. Valenta, Luminescence Spectroscopy of Semiconductors, Luminescence Spectroscopy of Semiconductors. 9780199588336 (2012) 1–560. https://doi.org/10.1093/ACPROF:OSO/9780199588336.001.0001.

[31] A. Ramasubramaniam, Large excitonic effects in monolayers of molybdenum and tungsten dichalcogenides, Phys Rev B Condens Matter Mater Phys. 86 (2012) 115409. https://doi.org/10.1103/PHYSREVB.86.115409/FIGURES/4/MEDIUM.

[32] D.Y. Qiu, F.H. da Jornada, S.G. Louie, Optical spectrum of MoS2: Many-body effects and diversity of exciton states, Phys Rev Lett. 111 (2013). https://doi.org/10.1103/PHYSREVLETT.111.216805.

[33] H.P. Komsa, A. v. Krasheninnikov, Effects of confinement and environment on the electronic structure and exciton binding energy of MoS2 from first principles, Phys Rev B Condens Matter Mater Phys. 86 (2012). https://doi.org/10.1103/PHYSREVB.86.241201.

[34] T.C. Berkelbach, M.S. Hybertsen, D.R. Reichman, Theory of neutral and charged excitons in monolayer transition metal dichalcogenides, Phys Rev B Condens Matter Mater Phys. 88 (2013) 045318. https://doi.org/10.1103/PHYSREVB.88.045318/FIGURES/3/MEDIUM.

[35] K.S. Thygesen, Calculating excitons, plasmons, and quasiparticles in 2D materials and van der Waals heterostructures, 2d Mater. 4 (2017) 022004. https://doi.org/10.1088/2053-1583/AA6432.

[36] A. Chernikov, T.C. Berkelbach, H.M. Hill, A. Rigosi, Y. Li, O.B. Aslan, D.R. Reichman, M.S. Hybertsen, T.F. Heinz, Exciton binding energy and nonhydrogenic Rydberg series in monolayer WS2, Phys Rev Lett. 113 (2014). https://doi.org/10.1103/PhysRevLett.113.076802.

[37] Z. Ye, T. Cao, K. O'Brien, H. Zhu, X. Yin, Y. Wang, S.G. Louie, X. Zhang, Probing excitonic dark states in single-layer tungsten disulphide, Nature 2014 513:7517. 513 (2014) 214–218. https://doi.org/10.1038/nature13734.

[38] M.M. Ugeda, A.J. Bradley, S.F. Shi, F.H. da Jornada, Y. Zhang, D.Y. Qiu, W. Ruan, S.K. Mo, Z. Hussain, Z.X. Shen, F. Wang, S.G. Louie, M.F. Crommie, Giant bandgap renormalization and excitonic effects in a monolayer transition metal dichalcogenide semiconductor, Nat Mater. 13 (2014) 1091–1095. https://doi.org/10.1038/NMAT4061.

[39] A. v. Stier, N.P. Wilson, G. Clark, X. Xu, S.A. Crooker, Probing the Influence of Dielectric Environment on Excitons in Monolayer WSe2: Insight from High Magnetic Fields, Nano Lett. 16 (2016) 7054–7060. https://doi.org/10.1021/ACS.NANOLETT.6B03276/ASSET/IMAGES/LARGE/NL-2016-03276J_0004.JPEG.

[40] K. He, N. Kumar, L. Zhao, Z. Wang, K.F. Mak, H. Zhao, J. Shan, Tightly bound excitons in monolayer WSe2, Phys Rev Lett. 113 (2014) 026803. https://doi.org/10.1103/PHYSREVLETT.113.026803/FIGURES/4/MEDIUM.

[41] T. Low, A. Chaves, J.D. Caldwell, A. Kumar, N.X. Fang, P. Avouris, T.F. Heinz, F. Guinea, L. Martin-Moreno, F. Koppens, Polaritons in layered two-dimensional materials, Nat Mater. 16 (2017) 182–194. https://doi.org/10.1038/NMAT4792.

[42] S. Latini, T. Olsen, K.S. Thygesen, Excitons in van der Waals heterostructures: The important role of dielectric screening, Phys Rev B Condens Matter Mater Phys. 92 (2015) 245123. https://doi.org/10.1103/PHYSREVB.92.245123/FIGURES/13/MEDIUM.

[43] A. Raja, A. Chaves, J. Yu, G. Arefe, H.M. Hill, A.F. Rigosi, T.C. Berkelbach, P. Nagler, C. Schüller, T. Korn, C. Nuckolls, J. Hone, L.E. Brus, T.F. Heinz, D.R. Reichman, A. Chernikov, Coulomb engineering of the bandgap and excitons in two-dimensional materials, Nat Commun. 8 (2017). https://doi.org/10.1038/ncomms15251.

[44] T. Mueller, E. Malic, Exciton physics and device application of two-dimensional transition metal dichalcogenide semiconductors, NPJ 2D Mater Appl. 2 (2018). https://doi.org/10.1038/s41699-018-0074-2.

[45] M. Sahin, F. Koç, A model for the recombination and radiative lifetime of trions and biexcitons in spherically shaped semiconductor nanocrystals, Appl Phys Lett. 102 (2013) 183103. https://doi.org/10.1063/1.4804183.

[46] A. Steinhoff, M. Florian, A. Singh, K. Tran, M. Kolarczik, S. Helmrich, A.W. Achtstein, U. Woggon, N. Owschimikow, F. Jahnke, X. Li, Biexciton fine structure in monolayer transition metal dichalcogenides, Nature Physics 2018 14:12. 14 (2018) 1199–1204. https://doi.org/10.1038/s41567-018-0282-x.

[47] X. Zheng, X. Zhang, Excitons in Two-Dimensional Materials, Advances in Condensed-Matter and Materials Physics - Rudimentary Research to Topical Technology. (2019). https://doi.org/10.5772/INTECHOPEN.90042.

[48] Y. You, X.X. Zhang, T.C. Berkelbach, M.S. Hybertsen, D.R. Reichman, T.F. Heinz, Observation of biexcitons in monolayer WSe2, Nature Physics 2014 11:6. 11 (2015) 477–481. https://doi.org/10.1038/nphys3324.

[49] D.K. Zhang, D.W. Kidd, K. Varga, Excited Biexcitons in Transition Metal Dichalcogenides, Nano Lett. 15 (2015) 7002–7005. https://doi.org/10.1021/ACS.NANOLETT.5B03009/ASSET/IMAGES/NL-2015-03009P_M006.GIF.

[50] F. Cadiz, S. Tricard, M. Gay, D. Lagarde, G. Wang, C. Robert, P. Renucci, B. Urbaszek, X. Marie, Well separated trion and neutral excitons on superacid treated MoS2 monolayers, Appl Phys Lett. 108 (2016) 251106. https://doi.org/10.1063/1.4954837.

[51] F. Gao, Y. Gong, M. Titze, R. Almeida, P.M. Ajayan, H. Li, Valley trion dynamics in monolayer MoSe2, Phys Rev B. 94 (2016) 245413. https://doi.org/10.1103/PHYSREVB.94.245413/FIGURES/5/MEDIUM.

[52] G. Wang, L. Bouet, D. Lagarde, M. Vidal, A. Balocchi, T. Amand, X. Marie, B. Urbaszek, Valley dynamics probed through charged and neutral exciton emission in monolayer WSe2, Phys Rev B

Condens Matter Mater Phys. 90 (2014) 075413. https://doi.org/10.1103/PHYSREVB.90.075413/FIGURES/4/MEDIUM.

[53] K.F. Mak, K.L. McGill, J. Park, P.L. McEuen, The valley hall effect in MoS2 transistors, Science (1979). 344 (2014) 1489–1492. https://doi.org/10.1126/SCIENCE.1250140/SUPPL_FILE/MAK-SM.PDF.

[54] H.S. Lee, M.S. Kim, H. Kim, Y.H. Lee, Identifying multiexcitons in Mo S2 monolayers at room temperature, Phys Rev B. 93 (2016) 140409. https://doi.org/10.1103/PHYSREVB.93.140409/FIGURES/4/MEDIUM.

[55] C. Casiraghi, A. Hartschuh, E. Lidorikis, H. Qian, H. Harutyunyan, T. Gokus, K.S. Novoselov, A.C. Ferrari, Rayleigh imaging of graphene and graphene layers, Nano Lett. 7 (2007) 2711–2717. https://doi.org/10.1021/NL071168M/ASSET/IMAGES/LARGE/NL071168MF00009.JPEG.

[56] A.C. Ferrari, J.C. Meyer, V. Scardaci, C. Casiraghi, M. Lazzeri, F. Mauri, S. Piscanec, D. Jiang, K.S. Novoselov, S. Roth, A.K. Geim, Raman spectrum of graphene and graphene layers, Phys Rev Lett. 97 (2006) 187401. https://doi.org/10.1103/PHYSREVLETT.97.187401/FIGURES/3/MEDIUM.

[57] C. Stampfer, F. Molitor, D. Graf, K. Ensslin, A. Jungen, C. Hierold, L. Wirtz, Raman imaging of doping domains in graphene on SiO2, Appl Phys Lett. 91 (2007) 241907. https://doi.org/10.1063/1.2816262.

[58] Y.Y. Wang, Z.H. Ni, T. Yu, Z.X. Shen, H.M. Wang, Y.H. Wu, W. Chen, A.T.S. Wee, Raman studies of monolayer graphene: The substrate effect, Journal of Physical Chemistry C. 112 (2008) 10637–10640. https://doi.org/10.1021/JP8008404/ASSET/IMAGES/LARGE/JP-2008-008404_0004.JPEG.

[59] J.U. Lee, D. Yoon, H. Kim, S.W. Lee, H. Cheong, Thermal conductivity of suspended pristine graphene measured by Raman spectroscopy, Phys Rev B Condens Matter Mater Phys. 83 (2011) 081419. https://doi.org/10.1103/PHYSREVB.83.081419/FIGURES/3/MEDIUM.

[60] J. Zabel, R.R. Nair, A. Ott, T. Georgiou, A.K. Geim, K.S. Novoselov, C. Casiraghi, Raman spectroscopy of graphene and bilayer under biaxial strain: Bubbles and balloons, Nano Lett. 12 (2012) 617–621. https://doi.org/10.1021/NL203359N/SUPPL_FILE/NL203359N_SI_001.PDF.

[61] A.C. Ferrari, Raman spectroscopy of graphene and graphite: Disorder, electron-phonon coupling, doping and nonadiabatic effects, Solid State Commun. 143 (2007) 47–57. https://doi.org/10.1016/J.SSC.2007.03.052.

[62] J.E. Lee, G. Ahn, J. Shim, Y.S. Lee, S. Ryu, Optical separation of mechanical strain from charge doping in graphene, Nature Communications 2012 3:1. 3 (2012) 1–8. https://doi.org/10.1038/ncomms2022.

[63] TUINSTRA F, KOENIG JL, Raman Spectrum of Graphite, J Chem Phys. 53 (2003) 1126. https://doi.org/10.1063/1.1674108.

[64] R.J. Nemanich, S.A. Solin, First- and second-order Raman scattering from finite-size crystals of graphite, Phys Rev B. 20 (1979) 392–401. https://doi.org/10.1103/PHYSREVB.20.392.

[65] A.C. Ferrari, D.M. Basko, Raman spectroscopy as a versatile tool for studying the properties of graphene, Nat Nanotechnol. 8 (2013) 235–246. https://doi.org/10.1038/NNANO.2013.46.

[66] S. Kataria, S. Wagner, T. Cusati, A. Fortunelli, G. Iannaccone, H. Pandey, G. Fiori, M.C. Lemme, S. Kataria, S. Wagner, H. Pandey, M.C. Lemme Graphene Based Nanotechnology, A. Fortunelli, M.C. Lemme, Growth-Induced Strain in Chemical Vapor Deposited Monolayer MoS2: Experimental and

Theoretical Investigation, Adv Mater Interfaces. 4 (2017) 1700031. https://doi.org/10.1002/ADMI.201700031.

[67] R. Samnakay, C. Jiang, S.L. Rumyantsev, M.S. Shur, A.A. Balandin, Selective chemical vapor sensing with few-layer MoS2 thin-film transistors: Comparison with graphene devices, Appl Phys Lett. 106 (2015) 023115. https://doi.org/10.1063/1.4905694.

[68] R. Frisenda, M. Drüppel, R. Schmidt, S. Michaelis de Vasconcellos, D. Perez de Lara, R. Bratschitsch, M. Rohlfing, A. Castellanos-Gomez, Biaxial strain tuning of the optical properties of single-layer transition metal dichalcogenides, Npj 2D Materials and Applications 2017 1:1. 1 (2017) 1–7. https://doi.org/10.1038/s41699-017-0013-7.

[69] S. Bertolazzi, J. Brivio, A. Kis, Stretching and breaking of ultrathin MoS 2, ACS Nano. 5 (2011) 9703–9709. https://doi.org/10.1021/NN203879F/SUPPL_FILE/NN203879F_SI_001.PDF.

[70] J.N. Coleman, M. Lotya, A. O'Neill, S.D. Bergin, P.J. King, U. Khan, K. Young, A. Gaucher, S. De, R.J. Smith, I. v. Shvets, S.K. Arora, G. Stanton, H.Y. Kim, K. Lee, G.T. Kim, G.S. Duesberg, T. Hallam, J.J. Boland, J.J. Wang, J.F. Donegan, J.C. Grunlan, G. Moriarty, A. Shmeliov, R.J. Nicholls, J.M. Perkins, E.M. Grieveson, K. Theuwissen, D.W. McComb, P.D. Nellist, V. Nicolosi, Two-dimensional nanosheets produced by liquid exfoliation of layered materials, Science (1979). 331 (2011) 568–571. https://doi.org/10.1126/SCIENCE.1194975/SUPPL_FILE/COLEMAN.SOM.PDF.

[71] Semiconductors and Semimetals, Volume 37 - 1st Edition, (n.d.). https://www.elsevier.com/books/semiconductors-and-semimetals/faber/978-0-12-752137-4 (accessed July 12, 2022).

[72] X. Li, M. Sun, C. Shan, Q. Chen, X. Wei, Mechanical Properties of 2D Materials Studied by In Situ Microscopy Techniques, Adv Mater Interfaces. 5 (2018) 1701246. https://doi.org/10.1002/ADMI.201701246.

[73] J. Xiang, W. Wang, L. Feng, C. Feng, M. Huang, P. Liu, X.F. Ren, B. Xiang, A Biaxial Strain Sensor Using a Single MoS2 Grating, Nanoscale Res Lett. 16 (2021) 1–7. https://doi.org/10.1186/S11671-021-03493-3/FIGURES/4.

[74] C. Palacios-Berraquero, D.M. Kara, A.R.P. Montblanch, M. Barbone, P. Latawiec, D. Yoon, A.K. Ott, M. Loncar, A.C. Ferrari, M. Atatüre, Large-scale quantum-emitter arrays in atomically thin semiconductors, Nature Communications 2017 8:1. 8 (2017) 1–6. https://doi.org/10.1038/ncomms15093.

[75] P. Bettotti, Hybrid Materials for Integrated Photonics, Advances in Optics. 2014 (2014) 1–24. https://doi.org/10.1155/2014/891395.

[76] O. Lopez-Sanchez, D. Lembke, M. Kayci, A. Radenovic, A. Kis, Ultrasensitive photodetectors based on monolayer MoS2, Nature Nanotechnology 2013 8:7. 8 (2013) 497–501. https://doi.org/10.1038/nnano.2013.100.

[77] O. Lopez-Sanchez, E. Alarcon Llado, V. Koman, A. Fontcuberta I Morral, A. Radenovic, A. Kis, Light generation and harvesting in a van der waals heterostructure, ACS Nano. 8 (2014) 3042–3048. https://doi.org/10.1021/NN500480U/ASSET/IMAGES/LARGE/NN-2014-00480U_0004.JPEG.

[78] A. Pospischil, M.M. Furchi, T. Mueller, Solar-energy conversion and light emission in an atomic monolayer p–n diode, Nature Nanotechnology 2014 9:4. 9 (2014) 257–261. https://doi.org/10.1038/nnano.2014.14.

[79] D. Costanzo, S. Jo, H. Berger, A.F. Morpurgo, Gate-induced superconductivity in atomically thin MoS2 crystals, Nat Nanotechnol. 11 (2016) 339–344. https://doi.org/10.1038/NNANO.2015.314.

[80] Y.C. Lin, D.O. Dumcenco, Y.S. Huang, K. Suenaga, Atomic mechanism of the semiconducting-to-metallic phase transition in single-layered MoS2, Nat Nanotechnol. 9 (2014) 391–396. https://doi.org/10.1038/NNANO.2014.64.

[81] S. Song, D.H. Keum, S. Cho, D. Perello, Y. Kim, Y.H. Lee, Room Temperature Semiconductor-Metal Transition of MoTe2 Thin Films Engineered by Strain, Nano Lett. 16 (2016) 188–193. https://doi.org/10.1021/ACS.NANOLETT.5B03481.

[82] S. Cho, S.H. Kang, H.S. Yu, H.W. Kim, W. Ko, S.W. Hwang, W.H. Han, D.H. Choe, Y.H. Jung, K.J. Chang, Y.H. Lee, H. Yang, S.W. Kim, Te vacancy-driven superconductivity in orthorhombic molybdenum ditelluride, 2d Mater. 4 (2017) 021030. https://doi.org/10.1088/2053-1583/AA735E.

[83] D.C. Elias, R.R. Nair, T.M.G. Mohiuddin, S. v. Morozov, P. Blake, M.P. Halsall, A.C. Ferrari, D.W. Boukhvalov, M.I. Katsnelson, A.K. Geim, K.S. Novoselov, Control of graphene's properties by reversible hydrogenation: Evidence for graphane, Science (1979). 323 (2009) 610–613. https://doi.org/10.1126/SCIENCE.1167130/SUPPL_FILE/ELIAS-SOM.PDF.

[84] K.S. Novoselov, A.K. Geim, S. v. Morozov, D. Jiang, Y. Zhang, S. v. Dubonos, I. v. Grigorieva, A.A. Firsov, Electric field in atomically thin carbon films, Science (1979). 306 (2004) 666–9. https://doi.org/10.1126/science.1102896.

[85] F. Ceballos, H. Zhao, F. Ceballos, H. Zhao, Ultrafast Laser Spectroscopy of Two-Dimensional Materials Beyond Graphene, Adv Funct Mater. 27 (2017) 1604509. https://doi.org/10.1002/ADFM.201604509.

[86] S.M. Pumera, Z. Sofer, M. Pumera, Z.K. Sofer, Towards stoichiometric analogues of graphene: graphane, fluorographene, graphol, graphene acid and others, Chem Soc Rev. 46 (2017) 4450–4463. https://doi.org/10.1039/C7CS00215G.

[87] Y. Chen, C. Chen, R. Kealhofer, H. Liu, Z. Yuan, L. Jiang, J. Suh, J. Park, C. Ko, H.S. Choe, J. Avila, M. Zhong, Z. Wei, J. Li, S. Li, H. Gao, Y. Liu, J. Analytis, Q. Xia, M.C. Asensio, J. Wu, Black Arsenic: A Layered Semiconductor with Extreme In-Plane Anisotropy, Advanced Materials. 30 (2018). https://doi.org/10.1002/ADMA.201800754.

[88] L.C. Gomes, A. Carvalho, Phosphorene analogues: Isoelectronic two-dimensional group-IV monochalcogenides with orthorhombic structure, Phys Rev B Condens Matter Mater Phys. 92 (2015) 085406. https://doi.org/10.1103/PHYSREVB.92.085406/FIGURES/6/MEDIUM.

[89] J.O. Island, A.J. Molina-Mendoza, M. Barawi, R. Biele, E. Flores, J.M. Clamagirand, J.R. Ares, C. Sánchez, H.S.J. van der Zant, R. D'Agosta, I.J. Ferrer, A. Castellanos-Gomez, Electronics and optoelectronics of quasi-1D layered transition metal trichalcogenides, 2d Mater. 4 (2017) 022003. https://doi.org/10.1088/2053-1583/AA6CA6.

[90] J.A. Silva-Guillén, E. Canadell, P. Ordejón, F. Guinea, R. Roldán, Anisotropic features in the electronic structure of the two-dimensional transition metal trichalcogenide TiS3: electron doping and plasmons, 2d Mater. 4 (2017) 025085. https://doi.org/10.1088/2053-1583/AA6B92.

[91] L. Li, W. Wang, P. Gong, X. Zhu, B. Deng, X. Shi, G. Gao, H. Li, T. Zhai, 2D GeP: An Unexploited Low-Symmetry Semiconductor with Strong In-Plane Anisotropy, Advanced Materials. 30 (2018) 1706771. https://doi.org/10.1002/ADMA.201706771.

[92] F. Lédée, G. Trippé-Allard, H. Diab, P. Audebert, D. Garrot, J.S. Lauret, E. Deleporte, Fast growth of monocrystalline thin films of 2D layered hybrid perovskite, CrystEngComm. 19 (2017) 2598–2602. https://doi.org/10.1039/C7CE00240H.

[93] K. Tran, G. Moody, F. Wu, X. Lu, J. Choi, K. Kim, A. Rai, D.A. Sanchez, J. Quan, A. Singh, J. Embley, A. Zepeda, M. Campbell, T. Autry, T. Taniguchi, K. Watanabe, N. Lu, S.K. Banerjee, K.L. Silverman, S. Kim, E. Tutuc, L. Yang, A.H. MacDonald, X. Li, Evidence for moiré excitons in van der Waals heterostructures, Nature 2019 567:7746. 567 (2019) 71–75. https://doi.org/10.1038/s41586-019-0975-z.

[94] A. Castellanos-Gomez, L. Vicarelli, E. Prada, J.O. Island, K.L. Narasimha-Acharya, S.I. Blanter, D.J. Groenendijk, M. Buscema, G.A. Steele, J. v. Alvarez, H.W. Zandbergen, J.J. Palacios, H.S.J. van der Zant, Isolation and characterization of few-layer black phosphorus, 2d Mater. 1 (2014) 025001. https://doi.org/10.1088/2053-1583/1/2/025001.

[95] H. Liu, A.T. Neal, Z. Zhu, Z. Luo, X. Xu, D. Tománek, P.D. Ye, Phosphorene: An unexplored 2D semiconductor with a high hole mobility, ACS Nano. 8 (2014) 4033–4041. https://doi.org/10.1021/NN501226Z/SUPPL_FILE/NN501226Z_SI_001.PDF.

[96] R.W. Keyes, The Electrical Properties of Black Phosphorus, Physical Review. 92 (1953) 580. https://doi.org/10.1103/PhysRev.92.580.

[97] H. Asahina, Y. Maruyama, A. Morita, Optical reflectivity and band structure of black phosphorus, Physica B+C. 117–118 (1983) 419–421. https://doi.org/10.1016/0378-4363(83)90546-6.

[98] K.F. Mak, C. Lee, J. Hone, J. Shan, T.F. Heinz, Atomically thin MoS2: a new direct-gap semiconductor, Phys. Rev. Lett. 105 (2010) 2–5. https://doi.org/10.1103/physrevlett.105.136805.

[99] A. Splendiani, L. Sun, Y. Zhang, T. Li, J. Kim, C.Y. Chim, G. Galli, F. Wang, Emerging photoluminescence in monolayer MoS2, Nano Lett. 10 (2010) 1271–1275. https://doi.org/10.1021/NL903868W.

[100] Q.H. Wang, K. Kalantar-Zadeh, A. Kis, J.N. Coleman, M.S. Strano, Electronics and optoelectronics of two-dimensional transition metal dichalcogenides, Nature Nanotechnology 2012 7:11. 7 (2012) 699–712. https://doi.org/10.1038/nnano.2012.193.

[101] H.R. Gutiérrez, N. Perea-López, A.L. Elías, A. Berkdemir, B. Wang, R. Lv, F. López-Urías, V.H. Crespi, H. Terrones, M. Terrones, Extraordinary room-temperature photoluminescence in triangular WS2 monolayers, Nano Lett. 13 (2013) 3447–3454. https://doi.org/10.1021/NL3026357.

[102] G. Eda, H. Yamaguchi, D. Voiry, T. Fujita, M. Chen, M. Chhowalla, Photoluminescence from chemically exfoliated MoS 2, Nano Lett. 11 (2011) 5111–5116. https://doi.org/10.1021/NL201874W/SUPPL_FILE/NL201874W_SI_001.PDF.

[103] R.J. Toh, Z. Sofer, J. Luxa, D. Sedmidubský, M. Pumera, 3R phase of MoS2 and WS2 outperforms the corresponding 2H phase for hydrogen evolution, Chemical Communications. 53 (2017) 3054–3057. https://doi.org/10.1039/C6CC09952A.

[104] H. Zeng, X. Cui, An optical spectroscopic study on two-dimensional group-VI transition metal dichalcogenides, Chem Soc Rev. 44 (2015) 2629–2642. https://doi.org/10.1039/C4CS00265B.

[105] S. Manzeli, D. Ovchinnikov, D. Pasquier, O. v. Yazyev, A. Kis, 2D transition metal dichalcogenides, Nature Reviews Materials 2017 2:8. 2 (2017) 1–15. https://doi.org/10.1038/natrevmats.2017.33.

[106] D. Xiao, G. bin Liu, W. Feng, X. Xu, W. Yao, Coupled spin and valley physics in monolayers of MoS 2 and other group-VI dichalcogenides, Phys Rev Lett. 108 (2012) 196802. https://doi.org/10.1103/PHYSREVLETT.108.196802/FIGURES/2/MEDIUM.

[107] K. Kobayashi, J. Yamauchi, Electronic structure and scanning-tunneling-microscopy image of molybdenum dichalcogenide surfaces, Phys Rev B. 51 (1995) 17085. https://doi.org/10.1103/PhysRevB.51.17085.

[108] K.F. Mak, C. Lee, J. Hone, J. Shan, T.F. Heinz, Atomically thin MoS2: A new direct-gap semiconductor, Phys Rev Lett. 105 (2010). https://doi.org/10.1103/PHYSREVLETT.105.136805.

[109] W. Zhao, Z. Ghorannevis, L. Chu, M. Toh, C. Kloc, P.H. Tan, G. Eda, Evolution of electronic structure in atomically thin sheets of ws 2 and wse2, ACS Nano. 7 (2013) 791–797. https://doi.org/10.1021/NN305275H/SUPPL_FILE/NN305275H_SI_001.PDF.

[110] Philipp Tonndorf, Robert Schmidt, Philipp Böttger, Xiao Zhang, Janna Börner, Andreas Liebig, Manfred Albrecht, Christian Kloc, Ovidiu Gordan, Dietrich R. T. Zahn, Steffen Michaelis de Vasconcellos, Rudolf Bratschitsch, Photoluminescence emission and Raman response of monolayer MoS2, MoSe2, and WSe2, Optics Express Vol. 21, Issue 4. (2013) 4908–4916. https://opg.optica.org/oe/fulltext.cfm?uri=oe-21-4-4908&id=249392 (accessed July 12, 2022).

[111] G. bin Liu, W.Y. Shan, Y. Yao, W. Yao, D. Xiao, Three-band tight-binding model for monolayers of group-VIB transition metal dichalcogenides, Phys Rev B Condens Matter Mater Phys. 88 (2013) 085433. https://doi.org/10.1103/PHYSREVB.88.085433/FIGURES/10/MEDIUM.

[112] K. Komider, J.W. González, J. Fernández-Rossier, Large spin splitting in the conduction band of transition metal dichalcogenide monolayers, Phys Rev B Condens Matter Mater Phys. 88 (2013) 245436. https://doi.org/10.1103/PHYSREVB.88.245436/FIGURES/4/MEDIUM.

[113] A.S. Mayorov, R. v. Gorbachev, S. v. Morozov, L. Britnell, R. Jalil, L.A. Ponomarenko, P. Blake, K.S. Novoselov, K. Watanabe, T. Taniguchi, A.K. Geim, Micrometer-scale ballistic transport in encapsulated graphene at room temperature, Nano Lett. 11 (2011) 2396–2399. https://doi.org/10.1021/NL200758B/ASSET/IMAGES/LARGE/NL-2011-00758B_0003.JPEG.

[114] S. v. Morozov, K.S. Novoselov, M.I. Katsnelson, F. Schedin, D.C. Elias, J.A. Jaszczak, A.K. Geim, Giant intrinsic carrier mobilities in graphene and its bilayer, Phys Rev Lett. 100 (2008) 016602. https://doi.org/10.1103/PHYSREVLETT.100.016602/FIGURES/4/MEDIUM.

[115] A.N. Obraztsov, E.A. Obraztsova, A. v. Tyurnina, A.A. Zolotukhin, Chemical vapor deposition of thin graphite films of nanometer thickness, Carbon N Y. 45 (2007) 2017–2021. https://doi.org/10.1016/J.CARBON.2007.05.028.

[116] S. Kataria, S. Wagner, J. Ruhkopf, A. Gahoi, H. Pandey, R. Bornemann, S. Vaziri, A.D. Smith, M. Ostling, M.C. Lemme, Chemical vapor deposited graphene: From synthesis to applications, Physica Status Solidi (a). 211 (2014) 2439–2449. https://doi.org/10.1002/PSSA.201400049.

[117] G. Fiori, F. Bonaccorso, G. Iannaccone, T. Palacios, D. Neumaier, A. Seabaugh, S.K. Banerjee, L. Colombo, Electronics based on two-dimensional materials, Nat Nanotechnol. 9 (2014) 768–779. https://doi.org/10.1038/NNANO.2014.207.

[118] A.K. Geim, K.S. Novoselov, THE RISE OF GRAPHENE, n.d.

[119] C. Lee, X. Wei, J.W. Kysar, J. Hone, Measurement of the elastic properties and intrinsic strength of monolayer graphene, Science (1979). 321 (2008) 385–388. https://doi.org/10.1126/SCIENCE.1157996/SUPPL_FILE/LEE-SOM.PDF.

[120] H.I. Rasool, C. Ophus, W.S. Klug, A. Zettl, J.K. Gimzewski, Measurement of the intrinsic strength of crystalline and polycrystalline graphene, Nature Communications 2013 4:1. 4 (2013) 1–7. https://doi.org/10.1038/ncomms3811.

[121] H. Tomori, A. Kanda, H. Goto, Y. Ootuka, K. Tsukagoshi, S. Moriyama, E. Watanabe, D. Tsuya, Introducing nonuniform strain to graphene using dielectric nanopillars, Applied Physics Express. 4 (2011) 075102. https://doi.org/10.1143/APEX.4.075102/XML.

[122] S. das Sarma, S. Adam, E.H. Hwang, E. Rossi, Electronic transport in two-dimensional graphene, Rev Mod Phys. 83 (2011) 407–470. https://doi.org/10.1103/REVMODPHYS.83.407/FIGURES/38/MEDIUM.

[123] Y. Liu, B. Xie, Z. Zhang, Q. Zheng, Z. Xu, Mechanical properties of graphene papers, J Mech Phys Solids. 60 (2012) 591–605. https://doi.org/10.1016/J.JMPS.2012.01.002.

[124] A.J. Mannix, B. Kiraly, M.C. Hersam, N.P. Guisinger, Synthesis and chemistry of elemental 2D materials, Nat Rev Chem. 1 (2017) 0014. https://doi.org/10.1038/S41570-016-0014.

[125] B. Radatović, V. Jadriško, S. Kamal, M. Kralj, D. Novko, N. Vujičić, M. Petrović, Macroscopic Single-Phase Monolayer Borophene on Arbitrary Substrates, ACS Appl Mater Interfaces. 14 (2022). https://doi.org/10.1021/ACSAMI.2C03678/ASSET/IMAGES/LARGE/AM2C03678_0010.JPEG.

[126] Z. Zhang, Y. Yang, E.S. Penev, B.I. Yakobson, Z. Zhang, Y. Yang, E.S. Penev, B.I. Yakobson, Elasticity, Flexibility, and Ideal Strength of Borophenes, Adv Funct Mater. 27 (2017) 1605059. https://doi.org/10.1002/ADFM.201605059.

[127] Z. Zhang, A.J. Mannix, Z. Hu, B. Kiraly, N.P. Guisinger, M.C. Hersam, B.I. Yakobson, Substrate-Induced Nanoscale Undulations of Borophene on Silver, Nano Lett. 16 (2016) 6622–6627. https://doi.org/10.1021/ACS.NANOLETT.6B03349/ASSET/IMAGES/LARGE/NL-2016-03349M_0004.JPEG.

[128] A.J. Mannix, X.F. Zhou, B. Kiraly, J.D. Wood, D. Alducin, B.D. Myers, X. Liu, B.L. Fisher, U. Santiago, J.R. Guest, M.J. Yacaman, A. Ponce, A.R. Oganov, M.C. Hersam, N.P. Guisinger, Synthesis of borophenes: Anisotropic, two-dimensional boron polymorphs, Science (1979). 350 (2015) 1513–1516. https://doi.org/10.1126/SCIENCE.AAD1080.

[129] B. Feng, J. Zhang, Q. Zhong, W. Li, S. Li, H. Li, P. Cheng, S. Meng, L. Chen, K. Wu, Experimental realization of two-dimensional boron sheets, Nat Chem. 8 (2016) 563–568. https://doi.org/10.1038/NCHEM.2491.

[130] A.J. Mannix, Z. Zhang, N.P. Guisinger, B.I. Yakobson, M.C. Hersam, Borophene as a prototype for synthetic 2D materials development, Nature Nanotechnology 2018 13:6. 13 (2018) 444–450. https://doi.org/10.1038/s41565-018-0157-4.

[131] W. Zhang, C.P. Chuu, J.K. Huang, C.H. Chen, M.L. Tsai, Y.H. Chang, C. te Liang, Y.Z. Chen, Y.L. Chueh, J.H. He, M.Y. Chou, L.J. Li, Ultrahigh-Gain Photodetectors Based on Atomically Thin Graphene-MoS2 Heterostructures, Scientific Reports 2014 4:1. 4 (2014) 1–8. https://doi.org/10.1038/srep03826.

[132] D. Pierucci, H. Henck, C.H. Naylor, H. Sediri, E. Lhuillier, A. Balan, J.E. Rault, Y.J. Dappe, F. Bertran, P. le Fèvre, A.T.C. Johnson, A. Ouerghi, Large area molybdenum disulphide- epitaxial graphene vertical Van der Waals heterostructures, Scientific Reports 2016 6:1. 6 (2016) 1–10. https://doi.org/10.1038/srep26656.

[133] S. Gao, Z. Wang, H. Wang, F. Meng, P. Wang, S. Chen, Y. Zeng, J. Zhao, H. Hu, R. Cao, Z. Xu, Z. Guo, H. Zhang, Graphene/MoS2/Graphene Vertical Heterostructure-Based Broadband Photodetector with High Performance, Adv Mater Interfaces. 8 (2021) 2001730. https://doi.org/10.1002/ADMI.202001730.

[134] I. Lee, W.T. Kang, W.T. Kang, J.E. Kim, Y.R. Kim, Y.R. Kim, U.Y. Won, Y.H. Lee, W.J. Yu, Photoinduced Tuning of Schottky Barrier Height in Graphene/MoS2Heterojunction for Ultrahigh Performance Short Channel Phototransistor, ACS Nano. 14 (2020) 7574–7580. https://doi.org/10.1021/ACSNANO.0C03425.

[135] S. Gao, Z. Wang, H. Wang, F. Meng, P. Wang, S. Chen, Y. Zeng, J. Zhao, H. Hu, R. Cao, Z. Xu, Z. Guo, H. Zhang, Graphene/MoS2/Graphene Vertical Heterostructure-Based Broadband Photodetector with High Performance, Adv Mater Interfaces. 8 (2021). https://doi.org/10.1002/ADMI.202001730.

[136] I. Lee, W.T. Kang, W.T. Kang, J.E. Kim, Y.R. Kim, Y.R. Kim, U.Y. Won, Y.H. Lee, W.J. Yu, Photoinduced Tuning of Schottky Barrier Height in Graphene/MoS2Heterojunction for Ultrahigh Performance Short Channel Phototransistor, ACS Nano. 14 (2020) 7574–7580. https://doi.org/10.1021/ACSNANO.0C03425/ASSET/IMAGES/LARGE/NN0C03425_0005.JPEG.

[137] H. Henck, D. Pierucci, J. Chaste, C.H. Naylor, J. Avila, A. Balan, M.G. Silly, M.C. Asensio, F. Sirotti, A.T.C. Johnson, E. Lhuillier, A. Ouerghi, Electrolytic phototransistor based on graphene-MoS2 van der Waals p-n heterojunction with tunable photoresponse, Appl Phys Lett. 109 (2016) 113103. https://doi.org/10.1063/1.4962551.

[138] D. Pierucci, H. Henck, C.H. Naylor, H. Sediri, E. Lhuillier, A. Balan, J.E. Rault, Y.J. Dappe, F. Bertran, P. le Fèvre, A.T.C. Johnson, A. Ouerghi, Large area molybdenum disulphide- epitaxial graphene vertical Van der Waals heterostructures, Sci Rep. 6 (2016). https://doi.org/10.1038/SREP26656.

[139] Y.C. Lin, R.K. Ghosh, R. Addou, N. Lu, S.M. Eichfeld, H. Zhu, M.Y. Li, X. Peng, M.J. Kim, L.J. Li, R.M. Wallace, S. Datta, J.A. Robinson, Atomically thin resonant tunnel diodes built from synthetic van der Waals heterostructures, Nature Communications 2015 6:1. 6 (2015) 1–6. https://doi.org/10.1038/ncomms8311.

[140] B. Pielić, D. Novko, I.Š. Rakić, J. Cai, M. Petrović, R. Ohmann, N. Vujičić, M. Basletić, C. Busse, M. Kralj, Electronic Structure of Quasi-Freestanding WS2/MoS2 Heterostructures, ACS Appl Mater Interfaces. 13 (2021) 50552–50563. https://doi.org/10.1021/ACSAMI.1C15412.

[141] Z. Zhang, P. Chen, X. Duan, K. Zang, J. Luo, X. Duan, Robust epitaxial growth of two-dimensional heterostructures, multiheterostructures, and superlattices, Science (1979). 357 (2017) 788–92. https://doi.org/10.1126/science.aan6814.

[142] P.K. Sahoo, S. Memaran, Y. Xin, L. Balicas, H.R. Gutiérrez, One-pot growth of two-dimensional lateral heterostructures via sequential edge-epitaxy, Nature. 553 (2018) 63–67. https://doi.org/10.1038/NATURE25155.

[143] C. Berger, A. Ougazzaden, J. Gigliotti, X. Li, S. Sundaram, D. Deniz, V. Prudkovskiy, J.P. Turmaud, Y. Hu, Y. Hu, F. Fossard, J.S. Mérot, A. Loiseau, G. Patriarche, Highly ordered boron nitride/epigraphene epitaxial films on silicon carbide by lateral epitaxial deposition, ACS Nano. 14 (2020) 12962–12971. https://doi.org/10.1021/ACSNANO.0C04164/ASSET/IMAGES/LARGE/NN0C04164_0004.JPEG.

[144] R. Xiang, T. Inoue, Y. Zheng, A. Kumamoto, Y. Qian, Y. Sato, M. Liu, D. Tang, D. Gokhale, J. Guo, K. Hisama, S. Yotsumoto, T. Ogamoto, H. Arai, Y. Kobayashi, H. Zhang, B. Hou, A. Anisimov, M. Maruyama, Y. Miyata, S. Okada, S. Chiashi, Y. Li, J. Kong, E.I. Kauppinen, Y. Ikuhara, K. Suenaga, S. Maruyama, One-dimensional van der Waals heterostructures, Science (1979). 367 (2020) 537–42. https://doi.org/10.1126/science.aaz2570.

[145] Y. Feng, H. Li, T. Inoue, S. Chiashi, S. v. Rotkin, R. Xiang, S. Maruyama, One-Dimensional van der Waals Heterojunction Diode, ACS Nano. 15 (2021) 5600–5609. https://doi.org/10.1021/ACSNANO.1C00657/ASSET/IMAGES/LARGE/NN1C00657_0007.JPEG.

[146] Y.C. Lin, R.K. Ghosh, R. Addou, N. Lu, S.M. Eichfeld, H. Zhu, M.Y. Li, X. Peng, M.J. Kim, L.J. Li, R.M. Wallace, S. Datta, J.A. Robinson, Atomically thin resonant tunnel diodes built from synthetic van der Waals heterostructures, Nat. Commun. 6 (2015) 7311. https://doi.org/10.1038/ncomms8311.

[147] N. Huo, J. Kang, Z. Wei, S.S. Li, J. Li, S.H. Wei, Novel and enhanced optoelectronic performances of multilayer MoS2-WS2 heterostructure transistors, Adv. Funct. Mater. 24 (2014) 7025–31. https://doi.org/10.1002/adfm.201401504.

[148] E. Rosencher, B. Vinter, P.G. Piva, Optoelectronics, (2002). https://doi.org/10.1017/CBO9780511754647.

[149] M. Massicotte, P. Frank, H.L. Koppens, Ultrafast optoelectronics in 2D materials and their heterostructures, 2017.

[150] J. Shang, X. Shen, C. Cong, N. Peimyoo, B. Cao, M. Eginligil, T. Yu, Observation of excitonic fine structure in a 2D transition-metal dichalcogenide semiconductor, ACS Nano. 9 (2015) 647–655. https://doi.org/10.1021/NN5059908.

[151] K. Hao, J.F. Specht, P. Nagler, L. Xu, K. Tran, A. Singh, C.K. Dass, C. Schüller, T. Korn, M. Richter, A. Knorr, X. Li, G. Moody, Neutral and charged inter-valley biexcitons in monolayer MoSe2, Nature Communications 2017 8:1. 8 (2017) 1–7. https://doi.org/10.1038/ncomms15552.

[152] S. Ovesen, S. Brem, C. Linderälv, M. Kuisma, T. Korn, P. Erhart, M. Selig, E. Malic, Interlayer exciton dynamics in van der Waals heterostructures, Communications Physics 2019 2:1. 2 (2019) 1–8. https://doi.org/10.1038/s42005-019-0122-z.

[153] J.S. Ross, P. Rivera, J. Schaibley, E. Lee-Wong, H. Yu, T. Taniguchi, K. Watanabe, J. Yan, D. Mandrus, D. Cobden, W. Yao, X. Xu, Interlayer Exciton Optoelectronics in a 2D Heterostructure p-n Junction, Nano Lett. 17 (2017) 638–643. https://doi.org/10.1021/ACS.NANOLETT.6B03398.

[154] Y. Chen, Y. Quek, Tunable bright interlayer excitons in few-layer black phosphorus based van der Waals heterostructures, 2d Mater. 5 (2018) 045031. https://doi.org/10.1088/2053-1583/AADF40.

[155] S. Latini, K.T. Winther, T. Olsen, K.S. Thygesen, Interlayer Excitons and Band Alignment in MoS2/hBN/WSe2 van der Waals Heterostructures, Nano Lett. 17 (2017) 938–945. https://doi.org/10.1021/ACS.NANOLETT.6B04275/ASSET/IMAGES/LARGE/NL-2016-042756_0006.JPEG.

[156] P.-H. Tan, Raman Spectroscopy of Two-Dimensional Materials, Springer Series in Materials Science. (2019) C1–C1. https://doi.org/10.1007/978-981-13-1828-3_12.

[157] A.C. Ferrari, J.C. Meyer, V. Scardaci, C. Casiraghi, M. Lazzeri, F. Mauri, S. Piscanec, D. Jiang, K.S. Novoselov, S. Roth, A.K. Geim, Raman spectrum of graphene and graphene layers, Phys Rev Lett. 97 (2006) 187401. https://doi.org/10.1103/PHYSREVLETT.97.187401/FIGURES/3/MEDIUM.

[158] C. Casiraghi, S. Pisana, K.S. Novoselov, A.K. Geim, A.C. Ferrari, Raman fingerprint of charged impurities in graphene, Appl Phys Lett. 91 (2007) 233108. https://doi.org/10.1063/1.2818692.

[159] J. Toporski, T. Dieing, O. Hollricher, eds., Confocal Raman Microscopy, 66 (2018). https://doi.org/10.1007/978-3-319-75380-5.

[160] A. Ferrari, J. Robertson, Interpretation of Raman spectra of disordered and amorphous carbon, Phys Rev B Condens Matter Mater Phys. 61 (2000) 14095–14107. https://doi.org/10.1103/PHYSREVB.61.14095.

[161] Interpretation of certain characteristics in Raman spectra of graphite and glassy carbon - NASA/ADS, (n.d.). https://ui.adsabs.harvard.edu/abs/1987OptSp..62..612B/abstract (accessed July 11, 2022).

[162] R. Schmidt, I. Niehues, R. Schneider, M. Drüppel, T. Deilmann, M. Rohlfing, S.M. de Vasconcellos, A. Castellanos-Gomez, R. Bratschitsch, Reversible uniaxial strain tuning in atomically thin WSe2, 2d Mater. 3 (2016) 021011. https://doi.org/10.1088/2053-1583/3/2/021011.

[163] T.M.G. Mohiuddin, A. Lombardo, R.R. Nair, A. Bonetti, G. Savini, R. Jalil, N. Bonini, D.M. Basko, C. Galiotis, N. Marzari, K.S. Novoselov, A.K. Geim, A.C. Ferrari, Uniaxial strain in graphene by Raman spectroscopy: G peak splitting, Grüneisen parameters, and sample orientation, Phys Rev B Condens Matter Mater Phys. 79 (2009) 205433. https://doi.org/10.1103/PHYSREVB.79.205433/FIGURES/6/MEDIUM.

[164] K. He, C. Poole, K.F. Mak, J. Shan, Experimental demonstration of continuous electronic structure tuning via strain in atomically thin MoS2, Nano Lett. 13 (2013) 2931–2936. https://doi.org/10.1021/NL4013166/SUPPL_FILE/NL4013166_SI_001.PDF.

[165] H.J. Conley, B. Wang, J.I. Ziegler, R.F. Haglund, S.T. Pantelides, K.I. Bolotin, Bandgap engineering of strained monolayer and bilayer MoS2, Nano Lett. 13 (2013) 3626–3630. https://doi.org/10.1021/NL4014748/SUPPL_FILE/NL4014748_SI_001.PDF.

[166] D. Lloyd, X. Liu, J.W. Christopher, L. Cantley, A. Wadehra, B.L. Kim, B.B. Goldberg, A.K. Swan, J.S. Bunch, Band Gap Engineering with Ultralarge Biaxial Strains in Suspended Monolayer MoS2, Nano Lett. 16 (2016) 5836–5841. https://doi.org/10.1021/ACS.NANOLETT.6B02615/ASSET/IMAGES/LARGE/NL-2016-02615M_0005.JPEG.

[167] S. Tongay, H. Sahin, C. Ko, A. Luce, W. Fan, K. Liu, J. Zhou, Y.S. Huang, C.H. Ho, J. Yan, D.F. Ogletree, S. Aloni, J. Ji, S. Li, J. Li, F.M. Peeters, J. Wu, Monolayer behaviour in bulk ReS2 due to electronic and vibrational decoupling, Nature Communications 2014 5:1. 5 (2014) 1–6. https://doi.org/10.1038/ncomms4252.

[168] Z. Peng, X. Chen, Y. Fan, D.J. Srolovitz, D. Lei, Strain engineering of 2D semiconductors and graphene: from strain fields to band-structure tuning and photonic applications, Light: Science & Applications 2020 9:1. 9 (2020) 1–25. https://doi.org/10.1038/s41377-020-00421-5.

[169] F. Xia, T. Mueller, Y.M. Lin, A. Valdes-Garcia, P. Avouris, Ultrafast graphene photodetector, Nat Nanotechnol. 4 (2009) 839–843. https://doi.org/10.1038/NNANO.2009.292.

[170] X. Duan, Y. Huang, R. Agarwal, C.M. Lieber, Single-nanowire electrically driven lasers, Nature 2003 421:6920. 421 (2003) 241–245. https://doi.org/10.1038/nature01353.

[171] K.K. Liu, W. Zhang, Y.H. Lee, Y.C. Lin, M.T. Chang, C.Y. Su, C.S. Chang, H. Li, Y. Shi, H. Zhang, C.S. Lai, L.J. Li, Growth of large-area and highly crystalline MoS 2 thin layers on insulating substrates, Nano Lett. 12 (2012) 1538–1544. https://doi.org/10.1021/NL2043612/SUPPL_FILE/NL2043612_SI_001.PDF.

[172] F.H. Yang, Modern metal-organic chemical vapor deposition (MOCVD) reactors and growing nitride-based materials, Nitride Semiconductor Light-Emitting Diodes (LEDs): Materials, Technologies and Applications. (2014) 27–65. https://doi.org/10.1533/9780857099303.1.27.

[173] Senkić Ana, Bajo Josip, Supina Antonio, Radatović Borna, Vujičić Nataša, Effects of CVD Growth Parameters on Global and Local Optical Properties of MoS2 Monolayers, in preparation, n.d.

[174] I. Niehues, A. Blob, T. Stiehm, R. Schmidt, V. Jadriško, B. Radatović, D. Čapeta, M. Kralj, S.M. de Vasconcellos, R. Bratschitsch, Strain transfer across grain boundaries in MoS2 monolayers grown by chemical vapor deposition, 2d Mater. 5 (2018) 031003. https://doi.org/10.1088/2053-1583/AABA9A.

[175] Unlocking the Potential of Molecular Beam Epitaxy - EE Times Asia, (n.d.). https://www.eetasia.com/unlocking-the-potential-of-molecular-beam-epitaxy/ (accessed July 11, 2022).

[176] W.P. Mccray, MBE deserves a place in the history books, (n.d.). www.nature.com/naturenanotechnology (accessed July 11, 2022).

[177] I. Shibasaki, N. Kuze, Mass production of sensors grown by MBE, Molecular Beam Epitaxy. (2013) 697–720. https://doi.org/10.1016/B978-0-12-387839-7.00031-2.

[178] V. Jadriško, B. Radatović, B. Pielić, C. Gadermaier, M. Kralj, N. Vujičić, Structural and optical characterization of nanometer sized MoS2/graphene heterostructures for potential use in optoelectronic devices, FlatChem. 34 (2022) 100397. https://doi.org/10.1016/J.FLATC.2022.100397.

[179] R. van Gastel, A.T. N'Diaye, D. Wall, J. Coraux, C. Busse, N.M. Buckanie, F.J. Meyer Zu Heringdorf, M. Horn Von Hoegen, T. Michely, B. Poelsema, Selecting a single orientation for millimeter sized graphene sheets, Appl Phys Lett. 95 (2009). https://doi.org/10.1063/1.3225554.

[180] J. Coraux, A.T. N'Diaye, M. Engler, C. Busse, D. Wall, N. Buckanie, F.J. Meyer Zu Heringdorf, R. van Gastel, B. Poelsema, T. Michely, Growth of graphene on Ir(111), New J Phys. 11 (2009). https://doi.org/10.1088/1367-2630/11/2/023006.

[181] J. Coraux, A.T. N'Diaye, C. Busse, T. Michely, Structural coherency of graphene on Ir(111), Nano Lett. 8 (2008) 565–570. https://doi.org/10.1021/NL0728874.

[182] J. Hall, B. Pielić, C. Murray, W. Jolie, T. Wekking, C. Busse, M. Kralj, T. Michely, Molecular beam epitaxy of quasi-freestanding transition metal disulphide monolayers on van der Waals substrates: A growth study, 2d Mater. 5 (2018). https://doi.org/10.1088/2053-1583/AAA1C5.

[183] A. Jain, P. Bharadwaj, S. Heeg, M. Parzefall, T. Taniguchi, K. Watanabe, L. Novotny, Minimizing residues and strain in 2D materials transferred from PDMS, Nanotechnology. 29 (2018). https://doi.org/10.1088/1361-6528/AABD90.

[184] D.A. Sanchez, Z. Dai, P. Wang, A. Cantu-Chavez, C.J. Brennan, R. Huang, N. Lu, Mechanics of spontaneously formed nanoblisters trapped by transferred 2D crystals, Proc. Natl Acad. Sci. USA. 115 (2018) 7884–9. https://doi.org/10.1073/pnas.1801551115.

[185] T. Ciuk, I. Pasternak, A. Krajewska, J. Sobieski, P. Caban, J. Szmidt, W. Strupinski, Properties of chemical vapor deposition graphene transferred by high-speed electrochemical delamination, Journal of Physical Chemistry C. 117 (2013) 20833–20837. https://doi.org/10.1021/JP4032139.

[186] D. Cao, H. Xiao, Q. Gao, X. Yang, C. Luan, H. Mao, J. Liu, X. Liu, Fabrication and improved photoelectrochemical properties of a transferred GaN-based thin film with InGaN/GaN layers, Nanoscale. 9 (2017) 11504–11510. https://doi.org/10.1039/C7NR03622A.

[187] J.D. Wood, G.P. Doidge, E.A. Carrion, J.C. Koepke, J.A. Kaitz, I. Datye, A. Behnam, J. Hewaparakrama, B. Aruin, Y. Chen, H. Dong, R.T. Haasch, J.W. Lyding, E. Pop, Annealing free, clean graphene transfer using alternative polymer scaffolds, Nanotechnology. 26 (2015). https://doi.org/10.1088/0957-4484/26/5/055302.

[188] I. Šrut Rakić, D. Čapeta, M. Plodinec, M. Kralj, Large-scale transfer and characterization of macroscopic periodically nano-rippled graphene, Carbon N Y. 96 (2016) 243–249. https://doi.org/10.1016/J.CARBON.2015.09.046.

[189] L. Koefoed, M. Kongsfelt, S. Ulstrup, A.G. Čabo, A. Cassidy, P.R. Whelan, M. Bianchi, M. Dendzik, F. Pizzocchero, B. Jørgensen, P. Bøggild, L. Hornekær, P. Hofmann, S.U. Pedersen, K. Daasbjerg, Facile electrochemical transfer of large-area single crystal epitaxial graphene from Ir(1 1 1), J Phys D Appl Phys. 48 (2015). https://doi.org/10.1088/0022-3727/48/11/115306.

[190] Z. Gong, Layer-Scale and Chip-Scale Transfer Techniques for Functional Devices and Systems: A Review, Nanomaterials 2021, Vol. 11, Page 842. 11 (2021) 842. https://doi.org/10.3390/NANO11040842.

[191] L. Gao, W. Ren, H. Xu, L. Jin, Z. Wang, T. Ma, L.P. Ma, Z. Zhang, Q. Fu, L.M. Peng, X. Bao, H.M. Cheng, Repeated growth and bubbling transfer of graphene with millimetre-size single-crystal grains using platinum, Nat Commun. 3 (2012). https://doi.org/10.1038/NCOMMS1702.

[192] L. Koefoed, M. Kongsfelt, S. Ulstrup, A.G. Čabo, A. Cassidy, P.R. Whelan, M. Bianchi, M. Dendzik, F. Pizzocchero, B. Jørgensen, P. Bøggild, L. Hornekær, P. Hofmann, S.U. Pedersen, K. Daasbjerg, Facile electrochemical transfer of large-area single crystal epitaxial graphene from Ir(1 1 1), J Phys D Appl Phys. 48 (2015). https://doi.org/10.1088/0022-3727/48/11/115306.

[193] H.S. Nalwa, A review of molybdenum disulfide (MoS2) based photodetectors: From ultra-broadband, self-powered to flexible devices, RSC Adv. 10 (2020) 30529–30602. https://doi.org/10.1039/D0RA03183F.

[194] B. Liu, Y. Chen, C. You, Y. Liu, X. Kong, J. Li, S. Li, W. Deng, Y. Li, H. Yan, Y. Zhang, High performance photodetector based on graphene/MoS2/graphene lateral heterostrurcture with Schottky junctions, J Alloys Compd. 779 (2019) 140–146. https://doi.org/10.1016/J.JALLCOM.2018.11.165.

[195] G. Froehlicher, E. Lorchat, S. Berciaud, Charge Versus Energy Transfer in Atomically Thin Graphene-Transition Metal Dichalcogenide van der Waals Heterostructures, Phys Rev X. 8 (2018). https://doi.org/10.1103/PHYSREVX.8.011007.

[196] J.I. Paredes, J.M. Munuera, Recent advances and energy-related applications of high quality/chemically doped graphenes obtained by electrochemical exfoliation methods, J Mater Chem A Mater. 5 (2017) 7228–7242. https://doi.org/10.1039/C7TA01711A.

[197] Y. Wang, Y. Zheng, X. Xu, E. Dubuisson, Q. Bao, J. Lu, K.P. Loh, Electrochemical delamination of CVD-grown graphene film: Toward the recyclable use of copper catalyst, ACS Nano. 5 (2011) 9927–9933. https://doi.org/10.1021/NN203700W.

[198] D. Brida, C. Manzoni, G. Cerullo, Phase-locked pulses for two-dimensional spectroscopy by a birefringent delay line, Optics Letters, Vol. 37, Issue 15, Pp. 3027-3029. 37 (2012) 3027–3029. https://doi.org/10.1364/OL.37.003027.

[199] A. Perri, B.E. Nogueira, D.E. Faria, D.C.T. Ferreira, D. Comelli, G. Valentini, F. Preda, D. Polli, A.M. de Paula, G. Cerullo, C. Manzoni, Hyperspectral imaging with a TWINS birefringent interferometer, Optics Express, Vol. 27, Issue 11, Pp. 15956-15967. 27 (2019) 15956–15967. https://doi.org/10.1364/OE.27.015956.

[200] MICROSTAT Microstat ™ liquid cryogen optical cryostats for microscopy, (n.d.).

[201] K. Bian, C. Gerber, A.J. Heinrich, D.J. Müller, S. Scheuring, Y. Jiang, Scanning probe microscopy, Nature Reviews Methods Primers 2021 1:1. 1 (2021) 1–29. https://doi.org/10.1038/s43586-021-00033-2.

[202] A.C. Anderson, M.E. Malinowski, P. Rev, E.J. Cotts, D.M. Miliotis, G.A. Northrop, G.A. Kneezel, A. v Granato, P.B. Bev, G. Binning, H. Rohrer, C. Gerber, E. Weibel, Surface Studies by Scanning Tunneling Microscopy, Phys Rev Lett. 49 (1982) 57. https://doi.org/10.1103/PhysRevLett.49.57.

[203] I. Horcas, R. Fernández, J.M. Gómez-Rodríguez, J. Colchero, J. Gómez-Herrero, A.M. Baro, WSXM: A software for scanning probe microscopy and a tool for nanotechnology, Review of Scientific Instruments. 78 (2007). https://doi.org/10.1063/1.2432410.

[204] C.Q.C.G. G Binnig, Atomic force microscope, Phys. Rev. Lett. 56 (1986) 930–933.

[205] Labs – Ultrafast spectroscopy group @Polimi, (n.d.). https://www.femtosecond.fisi.polimi.it/research/labs/ (accessed July 11, 2022).

[206] K.F. Mak, J. Shan, Photonics and optoelectronics of 2D semiconductor transition metal dichalcogenides, Nat Photonics. 10 (2016) 216–226. https://doi.org/10.1038/NPHOTON.2015.282.

[207] B. Radisavljevic, A. Radenovic, J. Brivio, V. Giacometti, A. Kis, Single-layer MoS2 transistors, Nat Nanotechnol. 6 (2011) 147–150. https://doi.org/10.1038/NNANO.2010.279.

[208] F.H.L. Koppens, T. Mueller, P. Avouris, A.C. Ferrari, M.S. Vitiello, M. Polini, Photodetectors based on graphene, other two-dimensional materials and hybrid systems, Nat Nanotechnol. 9 (2014) 780–793. https://doi.org/10.1038/NNANO.2014.215.

[209] F. Liu, Z. Chen, G. Fang, Z. Wang, Y. Cai, B. Tang, J. Zhou, S. Liang, V2O5 Nanospheres with Mixed Vanadium Valences as High Electrochemically Active Aqueous Zinc-Ion Battery Cathode, Nanomicro Lett. 11 (2019). https://doi.org/10.1007/S40820-019-0256-2.

[210] Y. Huang, E. Sutter, N.N. Shi, J. Zheng, T. Yang, D. Englund, H.J. Gao, P. Sutter, Reliable Exfoliation of Large-Area High-Quality Flakes of Graphene and Other Two-Dimensional Materials, ACS Nano. 9 (2015) 10612–10620. https://doi.org/10.1021/ACSNANO.5B04258.

[211] M. Chhowalla, H.S. Shin, G. Eda, L.J. Li, K.P. Loh, H. Zhang, The chemistry of two-dimensional layered transition metal dichalcogenide nanosheets, Nat Chem. 5 (2013) 263–275. https://doi.org/10.1038/NCHEM.1589.

[212] M. Bosi, Growth and synthesis of mono and few-layers transition metal dichalcogenides by vapour techniques: A review, RSC Adv. 5 (2015) 75500–75518. https://doi.org/10.1039/C5RA09356B.

[213] S. Vishwanath, P. Dang, H.G. Xing, Challenges and Opportunities in Molecular Beam Epitaxy Growth of 2D Crystals, Molecular Beam Epitaxy. (2018) 443–485. https://doi.org/10.1016/B978-0-12-812136-8.00017-7.

[214] L.A. Walsh, R. Addou, R.M. Wallace, C.L. Hinkle, Molecular Beam Epitaxy of Transition Metal Dichalcogenides, Molecular Beam Epitaxy. (2018) 515–531. https://doi.org/10.1016/B978-0-12-812136-8.00024-4.

[215] Y. Zhang, T.R. Chang, B. Zhou, Y.T. Cui, H. Yan, Z. Liu, F. Schmitt, J. Lee, R. Moore, Y. Chen, H. Lin, H.T. Jeng, S.K. Mo, Z. Hussain, A. Bansil, Z.X. Shen, Direct observation of the transition from indirect to direct bandgap in atomically thin epitaxial MoSe2, Nat Nanotechnol. 9 (2014) 111–115. https://doi.org/10.1038/NNANO.2013.277.

[216] M. Nakano, Y. Wang, Y. Kashiwabara, H. Matsuoka, Y. Iwasa, Layer-by-Layer Epitaxial Growth of Scalable WSe2 on Sapphire by Molecular Beam Epitaxy, Nano Lett. 17 (2017) 5595–5599. https://doi.org/10.1021/ACS.NANOLETT.7B02420.

[217] A. Ohtake, Y. Sakuma, Two-Dimensional WSe2/MoSe2Heterostructures Grown by Molecular-Beam Epitaxy, Journal of Physical Chemistry C. 125 (2021) 11257–11261. https://doi.org/10.1021/ACS.JPCC.1C02780.

[218] K. Lasek, J. Li, S. Kolekar, P.M. Coelho, L. Guo, M. Zhang, Z. Wang, M. Batzill, Synthesis and characterization of 2D transition metal dichalcogenides: Recent progress from a vacuum surface science perspective, Surf Sci Rep. 76 (2021). https://doi.org/10.1016/J.SURFREP.2021.100523.

[219] D. Chen, H. Xiao, J. Han, Nanopores in GaN by electrochemical anodization in hydrofluoric acid: Formation and mechanism, J Appl Phys. 112 (2012). https://doi.org/10.1063/1.4752259.

[220] D. Hwang, B.P. Yonkee, B.S. Addin, R.M. Farrell, S. Nakamura, J.S. Speck, S. DenBaars, Photoelectrochemical liftoff of LEDs grown on freestanding c-plane GaN substrates, Opt Express. 24 (2016) 22875. https://doi.org/10.1364/OE.24.022875.

[221] M.K. Kelly, R.P. Vaudo, V.M. Phanse, L. Goergens, O. Ambacher, M. Stutzmann, Large free-standing GaN substrates by hydride vapor phase epitaxy and laser-induced liftoff, Japanese Journal of Applied Physics, Part 2: Letters. 38 (1999). https://doi.org/10.1143/JJAP.38.L217/XML.

[222] M. Mikulics, J.G. Lu, L. Huang, P.L. Tse, J.Z. Zhang, J. Mayer, H. Hardtdegen, Laser micro annealing conditioning for the suppression of statistical scatter in freestanding Sb2Te3 nanowire resistance, FlatChem. 21 (2020). https://doi.org/10.1016/J.FLATC.2020.100164.

[223] M. Mikulics, H.H. Hardtdegen, Fully photon operated transmistor / all-optical switch based on a layered Ge1Sb2Te4 phase change medium, FlatChem. 23 (2020) 100186. https://doi.org/10.1016/J.FLATC.2020.100186.

[224] F. Dross, J. Robbelein, B. Vandevelde, E. van Kerschaver, I. Gordon, G. Beaucarne, J. Poortmans, Stress-induced large-area lift-off of crystalline Si films, Appl Phys A Mater Sci Process. 89 (2007) 149–152. https://doi.org/10.1007/S00339-007-4195-2.

[225] S.W. Bedell, D. Shahrjerdi, B. Hekmatshoar, K. Fogel, P.A. Lauro, J.A. Ott, N. Sosa, D. Sadana, Kerf-less removal of Si, Ge, and III-V layers by controlled spalling to enable low-cost PV technologies, IEEE J Photovolt. 2 (2012) 141–147. https://doi.org/10.1109/JPHOTOV.2012.2184267.

[226] D. Shahrjerdi, S.W. Bedell, C. Ebert, C. Bayram, B. Hekmatshoar, K. Fogel, P. Lauro, M. Gaynes, T. Gokmen, J.A. Ott, D.K. Sadana, High-efficiency thin-film InGaP/InGaAs/Ge tandem solar cells enabled by controlled spalling technology, Appl Phys Lett. 100 (2012). https://doi.org/10.1063/1.3681397.

[227] N. Fu, G.S. Sauer, S. Lin, Electrocatalytic Radical Dichlorination of Alkenes with Nucleophilic Chlorine Sources, J Am Chem Soc. 139 (2017) 15548–15553. https://doi.org/10.1021/JACS.7B09388.

[228] N. Ehlen, J. Hall, B. v. Senkovskiy, M. Hell, J. Li, A. Herman, D. Smirnov, A. Fedorov, V. Yu Voroshnin, G. di Santo, L. Petaccia, T. Michely, A. Grüneis, Narrow photoluminescence and Raman peaks of epitaxial MoS2 on graphene/Ir(1 1 1), 2d Mater. 6 (2019). https://doi.org/10.1088/2053-1583/AAEBD3.

[229] H. Hattab, A.T. N'Diaye, D. Wall, G. Jnawali, J. Coraux, C. Busse, R. van Gastel, B. Poelsema, T. Michely, F.J. Meyer Zu Heringdorf, M. Horn-Von Hoegen, Growth temperature dependent graphene alignment on Ir(111), Appl Phys Lett. 98 (2011). https://doi.org/10.1063/1.3548546.

[230] M. v. Bollinger, J. v. Lauritsen, K.W. Jacobsen, J.K. Nørskov, S. Helveg, F. Besenbacher, One-dimensional metallic edge states in MoS2, Phys Rev Lett. 87 (2001). https://doi.org/10.1103/PHYSREVLETT.87.196803.

[231] Z. Sun, S.K. Hämäläinen, J. Sainio, J. Lahtinen, D. Vanmaekelbergh, P. Liljeroth, Topographic and electronic contrast of the graphene moiré on Ir(111) probed by scanning tunneling microscopy and noncontact atomic force microscopy, Phys Rev B Condens Matter Mater Phys. 83 (2011). https://doi.org/10.1103/PHYSREVB.83.081415.

[232] Pielić Borna, Van der Waals epitaxy of two-dimensional transition metal disulphides, Faculty of Science, University of Zagreb, 2021.

[233] I. Šrut Rakić, D. Čapeta, M. Plodinec, M. Kralj, Large-scale transfer and characterization of macroscopic periodically nano-rippled graphene, Carbon N Y. 96 (2016) 243–249. https://doi.org/10.1016/J.CARBON.2015.09.046.

[234] K. Kouroupis-Agalou, A. Liscio, E. Treossi, L. Ortolani, V. Morandi, N.M. Pugno, V. Palermo, Fragmentation and exfoliation of 2-dimensional materials: A statistical approach, Nanoscale. 6 (2014) 5926–5933. https://doi.org/10.1039/C3NR06919B.

[235] L.A. Barrales-Mora, 2D and 3D Grain Growth Modeling and Simulation, (2008) 130. https://books.google.com/books?id=E3Q0YNZod0wC&pgis=1 (accessed July 12, 2022).

[236] E. Starodub, A. Bostwick, L. Moreschini, S. Nie, F. el Gabaly, K.F. McCarty, E. Rotenberg, In-plane orientation effects on the electronic structure, stability, and Raman scattering of monolayer graphene on Ir(111), Phys Rev B Condens Matter Mater Phys. 83 (2011). https://doi.org/10.1103/PHYSREVB.83.125428.

[237] Z.Y. Zhu, Y.C. Cheng, U. Schwingenschlögl, Giant spin-orbit-induced spin splitting in two-dimensional transition-metal dichalcogenide semiconductors, Phys Rev B Condens Matter Mater Phys. 84 (2011). https://doi.org/10.1103/PHYSREVB.84.153402.

[238] A.D. Yoffe, Low-dimensional systems: quantum size effects and electronic properties of semiconductor microcrystallites (zero-dimensional systems) and some quasi-two-dimensional systems, Adv Phys. 42 (1993) 173–262. https://doi.org/10.1080/00018739300101484.

[239] H. Zhang, Ultrathin Two-Dimensional Nanomaterials, ACS Nano. 9 (2015) 9451–9469. https://doi.org/10.1021/ACSNANO.5B05040.

[240] X. Fan, D.J. Singh, W. Zheng, Valence Band Splitting on Multilayer MoS2: Mixing of Spin-Orbit Coupling and Interlayer Coupling, Journal of Physical Chemistry Letters. 7 (2016) 2175–2181. https://doi.org/10.1021/ACS.JPCLETT.6B00693.

[241] T. Cheiwchanchamnangij, W.R.L. Lambrecht, Quasiparticle band structure calculation of monolayer, bilayer, and bulk MoS 2, Phys Rev B Condens Matter Mater Phys. 85 (2012). https://doi.org/10.1103/PHYSREVB.85.205302.

[242] K. Wang, B. Paulus, Tuning the binding energy of excitons in the MoS2monolayer by molecular functionalization and defective engineering, Physical Chemistry Chemical Physics. 22 (2020) 11936–11942. https://doi.org/10.1039/D0CP01239D.

[243] W. Lin, P. Zhuang, H. Chou, Y. Gu, R. Roberts, W. Li, S.K. Banerjee, W. Cai, D. Akinwande, Electron redistribution and energy transfer in graphene/MoS2 heterostructure, Appl Phys Lett. 114 (2019). https://doi.org/10.1063/1.5088512.

[244] T. Pham, P. Ramnani, C.C. Villarreal, J. Lopez, P. Das, I. Lee, M.R. Neupane, Y. Rheem, A. Mulchandani, MoS2-graphene heterostructures as efficient organic compounds sensing 2D materials, Carbon N Y. 142 (2019) 504–512. https://doi.org/10.1016/J.CARBON.2018.10.079.

[245] Y. Li, Z. Qi, M. Liu, Y. Wang, X. Cheng, G. Zhang, L. Sheng, Photoluminescence of monolayer MoS2 on LaAlO3 and SrTiO3 substrates, Nanoscale. 6 (2014) 15248–15254. https://doi.org/10.1039/C4NR04602A.

[246] Y. Cao, Z. Wang, Q. Bian, Z. Cheng, Z. Shao, Z. Zhang, H. Sun, X. Zhang, S. Li, H. Gedeon, L. Liu, X. Wang, H. Yuan, M. Pan, Phonon modes and photonic excitation transitions of MoS2 induced by top-deposited graphene revealed by Raman spectroscopy and photoluminescence, Appl Phys Lett. 114 (2019). https://doi.org/10.1063/1.5083104.

[247] D. Sercombe, S. Schwarz, O. del Pozo-Zamudio, F. Liu, B.J. Robinson, E.A. Chekhovich, I.I. Tartakovskii, O. Kolosov, A.I. Tartakovskii, Optical investigation of the natural electron doping in thin MoS 2 films deposited on dielectric substrates, Sci Rep. 3 (2013). https://doi.org/10.1038/SREP03489.

[248] F. Cadiz, E. Courtade, C. Robert, G. Wang, Y. Shen, H. Cai, T. Taniguchi, K. Watanabe, H. Carrere, D. Lagarde, M. Manca, T. Amand, P. Renucci, S. Tongay, X. Marie, B. Urbaszek, Excitonic linewidth approaching the homogeneous limit in MoS2-based van der Waals heterostructures, Phys Rev X. 7 (2017). https://doi.org/10.1103/PHYSREVX.7.021026.

[249] G. Moody, C. Kavir Dass, K. Hao, C.H. Chen, L.J. Li, A. Singh, K. Tran, G. Clark, X. Xu, G. Berghäuser, E. Malic, A. Knorr, X. Li, Intrinsic homogeneous linewidth and broadening mechanisms of

excitons in monolayer transition metal dichalcogenides, Nat Commun. 6 (2015). https://doi.org/10.1038/NCOMMS9315.

[250] J.F. Gonzalez Marin, D. Unuchek, K. Watanabe, T. Taniguchi, A. Kis, MoS2 photodetectors integrated with photonic circuits, NPJ 2D Mater Appl. 3 (2019). https://doi.org/10.1038/S41699-019-0096-4.

[251] G. Migliato Marega, Z. Wang, M. Paliy, G. Giusi, S. Strangio, F. Castiglione, C. Callegari, M. Tripathi, A. Radenovic, G. Iannaccone, A. Kis, Low-Power Artificial Neural Network Perceptron Based on Monolayer MoS2, ACS Nano. 16 (2022) 3684–3694. https://doi.org/10.1021/ACSNANO.1C07065.

[252] L. Gammelgaard, J.M. Caridad, A. Cagliani, D.M.A. MacKenzie, D.H. Petersen, T.J. Booth, P. Bøggild, Graphene transport properties upon exposure to PMMA processing and heat treatments, 2d Mater. 1 (2014). https://doi.org/10.1088/2053-1583/1/3/035005.

[253] H. Li, Q. Zhang, C.C.R. Yap, B.K. Tay, T.H.T. Edwin, A. Olivier, D. Baillargeat, From bulk to monolayer MoS 2: Evolution of Raman scattering, Adv Funct Mater. 22 (2012) 1385–1390. https://doi.org/10.1002/ADFM.201102111.

[254] K. Uchinokura, T. Sekine, E. Matsuura, Raman scattering by silicon, Solid State Commun. 11 (1972) 47–49. https://doi.org/10.1016/0038-1098(72)91127-1.

[255] S. Najmaei, P.M. Ajayan, J. Lou, Quantitative analysis of the temperature dependency in Raman active vibrational modes of molybdenum disulfide atomic layers, Nanoscale. 5 (2013) 9758–9763. https://doi.org/10.1039/C3NR02567E.

[256] S. Mignuzzi, A.J. Pollard, N. Bonini, B. Brennan, I.S. Gilmore, M.A. Pimenta, D. Richards, D. Roy, Effect of disorder on Raman scattering of single-layer Mo S2, Phys Rev B Condens Matter Mater Phys. 91 (2015). https://doi.org/10.1103/PHYSREVB.91.195411.

[257] G.P. Srivastava, I.O. Thomas, Temperature-dependent Raman linewidths in transition-metal dichalcogenides, Phys Rev B. 98 (2018). https://doi.org/10.1103/PHYSREVB.98.035430.

[258] S. Najmaei, Z. Liu, P.M. Ajayan, J. Lou, Thermal effects on the characteristic Raman spectrum of molybdenum disulfide (MoS 2) of varying thicknesses, Appl Phys Lett. 100 (2012). https://doi.org/10.1063/1.3673907.

[259] S. Sarkar, I. Maity, H.L. Pradeepa, G. Nayak, L. Marty, J. Renard, J. Coraux, N. Bendiab, V. Bouchiat, S. Das, K. Majumdar, M. Jain, A. Bid, Anharmonicity in Raman-active phonon modes in atomically thin MoS2, Phys Rev B. 101 (2020). https://doi.org/10.1103/PHYSREVB.101.205302.

[260] C. Lee, H. Yan, L.E. Brus, T.F. Heinz, J. Hone, S. Ryu, Anomalous lattice vibrations of single- and few-layer MoS2, ACS Nano. 4 (2010) 2695–2700. https://doi.org/10.1021/NN1003937/SUPPL_FILE/NN1003937_SI_001.PDF.

[261] N.A. Lanzillo, A. Glen Birdwell, M. Amani, F.J. Crowne, P.B. Shah, S. Najmaei, Z. Liu, P.M. Ajayan, J. Lou, M. Dubey, S.K. Nayak, T.P. O'Regan, Temperature-dependent phonon shifts in monolayer MoS2, Appl Phys Lett. 103 (2013). https://doi.org/10.1063/1.4819337.

[262] C. Thomsen, S. Reich, Double resonant raman scattering in graphite, Phys Rev Lett. 85 (2000) 5214–5217. https://doi.org/10.1103/PHYSREVLETT.85.5214.

[263] I. Pócsik, M. Hundhausen, M. Koós, L. Ley, Origin of the D peak in the Raman spectrum of microcrystalline graphite, J Non Cryst Solids. 227–230 (1998) 1083–1086. https://doi.org/10.1016/S0022-3093(98)00349-4.

[264] A. Jorio, Raman Spectroscopy in Graphene-Based Systems: Prototypes for Nanoscience and Nanometrology, ISRN Nanotechnology. 2012 (2012) 1–16. https://doi.org/10.5402/2012/234216.

[265] A.C. Ferrari, J. Robertson, Raman spectroscopy of amorphous, nanostructured, diamondlike carbon, and nanodiamond, Philosophical Transactions of the Royal Society of London. Series A: Mathematical, Physical and Engineering Sciences. 362 (2004) 2477–2512. https://doi.org/10.1098/RSTA.2004.1452.

[266] A. Eckmann, A. Felten, A. Mishchenko, L. Britnell, R. Krupke, K.S. Novoselov, C. Casiraghi, Probing the nature of defects in graphene by Raman spectroscopy, Nano Lett. 12 (2012) 3925–3930. https://doi.org/10.1021/NL300901A/SUPPL_FILE/NL300901A_SI_001.PDF.

[267] A. Grüneis, B. v. Senkovskiy, A. v. Fedorov, M. Hell, S. Michel, Ultrahigh Vacuum Optical Spectroscopy of Chemically Functionalized Graphene Nanoribbons, Encyclopedia of Interfacial Chemistry: Surface Science and Electrochemistry. (2018) 367–374. https://doi.org/10.1016/B978-0-12-409547-2.14168-X.

[268] L. Li, I. Lee, D. Lim, M. Kang, G.H. Kim, N. Aoki, Y. Ochiai, K. Watanabe, T. Taniguchi, Raman shift and electrical properties of MoS2 bilayer on boron nitride substrate, Nanotechnology. 26 (2015) 295702. https://doi.org/10.1088/0957-4484/26/29/295702.

[269] S. Karamat, S. Sonuşen, Çelik, Y. Uysalli, E. Özgönül, A. Oral, Synthesis of few layer single crystal graphene grains on platinum by chemical vapour deposition, Progress in Natural Science: Materials International. 25 (2015) 291–299. https://doi.org/10.1016/J.PNSC.2015.07.006.

[270] R.S. Weatherup, B. Dlubak, S. Hofmann, Kinetic control of catalytic CVD for high-quality graphene at low temperatures, ACS Nano. 6 (2012) 9996–10003. https://doi.org/10.1021/NN303674G/SUPPL_FILE/NN303674G_SI_001.PDF.

[271] S. Gilbertson, T. Durakiewicz, J.-X. Zhu, A.D. Mohite, A. Dattelbaum, G. Rodriguez, Direct measurement of quasiparticle lifetimes in graphene using time-resolved photoemission, Journal of Vacuum Science & Technology B, Nanotechnology and Microelectronics: Materials, Processing, Measurement, and Phenomena. 30 (2012) 03D116. https://doi.org/10.1116/1.4715440.

[272] I. Childres, L.A. Jauregui, J. Tian, Y.P. Chen, Effect of oxygen plasma etching on graphene studied using Raman spectroscopy and electronic transport measurements, New J Phys. 13 (2011) 025008. https://doi.org/10.1088/1367-2630/13/2/025008.

[273] H.A. Chen, W.C. Chen, H. Sun, C.C. Lin, S.Y. Lin, Scalable MoS2/graphene hetero-structures grown epitaxially on sapphire substrates for phototransistor applications, Semicond Sci Technol. 33 (2018) 025007. https://doi.org/10.1088/1361-6641/AAA3B7.

[274] X. Li, J. Wu, N. Mao, J. Zhang, Z. Lei, Z. Liu, H. Xu, A self-powered graphene–MoS2 hybrid phototransistor with fast response rate and high on–off ratio, Carbon N Y. 92 (2015) 126–132. https://doi.org/10.1016/J.CARBON.2015.03.064.

[275] Y. Liu, P. Stradins, S.H. Wei, Van der Waals metal-semiconductor junction: Weak Fermi level pinning enables effective tuning of Schottky barrier, Sci Adv. 2 (2016). https://doi.org/10.1126/SCIADV.1600069/SUPPL_FILE/1600069_SM.PDF.

[276] R. Kappera, D. Voiry, S.E. Yalcin, B. Branch, G. Gupta, A.D. Mohite, M. Chhowalla, Phase-engineered low-resistance contacts for ultrathin MoS2 transistors, Nature Materials 2014 13:12. 13 (2014) 1128–1134. https://doi.org/10.1038/nmat4080.

[277] H. Xu, J. Yi, X. She, Q. Liu, L. Song, S. Chen, Y. Yang, Y. Song, R. Vajtai, J. Lou, H. Li, S. Yuan, J. Wu, P.M. Ajayan, 2D heterostructure comprised of metallic 1T-MoS2/Monolayer O-g-C3N4 towards efficient photocatalytic hydrogen evolution, Appl Catal B. 220 (2018) 379–385. https://doi.org/10.1016/J.APCATB.2017.08.035.

[278] Physics of Semiconductor Devices, 3rd Edition | Wiley, (n.d.). https://www.wiley.com/en-us/Physics+of+Semiconductor+Devices%2C+3rd+Edition-p-9780470068328 (accessed July 12, 2022).

[279] D. Kufer, G. Konstantatos, Highly sensitive, encapsulated MoS2 photodetector with gate controllable gain and speed, Nano Lett. 15 (2015) 7307–13. https://doi.org/10.1021/acs.nanolett.5b02559.

[280] Y.C. Kim, V.T. Nguyen, S. Lee, J.Y. Park, Y.H. Ahn, Evaluation of Transport Parameters in MoS2/Graphene Junction Devices Fabricated by Chemical Vapor Deposition, ACS Appl Mater Interfaces. 10 (2018) 5771–5778. https://doi.org/10.1021/ACSAMI.7B16177/ASSET/IMAGES/LARGE/AM-2017-16177W_0005.JPEG.

[281] R. Doolen, R. Laitinen, F. Parsapour, D.F. Kelley, Trap state dynamics in MoS2 nanoclusters, Journal of Physical Chemistry B. 102 (1998) 3906–3911. https://doi.org/10.1021/JP9805252/ASSET/IMAGES/LARGE/JP9805252F00008.JPEG.

[282] C.I. Butoi, B.T. Langdon, D.F. Kelley, Electron-transfer dynamics in DTDCI/MoS2 and DTDCI/WS2 nanoclusters, Journal of Physical Chemistry B. 102 (1998) 9635–9639. https://doi.org/10.1021/JP983008S/ASSET/IMAGES/MEDIUM/JP983008SE00004.GIF.

[283] Z.X. Gan, L.Z. Liu, H.Y. Wu, Y.L. Hao, Y. Shan, X.L. Wu, P.K. Chu, Quantum confinement effects across two-dimensional planes in MoS2 quantum dots, Appl Phys Lett. 106 (2015) 233113. https://doi.org/10.1063/1.4922551.

[284] X. Zhang, Y. Zhang, Y. Wang, S. Kalytchuk, S. v. Kershaw, Y. Wang, P. Wang, T. Zhang, Y. Zhao, H. Zhang, T. Cui, Y. Wang, J. Zhao, W.W. Yu, A.L. Rogach, Color-switchable electroluminescence of carbon dot light-emitting diodes, ACS Nano. 7 (2013) 11234–11241. https://doi.org/10.1021/NN405017Q/ASSET/IMAGES/LARGE/NN-2013-05017Q_0005.JPEG.

[285] D. Gopalakrishnan, D. Damien, M.M. Shaijumon, MoS2 quantum dot-interspersed exfoliated MoS2 nanosheets, ACS Nano. 8 (2014) 5297–5303. https://doi.org/10.1021/NN501479E/SUPPL_FILE/NN501479E_SI_001.PDF.

[286] W. Qiao, S. Yan, X. He, X. Song, Z. Li, X. Zhang, W. Zhong, Y. Du, Effects of ultrasonic cavitation intensity on the efficient liquid-exfoliation of MoS 2 nanosheets, RSC Adv. 4 (2014) 50981–50987. https://doi.org/10.1039/C4RA09001B.

[287] C. Murray, C. van Efferen, W. Jolie, J.A. Fischer, J. Hall, A. Rosch, A. v. Krasheninnikov, H.P. Komsa, T. Michely, Band Bending and Valence Band Quantization at Line Defects in MoS2, ACS Nano. 14 (2020) 9176–9187. https://doi.org/10.1021/ACSNANO.0C04945/ASSET/IMAGES/MEDIUM/NN0C04945_M015.GIF.

[288] C. van Efferen, C. Murray, J. Fischer, C. Busse, H.P. Komsa, T. Michely, W. Jolie, Metal-insulator transition in monolayer MoS2 via contactless chemical doping, 2d Mater. 9 (2022) 025026. https://doi.org/10.1088/2053-1583/AC5D0F.

[289] Y. Ouyang, Y. Zhou, Y. Zhang, Q. Li, J. Wang, Double-edged roles of intrinsic defects in two-dimensional MoS2, Trends Chem. 4 (2022) 451–463. https://doi.org/10.1016/J.TRECHM.2022.02.006.

[290] R. Xiang, T. Inoue, Y. Zheng, A. Kumamoto, Y. Qian, Y. Sato, M. Liu, D. Tang, D. Gokhale, J. Guo, K. Hisama, S. Yotsumoto, T. Ogamoto, H. Arai, Y. Kobayashi, H. Zhang, B. Hou, A. Anisimov, M. Maruyama, Y. Miyata, S. Okada, S. Chiashi, Y. Li, J. Kong, E.I. Kauppinen, Y. Ikuhara, K. Suenaga, S. Maruyama, One-dimensional van der Waals heterostructures, Science (1979). 367 (2020) 537–42. https://doi.org/10.1126/science.aaz2570.

[291] Y. Feng, H. Li, T. Inoue, S. Chiashi, S. v. Rotkin, R. Xiang, S. Maruyama, One-dimensional van der Waals heterojunction diode, ACS Nano. 15 (2021) 5600–9. https://doi.org/10.1021/acsnano.1c00657.

[292] L. Britnell, R. v. Gorbachev, R. Jalil, B.D. Belle, F. Schedin, A. Mishchenko, T. Georgiou, M.I. Katsnelson, L. Eaves, S. v. Morozov, N.M.R. Peres, J. Leist, A.K. Geim, K.S. Novoselov, L.A. Ponomarenko, Field-effect tunneling transistor based on vertical graphene heterostructures, Science (1979). 335 (2012) 947–50. https://doi.org/10.1126/science.1218461.

[293] L. Liu, C. Liu, L. Jiang, J. Li, Y. Ding, S. Wang, Y.G. Jiang, Y. bin Sun, J. Wang, S. Chen, D.W. Zhang, P. Zhou, Ultrafast non-volatile flash memory based on van der Waals heterostructures, Nat. Nanotechnol. 16 (2021) 874–81. https://doi.org/10.1038/s41565-021-00921-4.

[294] H. Xu, J. Wu, Q. Feng, N. Mao, C. Wang, J. Zhang, High responsivity and gate tunable graphene-MoS2 hybrid phototransistor, Small. 10 (2014) 2300–6. https://doi.org/10.1002/smll.201303670.

[295] F. Withers, O. del Pozo-Zamudio, A. Mishchenko, A.P. Rooney, A. Gholinia, K. Watanabe, T. Taniguchi, S.J. Haigh, A.K. Geim, A.I. Tartakovskii, K.S. Novoselov, Light-emitting diodes by band-structure engineering in van der Waals heterostructures, Nat. Mater. 14 (2015) 301–6. https://doi.org/10.1038/nmat4205.

[296] Y.C. Lin, R.K. Ghosh, R. Addou, N. Lu, S.M. Eichfeld, H. Zhu, M.Y. Li, X. Peng, M.J. Kim, L.J. Li, R.M. Wallace, S. Datta, J.A. Robinson, Atomically thin resonant tunnel diodes built from synthetic van der Waals heterostructures, Nat. Commun. 6 (2015) 7311. https://doi.org/10.1038/ncomms8311.

[297] K. Godin, C. Cupo, E.H. Yang, Reduction in Step Height Variation and Correcting Contrast Inversion in Dynamic AFM of WS2 Monolayers, Scientific Reports 2017 7:1. 7 (2017) 1–11. https://doi.org/10.1038/s41598-017-18077-4.

[298] C.J. Shearer, A.D. Slattery, A.J. Stapleton, J.G. Shapter, C.T. Gibson, Accurate thickness measurement of graphene, Nanotechnology. 27 (2016). https://doi.org/10.1088/0957-4484/27/12/125704.

[299] V. Jadriško, B. Radatović, B. Pielić, C. Gadermaier, M. Kralj, N. Vujičić, Structural and optical characterization of nanometer sized MoS2/graphene heterostructures for potential use in optoelectronic devices, FlatChem. (2022) 100397. https://doi.org/10.1016/J.FLATC.2022.100397.

[300] T.S. Jeong, C.J. Youn, M.S. Han, J.W. Yang, K.Y. Lim, Electric-field-induced quenching effect of Raman scattering in Mg-doped p-GaN, Appl Phys Lett. 83 (2003) 3483. https://doi.org/10.1063/1.1623337.

[301] P.D. Cunningham, A.T. Hanbicki, K.M. McCreary, B.T. Jonker, Photoinduced Bandgap Renormalization and Exciton Binding Energy Reduction in WS2, ACS Nano. 11 (2017) 12601–12608. https://doi.org/10.1021/ACSNANO.7B06885/ASSET/IMAGES/LARGE/NN-2017-06885E_0009.JPEG.

[302] C. Zhang, H. Wang, W. Chan, C. Manolatou, F. Rana, Absorption of light by excitons and trions in monolayers of metal dichalcogenide Mo S2: Experiments and theory, Phys Rev B Condens Matter Mater Phys. 89 (2014) 205436. https://doi.org/10.1103/PHYSREVB.89.205436/FIGURES/8/MEDIUM.

[303] K.P. O'Donnell, X. Chen, Temperature dependence of semiconductor band gaps, Appl Phys Lett. 58 (1998) 2924. https://doi.org/10.1063/1.104723.

[304] Y. Wang, Z. Wang, W. Yao, G. bin Liu, H. Yu, Interlayer coupling in commensurate and incommensurate bilayer structures of transition-metal dichalcogenides, Phys Rev B. 95 (2017) 115429. https://doi.org/10.1103/PHYSREVB.95.115429/FIGURES/8/MEDIUM.

[305] X. Li, J.T. Mullen, Z. Jin, K.M. Borysenko, M. Buongiorno Nardelli, K.W. Kim, Intrinsic electrical transport properties of monolayer silicene and MoS2 from first principles, Phys Rev B Condens Matter Mater Phys. 87 (2013) 115418. https://doi.org/10.1103/PHYSREVB.87.115418/FIGURES/10/MEDIUM.

[306] N. Saigal, S. Ghosh, Evidence for two distinct defect related luminescence features in monolayer MoS2, Appl Phys Lett. 109 (2016) 122105. https://doi.org/10.1063/1.4963133.

[307] I. Niehues, R. Schmidt, M. Drüppel, P. Marauhn, D. Christiansen, M. Selig, G. Berghäuser, D. Wigger, R. Schneider, L. Braasch, R. Koch, A. Castellanos-Gomez, T. Kuhn, A. Knorr, E. Malic, M. Rohlfing, S. Michaelis De Vasconcellos, R. Bratschitsch, Strain Control of Exciton-Phonon Coupling in Atomically Thin Semiconductors, Nano Lett. 18 (2018) 1751–1757. https://doi.org/10.1021/ACS.NANOLETT.7B04868/ASSET/IMAGES/LARGE/NL-2017-04868T_0004.JPEG.

[308] S. Kim, A. Konar, W.S. Hwang, J.H. Lee, J. Lee, J. Yang, C. Jung, H. Kim, J.B. Yoo, J.Y. Choi, Y.W. Jin, S.Y. Lee, D. Jena, W. Choi, K. Kim, High-mobility and low-power thin-film transistors based on multilayer MoS2 crystals, Nat Commun. 3 (2012). https://doi.org/10.1038/NCOMMS2018.

[309] X. Liu, D. Qu, J. Ryu, F. Ahmed, Z. Yang, D. Lee, W. Jong Yoo, X. Liu, D. Qu, J. Ryu, F. Ahmed, Z. Yang, D. Lee, W.J. Yoo, P-Type Polar Transition of Chemically Doped Multilayer MoS2 Transistor, Advanced Materials. 28 (2016) 2345–2351. https://doi.org/10.1002/ADMA.201505154.

[310] H. Li, Z. Yin, Q. He, H. Li, X. Huang, G. Lu, D.W.H. Fam, A.I.Y. Tok, Q. Zhang, H. Zhang, Fabrication of Single- and Multilayer MoS2 Film-Based Field-Effect Transistors for Sensing NO at Room Temperature, Small. 8 (2012) 63–67. https://doi.org/10.1002/SMLL.201101016.

[311] S. Das, H.Y. Chen, A.V. Penumatcha, J. Appenzeller, High performance multilayer MoS2 transistors with scandium contacts, Nano Lett. 13 (2013) 100–105. https://doi.org/10.1021/NL303583V.

[312] X. Zhang, H. Nan, S. Xiao, X. Wan, X. Gu, A. Du, Z. Ni, K. (Ken) Ostrikov, Transition metal dichalcogenides bilayer single crystals by reverse-flow chemical vapor epitaxy, Nat Commun. 10 (2019). https://doi.org/10.1038/s41467-019-08468-8.

[313] M. Velický, M.A. Bissett, C.R. Woods, P.S. Toth, T. Georgiou, I.A. Kinloch, K.S. Novoselov, R.A.W. Dryfe, Photoelectrochemistry of Pristine Mono- and Few-Layer MoS2, Nano Lett. 16 (2016) 2023–2032. https://doi.org/10.1021/ACS.NANOLETT.5B05317/ASSET/IMAGES/NL-2015-05317Y_M006.GIF.

[314] J. Pei, J. Yang, R. Xu, Y.H. Zeng, Y.W. Myint, S. Zhang, J.C. Zheng, Q. Qin, X. Wang, W. Jiang, Y. Lu, Exciton and Trion Dynamics in Bilayer MoS2, Small. 11 (2015) 6384–6390. https://doi.org/10.1002/SMLL.201501949.

[315] B.W.H. Baugher, H.O.H. Churchill, Y. Yang, P. Jarillo-Herrero, Intrinsic electronic transport properties of high-quality monolayer and bilayer MoS2, Nano Lett. 13 (2013) 4212–4216. https://doi.org/10.1021/NL401916S/SUPPL_FILE/NL401916S_SI_001.PDF.

[316] H. Terrones, M. Terrones, Bilayers of transition metal dichalcogenides: Different stackings and heterostructures, J Mater Res. 29 (2014) 373–382. https://doi.org/10.1557/JMR.2013.284/FIGURES/7.

[317] J. Zhang, J. Wang, P. Chen, Y. Sun, S. Wu, Z. Jia, X. Lu, H. Yu, W. Chen, J. Zhu, G. Xie, R. Yang, D. Shi, X. Xu, J. Xiang, K. Liu, G. Zhang, J. Zhang, P. Chen, Y. Sun, S. Wu, X.B. Lu, H. Yu, W. Chen, J.Q. Zhu, R. Yang, D.X. Shi, X.L. Xu, G.Y. Zhang, J.H. Wang, K.H. Liu, Z.Y. Jia, J.Y. Xiang, G.B. Xie, Observation of Strong Interlayer Coupling in MoS2/WS2 Heterostructures, Advanced Materials. 28 (2016) 1950–1956. https://doi.org/10.1002/ADMA.201504631.

[318] A. Castellanos-Gomez, R. Roldán, E. Cappelluti, M. Buscema, F. Guinea, H.S.J. van der Zant, G.A. Steele, Local strain engineering in atomically thin MoS2, Nano Lett. 13 (2013) 5361–5366. https://doi.org/10.1021/NL402875M/SUPPL_FILE/NL402875M_SI_001.PDF.

[319] F. Carrascoso, H. Li, R. Frisenda, A. Castellanos-Gomez, Strain engineering in single-, bi- and tri-layer MoS2, MoSe2, WS2 and WSe2, Nano Research 2020 14:6. 14 (2020) 1698–1703. https://doi.org/10.1007/S12274-020-2918-2.

[320] R. Frisenda, Y. Niu, P. Gant, A.J. Molina-Mendoza, R. Schmidt, R. Bratschitsch, J. Liu, L. Fu, D. Dumcenco, A. Kis, D.P. de Lara, A. Castellanos-Gomez, Micro-reflectance and transmittance spectroscopy: a versatile and powerful tool to characterize 2D materials, J Phys D Appl Phys. 50 (2017) 074002. https://doi.org/10.1088/1361-6463/AA5256.

[321] R.J. Gelly, D. Renaud, X. Liao, B. Pingault, S. Bogdanovic, G. Scuri, K. Watanabe, T. Taniguchi, B. Urbaszek, H. Park, M. Lončar, Probing dark exciton navigation through a local strain landscape in a WSe2 monolayer, Nature Communications 2022 13:1. 13 (2022) 1–7. https://doi.org/10.1038/s41467-021-27877-2.

[322] R. Frisenda, A. Castellanos-Gomez, Strain creates a trion factory, Nature Photonics 2020 14:5. 14 (2020) 269–270. https://doi.org/10.1038/s41566-020-0625-x.

[323] S.B. Desai, G. Seol, J.S. Kang, H. Fang, C. Battaglia, R. Kapadia, J.W. Ager, J. Guo, A. Javey, Strain-induced indirect to direct bandgap transition in multilayer WSe 2, Nano Lett. 14 (2014) 4592–4597. https://doi.org/10.1021/NL501638A/SUPPL_FILE/NL501638A_SI_001.PDF.

[324] I. Niehues, P. Marauhn, T. Deilmann, D. Wigger, R. Schmidt, A. Arora, S. Michaelis De Vasconcellos, M. Rohlfing, R. Bratschitsch, Strain tuning of the Stokes shift in atomically thin semiconductors, Nanoscale. 12 (2020) 20786–20796. https://doi.org/10.1039/D0NR04557H.

[325] K. Xu, Y. Xu, H. Zhang, B. Peng, H. Shao, G. Ni, J. Li, M. Yao, H. Lu, H. Zhu, C.M. Soukoulis, The role of Anderson's rule in determining electronic, optical and transport properties of transition metal dichalcogenide heterostructures, Physical Chemistry Chemical Physics. 20 (2018) 30351–30364. https://doi.org/10.1039/C8CP05522J.

[326] A. Raja, M. Selig, G. Berghaüser, J. Yu, H.M. Hill, A.F. Rigosi, L.E. Brus, A. Knorr, T.F. Heinz, E. Malic, A. Chernikov, Enhancement of Exciton-Phonon Scattering from Monolayer to Bilayer WS2, Nano Lett. 18 (2018) 6135–6143. https://doi.org/10.1021/ACS.NANOLETT.8B01793.

[327] S. Dal Conte, C. Trovatello, C. Gadermaier, G. Cerullo, Ultrafast Photophysics of 2D Semiconductors and Related Heterostructures, Trends Chem. 2 (2020) 28–42. https://doi.org/10.1016/J.TRECHM.2019.07.007.

[328] Z. Nie, Y. Shi, S. Qin, Y. Wang, H. Jiang, Q. Zheng, Y. Cui, Y. Meng, F. Song, X. Wang, I.C.E. Turcu, X. Wang, Y. Xu, Y. Shi, J. Zhao, R. Zhang, F. Wang, Tailoring exciton dynamics of monolayer transition metal dichalcogenides by interfacial electron-phonon coupling, Communications Physics 2019 2:1. 2 (2019) 1–8. https://doi.org/10.1038/s42005-019-0202-0.

[329] M. Palummo, M. Bernardi, J.C. Grossman, Exciton radiative lifetimes in two-dimensional transition metal dichalcogenides, Nano Lett. 15 (2015) 2794–2800. https://doi.org/10.1021/NL503799T/SUPPL_FILE/NL503799T_SI_001.PDF.

[330] Z.E. Eroglu, O. Comegys, L.S. Quintanar, N. Azam, S. Elafandi, M. Mahjouri-Samani, A. Boulesbaa, Ultrafast dynamics of exciton formation and decay in two-dimensional tungsten disulfide (2D-WS2) monolayers, Physical Chemistry Chemical Physics. 22 (2020) 17385–17393. https://doi.org/10.1039/D0CP03220D.

[331] N.A. Vinogradov, A. Lyalin, T. Taketsugu, A.S. Vinogradov, A. Preobrajenski, Single-Phase Borophene on Ir(111): Formation, Structure, and Decoupling from the Support, ACS Nano. 13 (2019) 14511–14518. https://doi.org/10.1021/ACSNANO.9B08296.

[332] K.M. Omambac, M. Petrović, P. Bampoulis, C. Brand, M.A. Kriegel, P. Dreher, D. Janoschka, U. Hagemann, N. Hartmann, P. Valerius, T. Michely, F.J. Meyer Zu Heringdorf, M. Horn-Von Hoegen, Segregation-Enhanced Epitaxy of Borophene on Ir(111) by Thermal Decomposition of Borazine, ACS Nano. 15 (2021) 7421–7429. https://doi.org/10.1021/ACSNANO.1C00819.

[333] P. Giannozzi, O. Andreussi, T. Brumme, O. Bunau, M. Buongiorno Nardelli, M. Calandra, R. Car, C. Cavazzoni, D. Ceresoli, M. Cococcioni, N. Colonna, I. Carnimeo, A. Dal Corso, S. de Gironcoli, P. Delugas, R.A. Distasio, A. Ferretti, A. Floris, G. Fratesi, G. Fugallo, R. Gebauer, U. Gerstmann, F. Giustino, T. Gorni, J. Jia, M. Kawamura, H.Y. Ko, A. Kokalj, E. Kücükbenli, M. Lazzeri, M. Marsili, N. Marzari, F. Mauri, N.L. Nguyen, H. v. Nguyen, A. Otero-De-La-Roza, L. Paulatto, S. Poncé, D. Rocca, R. Sabatini, B. Santra, M. Schlipf, A.P. Seitsonen, A. Smogunov, I. Timrov, T. Thonhauser, P. Umari, N. Vast, X. Wu, S. Baroni, Advanced capabilities for materials modelling with quantum ESPRESSO, J. Phys.: Condens. Matter. 29 (2017) 465901. https://doi.org/10.1088/1361-648x/aa8f79.

[334] D.R. Hamann, Optimized norm-conserving Vanderbilt pseudopotentials, Phys Rev B Condens Matter Mater Phys. 88 (2013). https://doi.org/10.1103/PHYSREVB.88.085117.

[335] S. Baroni, S. de Gironcoli, A. Dal Corso, P. Giannozzi, Phonons and related crystal properties from density-functional perturbation theory, Rev Mod Phys. 73 (2001) 515–562. https://doi.org/10.1103/REVMODPHYS.73.515.

[336] A.T. N'Diaye, R. van Gastel, A.J. Martínez-Galera, J. Coraux, H. Hattab, D. Wall, F.J.M. Zu Heringdorf, M.H. von Hoegen, J.M. Gómez-Rodríguez, B. Poelsema, C. Busse, T. Michely, In situ observation of stress relaxation in epitaxial graphene, New J Phys. 11 (2009). https://doi.org/10.1088/1367-2630/11/11/113056.

[337] M. Velický, A. Rodriguez, M. Bouša, A. v. Krayev, M. Vondráček, J. Honolka, M. Ahmadi, G.E. Donnelly, F. Huang, H.D. Abrunã, K.S. Novoselov, O. Frank, Strain and Charge Doping Fingerprints of

the Strong Interaction between Monolayer MoS2and Gold, Journal of Physical Chemistry Letters. 11 (2020) 6112–6118. https://doi.org/10.1021/ACS.JPCLETT.0C01287.

[338] L. Li, J.F. Schultz, S. Mahapatra, Z. Lu, X. Zhang, N. Jiang, Chemically identifying single adatoms with single-bond sensitivity during oxidation reactions of borophene, Nat Commun. 13 (2022). https://doi.org/10.1038/S41467-022-29445-8.

[339] L. Li, J.F. Schultz, S. Mahapatra, X. Liu, C. Shaw, X. Zhang, M.C. Hersam, N. Jiang, Angstrom-Scale Spectroscopic Visualization of Interfacial Interactions in an Organic/Borophene Vertical Heterostructure, J Am Chem Soc. 143 (2021) 15624–15634. https://doi.org/10.1021/JACS.1C04380.

[340] X. Zhang, X.F. Qiao, W. Shi, J. bin Wu, D.S. Jiang, P.H. Tan, Phonon and Raman scattering of two-dimensional transition metal dichalcogenides from monolayer, multilayer to bulk material, Chem Soc Rev. 44 (2015) 2757–2785. https://doi.org/10.1039/C4CS00282B.

[341] Y. Zhang, H. Guo, W. Sun, H. Sun, S. Ali, Z. Zhang, R. Saito, T. Yang, Scaling law for strain dependence of Raman spectra in transition-metal dichalcogenides, Journal of Raman Spectroscopy. 51 (2020) 1353–1361. https://doi.org/10.1002/JRS.5908.

[342] C.H.A. Wong, M. Pumera, Electrochemical Delamination and Chemical Etching of Chemical Vapor Deposition Graphene: Contrasting Properties, Journal of Physical Chemistry C. 120 (2016) 4682–4690. https://doi.org/10.1021/ACS.JPCC.6B00329.

[343] S. Sheng, J. bin Wu, X. Cong, Q. Zhong, W. Li, W. Hu, J. Gou, P. Cheng, P.H. Tan, L. Chen, K. Wu, Raman spectroscopy of two-dimensional borophene sheets, ACS Nano. 13 (2019) 4133–4139. https://doi.org/10.1021/ACSNANO.8B08909.

[344] C.M. Chow, H. Yu, A.M. Jones, J. Yan, D.G. Mandrus, T. Taniguchi, K. Watanabe, W. Yao, X. Xu, Unusual Exciton-Phonon Interactions at van der Waals Engineered Interfaces, Nano Lett. 17 (2017) 1194–1199. https://doi.org/10.1021/ACS.NANOLETT.6B04944.

[345] P. Amsalem, L. Giovanelli, J.M. Themlin, T. Angot, Electronic and vibrational properties at the ZnPc/Ag(110) interface, Phys Rev B Condens Matter Mater Phys. 79 (2009). https://doi.org/10.1103/PHYSREVB.79.235426.

[346] N. Scheuschner, R. Gillen, M. Staiger, J. Maultzsch, Interlayer resonant Raman modes in few-layer MoS2, Phys Rev B Condens Matter Mater Phys. 91 (2015). https://doi.org/10.1103/PHYSREVB.91.235409.

[347] Y. Zhao, X. Luo, J. Zhang, J. Wu, X. Bai, M. Wang, J. Jia, H. Peng, Z. Liu, S.Y. Quek, Q. Xiong, Interlayer vibrational modes in few-quintuple-layer Bi2Te3 and Bi2Se3 two-dimensional crystals: Raman spectroscopy and first-principles studies, Phys Rev B Condens Matter Mater Phys. 90 (2014). https://doi.org/10.1103/PHYSREVB.90.245428.

[348] Q. Xiang, X. Yue, Y. Wang, B. Du, J. Chen, S. Zhang, G. Li, C. Cong, T. Yu, Q. Li, Y. Jin, Unveiling the origin of anomalous low-frequency Raman mode in CVD-grown monolayer WS2, Nano Res. 14 (2021) 4314–4320. https://doi.org/10.1007/S12274-021-3769-1.

[349] L. Liang, J. Zhang, B.G. Sumpter, Q.H. Tan, P.H. Tan, V. Meunier, Low-Frequency Shear and Layer-Breathing Modes in Raman Scattering of Two-Dimensional Materials, ACS Nano. 11 (2017) 11777–11802. https://doi.org/10.1021/ACSNANO.7B06551.

[350] M. Gao, X.W. Yan, J. Wang, Z.Y. Lu, T. Xiang, Electron-phonon coupling in a honeycomb borophene grown on Al(111) surface, Phys Rev B. 100 (2019). https://doi.org/10.1103/PHYSREVB.100.024503.

[351] T. Aizawa, S. Suehara, S. Otani, Phonon dispersion of a two-dimensional boron sheet on Ag(111), Phys Rev Mater. 5 (2021). https://doi.org/10.1103/PhysRevMaterials.5.064004.

[352] Raman spectrum of Polymethyl methacrylate | PublicSpectra, (n.d.). https://publicspectra.com/Raman/Polymethyl%20methacrylate (accessed July 12, 2022).

Valentino Jadriško, mag. phys.
● Adress: Radnička cesta 38, 10 000 Zagreb, Croatia ● DoB:08.02.1992. ● e-mail: vjadrisko@gmail.com

Education

2017 – **Postgraduate doctoral program: Atomic and Molecular physics; Faculty of Science, University of Zagreb**
- PhD thesis topic defence in 2020: "Optics of van der Waals Layered Systems'' under the mentorship of dr. sc. Nataša Vujičić

2011 – 2017 **Faculty of Science, Physics department: research physics, University of Zagreb**
- Master Thesis: "Optical properties of transition metal dichalcogenides"

Experience

2017 – **Institute of Physics, Zagreb, Croatia**
PhD candidate, mentor Dr. sc. Nataša Vujičić under the research group of Dr. sc. Marko Kralj
- Development of new advanced optical methods combining low temperature, strain & transport measurements
- Investigating optical properties at low temperatures, strain and different types of doping

February 2020 – **Work with group of prof. dr. Giulio Cerullo**
Politecnico di Milano, Milan, Italy
- Ultrafast dynamics of strained atomically thin 2D materials with Dr. Christoph Gadermaier and Dr. Luca Moretti
- Hyperspectral imaging of strained atomically thin 2D materials with Dr. Gianluca Valentini and Dr. Cristian Manzoni

2019 – 2021 **Faculty of Science, Physics department, University of Zagreb**
Teaching assistant, prof. dr. sc. Mario Novak & doc. dr. sc. Damjan Pelc
- Course "Advanced Laboratory Physics 1 & 2" and "Laboratory Physics 3 & 4 " in the 6th semester

2018 – 2019 **Zagreb University of Applied Sciences**
Teaching assistant, prof. Alemka Knapp
- Course "Physics" in the 1st semester

2014 – 2017 **Institute of Physics, Zagreb, Croatia**
Student, research group of Dr. sc. Marko Kralj
- Research related to growth of graphene on stepped surfaces under UHV conditions under the supervision of Dr. sc. Iva Šrut Rakić
- Investigation of optical properties of 2D materials under the supervision of Dr. sc. Nataša Vujičić

2012 – 2021 **Private tutor, Zagreb, Hrvatska**
- Working on daily basis with pupils and students from elementary to university level. Private schools Presto and Carpe Diem.

September 2015 – December 2015 **Institute for Semiconducting Physics, Johannes Kepler Universitat, Linz, Austria**
Research assistant, ERASMUS internship, research group of Dr. Georgios Katsaros
- Investigating spin orbit interaction in quantum dots towards enabling quantum computers
- Using COMSOL for simulating strain, electric potential & capacitance in SiGe nanostructures

Summer 2015 **Croatian Pension Investment Company Ltd., Zagreb, Croatia**
Intern, closed equity fund „Kapitalni fond"
- Valuation of companies using multiples, discounted cash flow and analysis of financial statements on Zagreb Stock Exchange

Science projects

2020 – **Bilateral project: "Organic semiconductor nanostructures on two-dimensional transition metal dichalcogenide substrates"**
Associate, Austrian-Croatian bilateral project led by Dr. Marko Kralj

2018 – **Photoexcitations in 2D Semiconductors**
Associate, Croatian National Science Foundation project led by Dr. Nataša Vujičić
- Researching optical properties of two dimensional materials & devices

2017 – **Center for Advanced Laser Techniques – CALT**
Associate, infrastructural project led by Dr. Damir Aumiler
- Procurement committees for new equipment & research

2017 – **Center of Excellence for Advanced Materials and Sensing Devices: Science of Graphene and Related 2D Structures**
Associate, infrastructural project led by Dr. Marko Kralj
- Procurement committees for new equipment & research

2017 – 2019 **Optical properties of transition metal dichalcogenide heterostructures**
Associate, Croatian National Science Foundation project led by Dr. Marko Kralj

November 2017 **Collaboration with group of Dr. R. Bratschitsch**
Associate, Westfälische Wilhelms-Universität Münster, Germany
- Investigation of single photon emitters, mechanical & optical properties under strain and ultrafast dynamics of CVD TMDs

March 2017 **Time resolved photoluminiscence, collaboration with Dr. sc. Luca Moretti and Dr. sc. C. D'Andrea**
Associate, Institute of Physics Zagreb, Croatia; Politecnico di Milano & Instituto Italiano di Tecnologia, Milano,
- Spectral and time dynamics of trion and exciton population in CVD grown MoS_2 monolayers for different levels of photodoping

January 2017 – February 2017 **Bilateral project: "Growth and characterization of functional 2D materials based on graphene and dichalcogenides"**
Associate, Institute of Physics Zagreb, Croatia and Jožef Stefan Institute, Ljubljana, Slovenia
- Investigation of optical properties using Raman and photoluminescence spectroscopy in room and low temperature

November 2016 **Bilateral project: "Intercalation of epitaxial dichalcogenides"**
Associate, Institute of Physics Zagreb, Croatia and Institute for Material Physics Universty of Munster, Germany
- Use of Ultra High Vacuum chamber, STM and LEED during growth procedure of 2D material TaS_2

October 2016 **Bilateral project: "Tuning many-body interactions in graphene by Cesium intercalation "**
Associate, Institute of Physics Zagreb, Croatia and Institute of Physics Belgrade, Serbia
- Investigation of CVD grown graphene on Ir(111) intercalated with cesium with Raman, photoluminescence, AFM and KPFM

Published and in preparation scientific articles

2022 **Strain influence on different stacking of bilayer TMDS**
V. Jadriško et al, **In preparation**

2022 **Vertical and lateral epitaxial grown WS_2/MoS_2/graphene heterostructures – manipulation and characterizazion**
V. Jadriško et al, **In preparation**

2022 **Structural and optical characterization of nanometer sized MoS_2/graphene heterostructures for potential use in optoelectronic devices**
V. Jadriško et al, **FlatChem Volume 34, July 2022, 100397**

2022 **Macroscopic Single-Phase Monolayer Borophene on Arbitrary Substrates**
B. Radatović, V. Jadriško, S. Kamal, M. Kralj, N. Vujičić, and M. Petrović, ***ACS Appl. Mater. Interfaces* 2022, 14, 18, 21727–21737**

February 2018 **Strain transfer across grain boundaries in MoS_2 monolayers grown by chemical vapor deposition**
Iris Niehues et al. 2018, **2D Mater. 5 031003**

Conferences & Schools

May 2022 **MRS Spring Meeting 2022**
Honolulu, USA
- Oral presentation: "**High optical quality TMD heterostructures obtained from MBE growth and subsequent transfer onto Si/SiO_2 wafers"**

October 2021 **Graphene 2021**
Grenoble, France,
- Poster presentation: "**Optical characterisation of MBE grown TMD heterostructures transferred to silicon wafers"**

January 2020 **Health Tech Hub Styria Pitch & Partner**
Graz, Austria
- Research & innovation in health sector

September 2019 **4th Annual European Forum on Nanoscale IR Spectroscopy**
Amsterdam, Netherlands
- s-SNOM applications and forefront research

September 2019 **Flatlands beyond Graphene**
Toulouse, France
- Poster presentation: **"Straining twisted bilayers of transition metal dichalcogenides"**

July 2019 **Summer School in Physics of Sensing and Processing**
Bologna, Italy

June 2018 & 2019 **Summer School for Young Physicist**
Veli Lošinj, Croatia

November 2018 **11th meeting of Croatian Physical Society – HFD**
Beli Manastir, Croatia
- Presentation title: **"Optical properties of flexible 2D materials"**

September 2018 **Flatlands beyond Graphene**

Leipzig, Germany
- Poster presentation: **"Modulation of optical response in atomically thin 2D materials"**

August 2017 **PHOTONICA 2017 - The International School and Conference on Photonics**
Belgrade, Serbia
- Poster presentation: **"Tuning exciton and trion population in MoS_2 with photodoping"**

June 2017 **"Workshop on Modern Trends in Solid State Quantum Physics"**
Institute for Science and Technology - IST, Klosterneuburg, Austria
- Overview of research related to topological insulator, 2D materials, nanophotonics and low temperature physics

January 2017 **"Winter School on Photophysics of Hybrid Interfaces"**
NanoSpectroscopy COST training school, Ambroz pod Krvavcem, Slovenia
- Photophysics of optoelectronic devices and introduction to latest achievements in this field

Scholarships and awards

October 2018 **Croatian Physical Society best presentation award on 11th meeting of HFD**
- Presentation title: **"Optical properties of flexible 2D materials"**

August 2017 **European Physical Society best poster award on PHOTONICA 2017 and Optical Society of America scholarship**
- Poster title: **"Tuning exciton and trion population in MoS_2 with photodoping"**

June 2015 **ERASMUS+ scholarship on the Institute for semiconducting physics of Johannes Kepler University, Linz, Austria**

Skills and other information

Languages
- Fluent in Croatian (mother language), English (FCE), basic German and Russian knowledge

Computer skills
- MS Office, Adobe Ilustrator, Origin Pro, C, COMSOL, LabView, Python

Interests
- Capital markets, boxing, Ving Tsun, automotive sport